Towards greener chemistry of battery : Using X-ray tomography in Li-O2 battery and a recyclable cathode

Zeliang Su

Thèse de Doctorat

Mention Chimie Analytique
Spécialité Tomographie aux Rayons X

présentée à ***l'Ecole Doctorale SCIENCES, TECHNOLOGIE, SANTÉ (ED 585)***

de l'Université de Picardie Jules Verne

Zeliang Su

pour obtenir le grade de Docteur

Towards Greener Chemistry of battery: Using X-ray Tomography in Li-O_2 battery and a recyclable cathode

Soutenue le 10 novembre 2021, après avis des rapporteurs, devant le jury d'examen :

Alexis Grimaud	**Chargé de Recherche, CNRS, Collège de France**	**Rapporteur**
Claire Villevieille	**Directrice de Recherche CNRS, Université Grenoble-Alpes**	**Rapporteuse**
Eric Maire	**Directeur de Recherche CNRS, INSA Lyon**	**Examinateur**
Etienne Decencière	**Directeur de Recherche, Mines ParisTech**	**Examinateur**
Alejandro A. Franco	**Professeur, Université de Picardie Jules Verne/LRCS**	**Directeur de thèse**
Arnaud Demortière	**Chargé de Recherche CNRS, LRCS**	**Co-directeur de thèse**
Stefan Freunberger	**Assistant Professeur, IST, Austria**	**Invité**
Julio Da Silva	**Chargé de Recherche CNRS, Institut Néel Grenoble**	**Invité**

"

We don't quit, we don't cower, we don't run.

We endure and we conquer.

"

– Kobe Bryant

To my friends, my family
Ziyin, and the future me

Preface

Chapter 2, in full, is a reprint of the material “X-ray Nanocomputed Tomography in Zernike Phase Contrast for Studying 3D Morphology of Li−O2 Battery Electrode” as it appears in ACS Applied Energy Materials, 2020, 3, 4093−4102. Zeliang Su, Vincent De Andrade, Sorina Cretu, Yinghui Yin, Michael J. Wojcik, Alejandro A. Franco, and Arnaud Demortière. The dissertation author was the primary investigator and author of this paper.

Chapter 3, in part, is currently on submission for publication of the material “Facile synthesis of a self-standing and recyclable binder-free cathode for Li-O_2 battery”. The dissertation author was the primary investigator and author of this paper.

Chapter 4, in full, is an adapted reprint of an in reviewing publication “Towards a Local In-situ X-ray nano-Computed Tomography under realistic cycling condition for Battery Research”. The dissertation author was the primary investigator and author of this paper.

Chapter 5, in part, is an adapted reprint of an in reviewing publication “Artificial Neural Network Approach for Multiphase Segmentation of Battery Electrode Nano-CT Images”. The dissertation author was the primary investigator and author of this paper.

Summary

To meet the challenge of energy demand for the total decarbonization of the society, greener and higher energy density technology must be developed. The Li-O_2 battery (LOB), considered as one of the most promising post Li-ion technologies, has been investigated. More specifically, 3D imaging technique using X-ray tomography has been developed to study the electrochemical reaction and transport phenomena in the cathode of this battery.

To overcome the transparency of the light elements in the cathode of LOB under X-ray, we deployed the in-line Zernike Phase Contrast during the acquisition. With this technique, the pore networks in the cathode at different state of discharge have been extracted. The non-dissolution of discharged products can also be observed in 3D.

A simple synthesis of a binder-free self-standing was developed. This material is self-standing and easily upscalable. A study of recyclability of this material was conducted. We showed that this material can be fully recovered by inexpensive solvent after the cycling.

We pushed forward our 3D investigation into 4D with time steps to understand the dynamics within the Li-O_2 battery. An in-house coin-cell like in situ cell was designed. The time-resolved volumes of the new material have been analyzed by a particle tracking algorithm.

Massive data has been collected during this work. The segmentation has become the most time-consuming in our data processing workflow. We have employed the deep learning to tackle this problem. The hyperparameters optimization problem has been discussed and some reflections on the ground truth have been brought out. We attempted to further generalize our neural network to a broader range of material. For this, the technique transfer learning has been employed.

Résumé

Pour relever le défi de la demande d'énergie pour la décarbonation totale de la société, une technologie plus verte et plus énergétique doit être développée. La batterie Li-O_2, considérée comme l'une des technologies post-Li-ion prometteuses, a été étudiée. Plus précisément, une technique d'imagerie 3D utilisant la tomographie par rayons X a été développée pour étudier la réaction électrochimique et les phénomènes de transport dans la cathode de cette batterie.

Pour s'affranchir de la transparence des éléments lumineux en cathode sous rayons X, nous avons déployé le Zernike Phase Contrast durant l'acquisition. Les réseaux de pores de la cathode à différents états de décharge ont été extraits. Une non-dissolution des produits rejetés a été étudiée en 3D.

Une synthèse facile d'un autoportant sans liant a été développée. Ce matériau est autonome et facilement évolutif. Une étude de sa recyclabilité a été menée. Nous avons montré que ce matériau peut être entièrement récupéré après le cyclage par un solvant peu coûteux.

Nous avons avancé notre enquête 3D en 4D avec des pas de temps pour comprendre la dynamique de la batterie Li-O_2. Une pile bouton interne comme une cellule in situ a été conçue. Les volumes résolus en temps ont été analysés par un algorithme de suivi des particules.

Des données massives ont été recueillies au cours de ce travail. La segmentation est devenue la plus chronophage dans notre workflow de traitement des données. Nous avons utilisé l'apprentissage en profondeur pour résoudre ce problème. Le problème d'optimisation des hyperparamètres a été discuté et quelques réflexions sur la vérité terrain ont été mises en évidence. Nous avons tenté de généraliser davantage notre réseau de neurones à un plus large éventail de matériaux. Pour cela, la technique d'apprentissage par transfert a été employée.

Acknowledgements

First and foremost, I am very grateful to the jury members, Dr Alexis Grimaud, Dr Claire Villevielle, Prof. Eric Maire, Dr. Etienne Decencière, Dr. Stefan Freunberger, and Dr. Julio Da Silva for their interest in this work and providing examination and advice on this work.

I would like also to express my gratitude to my supervisors, Dr. Arnaud Demortière and Prof. Alejandro. A. Franco. I am grateful for both constantly providing your guidance and advice in this project. Arnaud, I cannot imagine have come so far in this project, starting from catching up other teams to publishing papers. What a journey! It would not happen without all your great ideas. I would like to thank you for sharing your expertise of microscopist and for trying to help me to become one of them, although I am definitely not made for it. I will never thank you enough for helping me to improve the proposals, the writing, and the presentations. Alejandro, I should admit that you almost convinced me to study Li-ion battery with your super interesting and dynamic project. I just believed that the LOB was not 'desperate' (quoted from someone else) and there was still a lot to play with. You were always the one giving the wisest advice during this PhD. Surely, I still have a lot to learn from both of you and will never enough. I apologize that I am stubborn and very difficult to manage, because sometimes having different vision on the project and sometimes not stopping until proving myself wrong. So thank you both for being tolerant and at the right place and right time, coaching me in your styles. And also without your open mind, it would not have this rich experience and the current thesis, including plenty of topics. Your high standard on every detail of this work shows me the way to explore a better researcher and more rigorous professional on me.

Without forgetting all our collaborators, Dr. Vincent De Andrade, Dr. Michael J. Wojcik, Dr. Etienne Décencière, Dr. Christophe Le Bourlot, Dr. Israël Temprano, Dr. Elena Shevchenko, and Prof. Clare P. Grey. From whom, I have received precious advice and expertise in their domains on this work and avoid some detours.

My special acknowledgement goes to my colleague, flatmate, and pal, Tuan-Tu Nguyen. Without whom, this journey would have been way too limpid. Those moments, discussing the segmentation and the electrochemistry; those moments, hands shaking, heart beating to accomplish those one-shot experiments 5 a.m. in the morning on the laser machine; those moment, adrenaline and caffeine overdosed, no-matter-what solve the problem in 48h on the beamline… become the most memorizable experiences of my life.

There were also a lot of frustrations in this journey. I would not make it without the full support of my family and my girlfriend. Having someone to talk to was very important to get through the tough time during the Covid and the moments I got lost. And a deep thought to my grandma, I hope that she would be happy seeing all this.

My deepest appreciation goes to the big family LRCS, the team microscopy, Sorina, Cretu, Nicolas Folastre, Arash Jamali, Carine Davoisne, Loïc Dupont, and other colleagues and PhDs. Working in a big battery laboratory and discussing with the most brilliant scientists in the battery field gave me a lot of inspirations. Most importantly, aside the scientific research, they colored a bit the monotonous daily life of Amiens.

Lastly, I gratefully acknowledge the Fonds Europeen de Developpement Regional (FEDER), the University Picardie Jules Verne (UPJV), and the Ministry of Higher Education, Research and Innovation for funding this project and the Centre national de la research scientific (CNRS) and Platform de Microscopie Electronique (PME – UPJV) for equipment supports.

Chapter 1

Introduction

1.1. The Earth in 'fever'

By the time I am writing this thesis manuscript, the pandemic Covid-19 has hit globally over 125 millions of people and 2.5 million people have lost their lifes, and many countries are in the 3rd wave of lockdown. The US has changed a president, who cares about the climate and is willing to invest in greener energy. Meanwile, Tesla car company has sold in the globe 499 k electric vehicles within a year and Audi has announced stopping henceforth the R&D of combustion engine and become a fully EV manufacturer within 10 years. The global investment in battery manufacturing surges to 500 billions and the global battery production surpasses 500 GWh. To make it an affordable technology for everyone, many efforts have been devoted in lowering the price of Li-ion battery (LIB). For the first time in 2020, it has gone below 100 $ per kWh in massive production in China for the electric buses[1].

Although some climato-sceptics and politicians distort and devaluate the scientific evidences of the global warming for their own interests[2], it is an indisputable fact that the climate has been changed by anthropogenic activities[3–5]. In the past 70 years since the second world war, our world has been beneficial from the 2nd industrial revolution and the blooming technologies. From the combustion engine in the late 19th to computers and Internet of the 21st centuries, these technologies have revolutionized the way of transport, exchange and communication and accelerated the modernization of the society.

However, if we take a glimpse throughout today's society, the present economic system is built upon the petroleum, gas, and coal since the mid 50s of 20th centuries. Despite the efforts on the vulgarization of global warming in the last two decades, **there are still up to 93% (Fig 1a) of the worldwide energy consumption in 2019 are from fossil energy.** The crucial fact is that this partition of consumption tends to increase with the total energy consumption and seems not to be diminishing. The accompanied CO_2 emission has thus skyrocketed. According to the world's most reliable NASA Hawaiian Observatory, the CO_2 content in the atmosphere has increased by 32% since 1950 (in Figure 1a, data acquired and re-organized from Lüthi et al.[6]) and the monthly temperature of the Earth (in Figure 1b land and ocean included, data acquired and re-organized from[7]) in average has surpassed 1 degree since the beginning of the last centuries. Our planet has launched several warnings. Figure 1c shows the surface area of the Glaciers in north pole has substantially retreated. According to Aschwanden *et al.*[8], the sea level will increase by 7 meters, if all the glaciers in Greenland melts. They also predicted there will be 8-45% of melting by the end of this centuries, which contributes up to 33 cm of the lift of sea level. This is only an

iceberg of the whole apocalyptic scenario of global warming. It is thus urgent to 'chill down' our planet to dodge the worst scenario by limiting the temperature below 2 degrees (Fig 1d) before the end of the 21st centuries as announced in the Paris Agreement in 2016[3,9].

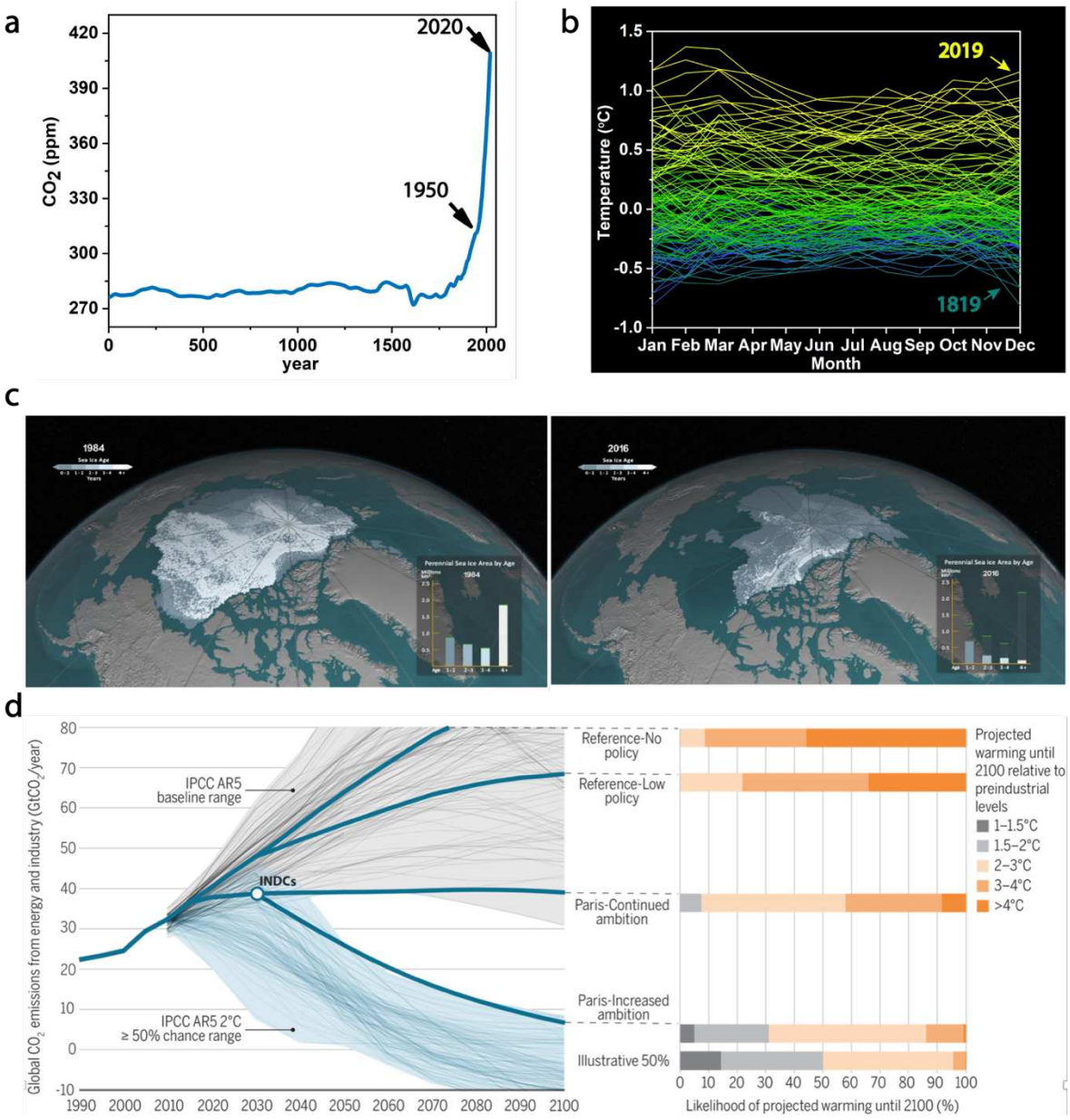

Figure 1. *a) the skyrocking concentration of CO_2 in the atmosphere b) the increasing global average temperature since 18th centuries c) a stark comparison of the rapidly retreating surface area of the Glaciers of northern pole. (images source: U.S. G Global Change Research Program[3]) d) different scenarios of temperatures by the end of this centuries (Adapted from source: [3] and [9])*

Recent studies[10–12] have opposed the traditional 'Richer is Greener' thought[13] of an N-shape economy. They have found that the reality is a U-shape correlation between the GDP growth and the CO_2 emission, where developed countries emit more carbon dioxide than the

developing ones. The outcomes of this are that digitalization and tertiarization did not help decreasing the emission. The climate is still being 'kidnapped' mainly due to the economic growth momentum that had been established upon the fossil fuel since long time. And unfortunately, the capital always sought to maximize the interests and assets. This should not be continued as our planet keep 'hitting the wall' and the anomaly climate events and disasters became more and more frequent (Fig 2, data adapted from EM-DAT[14]).

The past 2020 is an unforgettable year, not only because of the virus Covid-19 that took away world widely millions of lives but also all the tragic pictures of the climate that circulates on the internet. Wildfires did not halt this year all over the world (still in Brazil, in North America, and in Australia Fig 2a-c) burning down thousands of hectares of forest. The drought has caused the worst locust infestation in Africa and rapidly spread to India and China, 'looted' countless crop field (Fig 2d). The warmest winter of north pole (Fig 2e) ever recorded that changed the phenology and extinct species. And the floods inundated a lot of regions in east Asia (Fig 2f). The curves of the global warming and the number of disasters look familiar to the one of the Covid-19 burst out, remind us the catastrophe that might be ahead. Ignoring the gravity of the global warming is equivalent to the ignorance of the Covid-19 in early 2020, which brewed a disaster and finally inflicted irreversible damages.

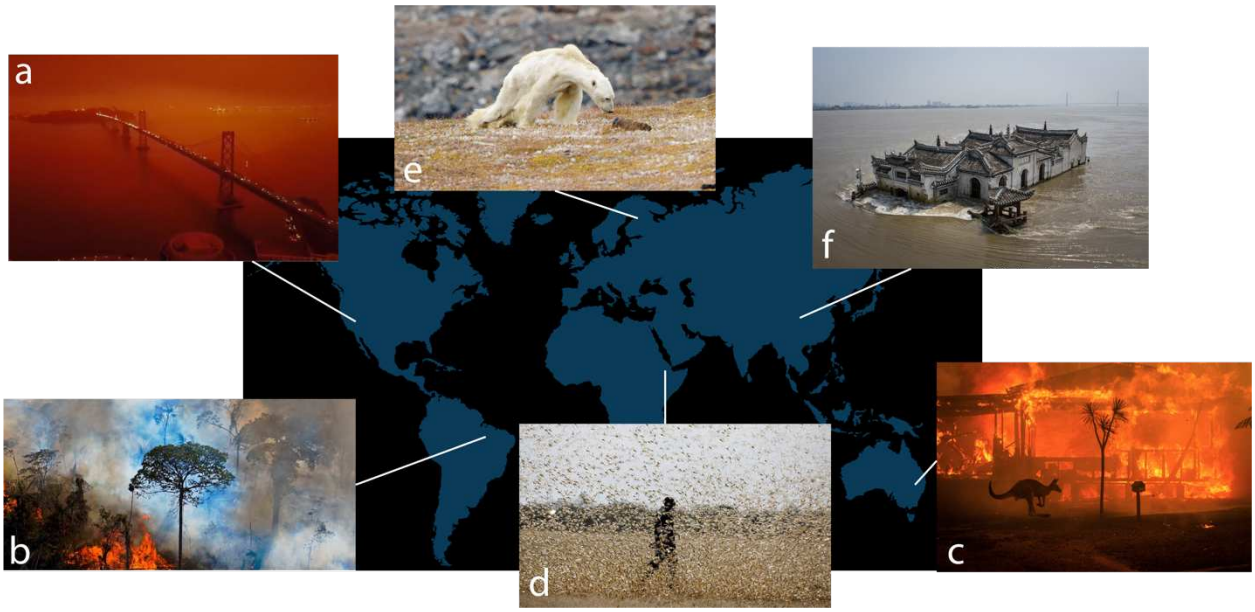

Figure 2. *Heart-wrenching pictures of meteorological and climatological disasters in 2020 caused by the unstable climate due to the global warming. a) the apocalyptic view in San Francesco of west coast of USA due to the forest fire in this region, as well as the 2020 nationwide wildfires in b) Amazon rainforest in Brazil (which was still going on in 2020, but less mediatized compared in 2019) and c) in Australia. d) the worst locust infestation in the past 70 years spread from Middle-Orient to Asia. e) the famous emaciated and starving polar bear capture by National-*

geographic photographer f) the heavy rains that leads to the severe flood in the central China (Images from Google and Bing, and data were adapted from EM-DAT the international disaster database)

1.2. Global energy consumption

After signing the Paris Agreement in 2016, where are we exactly now in the reduction of greenhouse gas emission? The CO_2 emission has decreased by 7 % in 2020, but at a cost of 4 % of GDP retreat globally[15]. According to a Union-Nation report (UN Environment Program) in 2019, we should reduce 7.6 % of emission[16] every year between 2020 and 2030 to meet the goal of the Paris Agreement. Hence, without finding substitution for the fossil fuel energy (as the GDP and the CO_2 is to some extend correlated), an economic activity reduction equivalent to every year a Covid should be achieved to make it possible of maintaining the planet under an increase of 1.5 ºC by the end of this century. This is a daunting challenge.

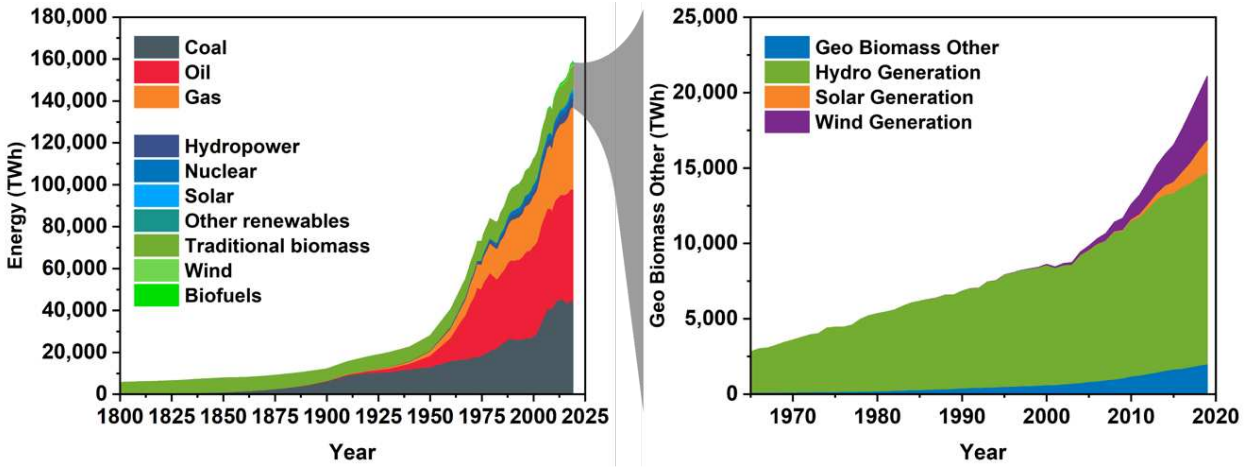

Figure 3. *Partitions of the global energy production and consumption evolution of the different primary energy consumption of the last two centuries, and on the right-hand side the evolution of the renewable energies*

From Fig 3a, we see the global energy consumption is rocketing since the 1950'. A clear progress of the utilization of clean energies can be seen. However, the part of clean and renewable energies generated by the solar, wind, hydro is still insignificant compared with the total consumption. Knowing that the exploitable clean solar and wind energy on earth is a magnitude above the global GDP[17–19], the room for the progress is immense. Due to the intermittent characters of these energy resources, the daily peaks of energy demand and production are not superposed. The excess energy generated should be converted into electrochemical (e.g., battery) or chemical (e.g., hydrogen) storage systems to allow to redistribute during the absence of sun and wind[19]. The only way to reverse CO_2 emission is to accelerate this economic transition of fossil fuel energy to the renewable one.

1.3. Analysis of EV market, richness of resources

Apart from the zero emission, the EVs have other advantages such as higher energy conversion rate and lower consumption (Table 1). Although the range of EVs in one charge can roughly catch up with the gasoline vehicles, up to date the time of charging and the number of charger facilities are still the main concerns of people to choose the EVs. However, the accelerations and the silence interior of the cockpit in EVs are the main attractive points. In some region, where the electricity is cheap, commute with EVs is more beneficial than a gasoline car.

	EV (Tesla 3)	Combustion Engine (2020)
Consumption (kWh/100km)	11.9	83.66 (9.4L gasoline 1L gasoline = 8.9 kWh)
Energy Price ($/100km)	1.57	6.35
Capacity (kWh)	100	400 – 580 (Average tank size 45 – 65 L)
Power	260 - 430 kW (349 - 644 hp)	250 - 375 kW (340 - 503hp)
Power-to-weight-ratio (kW/kg)	0.12	0.65
Propulsion system weight (kg)	480	381
Weight (kg)	1612 - 1847	1200 - 2000

Table 1. *Comparison of EV and combustion vehicle. The prices here is estimated with the 2019 US territory data and can vary according to the region.*

In 2020, the car sales are 280 M, 220 M, 273 M in EU, China, and US respectively. If replacing all these cars in these three regions by EVs that are equipped with 100 kWh battery packs, it represents a potential market of **77 TWh of battery**. However, it is reported that 60 M of vehicles enter the market every year (Figure 4) but merely 2.5 M (4%) of them are EVs. Highlight that the number one seller Tesla have delivered in worldwide an unprecedent score of 499 550 cars, with a total around 50 GWh of battery.

The forecast of the demand of Li-ion battery will surge from 285 GWh in 2019 to 2000 GWh in horizon 2030, production expands from 564 GWh to 2068 GWh by 2028 to equip 40 million

EVs[20]. Several countries have launched billions dollars production projects to meet this immense demand of battery in the coming years[21]. Nonetheless, we see that the current production is still in GWh range, which is a magnitude below the total potential TWh market. This is already challenging by decarbonizing the transport sector. Moreover, from the chart in Figure 4, we see that the decarbonization hinges not only on the electrification of vehicles but also in other sectors. The transport sector represents only 14% of the global energy consumption not even considering other energy intensive sectors such as agriculture and industry. In a word, the production of Li-ion battery (LIB) is currently in strong deficit and cannot satisfy the demand in the next few years.

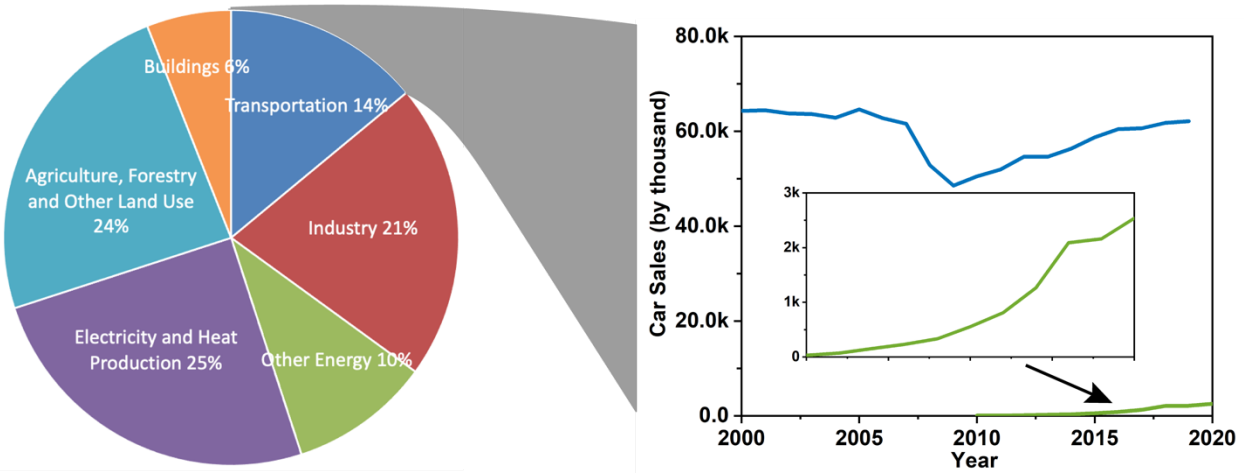

Figure 4. ***The structure of energy consumption in different domains.*** *The graph on the right shows the total car sales in blue and the electric vehicles sales evolution in green. The graph shows that the electrification starts to take off but still represents a small portion of the global car sales*

So why is it difficult the decarbonization? Part of it is because the scarcity of raw materials in the current Li-ion technology. It is well known that elements such as the cobalt is important in the Nickel-Manganese-Oxide cathode in Li-ion battery technology for the thermal stability and cyclability. This metal is a side-product from the mining of copper and nickel[22,23]. The main producer of cobalt locates in central-Africa, where its extraction is strongly dependent of the regional stability and geopolitics. With the expanding market of EVs, the surging demand of Li-ion battery will require more cobalt in the next few years. The price of battery will become more sensitive to the production of cobalt. Nowadays, the battery cost represents almost a third of the EV and is a main discriminator for the customer acceptance. Lowering the dependency of cobalt and the price of battery is a common goal of the EV manufacturers.

1.4. Heading to new chemistry for battery

Indeed, after 20 years of development since the 90s the Li-ion battery has almost reached the ceiling of its theoretical capacity. To accelerate the electrification, new battery technologies must be cheap, safe, low-carbon footprint during manufacturing in a large-scale, and a realizable unexpensive way of after lifespan treatement. To lessen the dependency of scarce elements and to break through the ceiling of existing LIB technology, new chemistries such as all-solid-state, Li-sulfur, and Li-O_2 batteries emerged as promising alternatives.

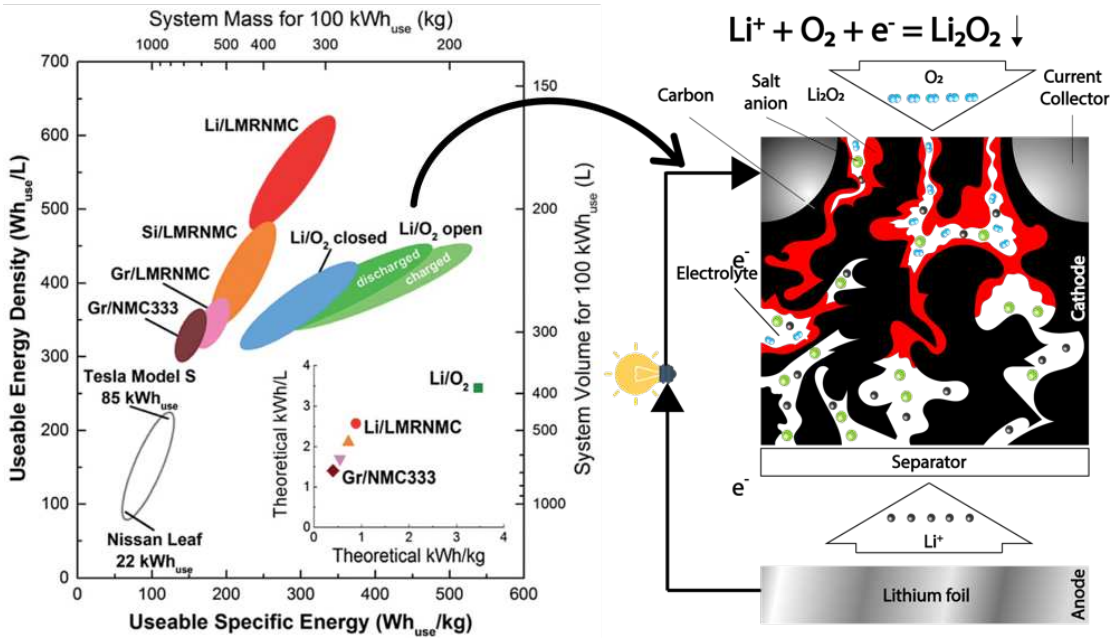

Figure 5. *(left)* ***the Ragone plot*** *of different battery technologies. Graph from K. G. Gallagher et al[24]. (right)* ***the schema*** *of principle of the Li-O_2 battery (LOB) adapted from Z. Su et al.[25].*

Some of these technologies are in the phase of maturation for upscaling and might be seen in certain applications in the next few years. For instances, start-ups like Solid Power have announced an all-solid-state battery prototype of 330 Wh/kg and is aiming for 400 Wh/kg by 2022. Another company, QuantumScape endosed by Nobel Prize Laureate Prof. Wittingham, has gone in public with their oxide-based electrolyte combining with the NMC cathode and the lithium foil. On the other hand, Oxis is an UK Li-sulfur company has already commercialized several models of Li-sulfur battery pack around 400-500 Wh/kg. However, with the highest specific energy among the mentioned technologies, the LOB (Figure 5 right), invented in 1996 by Abraham et al.[26], remains unready for upscaling. There is still a lot of unknown and debates in LOB. We will provide an overview of the issues in LOB in the following section.

1.5. State-of-the-art of Lithium-Oxygen Battery (LOB)

There are still a lot of challenges not solved in each part of LOB. Starting from the anode, the oxygen can cross over the electrolyte and react chemically with the lithium foil. The protection of lithium metal is hence necessary. The dendrite is also a concern for longer lifespan. The challenges with the electrolyte design are as difficult as for the anodic one. The well-studied and common electrolytes such as glymes for LOB have a O_2 solubility in range of mmol/L[27,28] at 1 atmosphere, which is unsignificant compared to the concentration of lithium cation. This limiting solubility of oxygen is the hindering factor for high C-rate application of LOB. People also search mediator for[29–31] the OER of cathode during the charge since the discharge product Li_2O_2 is hard to be electrochemically decomposed. For the same purpose, catalyst is used in the cathode. Franco *et al.* had carried out modeling[32–34] and qualitative studies to understand the mass transport within the cathode. And they further proposed sophisticated material structure to overcome the pore clogging problem[35,36].

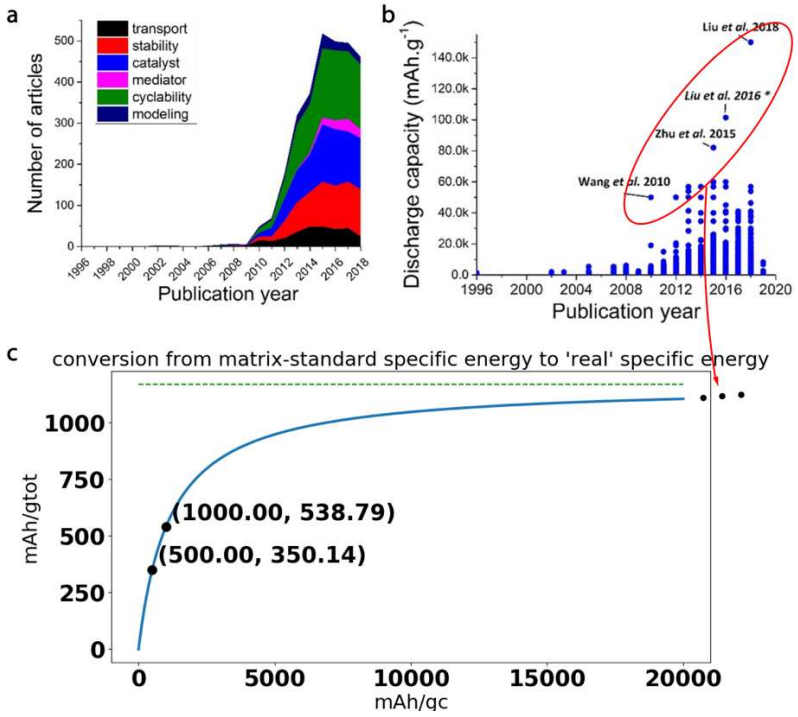

Figure 6. *a) text-mining categorized 1803 LOB articles according to 6 different topics between 1996-2018. b) from these articles, the extracted specific energies calculated by the mass of the porous matrix cathode material. Graphs in a) and b) are copied from A.Torayev et al.[37] c) the curve of conversion from mAh/g_{matrix} to the real specific energy expressed in mAh/g_{total} taking into account the mass of Li_2O_2. This conversion approaches the* ***asymptote expressed as*** $\frac{2\times F}{M_{Li2O2}} = 1168\ mAh/g$. *It is highlighted by the green dash line in c). And the equivalent specific energy is* ***2920Wh/kg with an average operating plateau at 2.5V.***

In the research field, scientists have deeply investigated in LOB in the past decades. Figure 6a plots the number of LOB publications per year in the last two decades from a work of Torayev *et al.*[37]. They analyzed the topic of 1803 papers by a text mining algorithm. We see that the main

direction of investigation and the most difficult obstacle of LOB is the cyclability, the catalyst and the stability. Among the 1.8 k articles analyzed by Torayev *et al.*, they have extracted the capacity in each article and have identified several articles, which reported striking discharge capacity (Fig 6b).

To elucidate the real capacity of LOB, they also pointed out that in contrast of the typical Li-ion battery, the real capacity of LOB should consider the mass of the product lithium peroxide as shown in Figure 6c, not the mass of matrix material like in most LOB papers. The carbon or other material are only served as a conductive matrix, hosting the discharge product Li_2O_2. The real active material is the oxygen dissolved in the electrolyte. Hence, more peroxide the matrix material can host, closer will approach the specific energy of lithium peroxide, which is **1168 mAh/g**.

Table 2 lists non exhaustively the main challenges and topics in each part of LOB. At the anode part, at high current density, the lithium ion will be reduced and deposited at some preferential area forming dendrite[38–40] or inactive lithium[41]. The dendrite can perforate the separator causing an internal short circuit. The second issue of the anode stems from the dissolved oxygen in the electrolyte, which can react chemically with the lithium or causing more complex electrochemical reaction during the cycling. Scientists used to develop film or other protection materials for limiting the access of oxygen onto the lithium.

On the electrolyte side, problems were often linked to the solubility of oxygen, which limits the high-rate application. Researchers are also looking for additives as redox mediator to facilitate the dissolution of peroxide during the charge. Other salts or additives such as $LiNO_3$ (chemically react with lithium forming Li_2O)[42] can form protective layer on the anode to prevent the passivation of oxygen.

Anode	Separator | Electrolyte	Cathode*
Dendrite Li protection O_2 crossover …	Mediator O_2 solubility O_2 diffusivity and permeability …	Catalyst Mass transport* Pore clogging* Cyclability* Side reaction / by-product …

Table 2. *A non-exhaustive table listing the problematics and topics in the LOB. The aspects that we investigated in this thesis are marked in red.*

On the cathode, the formed lithium peroxide is insulating[43,44]. And dissolving it during the charging is often difficult resulting in high over-potential. It is often believed that the 'sudden death' of LOB is due to the pore clogging by the accumulative non-dissolved lithium peroxide along the

cycling. Recent research focuses on developing porous materials and those with OER catalytic characteristic. It is well known that the porosity of the cathode material plays important role on the mass transport[45] in LOB. The other aspects, such as side reactions and by-products[46] during the cycling, are also frequently discussed in the literature.

For the above issues in LOB, there are promising work arounds reported in the recent literatures. We give herein a general overview on the latest works of LOB. The reversibility issue of lithium has been clearly reported in the references[47,48]. In these works, the irreversible formation of a transition layer on the lithium can be clearly seen by X-ray micro-CT (Fig 7a). A layer composed mainly by LiOH, lithium carbonate and some dead lithium that lost contact is formed during the cycling. This layer accumulates on thickness during the cycling and can reach few hundred µm. Hence, the cell failure is induced by this thick passivation layer, blocking the access in the volume of the lithium ions. To prevent the formation of this passivation layer, several groups use the ceramic ionic conductor[49] ceramic membrane and other gel or solid electrolyte[26,50] to isolate the lithium from the oxygen. However, this ceramic is monopolized by the Japanese and is extremely expensive and impossible to use in a large scale. Simple protections of lithium can be using the boric acid[51], and the 1,4-dioxacyclohexane (DOA)[52] that polymerize chemically at the surface of the lithium. Additives such as indium iodide[53] or salt LiTFSI[31] with weak fluorine bounding can form a protective layer *in situ* and electrochemically during the cycling. Other groups proposed also physical barrier against the moisture and oxygen such in (Fig 7b).

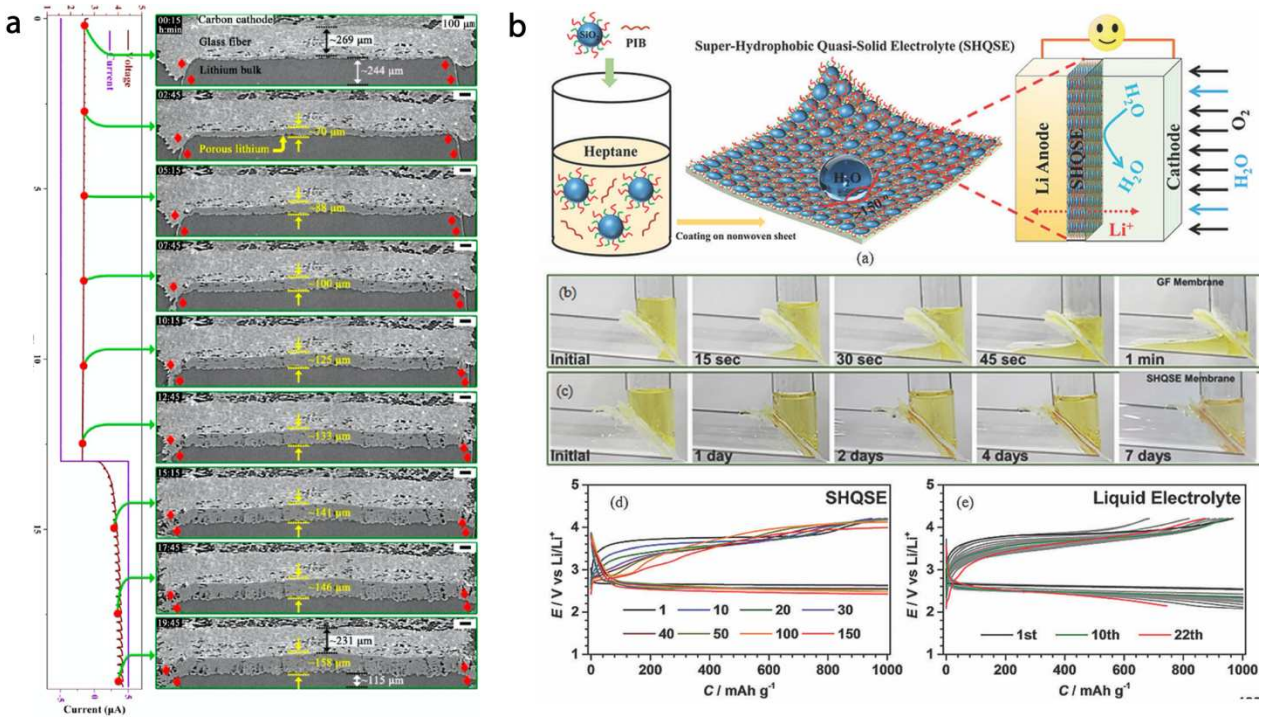

Figure 7. *Latest outstanding papers attempted to solve different issues in LOB. a) Menke et al.[48] used the micro-CT to show the irreversible layer formed on the anode lithium, which is harmful for the performance and often been ignored by the LOB community. b) A hydrophobic protection layer for the anode developed by Wu et al.[54]*

The addition of redox mediators is well known promoting the dissolution of Li_2O_2 in charging. The redox mediator firstly gets oxidized at the surface of carbon. It then diffuses in the electrolyte and further reacts with the peroxide, giving oxygen and lithium cation. For instances, TEMPO[29,31] and LiI[30,55] (Fig 8) are redox mediators that frequently reported in the literature. However, another critical review[56] have pinpointed the disadvantages of using RMs such as the corrosivity and the stability window. Elsewhere, Y. Ein-Eli *et al.*[57,58] has attempted to increase the oxygen intakes at high C-rate by adding perfluorocarbon in the electrolyte.

Ruthenium and ruthenium oxide[59–61] are often used as catalysts for OER to decorate the cathode. The advantages of ruthenium and its oxide is that their deposition can be done in sol-gel way. The catalytic mechanism on these noble metal doped materials is believed to be principally on the metal site. In contrast, with the N-doped materials[62–64], the catalytic area are on the doped material. Thanks to small size and higher density of catalyst sites[62], the catalytic effect is believed to be more outstanding. Carbon-free materials are also developed as it was shown in the early studies of LOB[65] that the carbon can react with superoxide at high voltage. Other side-reactions such as the polymer binder decomposition due to the presence of superoxide[66] and auto-decomposition of electrolyte[67] can hamper the cyclability of LOB.

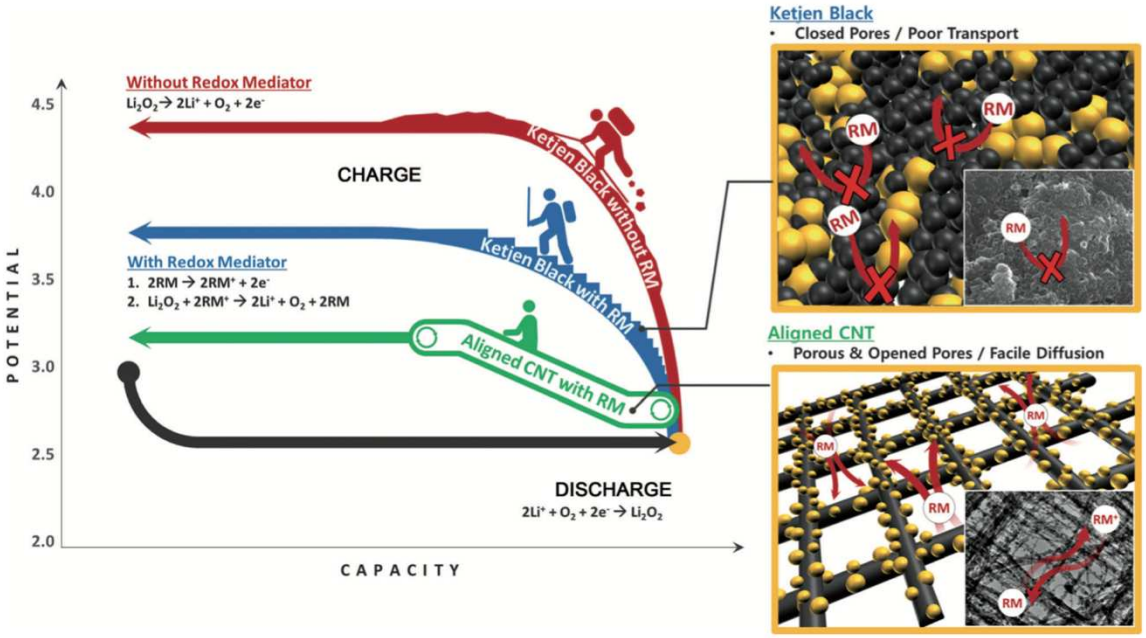

Figure 8. *The combination of a highly porous CNT material and the redox mediator to enable a long lifespan LOB by Lim et al.*[55]

Other latest topics in LOB includes making an anode/lithium-free LOB[68], starting by a Li_3N filled porous cathode and then charging the Li_3N giving the lithium on the anode. Teams found the light can catalyze the OER/ORR and designed photo-assisted LOB[69–71]. In addition, as the oxygen intake is slow in common electrolyte, to increase the areal energy capacity, one has developed flowing catholyte strategy[72] or adding perfluorocarbon[73] as additive to increase the reaction rate. People also attempted recently to cycle the LOB in more realistic condition including with presence of CO_2[74], moisture[75] (cycling in 2000 ppm forming the LiOH), and even within the nitrogen[76].

1.6. Frequently used characterization techniques in LOB

In the literature, many techniques of characterization have been used for studying the LOB. Imagery techniques such as SEM and TEM are mostly for the lithium peroxide morphology characterization. X-ray/electronic diffraction[47,77] and Raman[78] are frequently used for identifying the discharge products. And the thiosulfate with starch titration[79] is a chemical method for quantifying the Li_2O_2 amid all other by-products. Pressure monitoring and DEMS/OEMS[65,75] were used for dynamically determining the reaction and gas exchange rate.

To date, two techniques were used to characterize the mass transport in LOB: 1) Electrochemical Impedance Spectroscopy[80] 2) PFG-NMR[81]. In this manuscript, we introduce a third more robust technique : X-ray tomography[25,47,48] to visualize the cathode material, which give

intuitive insight of the electrode and enable the determination of bulk transport properties. Previous studies[47,48] using micro-scale resolution X-ray tomography have already shown great interests for characterizing the LOB. For investigating the cathode of LOB, which is the core topic in LOB, the resolution must be higher as the material contains sub-microscale pores and discharge species. In this manuscript, we will see the development of nano X-ray tomography in LOB, how it helps extracting species distribution and transport properties for different materials, and attempt to *in situ* 4D tomography for LOB.

1.7. Thesis structure

In this thesis, chapters are almost independent and can be read individually.

(Chapter 2) We first introduce the development of 3D imaging by synchrotron X-ray tomography for characterizing the cathode of the Li-O_2 battery (LOB). For tackling the low contrast issue between the carbon and the discharge product lithium peroxide, we coupled phase contrast techniques with the nanometric resolution transmission X-ray microscope (TXM) during the tomography acquisition.

(Chapter 3) We have developed a highly porous binder-free electrode with the multi-wall carbon nanotube (MWCNT). The synthesize is facile and easily scalable. Moreover, we will show in the last chapter a method to fully recycle this porous carbon material. This material was cycled until 500mAh/g at 40mA/g of CNT, which is 358mAh/g considering the mass of Li_2O_2 and equivalent to 875Wh/kg of energy density. The 'sudden death' occurred after several cycles and the material was reconditioned and recycled.

(Chapter 4) Using this cathode, we have pushed further the investigation of the LOB cathode by an in-situ X-ray tomography study. The cell design and the experimental details including beam alignment for the *in house* cell are detailed.

(Chapter 5) We have investigated in a convolutional neural network (CNN) for segmenting the different phases in the 3D volumes and carried experiments to understand the uncertainty in the semi-automatic supervised-learning way of segmentation. An open-source graphical software without coding acquirement has been put in place for training the CNNs for such a task. Within this software, users can visualize the outputs of the neural layers and transfer the neurons from a well-trained CNN model to improve the accuracy of a CNN onto new data.

(Chapter 6) We will summarize the achievements of this project and give some outlook of LOB in a modelling perspective

Chapter 2

Nano X-ray Computed-Tomography for Li-O_2 battery

In Li-O_2 battery, the transport property of ions and oxygen in LOB are determinant and directly linked to the performance of the battery. To obtain this properties such as tortuosity, typical approaches could be 1) using SEM to qualitatively comment on the opening of the pores and cannels in the material 2) or using pycnometer, BET, or other porosimeters to obtain the average porosity, then give an estimation of the global tortuosity by the Bruggman correction: $\mathrm{tortuosity} \sim \mathrm{porosity}^{-1.5}$ 3) or using a blocking electrolyte (to prevent other electrochemical reactions overriding the signal of transport phenomena that skews the results) in electrochemical impedance spectroscopy.

The X-ray Computed-Tomography can provide both (porosity and tortuosity, and the local ones). In this chapter, we will present how to use nano-XCT with the phase contrast technique to characterize the cathode of LOB and discuss the transport properties of a typical carbon black electrode.

2.1. Related works in determining transport properties in LOB

The discharge process of non-aqueous Li-O_2 battery undergoes the following overall electrochemical deposition reaction (Figure 1a) on the cathode side: $2Li^+ + 2e^- + O_2 \xrightarrow{discharge} Li_2O_2 \downarrow$ (E_0 = 2.96 V *vs* Li^+/Li). The recharge reaction is hardly reversible essentially due to the insulating nature of the discharge product Li_2O_2, the high electrolyte instability, the limited O_2 diffusivity in electrolyte and highly dependent of electrode architecture.[9,10]

The growth of Li_2O_2 can proceed following generally two parameters: current density and type of solvent utilized. High current density often issues thin film like lithium peroxide solution whereas the low one particle or toroid like. The solvent can also have an impact on the morphology of the Li_2O_2. A high donor number electrolyte conducts to a higher solution of the intermediate product LiO_2, which will further disproportionate to peroxide in the solution resulting in bigger Li_2O_2 particles size. Bao *et al.*[11] and Torayev *et al.*[12,13] highlighted with different modelling approaches the pore clogging impact on cycling. Explicit pristine carbon electrode structures (FIB-SEM by the first paper and X-ray tomography by the second) were used to simulate this peroxide evolution inside the pores. Latter suggested by their model the interconnectivity of pores plays a major role in the battery performance while the solution mechanism is implicated. The X-ray tomography is a useful characterization tool for more solid and direct characterization supports on this complex discussion.

In the literature, common imaging characterizations such as SEM[14,15] and TEM[16,17] are often used. One could barely directly interpret pore-clogging as the origin of sudden death due to the limitation of these techniques (outermost surface observation of SEM or structural degradation by dispersion during the sample preparation of TEM). Bardenhagen *et al.*[18] reported an *in-situ* impedance (PEIS) to probe indirectly the clogging by ascribing it to an increasing resistance and decreasing capacitance at mid-frequencies during the discharge. There is also an antecedent attempt by Nanda *et al.*[19] of tracking Li_2O_2 distribution inside a discharged cathode material by neutron tomography, which is highly sensitive to lithium. However, limited by the several dozen micrometers of resolution, authors make use of an unrealistic low specific surface graphite cathode.

We introduce the advanced X-ray computed tomography in synchrotron source to study architecture of Li-O_2 battery electrode from different cells at different states of discharge and charge. This technique has been widely applied in last decade in the battery and fuel cell field,

which exhibits a great potential for the characterization as well as refining or supporting the simultions.[20–24] The investigation of the Li-O_2 battery with the pure absorption X-ray tomography is extremely difficult due to the transparency of light elements. Nonetheless, several studies have demonstrated the phase imaging technique permits the observation on low absorbent components in batteries.[25–27]

2.2. Coupling phase contrast technique in XCT

Zernike phase contrast (ZPC) is one of the phase imaging techniques which is generally used in biological and medicine X-ray imaging for enhancing contrast among so-called phase objects containing light elements.[28–30] Figure 1b illustrates the optical line of a synchrotron X-ray Full Field Transmission Microscope. A parallel monochromatic beam is firstly converged onto the sample by a monocapillary condenser then passes through Fresnel Zone Plate (FZP) objective lens to magnify radiographies. By adding a gold phase ring objective (Figure 1b3) in the outcoming photon pathway, the phase retardation is added onto the transmittance. Two materials with the same absorbance but inducing different phase shifts will hence exhibit changes in amplitude which can be visualized as differences in image contrast.

There are four main unique advantages that X-ray Zernike Phase Contrast (ZPC) nano-tomography provides for the research of Li-O_2 battery: **(a)** enhanced contrast between carbon and discharge product Li_2O_2, **(b)** advanced resolution and large field of view, **(c)** quantitative studies on the 3D structure can be complemented by various algorithms and **(d)** non-destructive technique in favor of Operando experiment development.

In conventional X-ray transmission microscope, observing low absorption and similar contrast of carbon and Li_2O_2 is difficult (Figure 1c). These two materials have weak transmittance discrepancy for X-ray at 8 keV, applying phase contrast techniques is therefore mandatory. Figure 1d shows the flagrant contrast improvement of raw projections from the same sample of discharged electrode by pure absorption mode and Zernike Phase Contrast mode. We can see that signal-to-noise ratio is clearly enhanced with the Zernike mode (Figure 1e), which proves the technique efficiency in terms of contrast in our specific case.

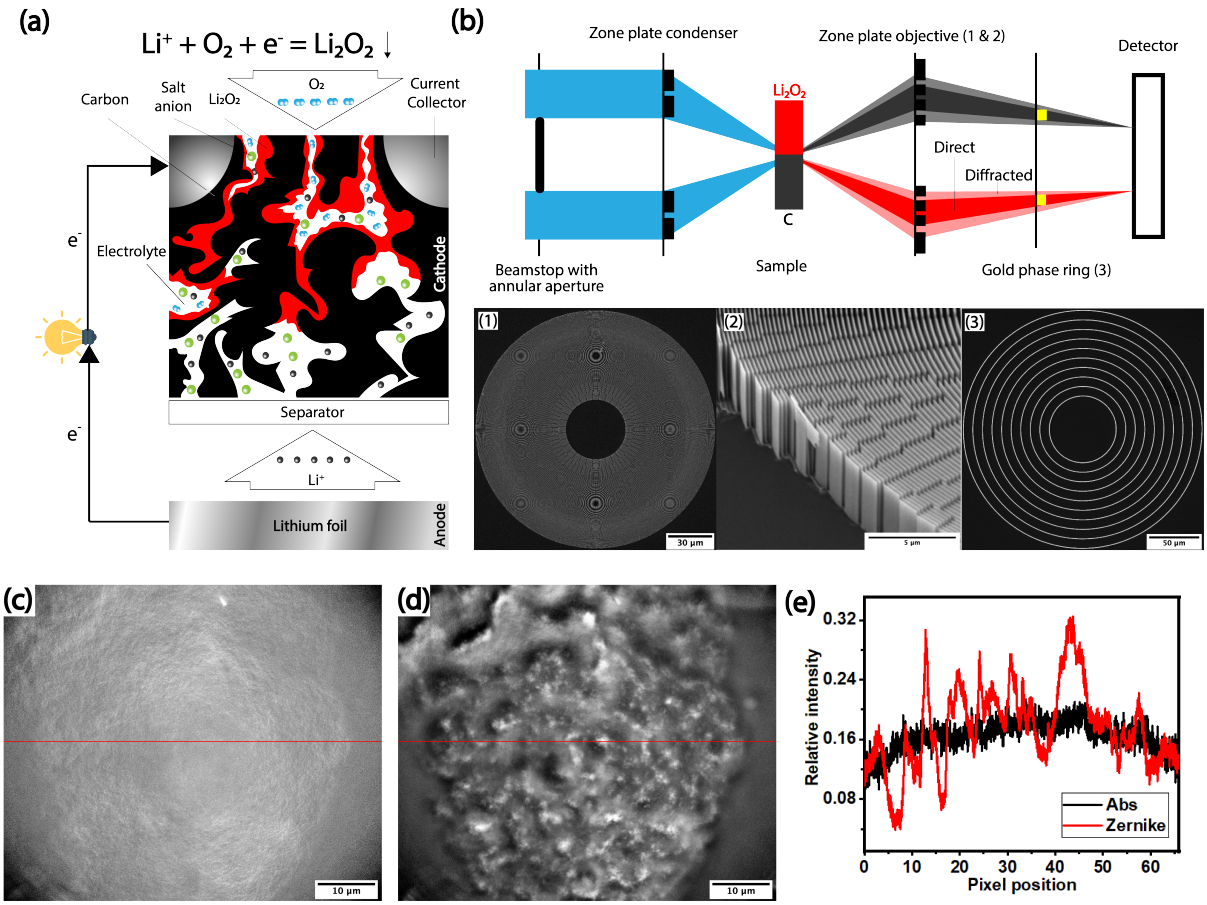

Figure 1. *(a) Schematic of different components in typical Li-O2 battery Swagelok setup: O_2 source, carbon-based porous cathode, nonaqueous electrolyte with lithium salt, separator and, Li foil anode. (b) Optical line of Full Field Transmission X-ray Microscopy with in-line Zernike Phase Contrast technique (APS Synchrotron ID-32-C beamline). In this description, a zone-plate type condenser is placed after the annular aperture of the beam-stop to converge an upstream coherent incident X-ray of Synchrotron onto the sample. And two downstream rays-paths respectively through low X-ray absorption lithium peroxide and carbon are shown. The direct ray (darker path) and the deviated rays (lighter path) are converged by another Zone plate. Only the direct rays are phase shifted by the gold phase ring. All rays interfere before the back focal plan. Phase discrepancy (Li_2O_2 vs C) is embedded into the initially similar transmission term of both materials which therefore displays better contrast. Inset SEM images expose the zone-plate optics utilized in the beamline. (c,d) Nano-CT images of Li-O2 electrode (carbon + Li_2O_2) with 50 nm of spatial resolution in pure absorption mode (c) and in Zernike Phase Contrast mode (d). (e) Comparison of line-profiles of projection of the same object in absorption mode and Zernike Phase Contrast mode.*

2.3. Experimental methods

2.3.a. Electrode preparation and electrochemical cycling

Carbon Super-P (industrial grade), PVdF (industrial grade) and NMP (Alfa Aesar) are mixed with a weight ratio of 9:1:30. The mixture is then alternatively mechanically stirred 2h and sonicated dispersed 30 minutes for 3 times. The homogeneous slurry obtained is drop-coated onto a metallic mesh (316L stainless steel 500µ) which is then dried on the hot-plate at 120°C

over 4 hours. The humidity is totally removed before battery assembling in a Büchy at 120°C over 10h with a liquid trap of Nitrogen liquid. Whatman Glassy Fiber Separators, Mylar foil, Swagelok and home-made O_2 environmental container 'Parfait' are all dried in oven at 70 °C before being entered into the argon filled Glovebox where H_2O and O_2 levels are lower than 0.1 ppm.

Scratched lithium foil, separator and cathode material are stacked in the home-made open Swagelok. 200µL of dimethyl sulfoxide DMSO (Alfa Aesar) with 1M of $LiClO_4$ (Alfa Aesar) concentration is added before being screwed together tightly. Entire is sealed in a home-made airtight 'Parfait' container. We saturated the electrolyte by half hour of O_2 flushing. The cell pressure is controlled at 1 bar. The battery is stabilized for 1 hour (OCV) then cycled in a rate of 40 mA per gram of carbon. VMP3 is used for the cycling.

2.3.b. Nano-CT sample preparation

The sample holder is pre-fabricated by well carving a mine (0.35 mm) under an optical microscope and glued vertically by epoxy onto a metallic needle. Pristine and cycled samples are chopped into tiny pieces. Under an optical microscope, one applies a tiny quantity of epoxy on the tip of the mine. A small piece with a size smaller than 0.05mm of cathode is lifted off by adhesive force of epoxy. The mounted sample is then airtightly sealed in a capillary Kapton tube in dry room.

2.3.c. SEM/TEM sample preparation

SEM and TEM samples are prepared in the Glovebox. The cathodes in different states-of-charge were washed by the pure electrolyte DMSO without salt. To yield a surface closed to current collector and far from the oxygen environment, we press the O_2-cathode onto the carbon tape then peel off the metallic grid. Inner surface is thus exposed. They were transferred with a damp-proof sample holder. All preparations are conducted in argon-filled glovebox. ASTAR and electron diffraction are detailed in the Annexes SI7.

2.3.d. Nano-Computed Tomography projections acquisition

The Nano-CT is performed in 32-ID-C station of Advanced Photon Sourced Synchrotron. Zone Plate condenser, in-line Zernike Phase ring, 8keV energy and a working distance of 3.4m are used which provides a pixel resolution of 27nm. More than 1900 projections with a uniform

angle tilt steps with total 180 degree have been collected using a scintillator (CdWO4, LuAG, GGG, Yag:Ce CCD) coupled with a CCD camera (Grasshopper3 5.0 MP GS3-U3-51S5M-C).

2.3.e. Tomography workflow

Image processing and tomographic reconstruction are performed with TomoPy Library. Notice that a supplementary image pre-processing step improve the quality of tomographic reconstruction is introduced in Annexes S1. All volumes are then reconstructed by GPU accelerated SIRT methode[82] for 200 iterations as a oversampling of number of projections thus no binning is used. A 3D median-filter is automatically applied for all volumes after reconstruction. For the segmentation and the visualization, we use respectively WEKA trainable segmentation (presented in Fig S4) implemented in Fiji and Avizo software.

Scheme 1. *X-ray Zernike Phase Contrast nano-CT workflowX-ray Zernike Phase Contrast nano-CT workflow*

2.4. Theoretical study of contrast in Zernike phase contrast

The Li_2O_2-carbon contrast index, which is proportional to the signal-to-noise-ratio for both absorption and Zernike, was calculated by constructing a wave-propagation model[83] (Annexes 2). This model simulates the pathway of X-ray and its interactions with carbon/Li_2O_2 as well as the phase shifting by Zernike phase ring. The figure 2a shows the evolution of the contrast indicator in both imaging mode as a function of the X-ray energy. The humane eyes accept Signal-to-Noise Ratio (SNR) of 5. We can see that at 8 keV the in-line Zernike Phase Contrast provides 81 times stronger contrast index between the carbon and Li_2O_2 than pure absorption which explains the improvement of SNR in Figure 1e. One should bear in mind that there is a compromise on the working energy. At lower energy, both imaging modes gives superior contrast, but the field of view (or depth of focus) is too small for battery materials and the strong value alternation between both modes induces difficulties in setting. We aim to observe the lithium peroxide distribution and morphology in the bulk. A slight tradeoff on an acceptable contrast by using a higher energy can gain on a larger field of view of 50 µm, which is more relevant for the present study.

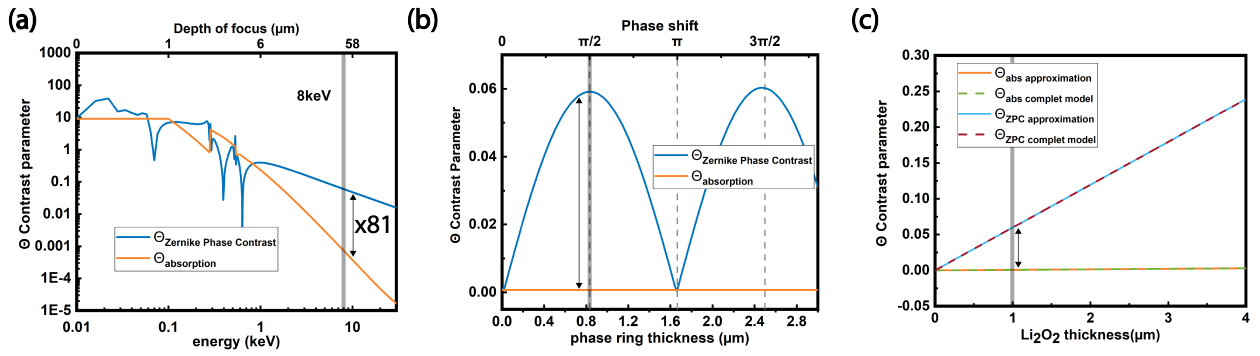

Figure 2. *(a) Contrast-energy simulation plot for pure absorption and in-line Zernike Phase Contrast shows 81 times higher contrast between Li_2O_2-Carbon at 8 keV energy and in the latter imaging mode. (b) Contrast-gold phase ring (assumed zero/weak absorption) thickness simulation plot indicating an optimal contrast at $\pi/2$ phase shift. (c) Contrast-Li_2O_2 thickness plot for both complete model and approximative one display for both a linearly contrast increasing while the lithium peroxide grows thicker.*

The contrast model demonstrates that the accessible optimal contrast is obtained for a $\pi/2$ phase ring corresponding to a phase ring thickness of 0.84 µm which we use for the experiment (Figure 2b). Figure 2c illustrates the Li_2O_2 thickness influence on the contrast: thicker the lithium peroxide is, better the contrast is versus the carbon. With the electrolyte DMSO and salt $LiClO_4$ used in this work, previous studies demonstrated large lithium peroxide formation with particle size can exceed several micrometers. The contrast-peroxide-thickness plot shows that the contrast remains largely superior to the absorption mode at all particle sizes of Li_2O_2 no matter the state-of-discharge.

2.5. Lithium peroxide spatial distribution

For preparing the tomography experiments, cathodes are beforehand cycled and dissembled then airtightly sealed in a capillary Kapton tube in dry room (detailed in Experimental Methods). The batteries start with an open circuit voltage around 3 V, which immediately followed by a long plateau at ~2.5 V as a function of current regiment until the cut-off voltage at 1.8 V (Figure 3b).

Tomography data are acquired within ID-32-C station of APS then reconstructed in house using Tomopy Library[84] with a workflow described in part 2.3.e of Experimental Methods. Some experimental parameter tunings for an image preprocessing that we called Pseudo-Phase-Retrieval (PPR) and a study of influence of different reconstruction algorithms are carried out (Annexes 1) in order to improving reconstruction quality. The PPR is a Fourier domain low-pass filter applied on projections before tomographic reconstruction for suppressing the border halo/shadow effect induced by ZPC. Furthermore, during the segmentation step in the

tomographic workflow, we substitute the classical threshold by a machine learning method. The classical threshold which is inaccurate splits phases simply on grayscale level in ignorance of all other image features, which induces errors such as severe edge confounding and is penalized easily by the presence of noise. The drawback of the direct threshold mode is overtaken by the use of WEKA trainable segmentation, which is shown and compared in Fig S4. This method intrinsically implemented local high-pass filter (such as bilateral and anisotropy diffusion) enhance the edge detection but less sensitive to the noise. The Figure 3a & 3c show respectively reconstructed intersection in the volume of the pristine and fully discharged cathode. The brighter and continuous domain is associated to the Li_2O_2 whereas the darker and grainy particles correspond to the carbon basing on the simulation then confirmed by TEM results (Fig S6-7). A stunning accuracy between raw image and segmented by a raindom forest approach in the plug-in of WEKA in Fiji are represented by a translucent color mask on the right half of Figure 3a&c.

A set of structures with 50 nm resolution (25 nm voxel size) and 500 pixels side length are depicted: the pristine electrode without cycling and the fully discharged cathode after the cut-off voltage. The pristine carbon framework is made of granular carbon particle bonded with the Polyvinylidine Floride (PVdF). It has a homogeneity of porosity at a large scale revealed by Figure 3d. But the inset zooms indicate that some intrinsic macro pores (>1 µm) are initially present in the structure. Regardless of several studies reported[85–87] such bi-porous structure tends to facilitate the mass transport; the premature cell death still occurs in our case at around the capacity of 1700 mAh/g.

Figure 3e shows the volume of the O_2-cathode after the collapse of voltage. The Li_2O_2 precipitates massively inside the electrode despite of the lack of space but with a heterogenous distribution. In contrast to the previous SEM studies[88], one can notice first and foremost that the mostly reported elongated or disk-like particles are both present. In the alongside inset zoom volume, the central peroxide particle even exceeds several micrometers. The surface of these particles is generally rough compared to the already described single particles on the surface of the electrode. This morphology seems to be a fusion of multiple Li_2O_2 particles and the growth of these Li_2O_2 particles might be constrained by the shape of the pores and curvature of carbon surface.

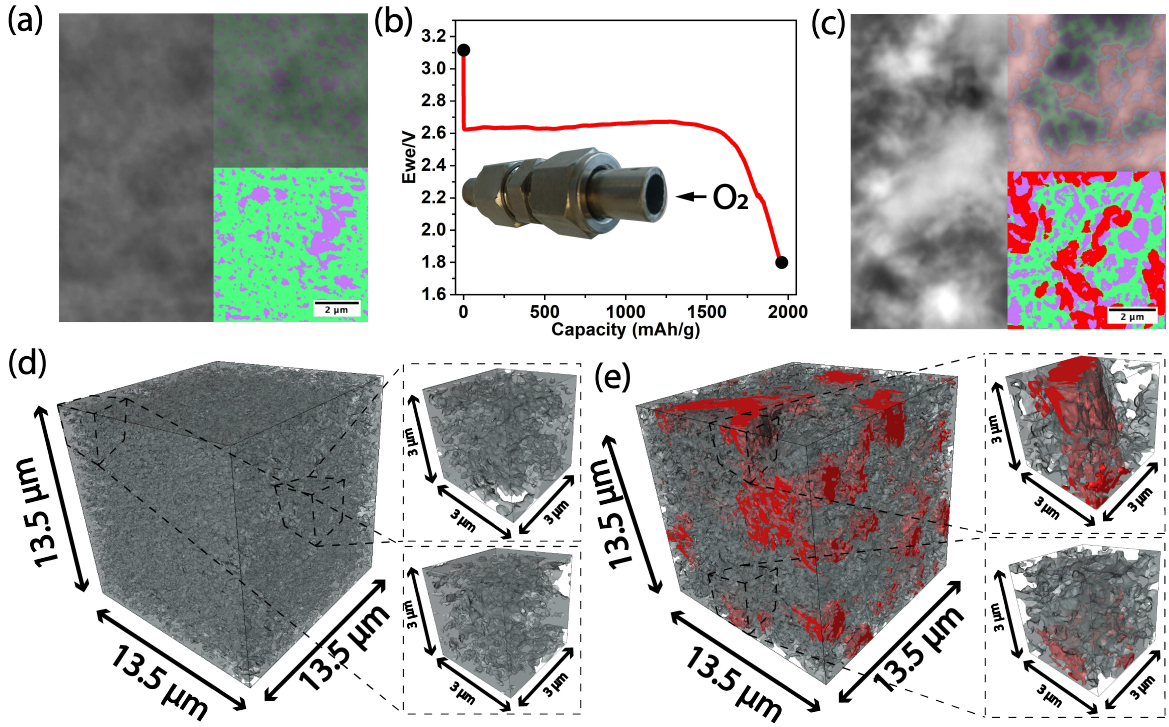

Figure 3. *(a) Tomographic reconstructed intersection of pristine cathode its right half covered with a mask of segmentation result by machine learning segmentation approach (green represents the carbon and purple the pore). (b) Electrochemical curve of the studied stainless-steel mesh drop-coated pristine O_2-cathode with carbon to binder weight ratio 9:1. The discharge is performed with a ~C/20 current density (40mA/g_{carbon}. The C-rate is arbitrarily chosen to be calculated by mAh/g_{carbon}, because all electrodes are from the same patch so similar surface area density). (c) Reconstructed intersection of the discharged cathode and its segmentation mask (red/green/purple: Li_2O_2/C/pore). The following 3D structures are with same colors code: red for lithium peroxide and transparent gray for carbon and void for pore. Two individual ex situ electrodes from different depth of discharge with its alongside zoom-ins are depicted. (d) The volume rendering of the pristine O_2-cathode and the zooms showing the initial presence of macropores. (e) Tomographic volume rendering of an O_2-cathode from the same patch as the previous one but independently and fully discharged. Top right zoom shows a massive lithium peroxide deposit and the bottom right intact zone without Li_2O_2.*

The current observation gives a direct indication and is in agreement of the aforementioned pore-clogging point of view[87,89]. In our cell configuration, the low current density at about C-rate of over 20 (40 mA/g_{carbon}) and the high donor number electrolyte DMSO are used. It is prone to a huge Li_2O_2 particle formation on the surface according to previous study[88]. In a high donor number electrolyte, lithium superoxide LiO_2 are firstly formed and escaped from the surface then disproportionate into O_2 and Li_2O_2 in the bulky pore space. The latter non-soluble product decreases the accessibility of ions and O_2 lead to a brisk and local mass depletion hindering the reaction. It explains the origin of the sudden death and there are still zones without peroxide even the reaction stops.

2.6. Analysis of extracted pore network from the tomography volumes

Besides, there is evidence of modification of carbon framework (gray color) before and after the discharge (between figure 4d and 4e). If one removes all the Li_2O_2 from the discharged volume and compare it with the pristine (Annexes 4), the pore sizes are clearly larger. According to recent studies of the oxygen reduction mechanism[9091,92], the LiO_2 is generated from the carbon-Li_2O_2 interface instead of a traditional explanation that Li_2O_2 are deposited from outside of the particle. A hypothesis could be that the expansion of the Li_2O_2 conducts to a morphology change of the carbon. And it is possible that at some area with less mechanical resistance, for example closed to the surface or areas where less binder is distributed, the structural deformation could be harsher.

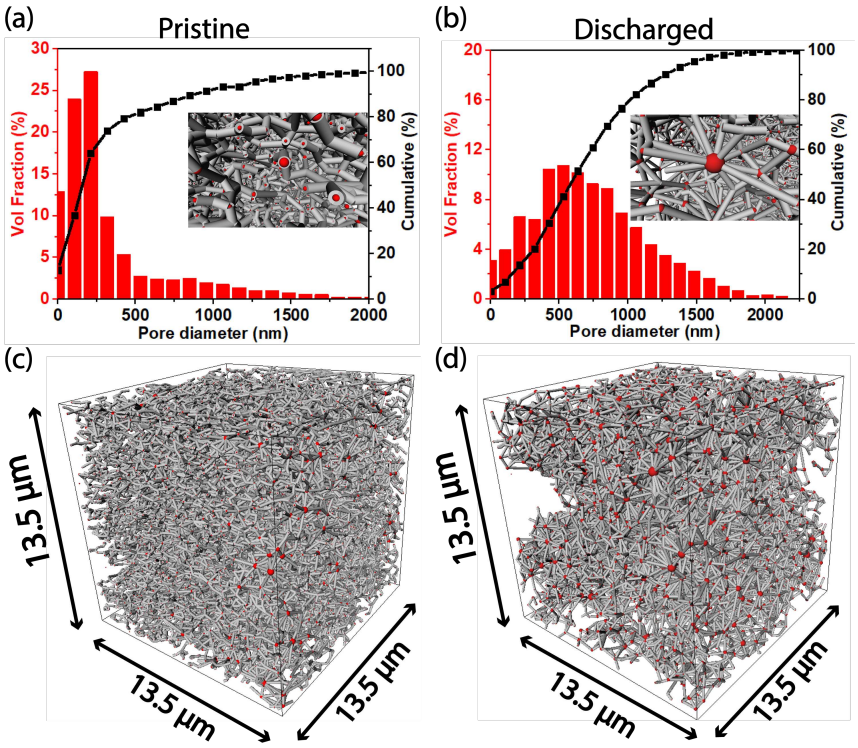

Figure 4. *(a) Pore Size Distributions (PSDs) of the pristine carbon and (b) of the discharged cathode with each an inset image of a zoom of the Pore Network Model (PNM). The latest is depicted by red spheres for pores of which diameter are as a function of its size and grey rods for length of connection between pores. Full Pore Network Model of (c) pristine and (d) discharged cathodes.*

To further quantify this modification, the pore network is extracted using the method of Dong et al[9394] by fitting spheres in pores. In the volumes depicted (Figure 4c-d or inset zooms in 4a-b), the red spheres and grey rod represent the pores and its connection. The diameter of the sphere is proportional to the pore size and length of the rods to the distance between two pores.

The pore size distributions of pristine and discharged cathode retrieved from the model are plotted in Figure 4a and 4b. The pristine has more than 70% of pore size population lower than 250 nm whereas the same proportion is shifted to 750 nm for the discharged one. It demonstrates directly that the pores get bigger after the discharge process. This valuable information on microscopic structural is impossible to obtain by SEM or TEM. This steric expansion effect is likewise observed in other types of battery[95,96] driving to the loss of connectivity between particles and the reactivity. Herein, we bring out with nano-CT that the Li-O_2 battery also suffers the structural modification during cycling due to the formation of Li_2O_2. Such expansion is believed to generate local constraint and a rearrangement of carbon domain resulting in irreversibility of the battery cycling.

2.7. Revealing the implied modification of material during electrochemical reaction

For a complementary study of volume expansion, SEM investigations of the cathode material using EDX element mapping have been carried out on Li_2O_2 particles inside the bulk electrode. Figure 5a exhibits Li_2O_2 particle of 2 µm long with a similar sharpened morphology that those previously observed by nano-CT. Here, it is worth to notice that an empty space and crack was developed close around Li_2O_2, which can be associated to a volume expansion consequence. The present results are thus consistent with Operando studies[97] that have already proved the mobility of the carbon matrix during the formation of Li_2O_2. In order to accurately quantify the carbon volume changes and determine the extent that the growth and dissolution of Li_2O_2 impact the microstructural electrode architecture, but also the binder degradation, further investigation is required.

The interface is a crucial parameter for electrochemical reactions inside Li-O_2 battery electrode that can be quantified by tomography technique at nanoscale. Figure 5b & 5c present respectively total interface of carbon/Li_2O_2 and carbon/porosity from the 3D architecture. From 3D analysis, we were able to quantify the carbon surface covered by Li_2O_2 and potentially that in contact with liquid electrolyte. The Li_2O_2 surface passivation is only of 28% on the carbon surface (Figure 4b), which reveals an under-use of electrode/electrolyte interface having as origin the clogging pores and limited O_2 diffusion. This local quantification of coverage brings to light on that a carbon electrode architecture having less tortuous pore network or a lower donor number electrolyte should be preferably used to avoid this local mass transport depletion. Furthermore, Li_2O_2 particles occupy 21% of pore volume, which explains also the n-folders lower effective capacity then the theoretical one. Using nano-CT Zernike phase contrast, we retrieve such import

information about interfacial states, with which experiment/theoretical discrepancy in terms of capacity can be better understood.

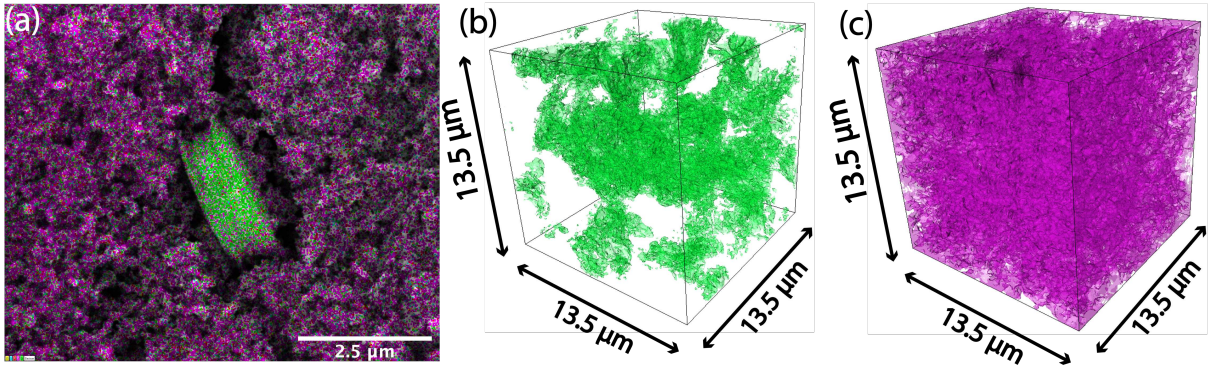

Figure 5. *(a) EDS-SEM element mapping of a Li_2O_2 particle deep inside the O_2-cathode peeled off from the current collector surface. Green color is oxygen signals and purple carbon. The associated EDS spectrum is in Annexes 5 (b) 28% of the carbon surface covered by Li_2O_2 of the discharged air-cathode and (c) the rest without Li_2O_2 occupancy which shows the inefficiency of surface usage.*

Finally, another cathode undergoes the same condition of discharge then recharged to 4.3V with the same C-rate. Reconstructed raw slices of the O_2-cathode are showed in the Figure 6a & 6c and the machine learning segmentation result are superimposed on the right half to compare.

Interestingly, the brighter domain associate with lithium peroxide becomes even larger than the discharged sample. We can explain it by the fact that the formation/decomposition of Li_2O_2 during charge is often accompanied by parasitic side reactions. It's well known and proved by several techniques[65,98,99] (NMR, DEMS) the instability of the main battery components (cathode, electrolyte) under high voltage recharge process. The Li_2CO_3 is reported as major byproduct in DMSO or ether electrolytes. The electron diffraction (Fig S7b) confirms the presence of Li_2CO_3 and huge quantity of Li_2SO_4 in our sample which is in agreement with the reported decomposition of the electrolyte and the carbon electrode[65]. The total tomographic volume of the recharge cathode is split into two parts with their small zooms beside and depicted in Figure 6d&e.

We can see that there is important amount of non-dissolve Li_2O_2 (mixture with Li_2CO_3 and Li_2SO_4) and an inhomogeneity of these residues from volume to volume. This mixture displays a slightly stronger brightness and more uniform morphology in X-ray Zernike Phase Contrast tomography then Li_2O_2 showed previously. The lithium carbonate and sulfate are difficult to filter out from other species in tomography due to its miniature quantity and the complexity of the overall system contrast (Annexes 2). We consider and segment these species as an entity of recharged product. Figure 6d displays frontier between the dissolve and non-dissolve domains. A gradient of

lithium peroxide vanishing from the bottom to the top indicates that the discharged product can dissolve faster than in some area others.

Obviously, the byproducts and the non-dissolved Li_2O_2 continue to occupy the porosity at the end charge and limit the accessibility of the oxygen reducing the capacity for the following discharge. These results in the hysteresis of the electrochemical curve (Figure 6b) of a 1.5V high polarization since the carbonate, sulfate and peroxide are all insulting which increase the ohmic drop in the system. It remains a crucial issue to resolve with new materials which imped the electrolyte/cathode decomposition on the recharge process. For this purpose, the current technique will be a robust tool for characterizing the Li-O_2 recharge process.

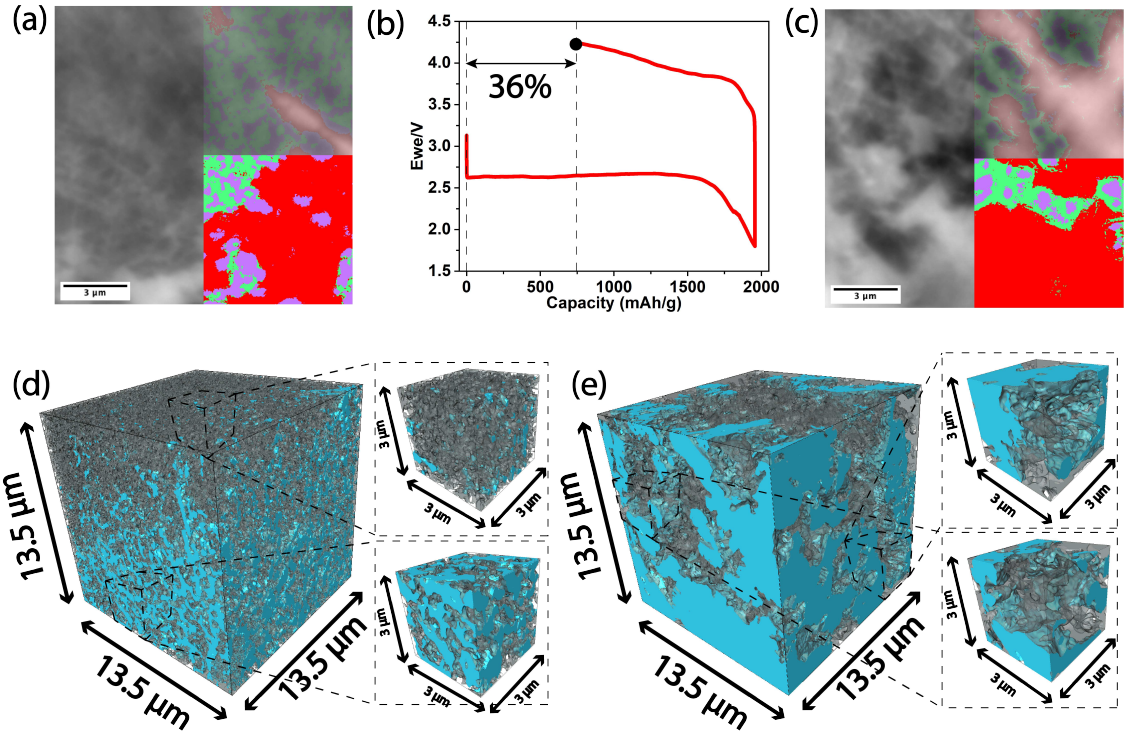

Figure 6. *(a) Reconstructed image of intersection and right half the segmentation mask of a recharged cathode. (b) Full electrochemical curve showing the hysteresis of the cycling with a 1.5V high polarization. (c) in contrast of (a), an area with severe degradation of electrode. (d) 3D visualization of an O_2-cathode recharged to 4.3 V depicting a gradient of the non-dissolution of lithium peroxide. The inset volumes illustrate the imbalanced residual distribution (e) volume with intense Li_2O_2 residuals and by products that occupy the majority of the pores.*

Interestingly, Table 1 shows changes of porosity and tortuosity. One can see in Fig 7 that the pristine structure is more compact with numerous tiny pores, whereas the discharged structure has clearly larger pores. The ion pathway in the electrolyte phase is wider after the fully discharge. On the other hand, the pore-clogging causes an abnormal tortuosity of 32.8. This finding seems to suggest that the deposition of lithium peroxide could deteriorate the material structure. To

confirm this postulate, a larger sampling should be done in the future, and we try to pursue this investigation in the chapter 4: *in situ* tomography for LOB.

	Pristine	Fully discharged	Recharged (with less concentrated residual)	Recharged
Porosity	19%	33%	36%	42%
Tortuosity by diffusion simulation	29.97	4.80	5.14	32.8

Table 1. *Porosity and tortuosity values obtained by Taufactor software. Porosity and tortuosity measurements are calculated by Matlab software Taufactor in different directions then averaged.*

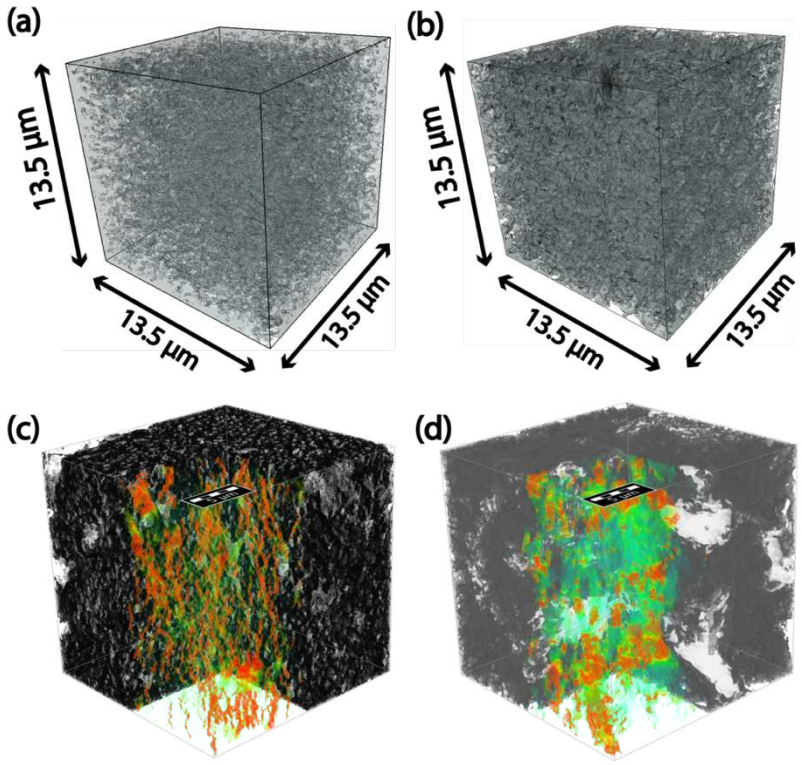

Figure 7. *3D structures of carbon matrix of (a) pristine (b) discharged cathode. Diffusion simulations visualization on the same structures c-d with Geodict. The flux of electrolyte is represented by green and red colors with respect to the flux density. Red areas are those with intense tightening of funnel and increases the flux intensity. White colors represent Li_2O_2 and dark color carbon as well as void for pores. c) & d) The diffusion simulation is performed with Geodict on these structures a) and b) and the results are shown in c) & d), respectively. Red colors represent areas that fluids tighten with a more tortuous pathway. The ion pathways are more extensive in the discharged cathode than in the pristine.*

2.8. Conclusions and Perspectives

In summary, we report the characterization of Li-O_2 battery using the coupling of the Transmission X-ray Microscopy with Zernike Phase Constrast X ray nano-tomography. The advanced resolution (50 nm), large field of view (50 µm) and contrast enhancement between light elements provide a unique opportunity to visualize phenomena in the bulky realistic cathode. We observe a pronounced inhomogeneity of formation of Li_2O_2 probably due to highly tortuous electrode and low diffusivity of oxygen. A massive degradation during the recharge is brought out which is origin of the decreasing cyclability of the battery. In this work, we demonstrated two disadvantages by using a high donor number electrolyte. First, the expansion of reduction product could deteriorate locally the structure which reduces the lifespan of the battery. The Li_2O_2 particles seem to preferentially aggregate at the same place. Second, thanks to the interface area and the pore network studies, we point out that pore clogging, occurring at local scale, could conduct to the inefficient usage of cathode. Hierarchical and well-arranged with lower tortuosity structures of electrode might make better benefit to the capacity.

Throughout the present paper, the powerful X-ray Zernike Phase Contrast nano-tomography for Li-O_2 battery provides intuitive visualizations and valuable quantitative information of lithium peroxide deposition. Besides, this technique can be also used in other part of the battery, for example lithium foil anode, separator for investigating transport properties. Finally, we will see in the following chapters the non-abrasive property and no-vacuum-needed environment of X-ray tomography is relevant to develop *in situ* experiments.

Important takeaways :

We investigated the lithium peroxide (Li_2O_2) and pore size distribution in lithium−O_2 battery electrodes at different states of charge using transmission X-ray microscopy coupled with Zernike phase contrast to carry out nanocomputed tomography. We report that such a technique enables us, at the nanoscale, to distinguish light elements such as carbon and Li_2O_2 in Li− O_2 battery cathode electrodes. We verified by wave-propagation simulation that this approach efficiently improves the contrast of images in comparison with pure absorption. The Li_2O_2 distribution and thickness, interphases, and pore network are visualized and quantified, giving a valuable insight into our cathode architecture. From this 3D analysis, we highlight modifications of the air-cathode morphology and the Li_2O_2 spatial organization as well as their potential implication in terms of carbon surface passivation and pore-clogging. After the full recharge process, this technique can also reveal the spatial distribution of the residual Li_2O_2 and other byproducts.

- Contrast Enhancement by Zernike Phase Contrast in nano-XCT for characterizing LOB
- In-line technique without adding acquisition time
- Enabled 3D characterizing in meso-scale in LOB

2.9. Annexes

Present Annexes provides firstly, a model demonstration for calculating the contrast in absorption and in Zernike Phase Contrast. Afterward, an empirical single distance phase retrieval image technique on nano-CT, which improves the signal-to-noise ratio, will be introduced. The 3D tomographic reconstruction for projections is then performed with versatile Tomopy Python Library. The study of impact with different algorithms in Tomopy is provided. The contact surface area, porosity, and tortuosity studies are performed by in-home code or Taufactor/Geodict software[1]. The 3D visualization is achieved by Avizo 9.5 (Thermo Fisher Scientific). The SEM and ASTAR TEM experiments will also be described.

2.9.a. Annexes 1:

We complete herein information of the workflow of image processing and tomography reconstruction with TomoPy library. Previous studies showed that low pass filter on the Fourier domain can correct Zernike Actifacts[2,3]. We apply a Fourier domain low pass filter which is based on a single image phase-retrieval algorithm implemented in Tomopy. We will call it pseudo-phase-retrieval (PPR) here. Applying the exact experimental parameters will drive to a memory leakage. We strategically fit parameters one by one and use the best combination to filter the projections then reconstruct the whole stack of images. One should pay attention to the name of the parameters that here doesn't have actual physical meanings which just aim to guide reader to match up the parameter in the Tomopy Library.

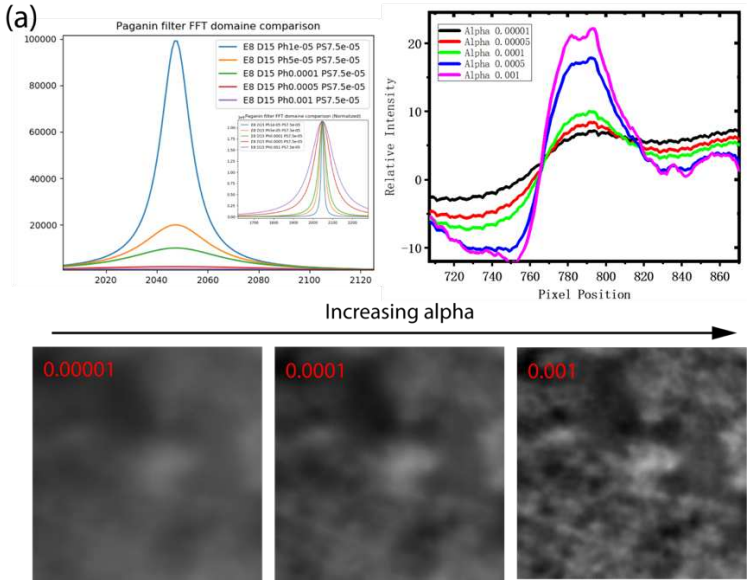

Figure S1. *Increasing both the alpha and the energy smears the filter shape and enlarge the mid-height width. Thus, high frequency and edges with a large gradient are conserved. However, increasing the energy risks to induce noises*

as showed in the case of 35keV. On the other hand, the mid-height width of the filter is inversely proportional to the distance. Low distance value is preferential.

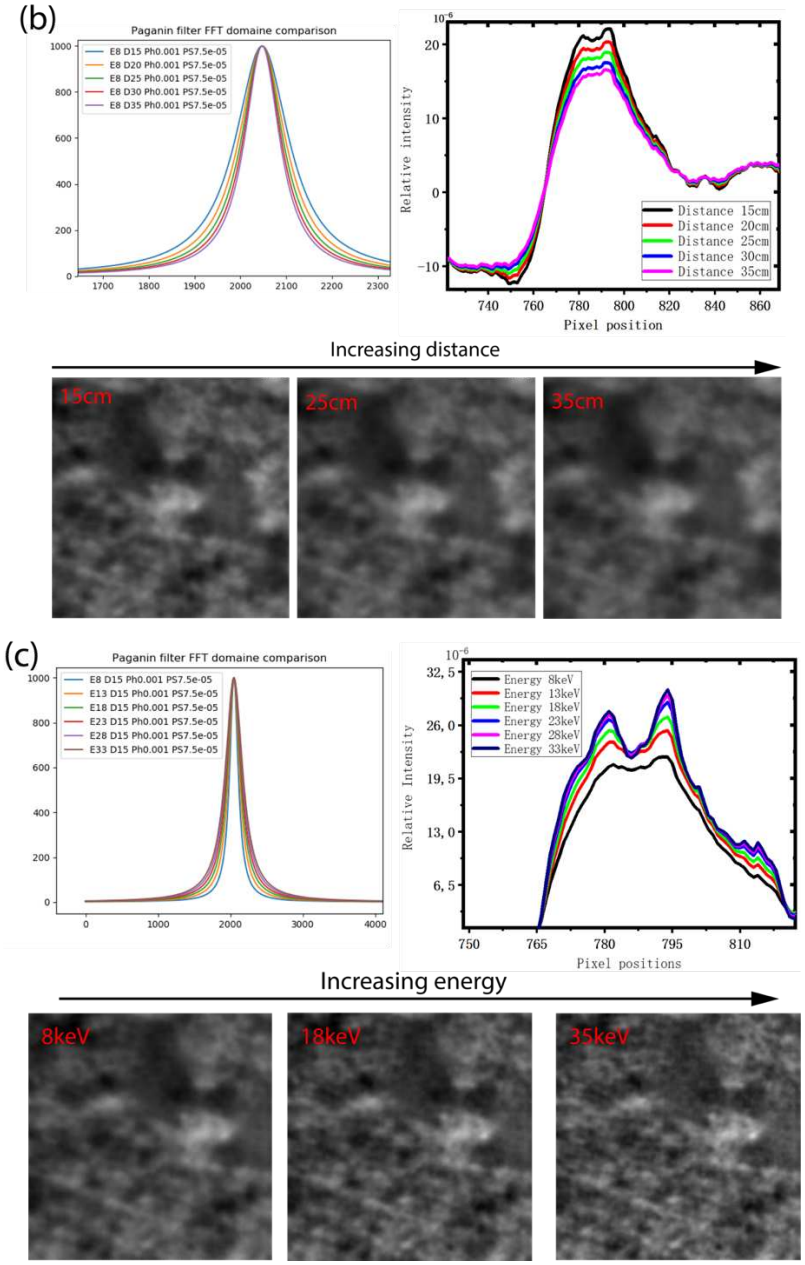

Figure S2. *Comparison of line profile on the top-left hand side of the PPR form in Fourier domain, line profile of filtered reconstruction and reconstructed image as a function of (a)internal alpha parameter with an inset of normalized filter form(b) distance parameter (c) energy parameter*

Several methods of reconstructions are compared. Gridrec and Filtered Back Procjection (FBP) which belongs to the family of analytical reconstructions are reconstructed without binning as we have deliberately over-sampling during acquisition. All these techniques (Gridrec, FBP, Conjugated Gradient Least Squares (CGLS), Maximum Entropy (EM), Simultaneous Algebraic Reconstruction Technique (SART), Simultaneous Iterative Reconstruction Technique (SIRT).

These methods are referred to [4–6]) display different charateristics. However, considering noise quantity and a better signal-to-noise ratio, we chose the SIRT for the final reconstruction.

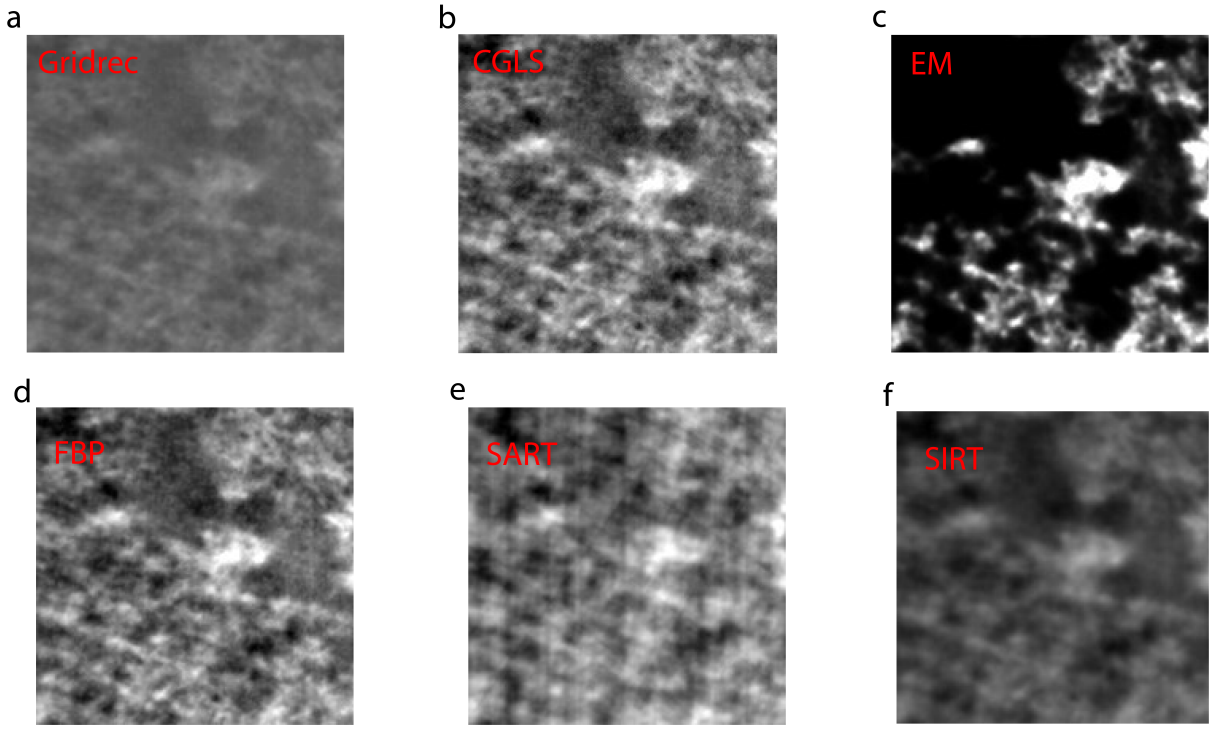

Figure S3. *Comparison of different Tomopy built-in reconstructions (a-f) Gridrec, CGLS (200 iterations), EM (200 iterations), FBP, SART (200iterations), SIRT (200 iterations) (middle) row profile of image of the same slice of carbon Super P/PVdF with these methods.*

After the whole stack reconstruction, the WEKA trainable segmentation is used to distribute Li_2O_2, carbon-binder, and pores domains. The WEKA plug-in can be found in FIJI. An image of tomography is firstly loaded in the interface. The experimenter put labels thereafter onto the image, as shown in Figure S2-3. A model is trained with tomography raw image and user's labels as ground truth. The random forest classification is run underground and preceded by feature filtering with FIJI implemented kernel. The following figure illustrates the advantages of WEKA while the overlapping of grayscale histogram happens. We can see from the bottom histogram the gray-level of each phase superimposes one into another, which is difficult to segment. In this case, the borders can only be coarsely segmented by the traditional threshold where the accuracy is low, as compared in the right part of S2-3. The machine learning-based method is more robust because morphological filters are applied, and the algorithm classifies phases from the filtered-out features. However, one should note that every segmentation has an intrinsic and inevitable error induced by the experimenter as a supervised machine learning method is used. Such error can vary from one experimenter to another depending on his knowledge and familiarity on the material. Herein, authors are familiar with the morphology and the composition of the material. Moreover, with the

interactive functionality, authors have spent sufficient time to correct and double-check the segmentation to ensure the minimum of error. We estimate the segmentation error should be the minority but do not rule out the possibility.

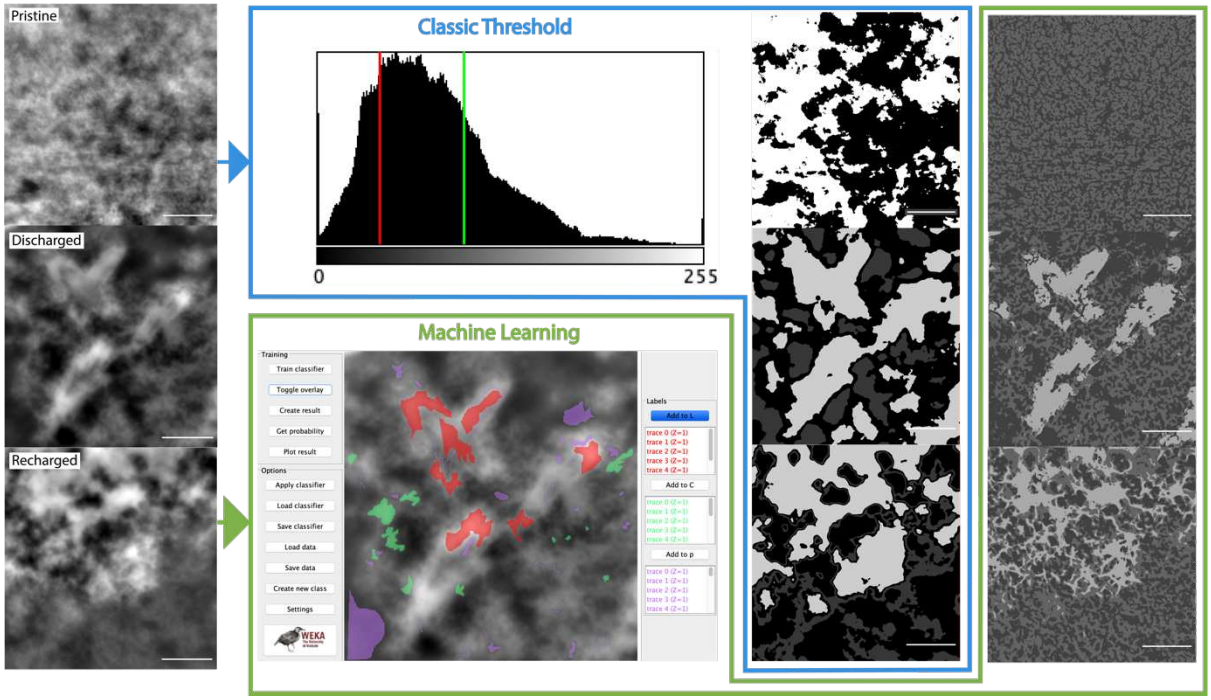

Figure S4. *(left) from top to the bottom reconstructed raw images of highly contrasted pristine, discharged GDE and recharged GDE. (green) interface and results of WEKA segmentation. (blue) classical threshold results. The scale bar of all images is 5µm.*

2.9.b. Annexes 2:

In this model, we assume that the pore has no effect of the wave on the amplitude and phase and a simple geometry by placing the lithium peroxide within a framework of carbon.

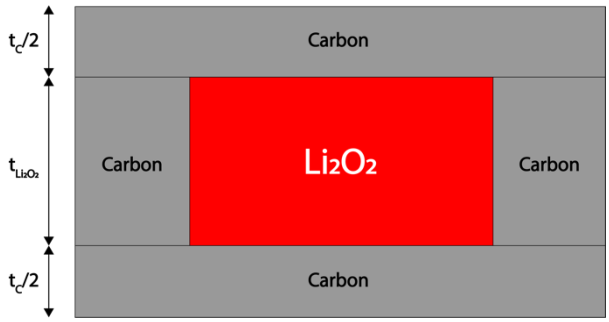

Figure S5. *illustrates the wave-propagation model of the interaction between x-ray and material.*

The refractive index of a material traversed by x-ray beam can be expressed:

$$n = 1 - \delta - i\beta \quad (1)$$

With the real part 1-δ and imagery part β

Contrast in absorption mode:

We refer to the Lambert-Beer relation to calculate the contrast. The attenuation is thus written:

$$I = I_0 e^{-\mu_{feature} t_{feature}} \quad (2)$$

With μ the linear absorption, where $\mu = \frac{4\pi\beta}{\lambda}$. The outcoming intensities of the beam through the carbon and lithium peroxide surrounded by carbon are:

$$I_{Li2O2,abs} = I_0 e^{-\mu_{Li2O2} t_{Li2O2}} e^{-\mu_C \mu_C} \quad (3)$$

$$I_{C,abs} = I_0 e^{-\mu_C (t_C + t_{Li2O2})} \quad (4)$$

The contrast can thus be expressed as following:

$$\Theta_{abs} = \frac{|I_{Li2O2} - I_C|}{\sqrt{I_{Li2O2} + I_C}} = \frac{\left| I_0 e^{-\mu_{Li2O2} t_{Li2O2}} e^{-\mu_C \mu_C} - I_0 e^{-\mu_C (t_C + t_{Li2O2})} \right|}{\sqrt{I_0 e^{-\mu_{Li2O2} t_{Li2O2}} e^{-\mu_C \mu_C} + I_0 e^{-\mu_C (t_C + t_{Li2O2})}}} \quad (5)$$

Supposing a weak absorbance of Li_2O_2 and carbon, where $\mu_{Li2O2} t_{Li2O2} \ll 1$ and $\mu_C t_{Li2O2} \ll 1$, and taking the limits of the exponential $\lim_{x \to 0} e^x = 1 + x$:

$$I_{Li2O2,abs} = I_0 (1 - \mu_{Li2O2} t_{Li2O2}) e^{-\mu_C \mu_C} \quad (6)$$

$$I_{C,abs} = I_0 (1 - \mu_C t_{Li2O2}) e^{-\mu_C \mu_C} \quad (7)$$

$$\Theta_{abs} = \frac{|\mu_{Li2O2} t_{Li2O2} - \mu_C t_{Li2O2}|}{\sqrt{\mu_{Li2O2} t_{Li2O2} - \mu_C t_{Li2O2}}} e^{-\mu_C t_C/2} \quad (8)$$

One can further simplify them to:

$$\Theta_{abs} \approx \frac{t_{Li2O2}}{\sqrt{2}} |\mu_{Li2O2} - \mu_C| e^{-\mu_C t_C/2} \quad (9)$$

With relation $\mu = \frac{4\pi\beta}{\lambda}$:

$$\Theta_{abs} \approx \frac{2\sqrt{2} t_{Li2O2}}{\lambda} |\beta_{Li2O2} - \beta_C| e^{-\mu_C t_C/2} \quad (10)$$

In-line Zernike Phase Contrast:

In this mode, the absorption and phase shift across both materials can be generalized to:

$$A_{Li2O2} = e^{\frac{-\mu_C t_C - \mu_{Li2O2} t_{L2O2}}{2} + i(\eta_C t_C + \eta_{Li2O2} t_{L2O2})} \quad (11)$$

$$A_C = e^{\frac{-\mu_C t_C - \mu_C t_{L2O2}}{2} + i(\eta_C t_{Li2O2} + \eta_C t_{L2O2})} \quad (12)$$

With the linear phase coefficient $\eta = \frac{2\pi\delta}{\lambda}$. The direct beam goes across the phase ring. By analogy, the amplitude and phase changes induced by only the carbon then the phase ring are hence:

$$A'_C = A_C \times T_{PhRing} = e^{\frac{-\mu_C t_C - \mu_C t_{L2O2} - \mu_{PhRing} t_{PhRing}}{2} + i(\eta_C t_C + \eta_C t_{L2O2} + \eta_{PhRing} t_{PhRing})} \quad (13)$$

$$A'^*_C = A_C \times T_{PhRing} = e^{\frac{-\mu_C t_C - \mu_C t_{L2O2} - \mu_{PhRing} t_{PhRing}}{2} - i(\eta_C t_C + \eta_C t_{L2O2} + \eta_{PhRing} t_{PhRing})} \quad (14)$$

$$I_{C,ZPC} = A'_C A'^*_C = e^{\frac{-\mu_C t_C - \mu_C t_{L2O2} - \mu_{PhRing} t_{PhRing}}{2}} \quad (15)$$

Now, replace the middle bloc of the carbon by Li_2O_2. The diffracted beam due to the presence of Li_2O_2 is $(A_{Li2O2} - A_C)$. The diffracted ray and direct phase shifted converge before the detector (reconsidering the downstream beam of Figure 1b), where the amplitude is the sum of both:

$$A'_{Li2O2} = A'_C + (A_{Li2O2} - A_C) \quad (16)$$
$$= e^{\frac{-\mu_C t_C - \mu_C t_{L2O2} - \mu_{PhRing} t_{PhRing}}{2} + i(\eta_C t_C + \eta_C t_{L2O2} + \eta_{PhRing} t_{PhRing})}$$
$$+ e^{\frac{-\mu_C t_C - \mu_{Li2O2} t_{L2O2}}{2} + i(\eta_C t_C + \eta_{Li2O2} t_{L2O2})}$$
$$- e^{\frac{-\mu_C t_C - \mu_C t_{L2O2}}{2} + i(\eta_C t_C + \eta_C t_{L2O2})}$$

$$A'^*_{Li2O2} = e^{\frac{-\mu_C t_C - \mu_C t_{L2O2} - \mu_{PhRing} t_{PhRing}}{2}} e^{-i(\eta_C t_C + \eta_C t_{L2O2} + \eta_{PhRing} t_{PhRing})} \quad (17)$$
$$+ e^{\frac{-\mu_C t_C - \mu_{Li2O2} t_{L2O2}}{2}} e^{-i(\eta_C t_C + \eta_{Li2O2} t_{L2O2})}$$
$$- e^{\frac{-\mu_C t_C - \mu_C t_{L2O2}}{2}} e^{-i(\eta_C t_C + \eta_C t_{L2O2})}$$

$$I_{Li2O2,ZPC} = A'_{Li2O2} A'^*_{Li2O2} \quad (18)$$
$$= e^{-\mu_C t_C - \mu_C t_{L2O2} - \mu_{PhRing} t_{PhRing}} + e^{-\mu_C t_C - \mu_{Li2O2} t_{L2O2}} + e^{-\mu_C t_C - \mu_C t_{L2O2}}$$
$$+ 2e^{-\mu_C t_C - \frac{\mu_C t_{L2O2} + \mu_C t_{L2O2} + \mu_{PhRing} t_{PhRing}}{2}} \sin(\eta_C t_{L2O2} - \eta_{Li2O2} t_{Li2O2})$$
$$- 2e^{-\mu_C t_C - \mu_C t_{L2O2} - \frac{\mu_{PhRing} t_{PhRing}}{2}} \cos(\eta_{PhRing} t_{PhRing})$$
$$- 2e^{-\mu_C t_C - \frac{\mu_{Li2O2} t_{L2O2} + \mu_C t_{L2O2}}{2}} \cos(\eta_{Li2O2} t_{L2O2} - \eta_C t_{Li2O2})$$

Additionally, if one considers weak phase shift of the Li_2O_2, C and uses a $\pi/2$ phase ring without absorption ($\eta_{Li2O2} t_{Li2O2} \ll 1$, $\eta_C t_{Li2O2} \ll 1$, $\eta_{PhRing} t_{PhRing} \ll \pi/2$, $\mu_{PhRing} \approx 0$, and $\lim_{x \to 0} \sin(x) = x$), equation (18) can be further simplified.

$$I_{Li2O2,ZPC} \approx I_0[1 + 2(\eta_{Li2O2} - \eta_C) t_{Li2O2}] e^{-\mu_C t_C/2} \quad (19)$$

$$I_{C,ZPC} \approx I_0 e^{-\mu_C t_C/2} \quad (20)$$

$$\Theta_{ZPC} \approx |\eta_{Li2O2} - \eta_C| e^{-\mu_C t_C/2} \quad (21)$$

$$\Theta_{ZPC} \approx \frac{2\sqrt{2} t_{Li2O2}}{\lambda} |\delta_{Li2O2} - \delta_C| e^{-\mu_C t_C/2} \quad (22)$$

Following is the table of parameters and their values for the simulation:

Name of parameters	Value/unity
Carbon density	1.9 g/cm^3
Carbon thickness	50nm (Carbon Super P, C_{50})
Li_2O_2 density	2.31 g/cm^3
Li_2O_2 thickness	1µm
Energy	8keV (APS: 32-ID-C)
Phase ring material	Gold
δ, β	Utilized Xraylib on Python
Contrast for species in this paper (same thickness assumed)	$C<Li_2CO_3 \approx Li_2SO_4 \approx Li_2O_2$

Table ST1. *Parameter and their values for the simulation*

2.9.c. Annexes 3:

A TEM ASTAR mapping for the discharged product and TEM study for the recharged product are provided.

Automated crystal orientation and phase mapping (ACOM) in TEM analysis has become more widely used for different material science analysis like alloys, thin films, nanocrystals metals, and more recently batteries[7–10]. In this study, an ACOM analysis was realized on Li-air discharged battery in a region of by of interest with 400 point on X and Y with a step size of 5 nm comparing the electron diffraction pattern in every point with all the orientation possible for all the structures using a Tecnai F20 S-TWIN (Spot size: 8, Camera length: 71 mm, Condenser 2 at 50µm).

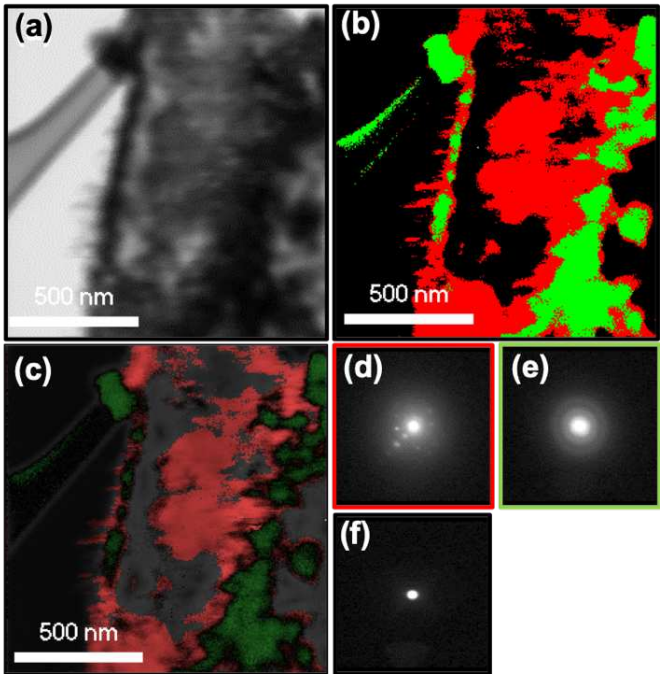

Figure S6. *(a) Virtual bright field image based on transmitted electron beam in the ASTAR series acquisition (b) Phase mapping based on treatment electron diffraction mapping acquired with Automated crystal orientation and phase mapping, CIF files of Li_2O_2 (50658, P63/mmc) has been used for pattern matching, (c) Combine map of virtual bright field, phase map and phase reliability (d, e, f) electron diffraction patterns of Lithium peroxide(in red), carbon (amorphous area in green) and inactive points acquired with ASTAR system.*

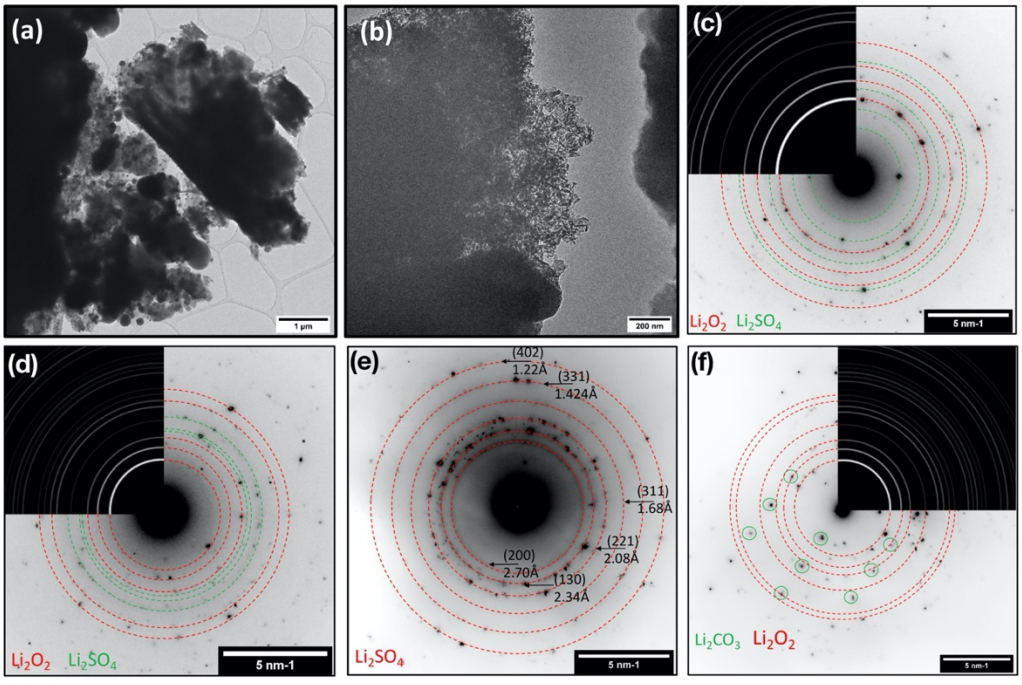

Figure S7. *(a,b) TEM images and (c-f) SAED pattern of the recharged Li-O2 battery electrode in which the Li_2O_2, Li_2SO_4 and Li_2CO_3 have been identified and indexed.*

2.9.d. Annexes 4:

The tomography data allows extracting positional, surface, and volume information. Figure S4b plots the profile of Li_2O_2 amount concerning the position in 3 reciprocally perpendicular and arbitrary directions. The three profiles average merely 8.88% with a standard deviation of 0.0297, 0.0282, and 0.0321 for directions 1, 2, and 3 respectively. We see that the spatial distributions of these three directions are similar but locally fluctuates strongly. Plate-like agglomerates are formed, as can be seen on the top of the volume. Particles are firstly separated by the watershed algorithm in Avizo software. Thence, the sphericity, defined by $\Psi_i = \frac{\pi^{1/3}(Volume_i)^{2/3}}{Area_i}$, is calculated on each particle. The majority (about 70%) of small peroxide particles are somewhat spherical which can be translated into the increasing tail closed to 1.0 sphericity in figure S7(c)

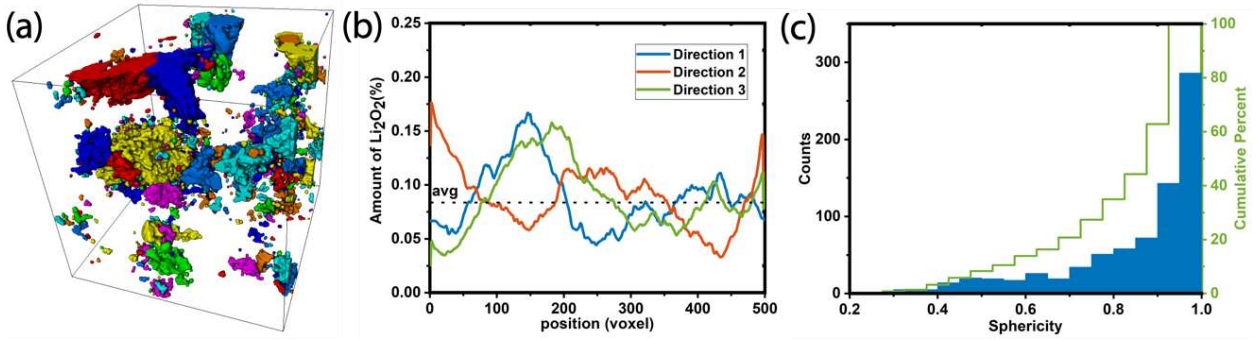

Figure S8. *(a) Li_2O_2 particles opened and labeled with different color by watershed algorithm. (b) Li_2O_2 distribution profile in 3 normal directions of the volume in Figure 3e. (c) Histogram of sphericity. The perfect roundness of a particle is 1 whereas 0 to the non-sphericity.*

We then carry out a coarse and naive calculation of the average thickness of the Li_2O_2 dividing the volume by the surface. Note that the Li_2O_2 volumes in the recharged samples are actually a mixture. All below average coverings are calculated out of a volume of 2460 μm^3 (13.5 x 13.5 x 13.5):

	Fully discharged	Mixture Recharged in Figure 5b	Mixture Recharged in Figure 5c
Li_2O_2/mixture volume(μm^3)	218.4813	109.716	609.2262477
Surface area density (μm^{-1})	2.94	3.49	6.88
Li_2O_2 Surface area (μm^2)	723.24	858.54	1761.28
Average thickness(nm)	30.2	127.8	82.6

Table ST2. *Regroups mixture volume, surface area density, lithium peroxide surface area and average thickness deduced previous physical properties*

2.9.e. Annexes 5:

Elements quantification by EDS-SEM is plot in Figure 5a. The values are considered as semi-quantitative by reason of the uneven (interaction electron-material) analyzed surface. The material is washed with the solvent DMSO (See Experimental Method), the sulfur is present, the presence of chlorine is susceptible to be the residual salt lithium chlorate.

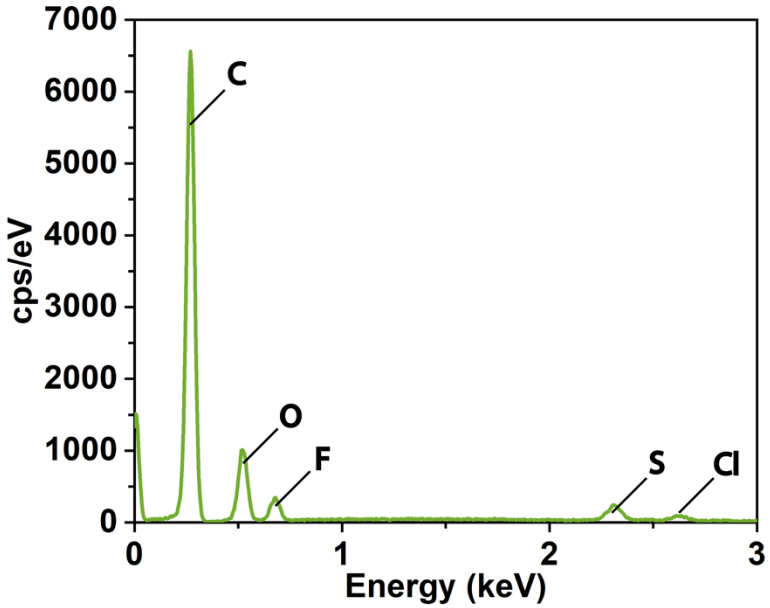

Figure S9. *Spectrum of SEM-EDS omitted from and attached with Figure 5a*

Element	Weight%	Weight% Sigma
C	73.86	0.31
O	16.72	0.26
F	4.91	0.16
S	3.12	0.11
Cl	1.38	0.09
Total:	100	

Table ST3. *massive percentage of each element deduced from Figure S9*

Chapter 3

Self-standing and recyclable binder-free cathode material for LOB

In the previous chapter, we have clearly shown the insufficient usage of the cathode due to a highly tortuous cathode. The material of cathode in LOB only plays a role of providing electron and hosting the lithium peroxide. The weight and volume fraction of host material should be minimized to maximize the capacity of the cathode.

In the current chapter, we propose a high porosity and low tortuosity material that can be easily upscaled. And we figured out also this material can be recovered after the cycling by the removal of discharge products.

3.1. Towards greener and costless chemistry

Mounting evidence shows the accelerating global warming effect, which insert urgency to investigate greener and more sustainable chemistry for energy applications[3,100]. The electrification of the transport and portable electronic sectors, with lithium battery technology is expanding at a staggering speed, spearheading this energy transition. Its global production has grown from 75 GWh in 2011 to 400 GWh in 2020 and is estimated to go over 1400 GWh in 2025, accounting for the under-construction giga-factories in major economies alone[21,101]. However, based on the Li-ion technology and EV market analysis, the forecast of the Ni and Co demand for 2030 will reach 2.5 times their global production capacity of the year 2016. Recently concerns have been raised on the shortage of these elements due to their geo-localization scarcity[22,23].

Moreover, there are growing concerns over the capacity of the disposal of end-of-life batteries. The commercial lithium traction battery has a lifespan averaging 8-10 years[102], and it has been a decade since the beginning of the electrification boom. Waves of millions of tons of lithium-ion batteries across the globe are retiring from the market every year. Many countries face the pressure of treating a tremendous amount of used Li-ion batteries in the past few years[103,104]. The energy density and coulombic efficiency are no more the only goals to achieve while developing new materials. Challenges are nowadays how to develop sustainable material of high energy density and of long lifespan as well as an associated efficient post material recovery process[105–107].

3.2. State-of-the-art in LOB cathode materials

The Li-O_2 battery (LOB) is often considered as a potential system to replace Li-ion technology in many applications, thanks to its outstanding energy density (>2920 Wh/kg)[108,109]. The cycle lifetime of LOB is often subject to the irreversibility of the cycling products on the cathode. As electrochemical round-trips progress, with relatively low coulombic efficiency, discharge product (as well as products of parasitic reactions) accumulate, the available surface at the air electrode diminish[110], which ultimately leads to the cell failure. Strategies usually proposed in the literature are 1) grafting catalysts or N-doped on cathode materials are reported beneficial for the charge[59–61,63,64]2) using redox mediator[111,29,30] to enhance the cyclability 3) stabilizing the conductive lithium superoxide as discharge product[112,113] or favor lithium hydroxide electrochemistry which engenders less side-reactions[75,114,115].

Besides, the parasitic reactions have been reported due to the presence of reactive intermediates during the ORR, such as singlet oxygen[116–118], and peroxide[66], as well as superoxide[66,113,119] in the LOB, which can lead to the binder degradation by the proton attraction[66,119]. This has led to the development of binder-free materials[120–124] for LOB.

In contrast with the lithium insertion material in Li-ion battery, the lithium conversion reaction nature of LOB enables a facile material recovery after the end of life. In this work, we combine the advantages of a binder-free material with an inexpensive solution of reconditioning or renewing the cycled cathodes for LOBs. We demonstrate that the binder-free material multi-wall carbon nanotube based (MWCNT or CNT in short hereafter) electrodes, cycled until forming thick covers of discharge products on the cathode surface to trigger the pore-clogging and cell death, this non-dissolved species on the electrode during the cycling can be easily removed by water, as well as regular acids without damaging MWCNTs. The washed electrodes can be then reused directly or, thanks to free-of-binder, resuspended to make new electrodes, with little difference in electrochemical performance.

3.3. Experimental methods

3.3.a. Materials preparation

The MWCNT powder was purchased from Nanotech Lab. 20mg of powder was added in 750 mL of Isopropanol. An ultrasonic probe (Sonoplus UW 2200) and a glace bath (Fig 1a) was used for the dispersion of CNT in the solution. 50% intermittent pulses of 200 W were used for 30 minutes. The solution was then centrifugated in 300mL bottles at 400 rpm for 45 minutes. The clear supernatant solute was vacuum filtrated with the GF/C^{TM} Whatman glassy microfiber filter, and the precipitation can go through again the same process. The solution of the second centrifugation became clearer, indicating that the dispersed MWCNT was less. The filtrated MWCNT is entangled and formed a self-standing porous electrode. Above a CNT loading of 2mg/cm^2, the electrode starts to be easily peeled off.

The above as-prepared electrodes were dried overnight in the Buchy at 120ºC and the 16µm thick Celgard (ENTEK 16 µm) and Whatman (Sigma) separators at 70ºC. The electrolyte 2M LiTFSI and 1M $LiNO_3$ in Dimethylacetamide is used[125]. The moisture of the electrolyte is measured at less than 100ppm by Karl Fischer and conserved with a molecular sieve. 100 µL for

the cycling experiment and 50μL more electrolyte is used for the experiment of capacity comparison for better wetting the SP@GDL and p-CNT.

3.3.b. Material reconditioning and recycling

The reconditioning step is as simple as soaking the cycled electrodes in the acid (see further Fig 6) and wait until it stops bubbling. The current collector usually detaches from the electrode during the bubbling, or one can wait until it is dry (we found that the electrode is easy to be broken when it is wet). In practice, we made a vacuum above the liquid to extract the gas trapped in the porosity to better impregnate the H_2O/acid into the structure. For the recycling, we harvested all the electrodes issued from the previous cycling experiments. First, it is washed subsequently by H_2O/acid and ethanol on a Buchner funnel. After weighting, it is re-dispersed by the same process of sonication, centrifugation, and filtration (with a smaller 2.5cm of diameter Buchner funnel, compared to the one in Figure 1).

3.3.c. Electrochemical measurements

For the capacity comparison for SP@GDL and MWCNT in Fig 2, the more fluffy Whatman glassy fiber separator was used because the electrolyte swallowing of the GDL is low. For the cycling of the p-/recon-/recyc-CNT electrodes, we directly used the filter of the vacuum filtration and added a Celgard on the anode side to slow down the oxygen percolation to the lithium foil and avoid the occasional short circuit issued from the CNT percolation in the Whatman filter indicated in the main text. The Operando pressure measurements and electrochemical cycling were done in parallel on a Bio-logic VSP within a Pressure Cell describe by F. Lepoivre *et al.*[126] and more details of calculating the e^-/O_2 ratio can be found in Figure S1. A 2h of open circuit voltage is systematically added before each galvanostatic cycling above.

3.3.d. Post-mortem characterizations

The *ex situ* X-ray holo-CT was done in 32-ID-C of APS. A specific pattern was graved by the laser beam of Zeiss Palm, and we used the epoxy-wetted pencil lead for retrieving a small tip for the tomography. The cycled electrodes are soaked in the pure dimethylacetamide to leach the salt and then dried in a vacuum without heating. For the Raman spectroscopy, the sample after drying is sealed between two slides of microscopy. We used a 532nm laser source of 10mW power with a diaphragm of 50 μm slit. For each sample in this work, we collected spectra at ten

different areas and for each area averaged 32 spectra of 1 second of exposure time. For the SEM, the samples were transferred from the dry room with a specific holder to minimize the contamination.

3.4. Facile synthesis of the p-CNT material

Several groups[121,127–129] have reported the use of carbon nanotubes in the construction of cathodes for LOBs. The as-purchased raw powder is vertical arrays of MWCNT used in this study are shown in Fig 1a and have diameters ranging from 5-30 nm and length averaging 100 μm. Such tightly aligned arrays of CNT have little porosity for Oxygen Reduction Reaction (ORR) and do not have long-range mechanical properties. The electrode cannot be made by compression or should add polymers as binder. To turn the commercial CNT powder into a self-standing (binder-free) electrode of coiled nanotube, a combination of ultrasonication and centrifugation are used (details see Experimental methods). The power was first dispersed into isopropanol, then vacuum filtered forming a homogeneous disc (Fig 1b). The first filtrate is often of dark color but rapidly turns into clear color due to the porosity of the glassy fiber filter allowing a small amount of CNT percolation, which is rapidly hindered by the first forming stack of entangled CNTs with smaller pores. It is worth noting that the filtration solvent can be reused. The filtrated CNT disc has a reflective black color and is flexible, as shown in the digital picture of Fig 1b-c.

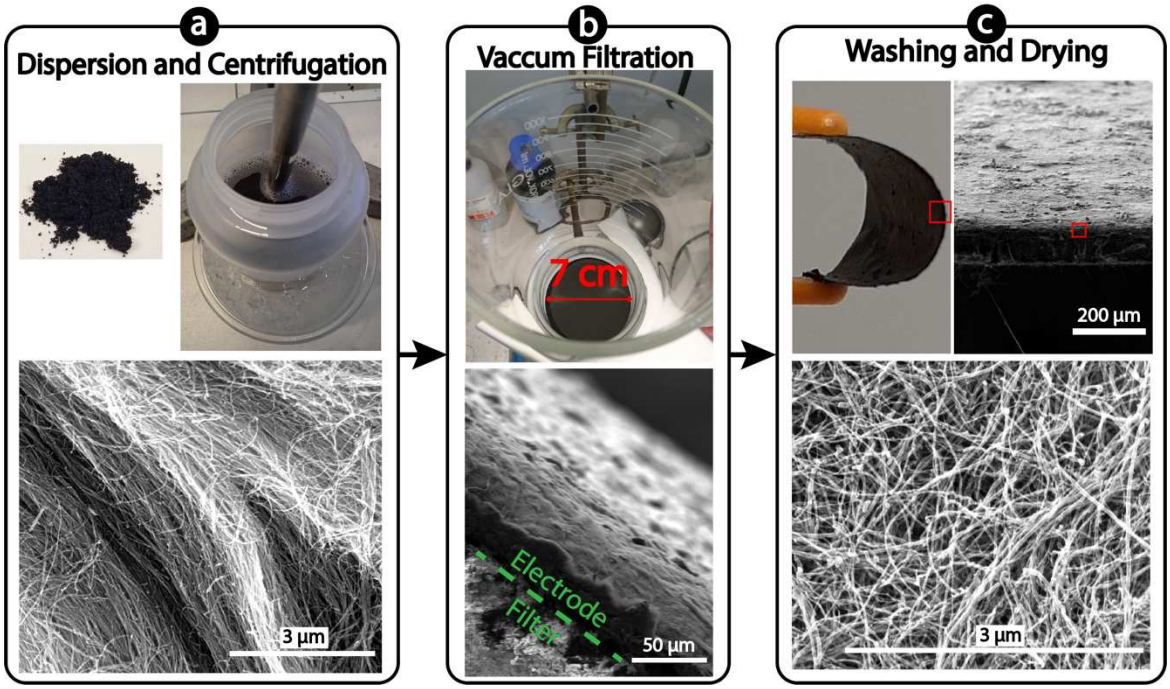

Figure 1. *Schematic diagram of material synthesis and recycling. (a) Digital picture of MWCNT powder and ultrasonic probe for the dispersion, and an SEM image of the aligned array CNT powder at the bottom. (b) Digital image of a p-CNT electrode on the top and the SEM image at the bottom. (c) Digital picture showing the flexibility of the p-CNT electrode and SEM images at different magnifications.*

The advantages of this binder-free preparation method are its simplicity and lack of material inhomogeneity issues due to the gradient of solvent evaporation or binder migration typically present in the typical casted carbon black electrodes[130]. This method can be easily scaled up in size and thickness. Increasing the size of the electrode requires a larger funnel, e.g., in Fig 1b, a 7 cm diameter disk of homogeneous electrode can be made. And thicker electrode can be obtained by a longer filtration (see Figure S2 SEMs in Annexes of this chapter).

3.5. Comparison between the p-CNT and traditional carbon black electrode

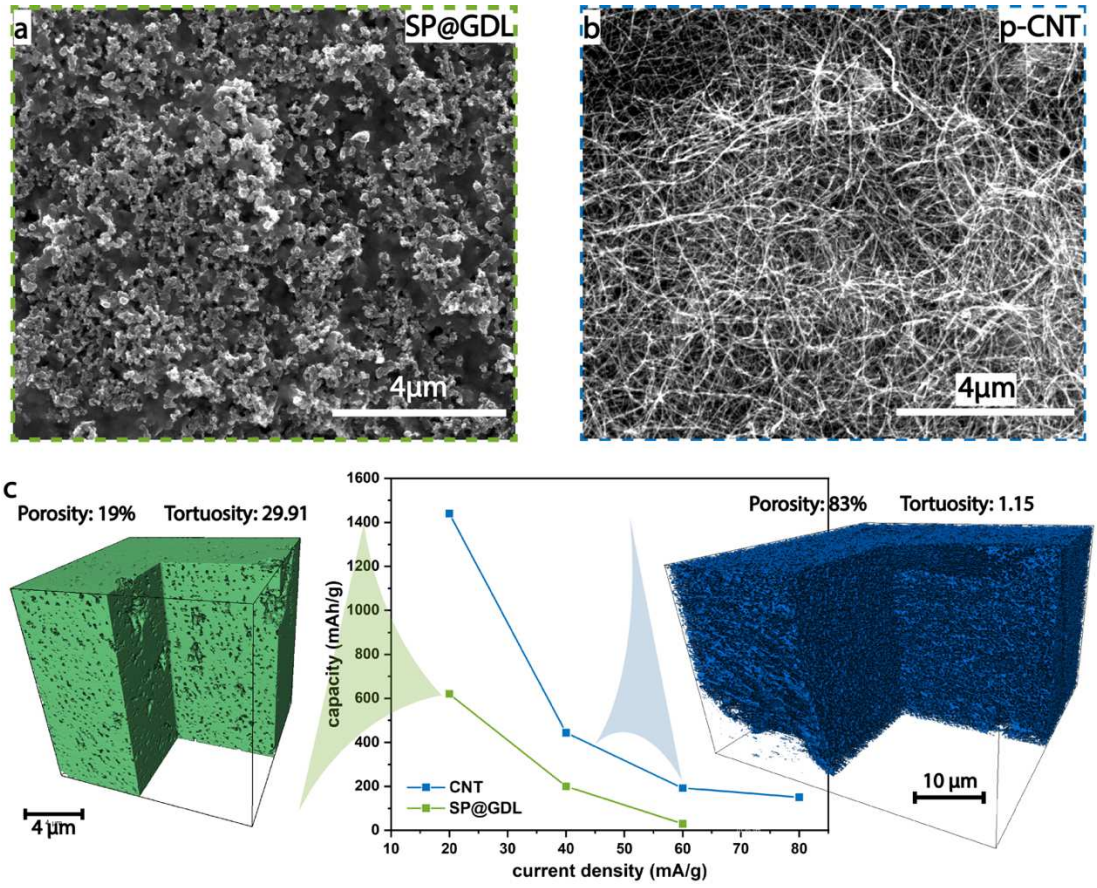

Figure 2. ***Structural and capacity comparison of SP@GDL and p-CNT.*** *SEM images a) the commercial SP@GDL material with binder and b) the pristine material p-CNT of this work c) A comparison of the deep discharge capacity at a different current density between these materials*

The as-prepared CNT material (p-CNT) has high porosity and an airier structure than the commercial SP@GDL material (or the drop-coated one in chapter 2). In the SEM images of the same magnification in Fig 2a and 2b, one can see through the pores in the p-CNT electrode, whereas the polymer in the SP@GDL firmly are connecting the carbon black particles that screens

the pathway of ion and oxygen, making a higher tortuosity. The tortuosity of pores in both materials was quantified by the X-ray tomography (depicted in Fig 2c, experimental details refer to experimental methods). The value of tortuosity depicted in Fig 2c is ten folds lower in the structure of p-CNT than the one in the carbon black part of SP@GDL. The meso- and macro- porosity is 0.83, higher in p-CNT than the 0.19 in SP@GDL, giving more space for the deposition of lithium peroxide. To prove the performance of the highly porous p-CNT material, deep discharges were performed using 2M LiTFSI 1M $LiNO_3$ in Dimethylacetamide reported by Yu et al.[125] (for electrochemistry details, please see Methods Section). The higher porosity and lower tortuosity of p-CNT promoted superior capacities at different current densities compared to SP@GDL electrodes, as shown in Figure 2c.

3.6. Cycling behavior of the p-CNT cathode

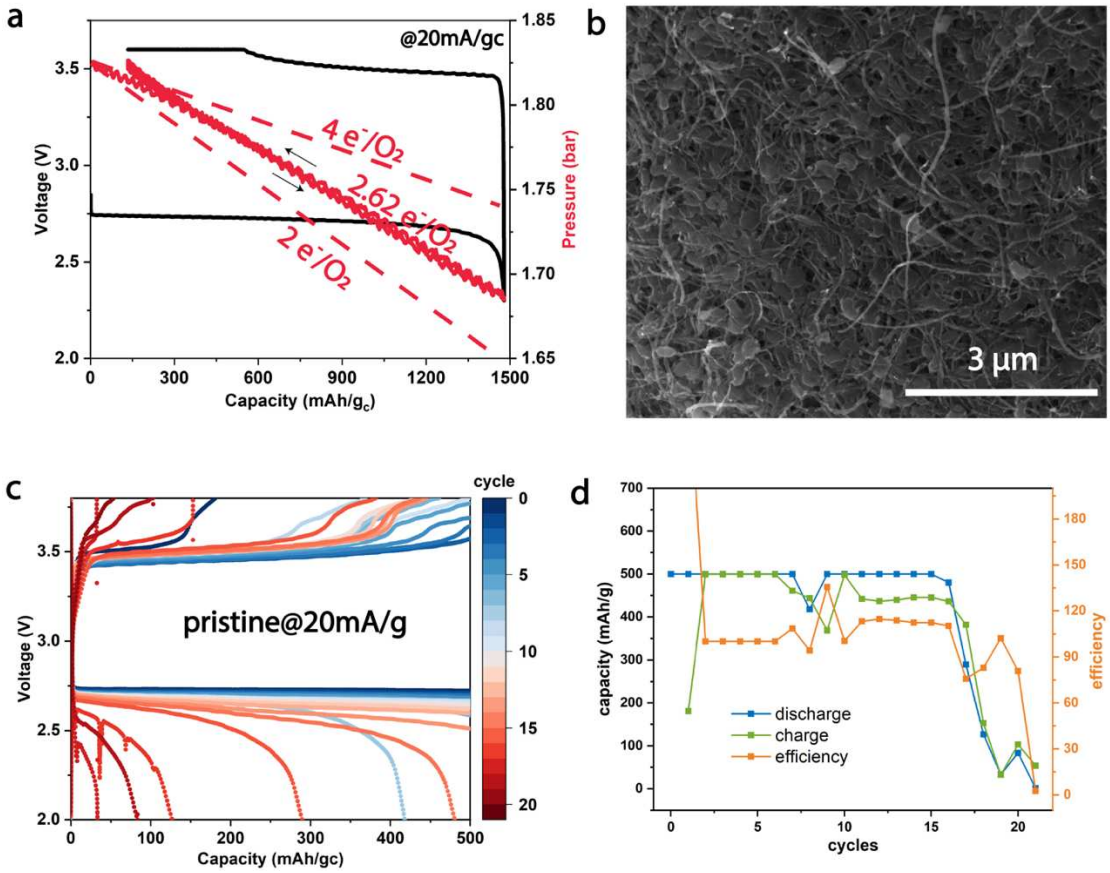

Figure 3. *p-CNT electrochemistry and discharge products analysis. a) First galvanostatic cycle with pressure change monitoring; b)SEM image of the cathode after discharge; c) Capacity-limited galvanostatic cycling and; d) Analysis of discharge-charge capacity and coulombic efficiency.*

Pressure monitoring during galvanostatic cycling suggests reversible Oxygen Reduction Reaction/Oxygen Evolution Reaction (ORR/OER) between 2.3V-3.6V depicted in Fig 3a. The

electron/O_2 ratio was found around 2.6 for the round trip, which is higher than the one associated with the ORR of Li_2O_2. This suggests that in this electrolyte, other parasitic reactions consuming more than two electrons per oxygen might be implied. The typical toroid and particle-like Li_2O_2 particles have been formed after the first discharge and confirmed by electronic microscopies (Fig 3b and S3). The EDS elemental mappings indicate traces of nitrogen, sulfur, and fluoride, which could be residues from the LiTFSI and nitrate salts in the electrolyte.

Fig 3c-d capacity-limited galvanostatic cycling in cells using p-CNT electrodes, where a characteristic ORR plateau above 2.6V can be observed all through the discharge process for up to 15 cycles. From cycle 16th the accumulation of discharge/parasitic products on the surface of the cathode reduces the capacity and the sudden cell death occurs thereafter at shorter capacities in subsequent cycles. The charge plateau observed initially at below 3.5 V is reduced from the first cycles, indicating incomplete discharge product removal, and thus progressive accumulation on the cathode surface. SEM images of cycled electrodes (after 21st cycle of Fig 3c) show a thick layer of solid deposits completely covering the surface of the p-CNT material (Fig 4a), as well as areas with larger toroid-like particles indicating incomplete removal of Li_2O_2 particles (Fig S8).

3.7. Inexpensive reconditioning and recycle

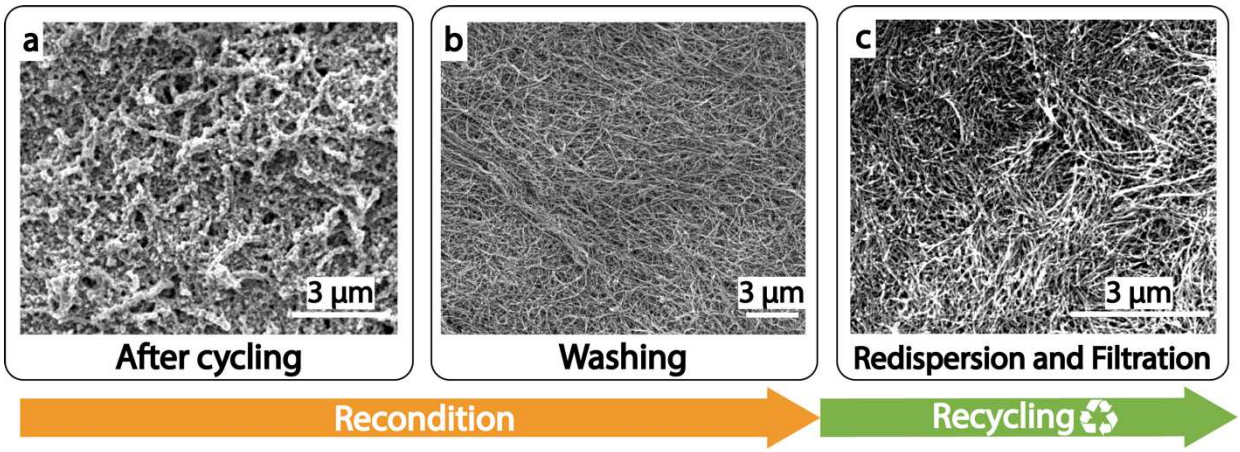

Figure 4. ***Material recovering scheme and electrochemistry of the reconditioned and recycled material.*** *a-c) SEM images of cycled, washed, and recycled electrodes, respectively.*

The previously used p-CNT electrode can be fully recovered for a second life. In industry, solvent evaporation is the most expensive procedure in battery manufacturing[131], making the binder removal a costly step in the material recovery. Beneficial from the absence of binder, the reclaiming of the material from the used p-CNT electrode is straightforward. After the p-CNT cell

death (Fig 4a), two ways of full recovery are possible. First (Fig 4b) is the in-place washing of the accumulated species on the CNT surface and then directly assembled in another battery. The second (Fig 4c) is to reinject the recovered CNTs into the dispersion and filtration procedures after the same washing step to reform a new electrode with a different size or thickness. The discharge products removal is simply soaking the electrode in acid or water (detailed in Experimental Section).

3.8. Analysis of the reconditioned and recycled electrodes

First, we examined the electrochemistry after the water-washing in both ways of reclaiming material. Similar cyclings were obtained to the one of p-CNT. The characteristic oxygen reduction in discharge plateaus are above 2.5V, and the oxygen evolution plateaus in charging at around 3.5V. The total cycle number with the same electrolyte is equally limited at 20 cycles. The discharge products remain Li_2O_2 toroids for both reconditioned and recycled electrodes, depicted in Fig 5c and 5f. The involved cell death mechanism is also the pore-clogging and surface passivation as in the p-CNT. The reproducibility of the electrochemistry and products characterization show the efficiency of the water-washing method and the material's renewability.

Second, the acid-washing[132] also exhibits recyclability of the material without damaging the CNT. Fig S6 shows the Raman shift of CNT soaked at regular acid of different pH. The under-peak area of both characteristic Raman bands (D band at 1338 cm^{-1}, G band at 1550 cm^{-1}, respectively) quantitatively associates with the disorder and in-plan order vibration in the CNT, respectively. Although it is well known that the mixture of acids nitrate and sulfate is a common reagent to oxidize the CNTs. Herein, both acid chloride and sulfate are tested separately. And the CNTs are intact after a series of different pH regular acid treatments, confirming that these regular acids do not affect the CNT. The electrochemistry shown in Fig S7 for acid-washed achieved the same cycling life as the water-washed one in Fig 5a-c.

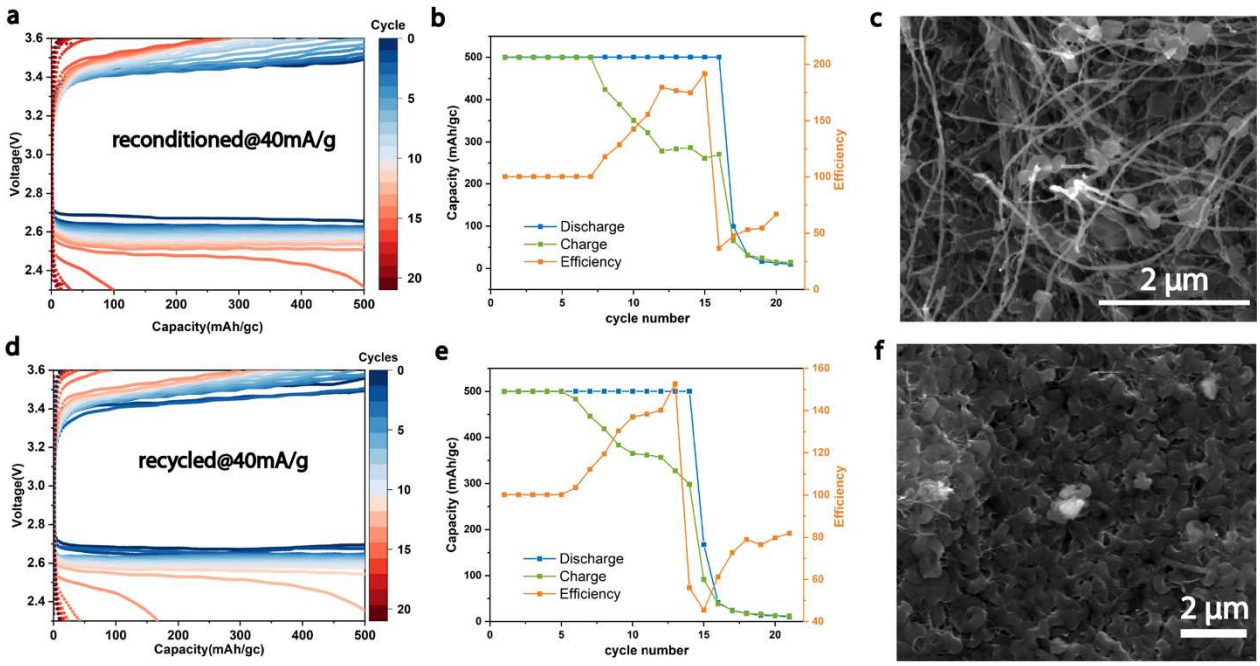

Figure 5. ***Reversible electrochemistry after the reconditioning and recycling.*** *a-c) are electrochemical curves of the round-trip, the capacity and coulombic efficiency within cycles, and SEM image of Li_2O_2 for reconditioned-CNT. g-h) are those with the recycled CNT electrode.*

3.9. Outlooks on the generalization of the recycling methods

In contrast with a previous study[132] using the acid as discharge product removal, we have extended the material recovering in LOB with the cheaper solvent water. Fig 6 shows the strong bubbling with acid in the washing step, whereas using water makes the bubbling less violent. It is worth noting that this violent bubbling of acid reagent could sometimes deteriorate our binder-free electrode. Indeed, the mechanism of washing are different for both solvents. For the water, the driving force is the solubility of species, which is similar to the first step reaction in the titration technique reported by McCloskey *et al.*[79]. The Li_2O_2 are firstly protonated by water into hydroperoxide and lithium hydroxide, which are soluble in water$Li_2O_2 + 2H_2O \rightarrow H_2O_2 + 2LiOH$. The hydroperoxide slowly turns into oxygen $H_2O_2 \rightarrow H_2O + O_2 \uparrow$, and small bubbles can be seen on the surface of the electrode (Fig 6). If a vacuum is made above the water to better extract the trapped gasses in the soaked electrode, this reaction is favorized and more bubbles can be observed.

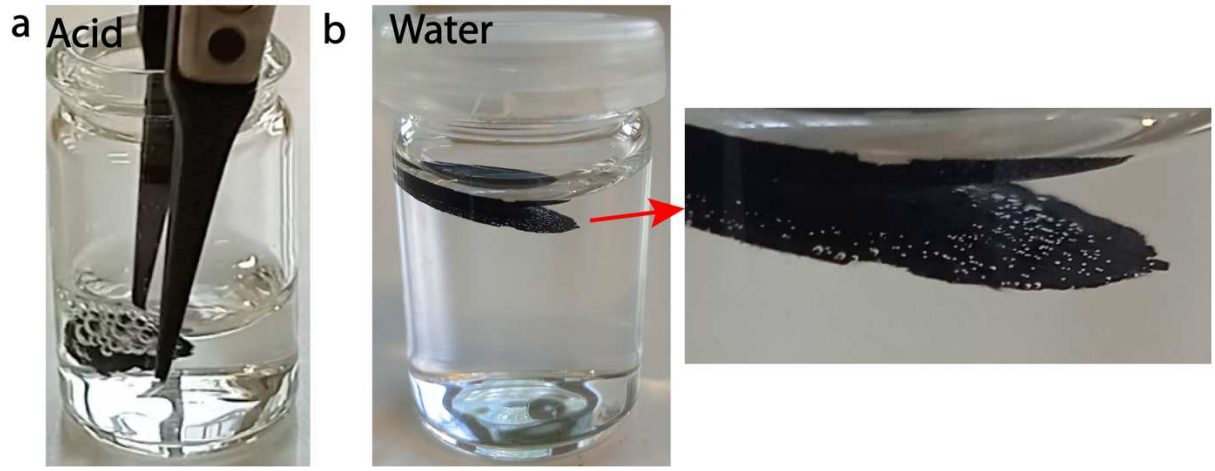

Figure 6. ***Gas bubble present while using acid and water for washing****. a) the electrode soaked in acid. b)The electrode soaked in water. The CNT is heavier than the water. The fact that the CNT is floating is an indicator that there is gas in the electrode. To better impregnate the electrode, we made vacuum above the solution in practice.*

From the recapitulative Table ST1, we see that most of the lithium salts are soluble in water. The LiOH formed by water-washing are also dissolved in water. Using acid will accelerate the protonation and eliminate the hydroxide. The reaction will be more efficient as the solubility of lithium with anion in regular acids (including chloride and sulfate) is higher. Noting that the solubility of the species in Table ST1 such as lithium hydroxide (127mg/mL) are in large excess. The quantity of Li_2O_2 formed then transformed into LiOH is less than 20 mg in a Swagelok battery. Therefore, using 2-3 mL of water can sufficiently wash all the discharge products in our case.

After the above analysis, we can generalize such recycling process to a broader range of products, as shown in table ST1. For instance, the frequently reported products or byproducts (e.g., Li_2CO_3, Li_2O) are soluble or partially soluble. Some of them are basic and, therefore, can react with the acid. The use of water as a renewing agent we proposed is of low cost. Most importantly, the washing agent issued from our approach can be directly injected in an industrial know-how process for recovering the lithium (precipitating lithium carbonate using sodium carbonate[133,134]). A future investigation could be retrieving the lithium carbonate and producing lithium metal by electrolysis to form a closed recycle circle of fully recyclable LOB. Other Metal-O_2 batteries such as Na-O_2, Zr-O_2, and Al-O_2 can also be beneficial from this method, as the acids can dissolve the metal oxide but not the carbon matrix as reported in this work.

3.10. Conclusions and Perspectives

In summary, an ultra-simple synthesis of a binder-free self-standing electrode for the Li-O_2 battery is reported. We demonstrated the recyclability of such material after being cycled and

strongly polarized by a thick cycling product covering. Two ways have been shown: 1) reconditioning the electrode or 2) reclaiming the carbon nanotube and reconstruct a new electrode. We have elucidated the involved reactions and the principles of such recycling method. Different from a previous work using acid[132], we have detailed a cheaper mechanism of using water for the material recovering. The applicability of this washing method by acid or water for other metal-O_2 batteries as mentioned will be further investigated. Surface spectroscopies such as XPS could be used to study whether terminations and groups on the nanotube surface are changed after the cycling.

In the next chapters, we base on this binder-free material and develop in situ X-ray tomography experiments and machine learning segmentation tool.

✅ Important takeaways :

The cell death of Li-O_2 battery (LOB) occurs due to the accumulating passivation of discharge products and the pore clogging during the cycling. We herein demonstrate an efficient method to renew the cycled LOB binder-free material after the cell death. Our inexpensive method consists of washing the cycling products and byproducts in the electrode. The material is self-standing without polymer binder and has an airy structure with high porosity. We show that the discharge products can be easily washed, and the material can be re-dispersed into the solvent and further made into a new electrode for a second life. We characterized by spectroscopies and microscopies the discharge products remain the same after the recycling. The current findings are helpful for building greener high-energy density Li-O_2 battery and potentially cutting the cost of manufacturing by recycling.

- Dispersion-filtration two steps synthesis of p-CNT
- Facile recyclability of LOB cathode and potential to generalize to other metal-O_2 battery
- Inexpensive method of material recovering

3.11. Annexes

Figure S1 shows the Oxygen flushing system and the Pressure-Cell of Collège de France developed by Lepoivre et al.[126]. The pressure captors are calibrated with the GPB 3300 absolute barometer. The Pressure-Cell with the Swagelok was firstly assembled in the Ar-filled glovebox and then replace the Ar by pure oxygen using the flushing system. During the cycling, the blue valve is closed, separating V_1 and $V_?$. The function of the highlighted parts with number in Figure S3 are as following:

1. *Female quick connect body (airtight without connecting to the male part)*
2. *Pressure captor OMEGA PX309-030A5V*
3. *Male quick connect body*
4. *An insulating ceramic gasket is placed inside the tube for isolating the Swagelok cell from the metallic column to avoid electric perturbation.*
5. *Metallic tube of bespoke length*
6. *Swagelok battery*

The volume $V_?$ of the column can vary each experiment due to the different compression of the spring in the Swagelok. To calculate the electron/O_2 ratio, the exact $V_?$ should be known. For this, after the cycling, we make a vacuum in the volume V_1(which is fixed and can be determined beforehand by filling a liquid and measure the volume of it). The pressure before opening the blue valve in Fig S3 denotes P_1. Then open the valve and the pressure drops, one notes P_2 for the pressure after the stabilization. The $V_?$ can now be calculated with the expression below.

$$V_? = \frac{V_1 P_2}{P_1 - P_2}$$

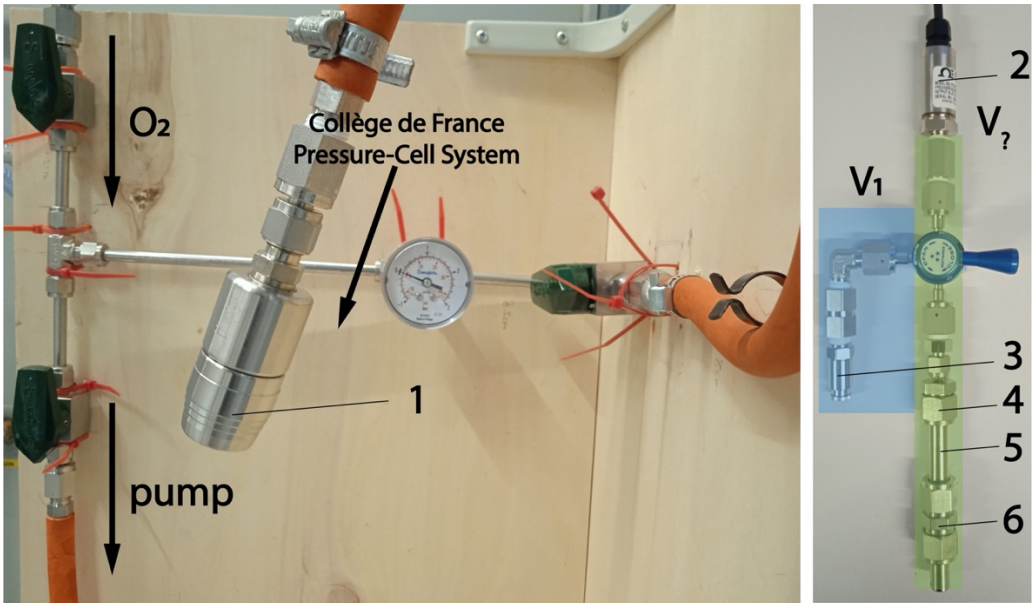

Figure S1. *The Collège-de-France Operando Pressure-Cell System. (left) the O2 filling panel (right) the Operando Pressure-Cell System with the battery Swagelok at the bottom.*

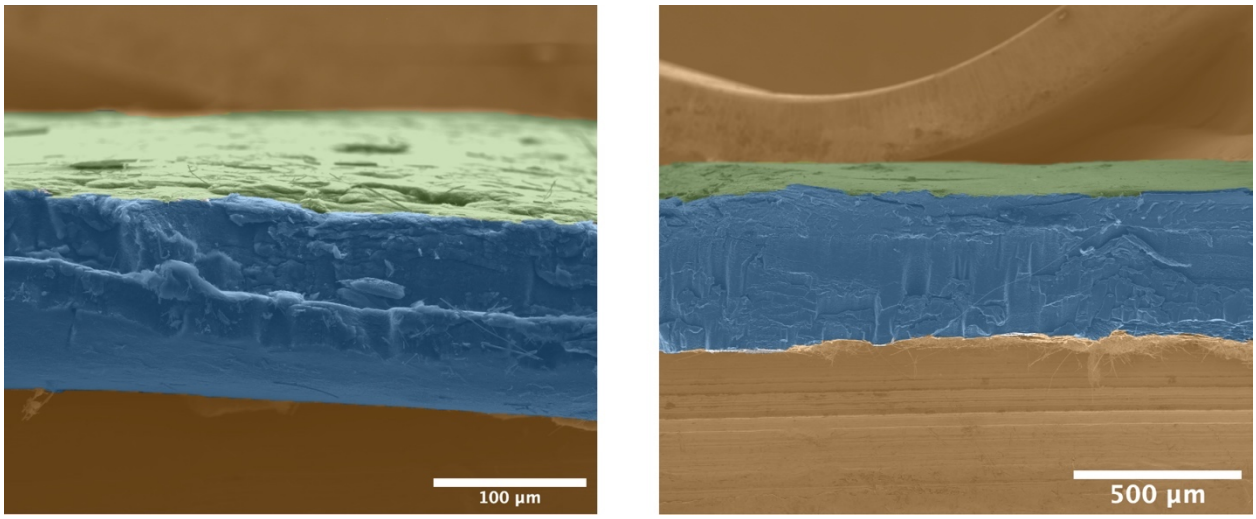

Figure S2. *SEM images of various thickness of p-CNT electrode. The thicknesses of these electrodes are 125 µm (left) and 406 µm (right), respectively.*

From Fig 3a, we see that 60% of the capacity can be recovered in the galvanostatic charging before the steep slope of increasing voltage above 3.6V. And a supplementary 30% of gas could be retrieved by holding the voltage at 3.6V. The cycling experiments of this work were arbitrarily performed between 2.3-3.6V in order to accelerate the accumulation of discharge products. The LOB at higher voltage does not implicate the lithium peroxide dissolution.

Fig S3 justifies this choice of the cutoff charging voltage. We see that holding the voltage above 3.6V results in no pressure evolution, which suggests that little oxygen evolution reaction at higher voltage. The potential plateau at 3.5V is followed by a steep slope. During the escalating voltage, a transition of pressure evolution can be seen, indicating that a different electrochemistry might be involved. In addition, holding the voltage at 4.0V does not allow to recover the initial amount of gas in the system.

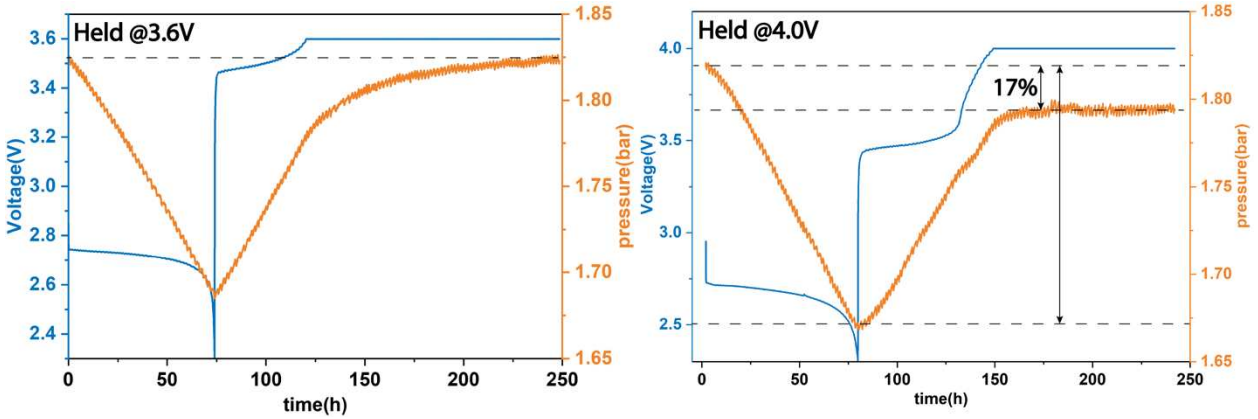

Figure S3. *Comparison of different charging cutoff voltage. (left) at 3.6V (right) at 4.0V. Holding at 4V does not imply the oxygen evolution reaction.*

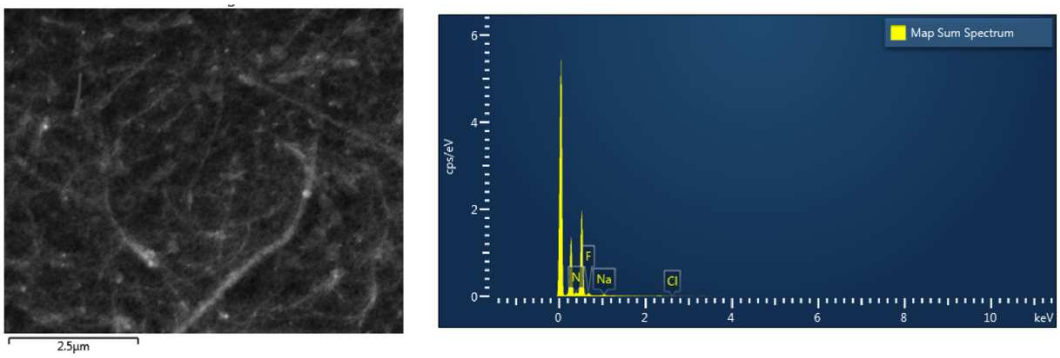

Element	Wt%	Wt% Sigma
C	36.18	0.44
N	2.93	0.44
O	55.76	0.51
F	2.23	0.22
Na	0.84	0.12
S	1.90	0.27
Cl	0.16	0.28
Total:	100.00	

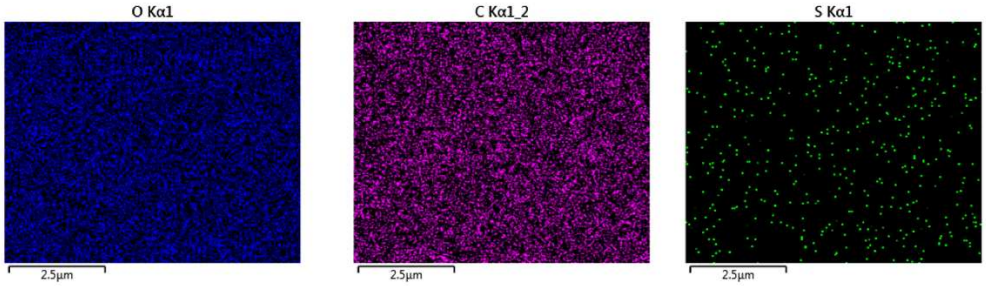

Figure S4. *SEM image and EDS analysis of some clogging part on the oxygen side of the cathode. The richness and distribution of oxygen mapping indicate.*

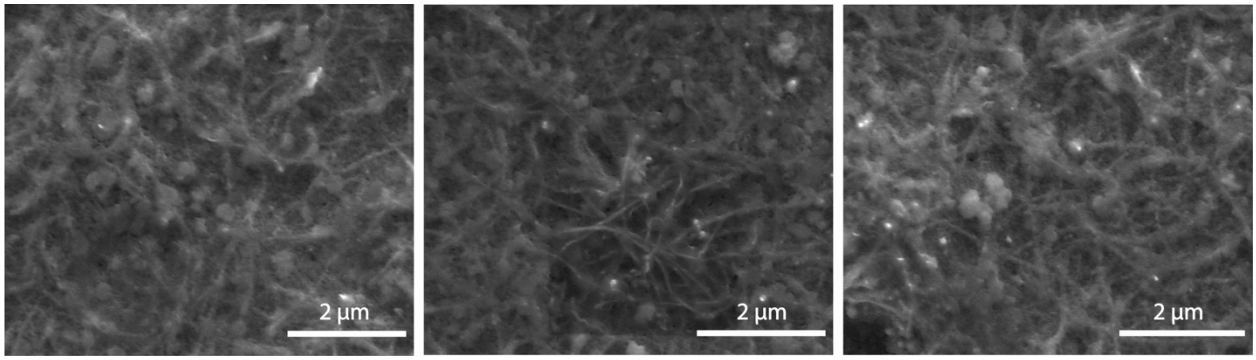

Figure S5. *More SEM images of the clogging on the O_2 side of the electrode*

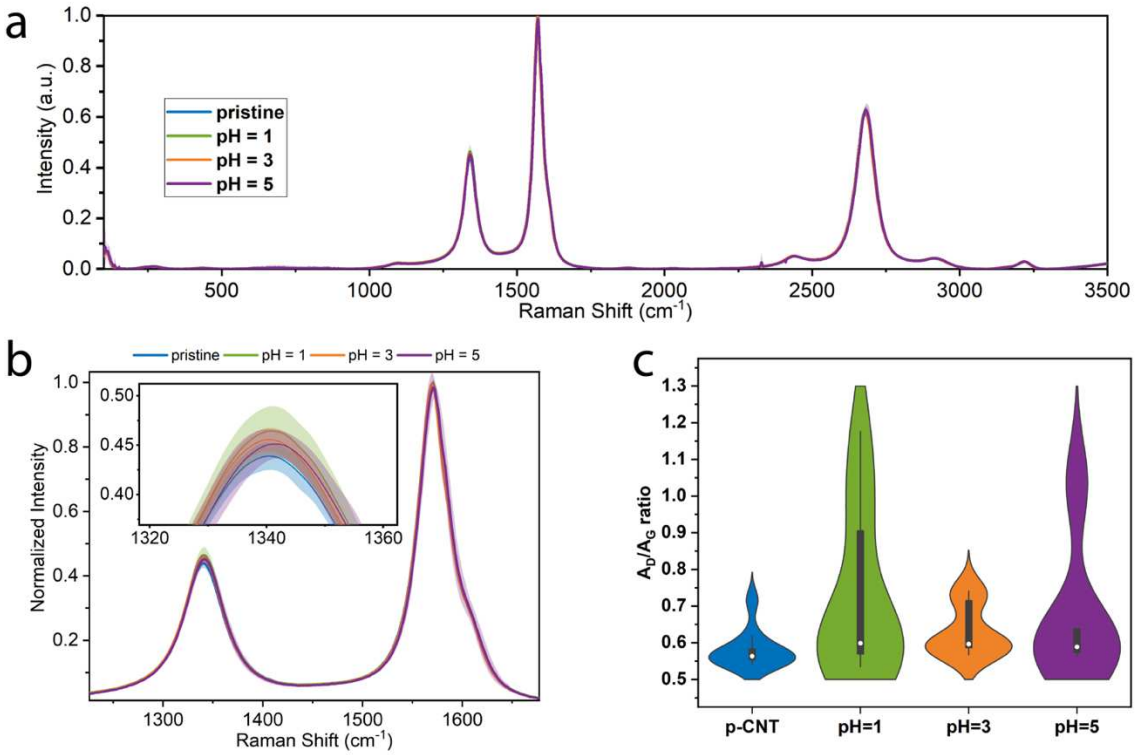

Figure S6. ***Degradation study of the MWCNT cathode by Raman.*** *a) Comparison of the Raman spectra of CNT electrodes treated by acid of different pH. b) the zoom of a) on the D and G bands and c) their under-peak ratio for p-CNT electrodes soaked in different pH.*

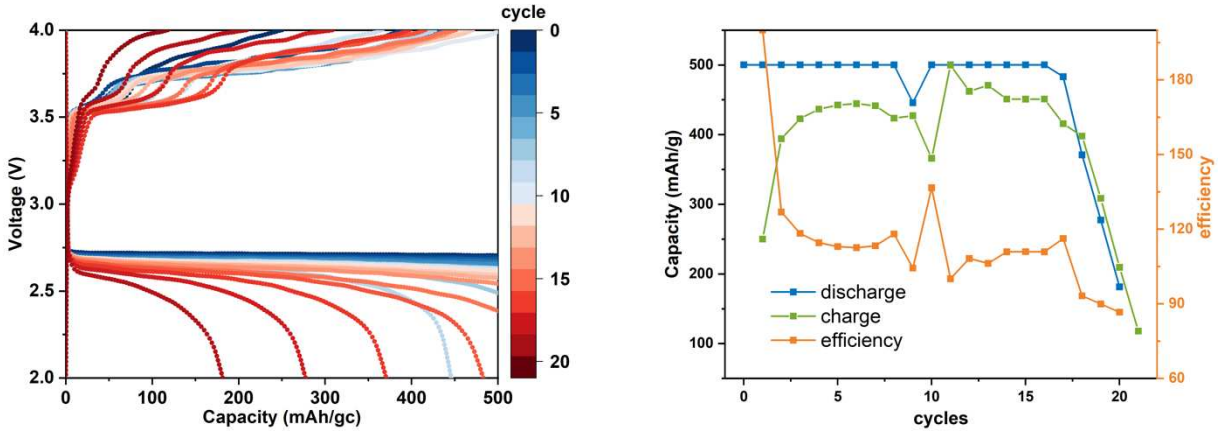

Figure S7. *Electrochemistry of acid reconditioned electrode. Shorter charging plateaus were obtained probably because of the presence of proton turning Li_2O_2 into H_2O_2, which is soluble and could not be reversed on the surface during the charge.*

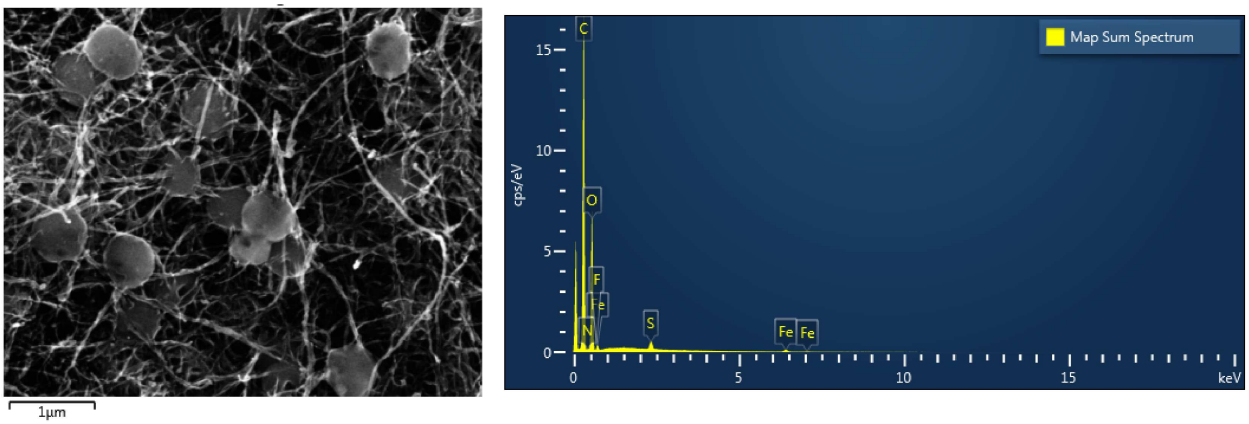

Element	Wt%	Wt% Sigma
C	58.71	0.14
N	0.00	0.31
O	37.44	0.13
F	1.38	0.08
S	0.87	0.02
Fe	1.60	0.06
Total:	100.00	

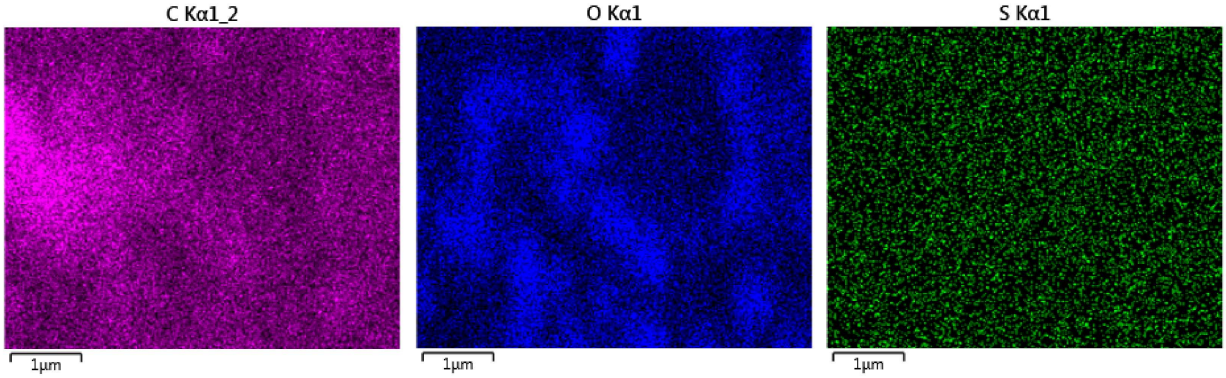

Figure S8. *EDS/SEM analysis of the discharge product in the recycled electrode. The sulfur and fluoride are traces of salt. And the Fe are precursor inside the nanotube which can be seen in TEM imaging.*

	Reactivity with acid	Reactivity with H_2O	Ref
Li_2O_2	H_2O_2, Li^+	H_2O_2, LiOH	[79]
LiOH	H_2O, Li^+	Soluble 127 mg/mL	[114,75]
Li_2CO_3	CO_2, H2O, Li^+	Mildly soluble 12.9 mg/mL	[104]
Li-R (strong base)	Protonation	Protonation	[41]
LiCl		Soluble 842 mg/mL	
Li_2SO_4		Soluble 349 mg/mL	

Table ST1. *A non-exclusive list of solubility and reaction of the products and by-products in LOB*

Chapter 4

Towards 4D time-resolved nano X-CT for LOB

Combining the outcomes from the previous chapters, we try to push forward our 3D investigation to 4D with time steps to understand the deposition of Li_2O_2. In the current chapter, we will present a novel *in situ* tomography cell (Tu-cell), how to conduct such experiment, and analyzed the obtained time-resolved volumes.

4.1. State-of-the-art in *in situ* X-ray tomography for batteries

Along with the compelling non-invasive property of XCT, *in situ*/operando experiments can also be deployed to study the kinetics aspects of the material at multiple scales. Up to date, the most intense development of *in situ*/operando CT experiments for batteries is done with micrometric resolution (µ-CT). Depending on the X-ray source and the sensors, the field of view varies from hundreds of micrometers to tens of millimeters. A Li-ion 18650 Li-ion battery can be directly 3D imaged, observing the thermal safety, electrode aging and volume changes during cell-scale cycling[135,136]. For the evolution of materials at the micrometric scale, one can investigate with in-house operando cells during the cycle. These cells are generally cylindrical with walls made of material transparent to X-rays such as PEEK and polyimide polymers. In these studies, the characterized electrode was cut into a small diameter disc to fit the in-situ cell and not to bypass the field of view.

Several groups have successfully conducted in-situ/operando µ-XCT with phase contrast techniques for Li-sulfur batteries because the sulfur in the cathode exhibits high contrast with other elements[135–138]. Yermukhambetova *et al.*[135] used Zernike phase contrast, while the Zielke *et al.*[137] used single distance phase retrieval to enhance the contrast of sulfur. Silicon as an anode in Li-ion battery has also been extensively investigated by *in situ* experiment on its volume expansion[139–141] during lithiation. Piestch et al.[139] combined XCT and scanning X-ray diffraction techniques to study the 3D lithiation of silicon on a bulk electrode scale. They were able to follow the in-depth profile of the $Li_{15}Si_4$ over time and show the volumetric changes. Vanpeene et al.[140–142] provided evidence of electrode cracking and gas release due to SEI formation using *in situ* XCT. Additionally, the *in situ* XCT has also been found particularly useful for interface detachment studies of all-solid-state battery[143]. Several studies[144–146] have employed *in situ* XCT experiments at nanoscale resolution with different cell designs. Wang *et al.*[144,145] visualized several Sn particles in time-resolved and in high resolution during lithiation and sodiation in an capillary cell, while Li *et al.*[146] visualized with *in situ* nano-XCT the (de)lithiation of primary germanium particles in a quartz *in situ* cell.

Over the last decades, many interests have been brought in metal-O_2 batteries due to their high energy densities[147,148]. These batteries have the commonly depositing or forming metal oxides during cycling. For example, the products of sodium oxides and tin oxides in Na-O_2[149] and Zin-O_2[150–152] batteries are micrometers and exhibit high X-ray contrast with a carbon matrix, making XCT a relevant and robust technique for characterization. Manke et al.[151] visualized

operando the transition from Zn to ZnO. They also compared the measured volume variations with the theoretical one. This group also conducted the *in situ* XCT on lithium for the Li-O_2 battery[153]. They put forward with the time-resolved 3D observation an irreversible formation of a transition layer on the lithium surface. This formed porous transition layer is mainly composed of LiOH and Li_2CO_3, which is formed by the presence of oxygen and the degradation of glyme-based electrolyte. Thanks to the time-resolved CT experiment, they found it thickened during cycling and attributed it to the poor reversibility. They pointed out that this is a hidden factor that is often ignored in the field of Li-O_2 battery (LOB) and other metal-air batteries but has severe consequences for the cyclability. On the cathode side, the size of the products and the material are on sub-micrometer scale and the contrast is quite low in pure absorption. The resolution and contrast of the micro-XCT absorption applied in their study are not adequate to capture the products in the O_2-cathode. In our previous study[110], we have investigated the phase contrast 3D imaging for enhancing the contrast of a cycled LOB cathode material and extracting its tortuosity and porosity. To meet the challenge of 3D imaging the products in a LOB cathode via an *in situ* system, we integrate our previous in-line Zernike Phase Contrast nano-CT method[110] into a new *in situ* XCT cell design.

In the current contribution, we report a novel approach to conduct *in situ* nano-XCT experiment for the Li-O_2 battery using an in-house electrochemical cell. A specific laser sample preparation was used to allow alignment between the beam and the focusing plan on an acquisition area, which does not exceed 60 µm. Zernike phase contrast was applied to enhance the contrast of Li_2O_2. The tomography acquisition and reconstruction with limited angles will be detailed. The spatial resolution reached 360 nm. The effect of the X-ray beam on electrochemistry is discussed, and potential ways for improvement for this experiment are then proposed. The time-resolved 3D volumes obtained during the discharge were injected into a particle tracking algorithm to study the motion of the formed particles.

4.2. Experimental methods

4.2.a. Cell design

The design of cells for X-ray tomography is the most essential part and will influence how the nano-CT experiment is carried *in situ*. There are several constraints related to the design of a nano-XCT cell. First, dead angles obscuring X-rays in the field of view (FoV) during the rotation should be limited. Dead angles can degrade the quality of the reconstruction, resulting in bifurcated streak artifacts that appear[154–159] on small objects and high curvature edges. These

artifacts can be easily identified because they have an identical orientation in the tomographic reconstruction plan (XY plan in Fig 1a) and throughout the stack. It has been reported that numerical reconstructions such as total variation reconstruction (TV) [154] as well as a coupling of emerging reconstruction algorithms with machine learning assisted in-painting techniques[155–159] can help mitigate these artifacts. Second, the X-ray absorbance of the components and their thickness should be controlled. Polyether ketone, polyimide, glassy carbon (GC), and berylium are often chosen for the main body or for the X-ray transparent window of the X-ray cell in the literature[160,161]. The thickness of the overall cross-section is critical in nano-XCT. We used simulators[162–164] to help estimate X-ray transmission and conceive the electrode thickness before performing the *in situ* nano-XCT experiment. Third, the difficulty of assembling cell must be considered. Deposition/coating[135,142,146] on a tip or mechanical shaping[140,142,144,145,153] are two common strategies in the literature for preparing materials for in-situ XCT cells. Our method is different, which is to use a laser to cut patterns into the electrodes (see the section 2.3). The following in-house disc geometry cell, TU-cell, allows electrochemical measurements to be conducted with realistically sized electrodes (Figure 1).

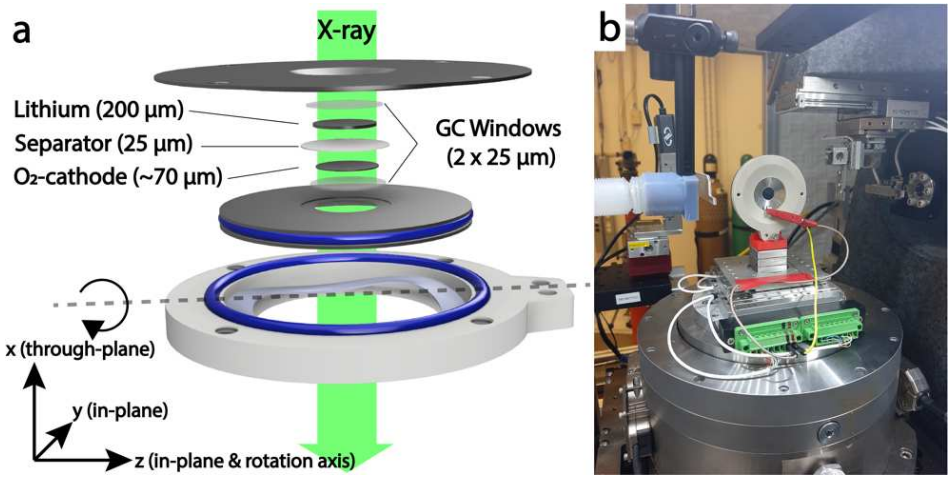

Figure 1. *Tu-cell and beam-line integration (a) A sketch of the Tu-cell and its components with the conventional axis throughout this work. (b) Image of the Tu-cell seated and connected to the rotation stage in the ID-32-C APS beamline. The red part under Tu-cell is a customized 3D printed component that can be personalized for adapting different beamlines.*

Tu-cell is designed with a flat, slim geometry and an inherently 30º of dead angles. It is made up of three parts (Fig 1a): a large stainless-steel cover (LSS), a movable stainless-steel (SS) disc in the middle and a Teflon base. The cover and the base are static, while the middle part is movable and compressed by a spring. Air tightness is ensured by two PEEK polymer rings compressed around the central disc and the Teflon base. Glassy carbon (GC) windows are glued, by a silver epoxy resin for the electronic conductivity, to the hollow indentation in the center of

both the SS disc and the cover. To avoid direct contact between electrolyte and silver epoxy, the spaces between the GC window and the LSS disc are coated with a chemically resistant silicate epoxy. Fig 1b shows the way that Tu-cell is integrated on the ID-32-C beamline of APS synchrotron.

4.2.b. Materials and synthesis

The lithium pellets were purchased from MSESupplie and the glassy carbon window from HTW Hochtemperatur-Werkstoffe GmbH. The separator is Celgard industrial grade and the self-standing binder-free carbon O_2-cathode is made of raw MWCNT from the NanoTech Lab®. To produce this CNT electrode, the MWCNT is first dispersed with isopropanol in a ratio of 12 mg/L with 1 hour of ultrasonication. This solution is then filtrated through a Whatman glassy fiber filter with a pore size of 1.2 µm until a loading electrode disc of 1.69 mg/cm^2 is obtained. The dispersed MWCNT has been retained on the filter and forms an entangled network. During the loading, the carbon paper made of entangled MWCNT is self-contained and can be easily peeled off the filter using tweezers. Its thickness is approximately 65 µm, roughly equal to the width of the FoV of the ID-32 TXM. The electrode is treated with chloric acid (~9% volume ratio) for 1 hour to reduce residual iron. During the treatment, a vacuum is made above the solution to extract the bubbles trapped in the porosity for better acid impregnation. It is then washed by abundant deionized water and ethanol before being dried in a vacuum oven for at least 2 hours at 120 ºC. The electrolyte we used is 2 M $LiNO_3$ in dimethylacetamide as described by Lepoivre et al.[126]. The electrolyte was dried and stored with an activated molecular sieve. Before the *in situ* experiment, it was bubbled in a vial with a syringe connected to a balloon filled with pure oxygen for about 30 min.

4.2.c. Laser sample preparation and beam alignment

The laser is frequently used to sculpt tiny pillars (a few tens of µm in diameter, which are as thin as a hair) for the *ex situ* nano-XCT[165]. However, it is not easy to use such a tiny tip in an *in situ* cell and mount it in the glovebox. The small amount of active material can also raise problems of reproducibility in electrochemistry, because it is difficult to control the mass loaded on the tip as well as to estimate a current. To remedy this, the experiment was conducted differently. The following laser top-down approach can use the same electrode size as in a coin-cell or Swagelok and apply the same current density.

We used the laser (Zeiss Palm laser micro-dissector) to cut patterns on the electrode to (1) reduce dead angles and (2) align the beam and the focus plan. On the 14 mm diameter CNT

electrode, we removed three squares (Fig 2a) with a side length of at least 5 times FoV (~250 µm) around the acquisition area (A_{acq}). The tomography A_{acq} is the small pillar between the two upper squares. As the axis of rotation of the Tu-cell is parallel to the plan of the electrodes, the X-rays pass through all the battery components. Details of the lithium and the separator were also imaged with the cathode in the parallel beam mode (Fig 2a, S1 and S2).

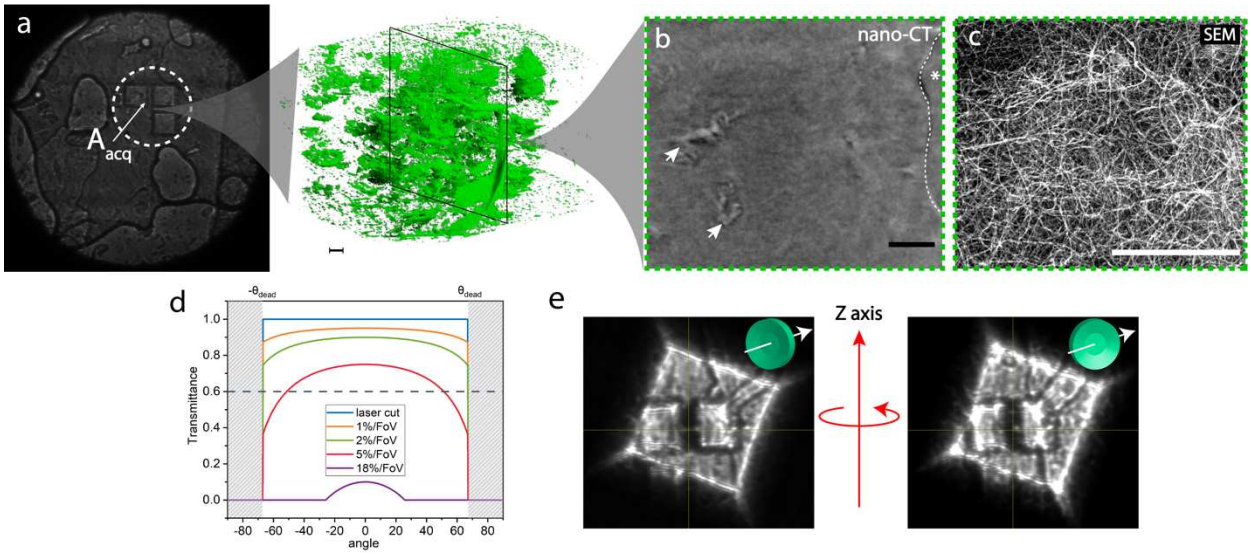

Figure 2. *Illustration of beam and focus alignment (a) the laser cut patterns in the X-ray beam in parallel beam mode (low resolution without magnification). The white dotted line circle highlights the patterns of squares cut by laser. And the acquisition area (Aacq) is the pillar between the two top squares. (b) The green volume shows the Aacq of the pristine material with pores and fibrils roughly segmented, and an ortho-slice of the raw CT volume. The asterisks spot the outside void cut by laser of the electrode. And the arrows point out the macro-pores in the material. (c) an SEM image of this material is shown on the side. The scale bars of (a-c) are 5 µm. (d) a simulated transmission rotation angle plot of Tu-cell with/without the laser-abraded assuming a homogeneous background. 0° corresponds to the through-plan x axis perpendicular to the plan of electrodes. Several examples of transmission without laser-cutting for materials of different absorbance in between 1-18% normalized by field of view (FoV) are also shown. The minimum transmission of 60% for good tomography quality is indicated by a dashed line (e) illustration on how to bring the center of rotation onto the Aacq. Two pictures of well aligned Tu-cell at 0º and 15º in the parallel beam mode are shown. When the focus plan is precisely on the carbon cathode, not on the lithium nor on the separator, the dark laser-shaped pillar should not deviate from the center of camera.*

Figure 2d shows the comparison of the theoretical transmission from different angles by removing (blue curve) and without removing the materials around the A_{acq} (other colors). Various absorbent materials (expressed as % by X-ray cross-sectional width) without laser cutting are plotted. We see that the transmission decreases with the angle of rotation θ when the thickness increases as a function of 1/cosθ. A 5% material per X-ray cross-section equivalent to a field of view will lose 40% transmission at ± 50°. And the aperture narrows further to ± 25° with 18% / FoV absorbance cross-sectional material. In practice, a transmission greater than 60% gives a better quality of reconstruction as indicated by the dotted line in Fig 2d. Other parameters such as the

beam energy and the thickness of the different components should be adjusted accordingly for better transmission.

Regarding the assembly of the Tu-cell, it is as easy as mounting a coin-cell battery. The squares are barely visible to the naked eye. The third square at the bottom right is not mandatory. But it increases the visibility and guide to vertically align the tiny pillar according to the vertical axis of the microscope. While mounting the cell, the pillar must be aligned with the corner, which has two holes for screws at the bottom of the Tu-cell that indicates the z direction. In a glove-bag filled with pure oxygen, we simply started by putting the O_2-cathode and then the Celgard separator on the LSS disc. Addition of 100µL of electrolyte pre-bubbled with oxygen wets the Celgard and the cathode. And finally, we ended up stacking neatly the lithium foil on top and closing the cell carefully with screws.

After the assembly, finding A_{acq} in TXM and aligning beam and focus is a decisive step in Tu-cell. As shown in Fig 2a and Fig S1, the squares are rather transparent, but they can be recognized by their noticeable shape. The weight of the materials removed from the squares is negligible (much less than 0.1 mg) compared to the entire X-ray window and the whole O_2-cathode. To increase the chances of finding the pattern under the microscope and limit the duration of the X-ray irradiation, dozens of these patterns separated by 1 to 2 mm were cut in the center of the electrode. These patterns were used to move the center of rotation on the A_{acq}. For this, we scrutinized a position on the through plan direction for the Tu-cell such that the dark pillar remains in the center of the camera while rotating the cell (Fig 2c). A quick shutter for the beam is mandatory during the above pattern search and position adjustment on the x-axis to minimize the X-ray dose. Note that the effective aperture angles will also be close to the theoretical one (±75º) if the A_{acq} is at the center of the transmission window. In this work, an effective opening of -67° to +67° was obtained.

4.2.d. Electrochemistry and Zernike Phase contrast

On the beamline, the electrochemical measurement was done with a potentiostat SP-200 of Bio-logic. We imposed galvanostatic pulses of 5 µA in the Tu-cell, which is equivalent to a current density of 0.004 mA/cm^2 (four-fold less as in a Swagelok) and ~C/15 of C-rate of the self-standing cathode in Tu-cell configuration.

In this experiment at 32-ID-C APS, a zone plate condenser, an in-line Zernike phase ring, 8 keV energy, and a working distance of 3.4 m were used, which provides a voxel size of 27 nm. The acquisitions were made during the relaxation periods marked by the dashed line in Fig 3a. 721 projections of one second of exposure have been collected using a scintillator (LuAG CCD) coupled with a CCD camera (Grasshopper3 5.0 MP GS3-U3-51S5M-C) in the effective aperture of 134°. The gold phase ring was placed downstream to the sample to induce Zernike Phase Contrast, which enhances the contrast of light elements. Fig S3 shows a comparison of the same projection between the absorption and phase contrast mode of TXM. The edges of the relief and a few small features have been emphasized by the Zernike phase contrast. All components are in compression, therefore steady and motionless CT acquisition can be achieved in Tu-cell.

4.2.e. Other *postmortem* sample preparations

The *postmortem* characterization samples were first washed with dimethylacetamide solvent in a dry room at less than 50 ppm humidity for at least 30 min to dissolve the salt. It is then transferred through a stainless-steel sample holder for SEM to avoid contamination from air and moisture. For the *ex situ* XCT, the CNT electrode was discharged at a current density of 20 µA/mg. A small piece of electrode was withdrawn by an epoxy wetted graphite tip and sealed in a Kapton tube in the dry room. 1200 projections were collected within 180º degree. The TEM sample preparation was also performed in the dry room. In a mortar, we added few drops of dimethylacetamide with a piece of discharged cathode and then grinded the mixture. We withdrew a drop of solution from the mortar with a pipette and deposited it on a TEM grid. It was then put onto the TEM sample holder and transferred within a bag filled with argon.

4.3. Reconstructed volumes and the segmentation

The projections background brightness in the range of aperture angles may vary. This is due to the uneven thickness of other components, such as lithium and the separator, the X-Ray beam crosses. Second, the overall transmission decreases slightly in the last few angles before the dark out of dead angles. Normalization by the average value of each projection can easily correct these problems of overall variation in brightness and improve the reconstruction.

The projections were reconstructed using the filtered back propagation in TomoPy[166] python package and filtered back by a kernel three 3D median filter. Six volumes on the characteristic discharge plateau were obtained. The depth of focus was 140 µm, which makes it

possible to see the streaks and textures of the surface of the lithium and of the separator (shown in Fig S3). These features scroll quickly in the background during rotation and are not captured by the reconstruction algorithm. Highly transparent spots in the foreground can still be correctly reconstructed into 3D contrasted particles (in Fig 3b & S4).

The scissor-shaped missing angle artifacts can be seen on the high curvature surface in the reconstruction plan (top view in Fig S4b), leaving bright gratings in the side and front views of Fig S4b and as evidenced by the circles in Fig S4c. These scissors like artifacts form 67º angles with the x and y axis, which correspond to the dead angles. They will be absent from the side and front views because of the delay effect. In other words, a particle's bright artifacts will appear as noise in another slice when we observe them in the side and front view. Thus, we choose a 2D segmentation performed in the side views to be less influenced by such artifacts.

The other time-resolved volumes are segmented together by the convolutional neural network (CNN) in SegmentPy software. To do this, three raw reconstruction slices in each volume are retrieved for training the network, which is in total eighteen images for six volumes in discharge. Eighteen out of the thirty pairs of raw/segmentation samples at different time steps have been placed in the training dataset and the other twelve are divided into validation and testing datasets, as described in chapter 5: Segmentation with Deep Learning. The lithium peroxides, other dark fibers (broken fragments of glassy fiber from the synthesis) and the electrolyte front have all been segmented into a single phase. The CNTs appears as a noisy shadow due to the resolution (in Fig 1b and 3b) and are not able to be segmented here. The scores of the CNN trained for segmentation can be found in Fig S5.

Dark particles appear starting with the first discharge volume. In general, they have a high contrast in the dark colors shown in the raw tomograms Fig 3b with the Zernike phase contrast. They are segmented into purple phases rendered in 3D in Fig 3a. These particles have different morphologies such as sphere and toroid. A few large fiber fragments can also be seen. The fibrils are actually broken fragments from the glass fiber filter that we use to make the self-standing carbon nanotube electrode (see section 2.2). The dark particles are the lithium peroxide formed in the first step and the other white particles are impurities which remain from the pristine state. It can be seen from the red inset particles on the right of Fig 3a that some are in incomplete shapes closed to semi-spheres and some are aggregates of toroid and sphere (also in Fig S4b & S4c). This suggests that at the beginning of Li_2O_2 germination, peroxides do not grow simultaneously and not at the same rate.

4.4. Oxygen limitation and beam effect: ex situ vs in situ nano-XCT

Fig 3 compares the *in situ* discharged volumes in the Tu-cell and an *ex situ* volume in a pressure controlled Swagelok system described in Lepoivre *et al.*[126]. The formation of Li_2O_2 in the Tu-cell (Fig 3b is rather scarce. The *ex situ* volume of control experiment in Fig 3d was retrieved from another CNT cathode in the same batch discharged at a current density of 20 mA/g and ending at the cut-off voltage of 2V (for the sample preparation, see section 2.5). 70% of this volume is filled by peroxides.

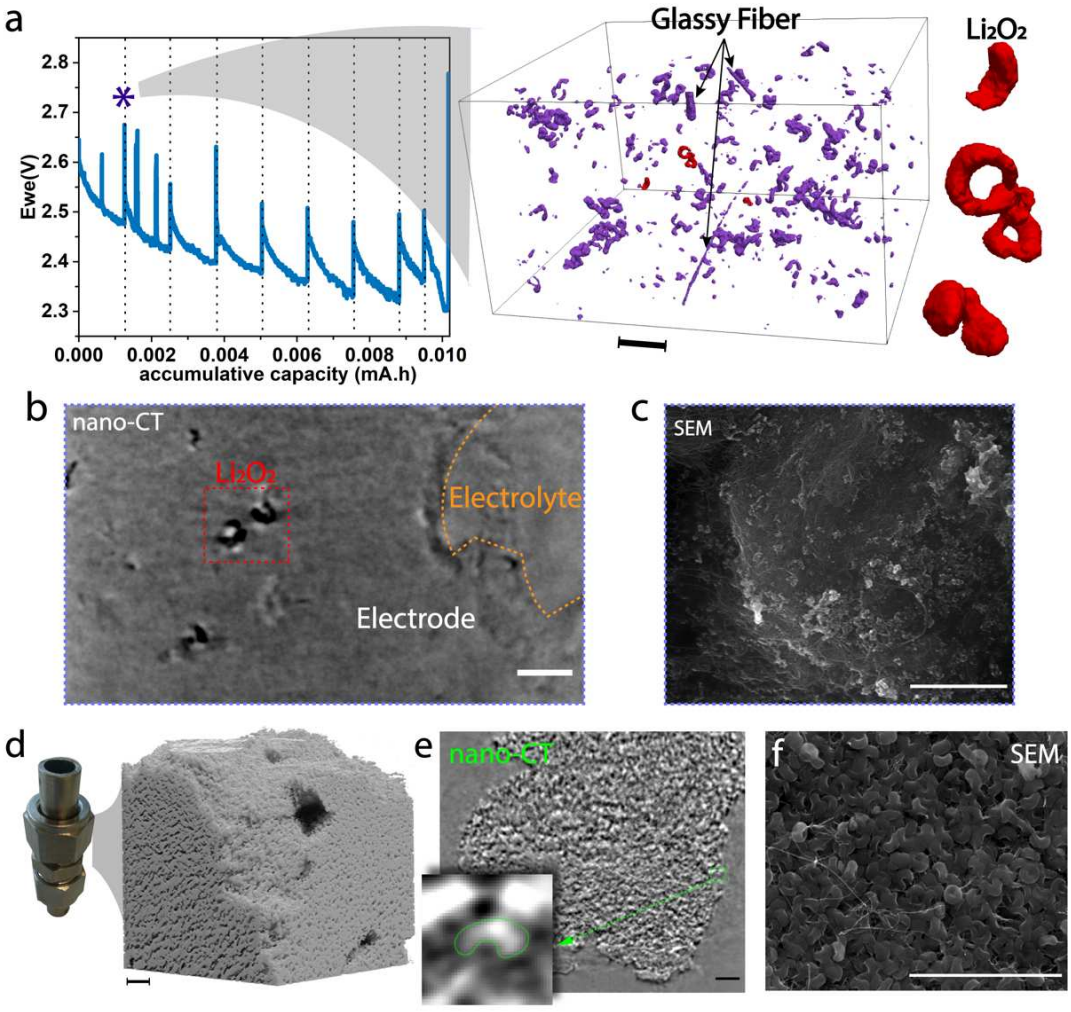

Figure 3. *Comparison of in situ and ex situ volumes. (a) The graph shows the discharge curve of the Tu-cell. The dashed lines indicate the relaxation phase where the tomographic acquisitions were made. On the top-right corner, a 3D rendering of the segmentation of the first in situ volume after 20 minutes of discharge. Three particles in the volume are highlighted in red. (b) is a cross-section of this volume. (c) a post-mortem SEM images of the cell. (d) a digital image of a Swagelok LOB and the rendering of an ex-situ CNT cathode filled with lithium peroxide. (e) A raw slice of the volume (d). The inset zoom is from the red rectangle at the right border of the material, in which we see one of the peroxide*

toroid laid parallel to the plan of the image. (f) the SEM image of this discharged electrode. All scale bars in this figure represent are 5 μm.

From the cross section and the SEM image, we see that the peroxides in Tu-cell are in a primary state of aggregation. Confirmation by post-mortem TEM/EDX (sample preparation in section 2.5) of the Li_2O_2 formation was performed in both *ex situ* and *in situ* (Fig S6 & S7). Some peroxide particles (in Fig 3a) are in uncompleted round shapes compared to the toroid-like peroxide formed in a Swagelok (in Fig 3d). There could be several reasons for the limited growth of Li_2O_2 in A_{acq}.

First, the Tu-cell is a closed system. It was mounted in 1 atm of pure oxygen and the amount of oxygen depends on the interior volume of the Tu-cell spaced by the stack of electrodes. It is estimated to be less than 1 mL (considering the thickness of the electrodes and the diameter of the LSS disc), unlike the 10 mL of the Swagelok configuration used in this study. The oxygen reduction plateau of oxygen reduction in Tu-cell is thus shorter.

We believe that the oxygen diffusion path is the second limited factor in chocking the growth of early germinated particles. In a typical Li-O_2 battery (Fig 3d), the direction of the oxygen diffusion is normal to the plan of the electrode. In the Tu-cell, oxygen must travel radially from the outside of the electrode disc to the center in order to reach the reaction point. A_{acq} is in the center of the electrode, approximately 5.6 mm away from the edge of the electrode. In-plan oxygen diffusion is in a millimeter range in the Tu-cell which contrasted with in-plan diffusion of the micrometer range in a typical Swagelok. Local oxygen depletion of A_{acq} was probably the cause of the hindrance as a result of the reaction. To shorten the oxygen diffusion distance to A_{acq}, a potential improvement in the experiment could be to split the electrode in half so that the central A_{acq} is exposed at the border and closer to the oxygen (A_{acq} should still position in the middle of the transmission window for the opening window).

Besides the limited amount and the long diffusion path of the oxygen, the beam effect could be another factor hindering the reaction. Although X-ray CT techniques are often considered non-invasive, in TXM mode, where the beam is focused and the photon flux is strongly condensed on the tiny A_{acq}, the impact of the beam should not be overlooked.

Here we use the CNT binder-free cathode that can (a) avoid dissociation of the binders in the electrolyte by the heat on the beam and the presence of organic solvent (the polymer chain

starts to move above the temperature of glass transition). (b) exclude the side reaction between the peroxide and the polymers for the simplicity of the involved reactions.

A fast shutter was used throughout this study to reduce X-ray irradiation to the *in situ* system and the shutter was only open when acquiring the CT scan and looking for patterns before the acquisitions. Nevertheless, the beam did impact the electrolyte. Both in parallel beam mode and in the TXM. First, in parallel mode without magnification, bubbles are created (Fig S2) and moved after several shutter opening plans at the same location. Second, with the converged nano-XCT beam onto the A_{acq}, a gas-liquid interphase in the south-west corner of the reconstructed volumes appears (a series of top-views in Fig S8). During the discharge, this interface gradually propagates towards the center of the cube, indicating that the amount of electrolyte is decreasing in A_{acq}. Interestingly, we noticed that a brownish product and a strong-smelling gas formed after experiment. This is typically the NO_2 of the lithium nitrate salt as described in the original article on this electrolyte[42]. Two Tu-cells were cycled under identical condition in the beam and outside the beam. We see that in Fig 3a & Fig S9 the beam clearly induced noises on the plateau and a higher polarization of about 100 mV. Notably, several spikes, might be also due to the beam, appeared at the beginning of the plateau during the galvanostatic pulses while the shutter is closed.

4.5. Particles tracking in subsequent time steps

After the segmentation step on the obtained volumes, different types of features are extracted: particles, inclusions, residual glassy fibrils, and liquid-gas interface. The segmented volumes are labelled (a unique identifier is given to each feature) and a set of properties is measured: including barycenter, volume, area, inertia matrix, main axis, sphericity. These analyses are performed for each tomographic volume. From this recovered data set, a tracking algorithm is established to connect features from one time step to another, based on discrete correlation method, in order to construct the tracks. To do this, a probability graph is built on the likelihood for each pair of features in an adjacent time step based on physical laws, geometric considerations and other compatibility criteria. Once the graph is constructed, the tracks are extracted using a shortest path algorithm, connecting each individual particle through the time axis. A track gives the trajectory of each individual particle and the evolution of its properties.

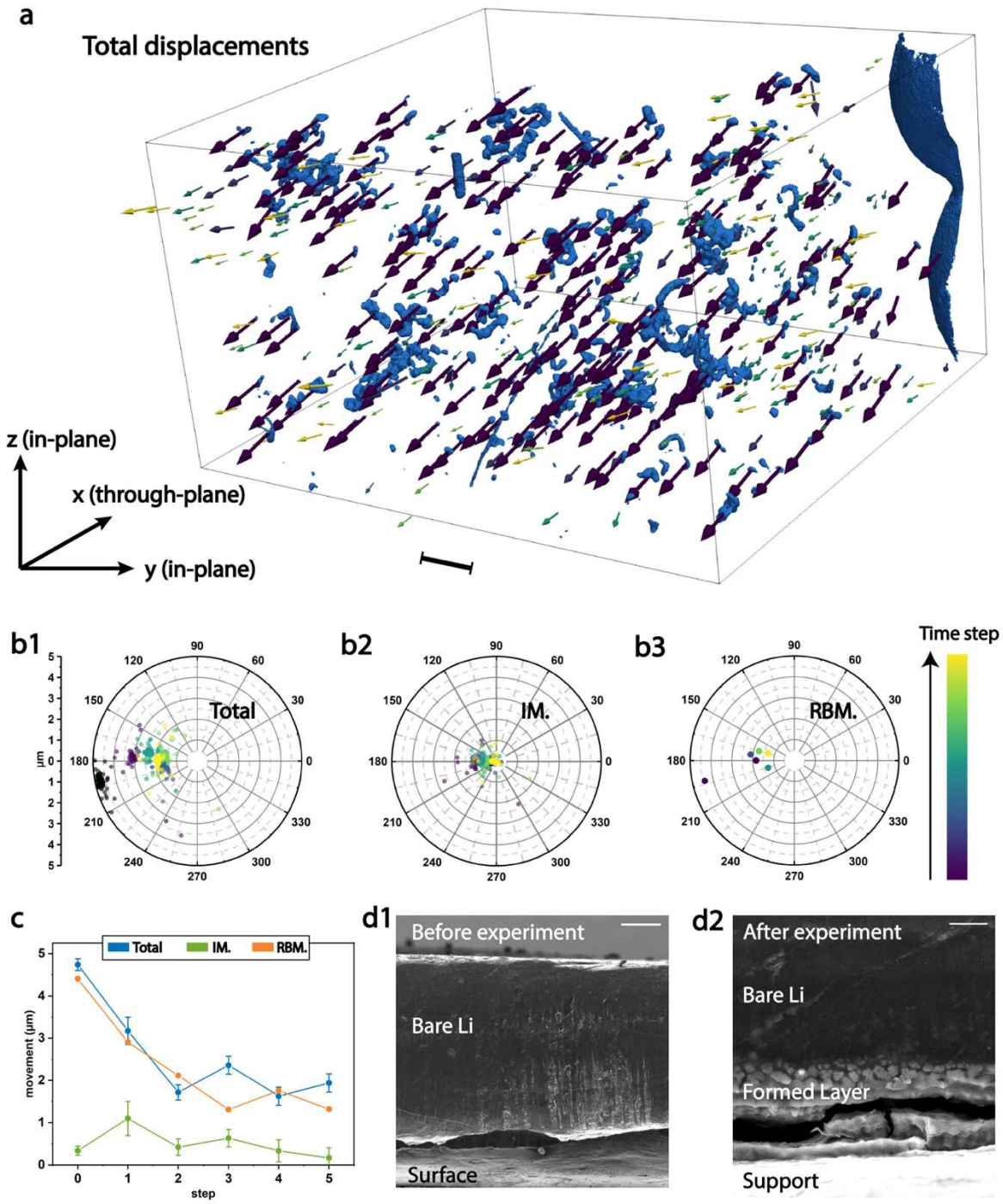

Figure 4. *Dynamics study of the time-resolved volumes (a) The 3D rendering of tracked total displacements (rigid body movement RBM + intra-particle movement IM) for all the particles in time steps. The size of arrows indicates the magnitude of movement, and its color indicates the time step. And the time step color bar is shared between the (a) and (b) plots. The scale bar in (a) . From left to right, b1-3) are respectively polar plots for total displacements, RBM, and IM projected on the plan XY (the movements on z direction are quasi-null), showing the distribution of motion vectors for each tracked particle at time t. The latitudes represent angle formed between the vector and the x axis at plan XY, and the longitude its module of the vector. c) plot of average module of displacement for all tracked particles with time. d1-2) SEM images comparison of the intersection of the pristine lithium foil and the post-experiment one. A thick non-uniform micrometric layer is formed on the surface of Li. The scalar bar in d1 represents 100 μm, and 20 μm for d2.*

In Fig 4a, the displacement vectors between time steps given by these tracks for each particle are shown (from dark colors to bright colors). It should be noted that the Tu-cell rests firmly on the stage by the attraction of magnets and that the cables rotate with the stage (Fig 1b), so no external force is causing these displacements. The evolution of the volume over time is shown in the series of images in (Fig S8). In this series of top-view, we see that the particles are moving roughly in the same direction, taking a big step at first in the x axis direction, then small displacements in the following steps. This is illustrated by the arrows in Fig 4a and plotted in the polar graph Fig 4b1.

We see that these movements are in the micrometer range (tens of voxels in Fig 4c), while the precision of the machine is in the nanometric range. These shifts clearly do not stem from the machine but from real steric changes within the battery.

We can divide the total displacements into an interparticle motion (4b2 or Fig S10) and a single directional rigid body motion (4b2 RBM or Fig S10). The RBM indicates that a force is applied globally on the A_{acq}. Here, the direction of this force points to the negative direction of the x, y axis on the horizontal plan. Note that the separator and lithium are in the positive direction of the x axis and the GC window on the negative side. We figured out that the origin of this force is in fact the formation of a cumulative porous transition layer formed on top of the lithium during cycling. This formation was highlighted in two other micro-CT studies of lithium for LOB[47,153]. The magnitude of RBM measured here is in the micrometer range that is in consistence with these studies. We further confirmed the presence of this transition layer by *post mortem* SEM (Fig 4d1 & 4d2) on the cross section of the discharged lithium in the Tu-cell. The composition of this layer is mainly nitrate and oxide, according to the EDS spectrum given in Fig S11. Indeed, the O_2-cathode is placed on the movable LSS disc (Fig 1a). The cathode is gradually pushed out of the FoV during the formation of the transition layer. Our experiment involves only the beginning of the first cycle, the reversibility of this transition layer formed in the electrolyte should be investigated in the future.

Interparticle motions (IMs), on the other hand, can track the local stresses between particles and indirectly reflect the changes in CNT matrix (we have questioned in chapter 2: Zernike Phase contrast) during the discharge. Fig 4b3 shows that the IMs of the peroxide particles formed are on average half of the RBM and the directions do not exceed a fan of 30º around the RBMs direction. IMs can be considered small and neglected in this work, and no obvious shear and expansion forces were observed to tear the bulky electrode in A_{acq} due to the reactions. We

can also see from Fig 4c that the first step of total displacement and RBM is substantial, then tend to stabilize at around 1.5 µm per step. This suggests that the growth rate of this layer is higher at the beginning and then slows down due to the oxygen depletion and accessibility of the bare lithium surface.

4.6. Conclusions and Perspectives

The current study has pushed forward the challenging development of the *in situ* nano-XCT experiment for lithium batteries. We have demonstrated the feasibility of high-resolution local tomography using the Zernike Phase Contrast for a low contrast Li-O_2 cathode. A carbon nanotube based O_2-cathode was used throughout this study and the nanotube matrix is almost visible. We have presented the *in-house* Tu-cell, which has the advantages of easy cell assembly and a good reproducibility in terms of electrochemistry. Specific laser sample preparation is required for beam alignment and allow the adjustment of the focus plan. The *in situ* volumes are compared to the *ex situ* results, where Li_2O_2 is massively formed. We have also discussed the important factors that can influence the quality of the operando tomography. By analyzing the resulting volumes, the growth of Li_2O_2 was found to be choked at the beginning of the *in situ* experiment. Several explanations have been given (a) long diffusion path of O_2 to A_{acq}, (b) local evaporation of the electrolyte due to the X-ray beam and (c) the lack of oxygen in the airtight design of the operando cell. Besides, we found that the formed lithium peroxide particles did not separate from each other which suggests that there is no local steric expansion or shrinkage. However, they all move roughly parallel in the same direction with each time step, suggesting an external force being applied to the A_{acq}.

Based the current findings, it would be necessary in the future work to add a gas outlet which can be connected to the rotation stage to extend the oxygen tank and obtain a longer plateau. In addition, the choice of electrolyte or the shape of the laser cutting pattern could be rethought. A less volatile electrolyte such as the long chain glymes or the ionic liquid and a more stable salt can replace in this experiment the DMA and $LiNO_3$. The laser-shaped pattern could have a more irregular and larger shape to facilitate the pattern searching in parallel beam mode. Higher X-ray energy can be used for higher transmission and less interaction between electrolyte and beam. The current results are particularly important as they have opened up the possibility of conducting a local in-situ nano-XCT using real world electrodes, an exact amount of electrolyte and realistic cycling conditions. The results of this investigation can also be generalized to other

battery systems. Other advanced battery materials can be beneficial and fitted in Tu-cell using the method of laser preparation and time-resolved 3D imaging.

Important takeaways :

Performing high resolution 3D imaging with transmission X-ray microscopy (TXM) in an *in situ* battery system is extremely challenging. We show herein a method to conduct an *in situ* nano-X ray Computed Tomography (nano-XCT) experiment assisted by the in-line phase contrast technique for low Z elements in batteries. A carbon-based O_2-cathode of Li-O_2 battery was used for this investigation and the time-resolved 3D volumes were obtained and successfully reconstructed. Our approach is to perform a nano-XCT by zooming directly into a laser-shaped area not larger than 50 µm in an in-house *in situ* cell. The rotation axis of the tomography of this cell being parallel to the plan of the electrode, a specific method of preparing the electrode by laser is required. This method is essential in this approach, which allows to minimize the dead angles, align the beam and adjust the focus plan. We have demonstrated *in situ* observation of the difficult light species, lithium peroxide, in a lithium-oxygen battery. The time-resolved 3D volumes obtained showed a force pushing the analyzed area out of the field of view. This is due to the thickening of the lithium foil during the electrochemical process. Although X-ray Computed-Tomography (XCT) is often considered non-invasive and beneficial for the development of an *in situ* experiment for battery research, here we discuss the effect of the focused beam at the nanoscale with a focusing X-ray beam. The current contribution opens possibilities of characterization of battery materials by local *in situ* nano-XCT under realistic cycling conditions.

- A flat coin-cell-like design of *in situ* X-ray tomography cell
- Laser sample preparation & beam alignment
- Zernike Phase Contrast enhancement for weak absorption particles

4.7. Annexes

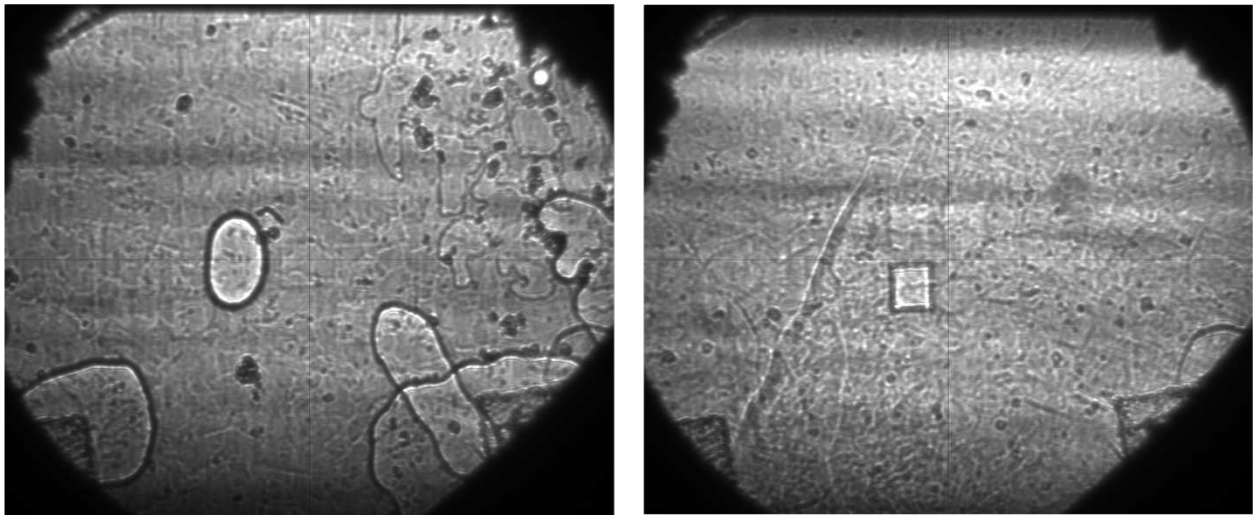

Figure S1. *The examples of the laser patterns in parallel beam mode There are 6 patterns in the picture on the left and 3 on the right.*

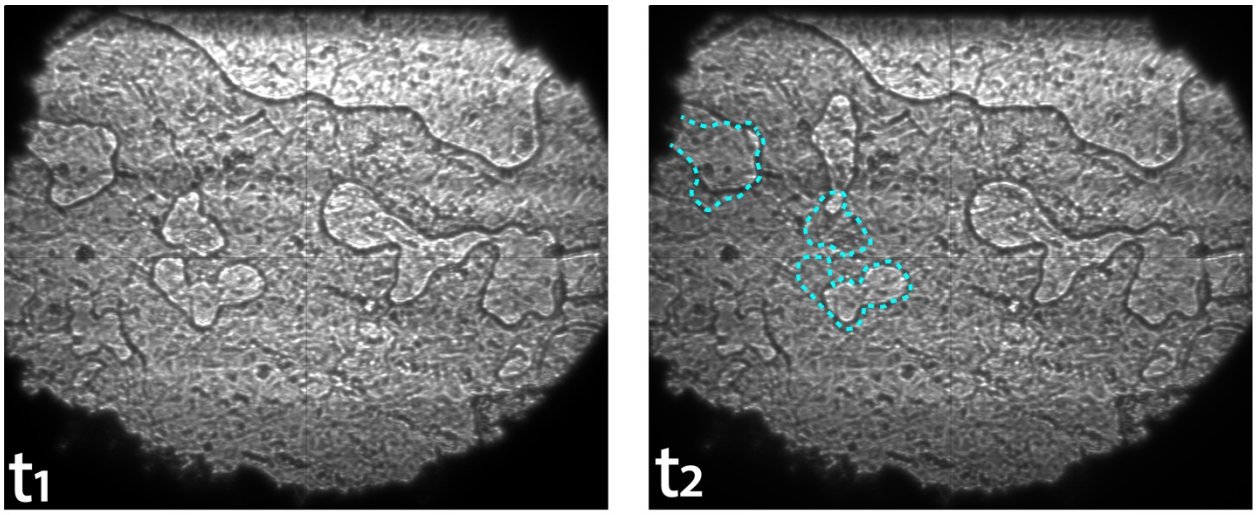

Figure S2. *front-line of the liquid moves before/under after the irradiation of the X-ray beam, where the dash line in frame t2 indicates the origin shape of the bubbles in frame t1*

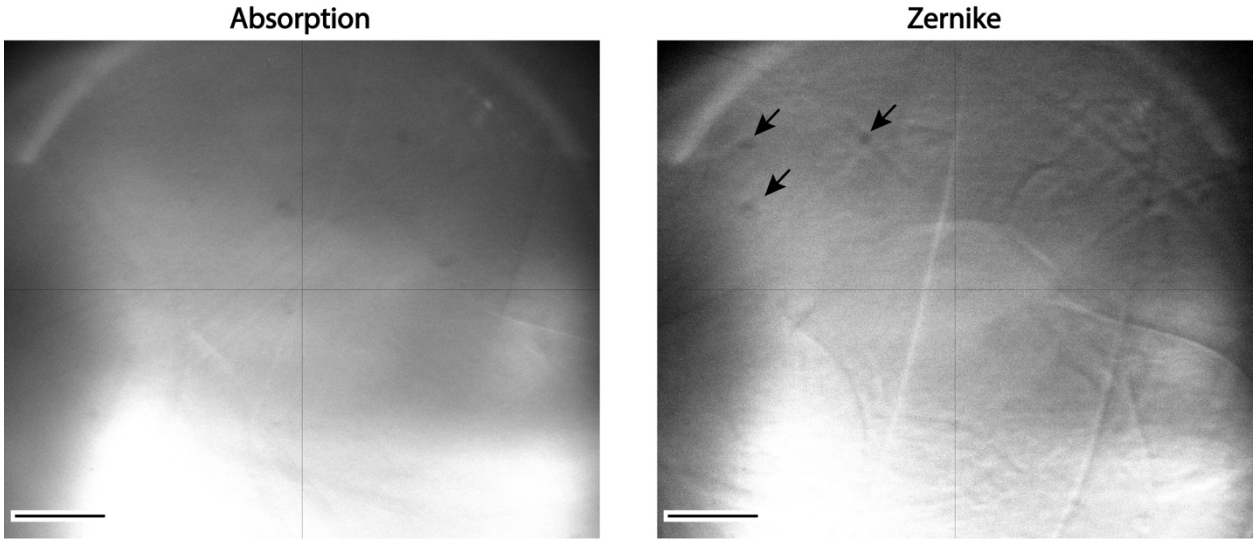

Figure S3. *Comparison of nano-CT in absorption (left) and in Zernike (right) projection. In Zernike phase contrast mode, the boundary of objects has been emphasized. Small features such as threes spots in the top-left rectangle became more visible in Zernike mode. Other features such as the large band vertically across the FoV are believed to be from the outside of the FoV, as it passes across rapidly the FoV during the rotation.*

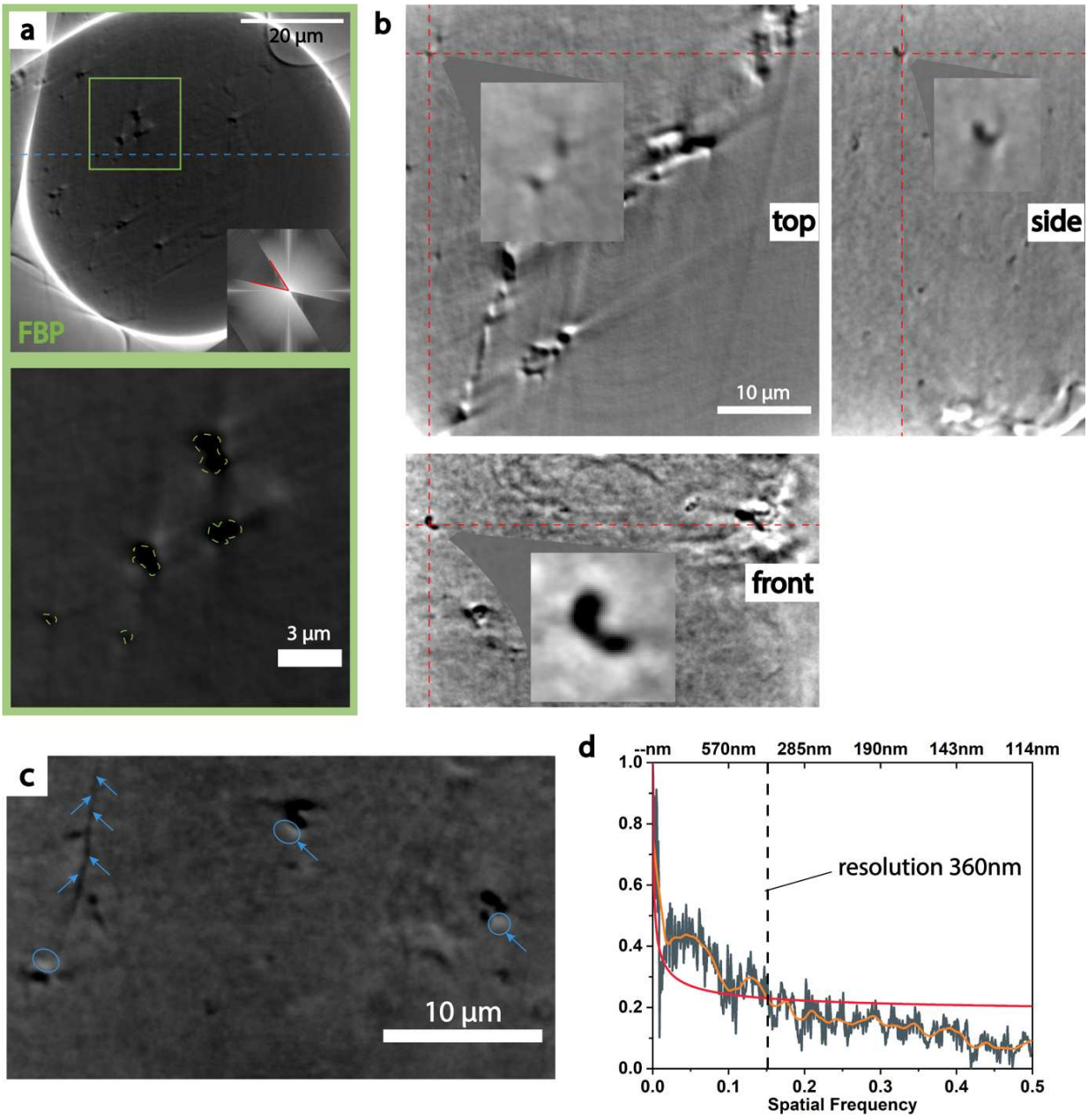

Figure S4. *a) an ortho-slice of the reconstruction of first discharged volume of the electrode. The inset image is the transformation Fourier of the reconstruction. The scissors-like missing angles artifacts results in two cones in the Fourier space. And the second at the bottom is a zoom on small particles. b) a set of planar top/side/front view highlights a toroid particle c) an ortho-slide shows the lithium peroxide and a glassy fiber highlighted by arrows. d) The voxel size is 27 nm and the resolution is estimated at ~6.2 pixel by Fourier Shell Correlation, which is equivalent to 360nm.*

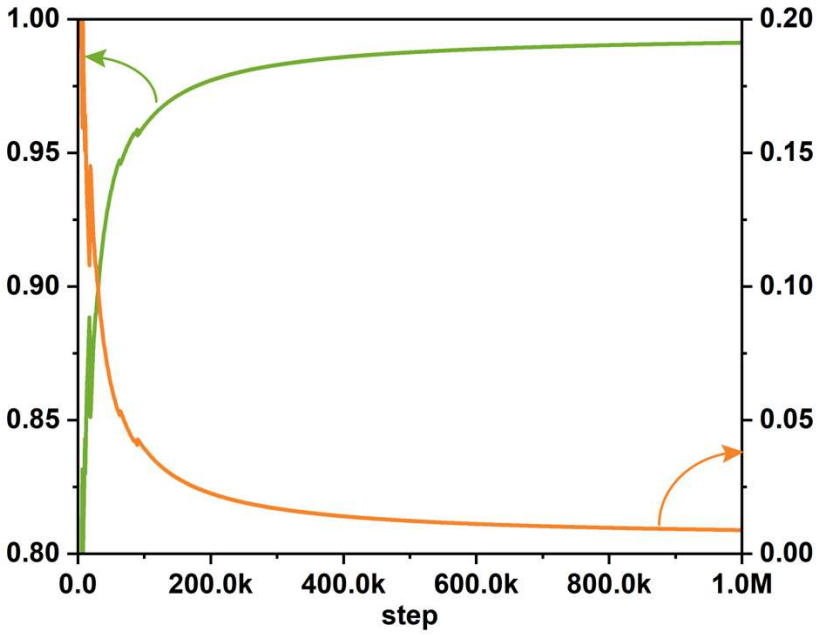

Figure S5. *training and validation curves of the neural network for the in-situ volumes. For each volume 5 slices are retrieved and entirely labelled. Three from each volume were used for training, the others for validation and testing.*

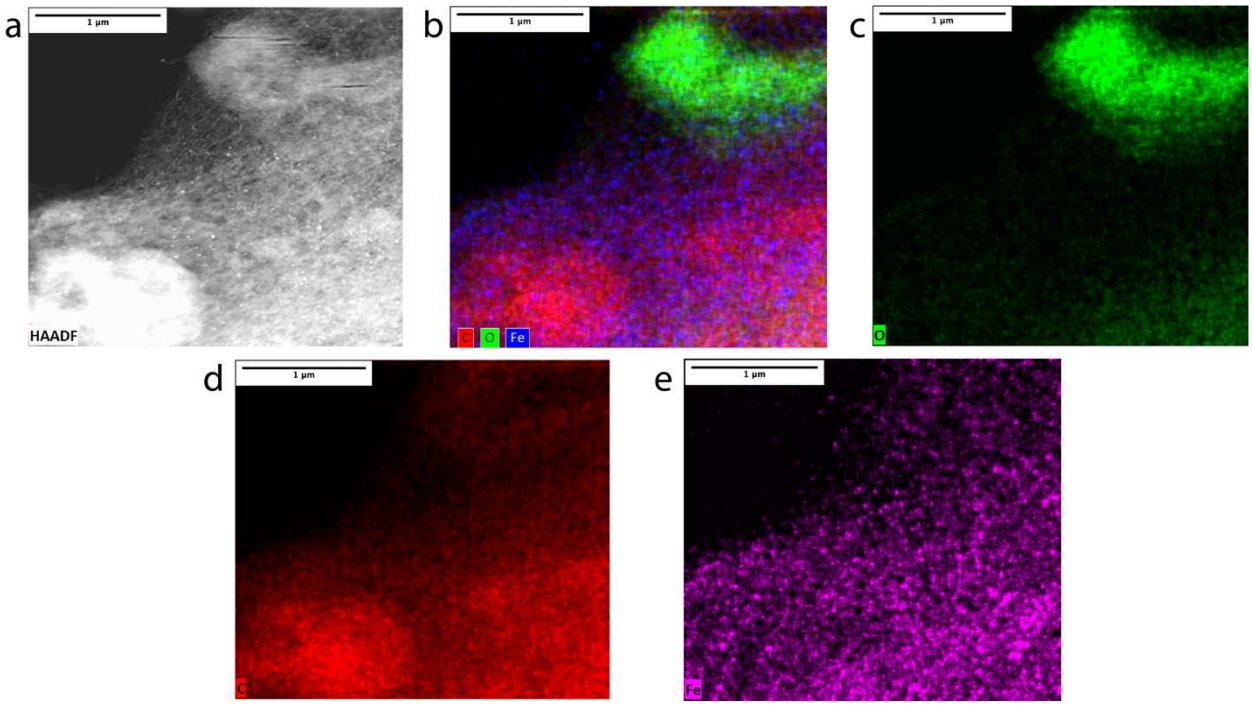

Figure S6. *TEM-EDS mapping of the discharged cathode in Tu-cell. The beam energy is 200keV. From a-e, are the grey scall mapping, combined cartography of the following three mappings, the mapping of oxygen, of carbon, and of iron, repectively.*

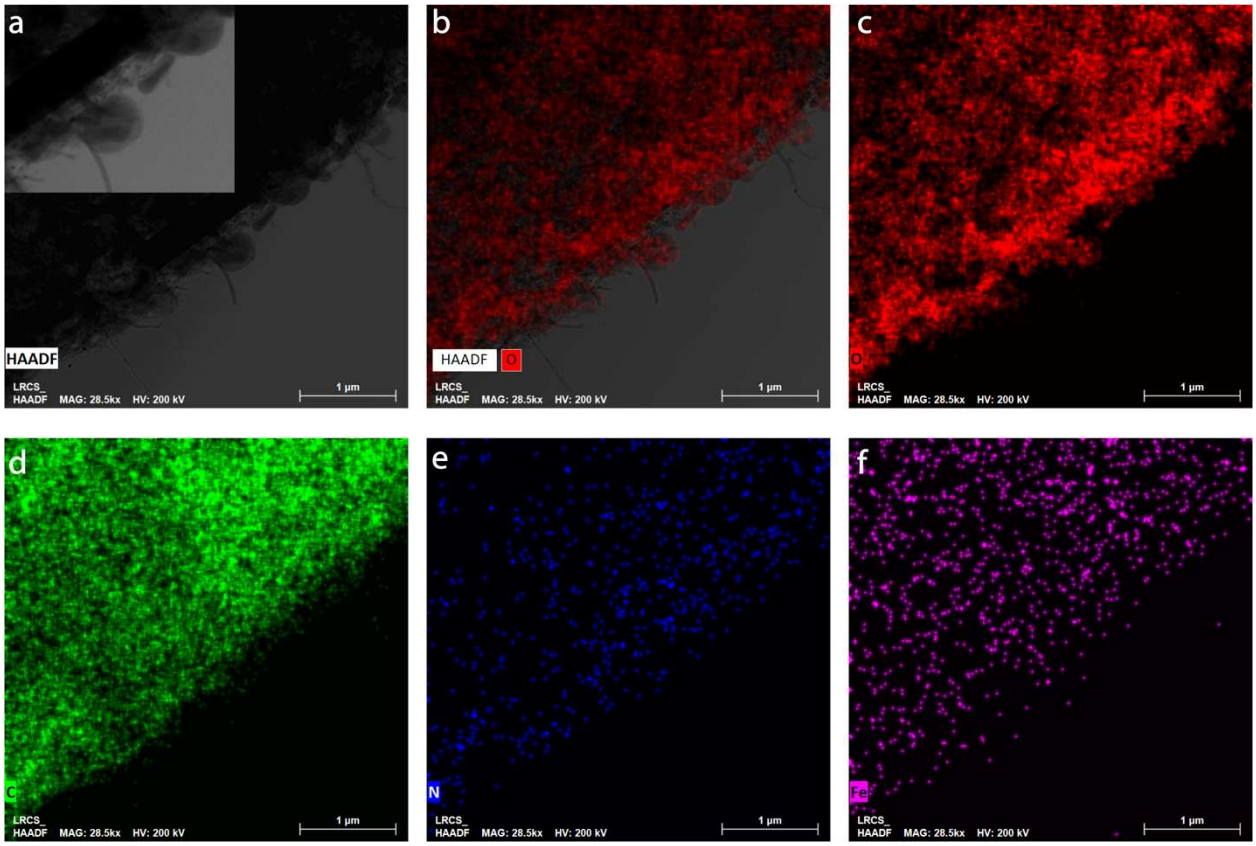

Figure S7. *STEM-EDS mapping of the discharged cathode in a Swagelok. The beam energy is 200keV. a) the STEM image and the zoom onto the lithium peroxide toroids. b) the overlay cartography of oxygen onto the STEM image. c-f) are the EDS mappings of oxygen, carbon, nitrogen, and iron, respectively.*

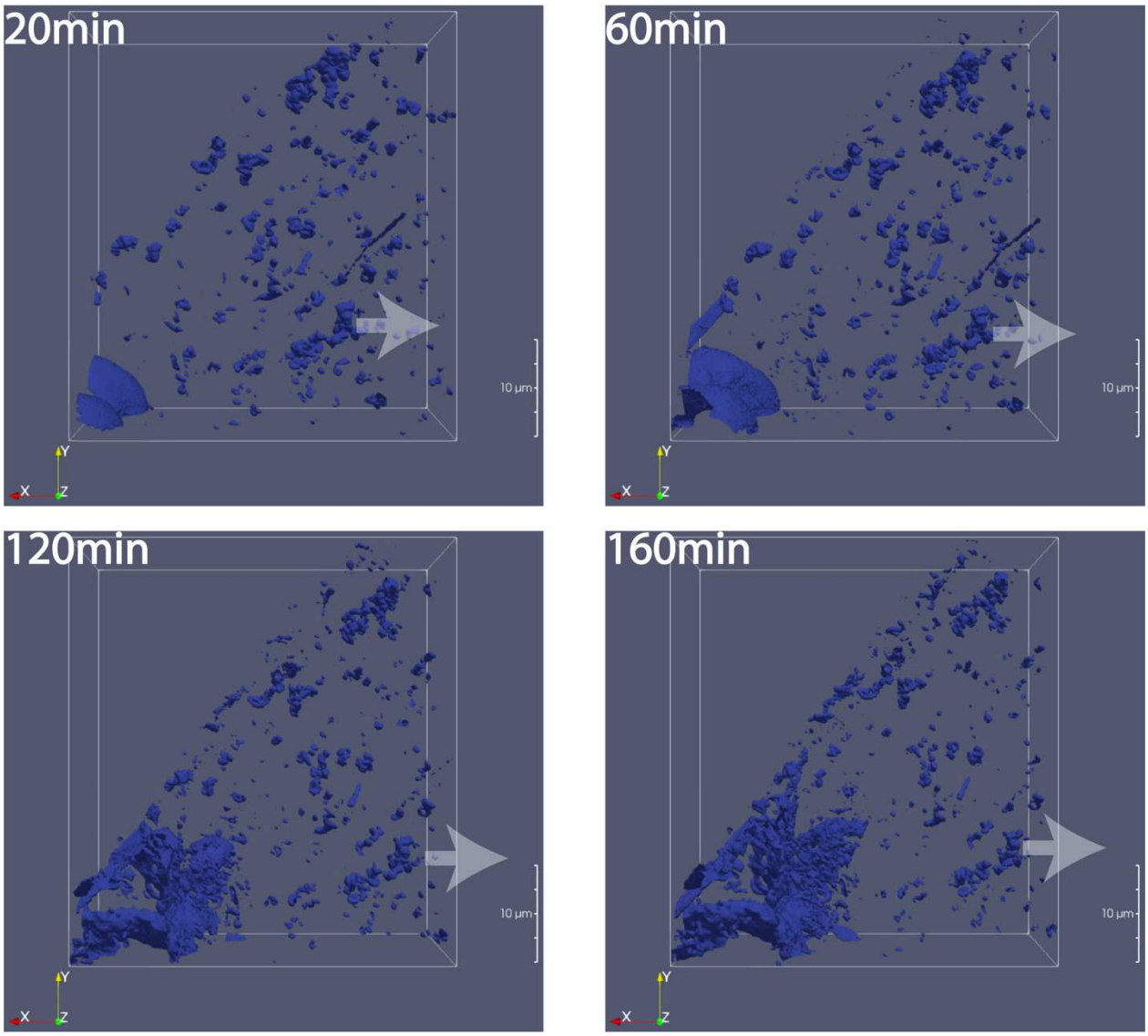

Figure S8. *A series of top-view images of the time-resolved volumes, showing the displacements of particles. The arrows indicate an aggregate of particles moving towards the walls of the volume with the other formed particles.*

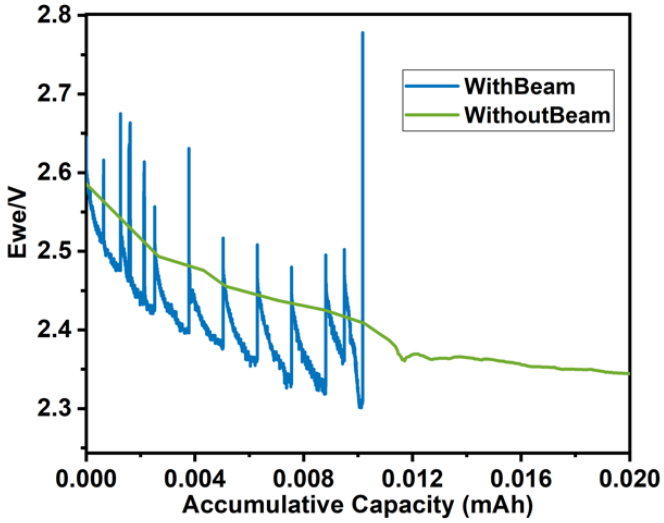

Figure S9. *Comparison of electrochemical curves with/without the beam in the Tu-Cell. Both batteries have been discharged at 5μA/cm^2.*

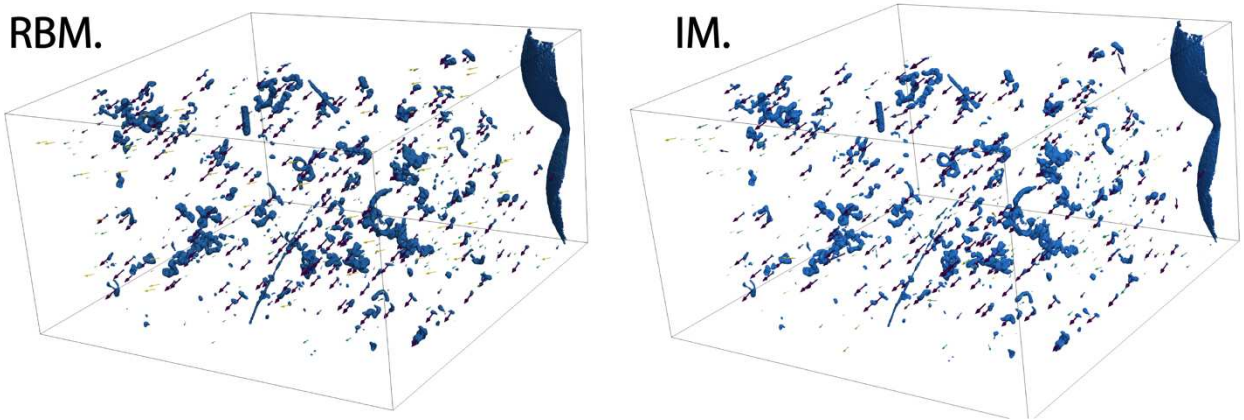

Figure S10. *The rendering in 3D for the rigid body movement and the intra-particle movements*

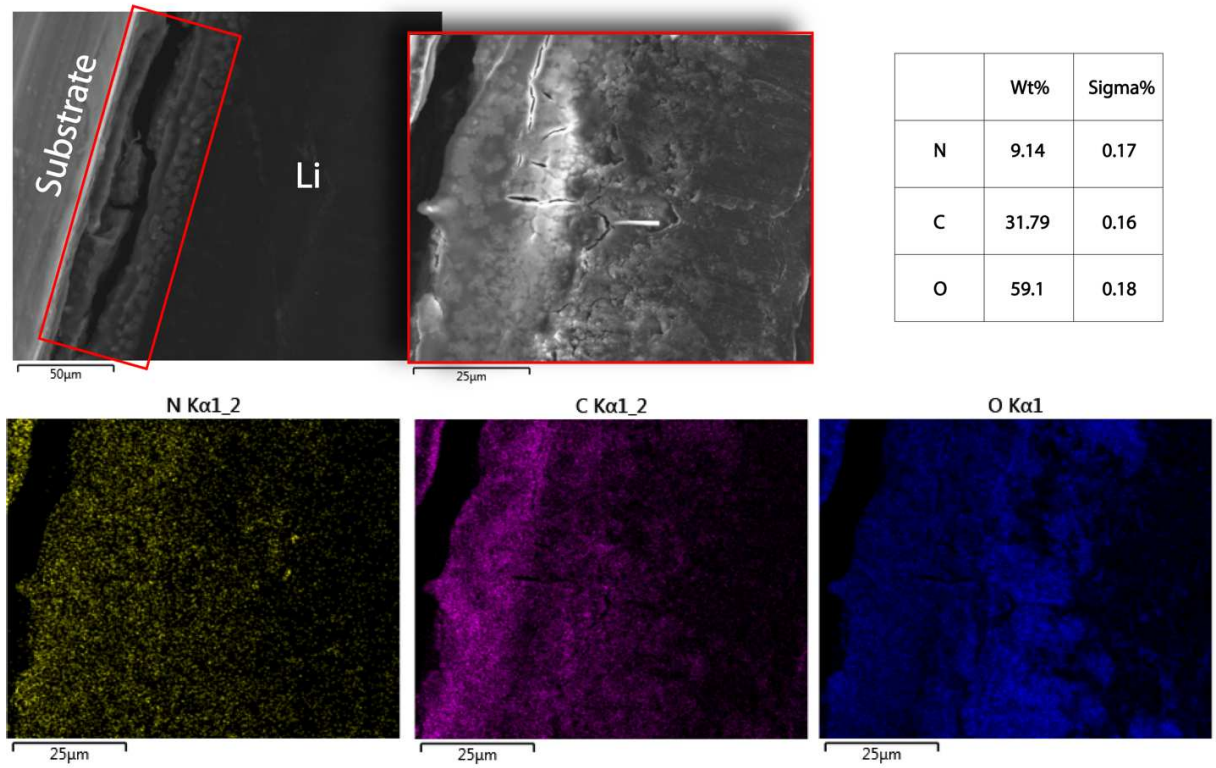

	Wt%	Sigma%
N	9.14	0.17
C	31.79	0.16
O	59.1	0.18

Figure S11. *SEM image and the EDS mappings of different elements of the surface of the used lithium. The lithium discharged in Tu-cell was collected and sliced into half in the dry room. The SEM/EDS mappings were done on the sliced intersection.*

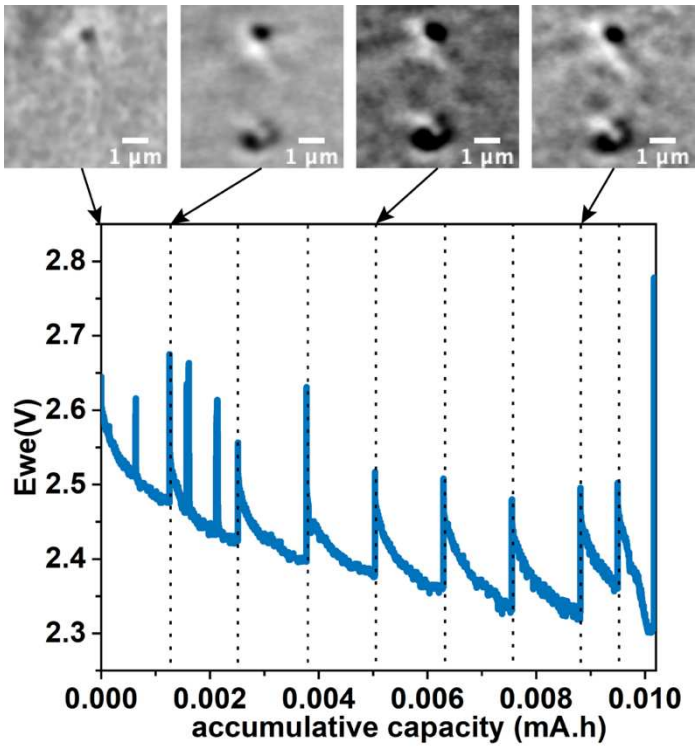

Figure S12. *Particle time evolution during the in situ experiment. We see that the hook-like particle formed before the first sequence of discharge. Both particles do not grow after their rapid apparition.*

Chapter 5

Deep learning for segmenting battery material XCT images

Throughout this thesis, the segmentation is the most time-consuming and tedious step in our workflow. Additionally, the previous chapter has open possibilities of *in situ* tomography characterization to other materials. There is a real need of automatizing or facilitating the segmentation of XCT images.

The current chapter is relatively independent from the previous ones. We developed the neural network for the sake of simplify this tedious task of segmentation. Instead of working on the Li-O_2 battery datasets, our approach is firstly starting by segmenting a standard and easier material in Li-ion battery, then generalize it backward LOB. By doing so, we cross-examined a larger sample from different experimenters and gained some reflections on the uncertainty of the segmentation. We will see the whole workflow of using deep learning in segmentation as well as a specific generalization technique called transfer learning.

5.1. Context of the segmentation in XCT for battery materials

The X-ray computed tomography (XCT) is a robust characterization tool in which the battery field has shown tremendous interest during the last decade[167–169]. It provides valuable 3D morphological information on the battery materials and electrode architectures. Its broad range of observation allows us to investigate nanometric particles, up to tens of nm resolution,[170] and the bulk electrode with a large field of view from tens of µm to 1 mm. For instance, nano-XCT techniques have been recently used to study, on the material level, phases spatial distribution[136], steric changes[171], 3D oxidation state evolution[172]. The micro-CTs are often employed on the cell level[173] and operando studies[174]. The use of synchrotron sources, the emergence of fast imaging detectors, and the advanced in situ/operando characterization spawn soaring data quantities and lead to unprecedented challenges in image processing and data management. The raw dataset often contains few gigabytes of projection and is then reconstructed into a stack of tomograms that typically includes a billion voxels for the analysis. The 3D analysis and electrochemical simulation are usually preceded by a step of semantic segmentation, which consists of digitally partitioning each voxel of the raw stack of tomograms (Figure 1a left part) into different phases (Figure 1a right part).

The segmented volume of XCT can be used as an input of electrochemical models[175–179] to simulate electrochemical performance, which helps to understand transport phenomena in the electrode and to design a better electrode architecture. Pietsch *et al.* [180] has firstly discussed the impact of segmentation on the determination of morphological and transport properties for commercial anode materials. They studied each parameter in XCT image post-processing and threshold segmentation. They observed that the variation in porosity and tortuosity due to the different segmentations could become considerable. Therefore, the data processing and segmentation step should be done carefully in the battery field. The straightforward method based on the gray levels (e.g., Fig 1c- top histogram) does not make it possible to achieve an accurate segmentation because of overlapping distributions associated with different phases. For nano-CT data, where high signal-to-noise-ratio is challenging to obtain and a wide variety of artifacts is present, the grayscale thresholding approach is not efficient enough, especially for complex composite materials.

5.2. State-of-the-art image segmentation methods

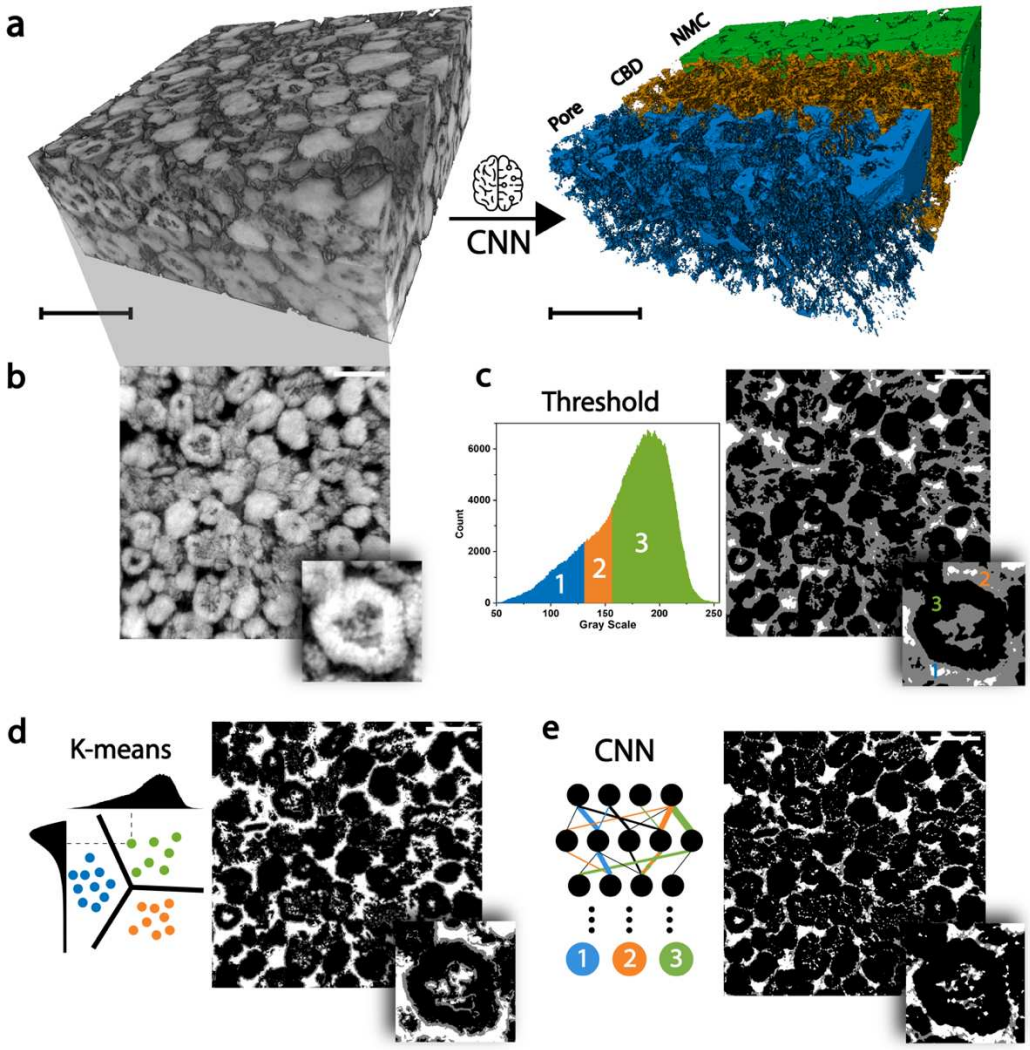

Figure 1. ***Comparison of multiphase segmentation by different methods.*** *a) Volume rendering illustrating the objective of turning raw 3D volume of NMC1 into a segmented one. NMC/CBD/pore are rendered respectively in green/orange/blue colors. b) selected cross-section from the previous raw volume with a zoom on an NMC particle and its surrounding environment. c) the histogram of b) on the left and on the right histogram thresholding result based on the theoretical volume fractions, where the black, grey, and white colors represent NMC, carbon-binder-domain, and pores. d) an illustration of applying automatic k-means for segmenting a 2D histogram of the raw tomogram and its Sobel filtered image. On the right, the result of this method. e) on the left, a scheme of artificial neural network, and on the right the output of CNN. All scale bars are 8 µm.*

Up to date, in the tomography field, the coupling of fixed feature extractors and a machine learning classifier, such as Random Forest[181,182], is one of the most widespread and efficient methods for facilitate image segmentation. Over the past decade, thanks to advances in the computing power, large-scale convolutional neural networks (CNN, see Method 1) have become easier to train. The CNN has thrived in automated segmentation and other similar computer vision problems in various fields such as satellite or astrological images[183,184], facial recognition[185],

camera-assisted vehicle autopilot[186,187], and medical imaging[187–192]. XCT images of battery materials contrast with the examples above as they typically contain crystals, agglomerates, polymers and porosities with complex morphologies and architectures so as to maximize electrochemical reaction rate. Liu *et al.*[193] investigated the degradation of a Li-ion NMC material with a Mask R-CNN that provided a quantitative instances-level particle identification despite the particle cracking. Labonte *et al.*[194] studied the binarization of a graphite anode micro-XCT dataset with a more sophisticated 3D neural network capable of providing a segmentation uncertainty map with a Monte Carlo approach.

For the first $LiNi_{0.5}Mn_{0.2}Co_{0.3}O_2$ (hereafter namely dataset NMC_1) cathode material, the goal is to distinguish the 3 phases in the electrode presented in the figure 1b: (a) the white NMC active material where the lithium is stored, (b) the carbon binder domain (CBD) of a mixture of polymer and carbon black surrounding the NMC, which maintains the mechanical cohesion of the material, and (c) the porosity impregnated by the liquid electrolyte where the ions circulate during the electrochemical reaction. The use of the thresholding approach (Fig 1c) or the automatic K-means method (Fig 1d) applying on a 2D histogram leads to an overestimation of the CBD phase and a coarse separation of the interfaces. These as-segmented volumes with the NMC particles are firmly surrounded by the CBD. For instance, the use of these volumes might induce a poor exchange on the NMC surface and result in a biased electrochemical simulation.

Our current contribution (Fig 1e) expands the portfolio for accurate multi-phase segmentation of battery CT images with a portable neural network architecture. We discuss the impact of hidden segmentation bias which has often been overlooked when applying an automatic algorithm. The article is organized as follows. First, we will present how our CNN is derived from existing architectures to optimize the performance. Then, we show the workflow of training a network from scratch in SegmentPy and improve the performance of a CNN by fine-tuning the hyperparameters. Details of our index-based connection between encoder-decoder architecture will be given. Our approach will be cross-validated with other battery nano-CT data. We show that the accuracy can be improved by reusing the kernels of a pre-trained network, namely transfer learning. Finally, we will identify the cognitive bias diluted in the labeled data and quantify their potential impacts on the material properties characterization.

5.3. CNN approach and the fundamentals

A convolutional neural network (CNN) is a branch of deep learning that mainly contains units of convolution. It is a mathematical model that artificially mimics the function of the neural network. For a segmentation task, it is trained to encode the features of the input image and give the associated segmentation on the output side without explicit feature extractors and instructions called by the experimenter.

The basic units of a CNN include (1) a convolutive kernel with trainable variables (or called hereafter weight) that perform feature filtering on the receiving data (Fig 2a). (2) Max-pooling (MP)/Up-sampling (UP) which modify the dimensions so that the following operations can act on a different scale of data (Fig 2b). These operators in this work appear in pairs and communicate with each other with indexes. The MPs on the first half of CNN (encoder) transmit the position information of max values to the UPs of the same level in the second half of CNN (decoder). (3) The activation function (e.g., different examples applied in this work in Fig 2c) is the switch of a neuron that is triggered upon receiving a value greater than the threshold. This function is added after the convolutive kernels to form a complete layer.

A typical representation of CNN (e.g., the optimized LRCS-Net) is shown in Fig 3, where the sheets illustrate the layers of these basic units. Other operations are added for specific purposes. For instance, batch normalization (BN) is usually added in the layers to reduce the effect of scale variance of different input channels of the previous layer. BN and its derivative techniques often lead to a faster convergence[195,196] (Fig 2d). The soft-max layer converts the output of CNN into a kind of phase probability map. Detailed definitions of all these basic operations can be found in Annexes Note 1. Stacking these layers sequentially and connecting the indexes bridges, as shown in Fig 3, forms a CNN.

The CNN is uniformly and randomly parameterized at the initial state with the method described by Glorot *et al.*[197] and should be trained by supervision with a series of raw tomograms as input and corresponding example of segmentation as output. The effective output of the network is compared to a given segmented sample in a loss function (or simply loss hereafter), denoted by $\mathbb{L}$ in Figure 3. The loss can be translated, to some extent, as the distance between the result and the expectation. Thanks to the differentiability of all the operations in the network and the propagation derived from the chain rule loss (also called back-propagation, which contrasts with a forward propagation by giving an input image and obtaining an output segmentation), it is

possible to calculate the partial derivative for each weight with respect to the loss. We optimize the weights with a gradient descent technique[198,199], which consists of shifting each weight by a certain amount against the sign of partial derivative. With a significant number of iterations of computing the forward/backward propagation and leveling weights, the overall network will converge to a point where the predicted result remains as expected. In simple words, the CNN "self-learns" to uncover hidden logic or representations from input images to output segmentation.

5.4. Computational and experimental methods

5.4.a. Sampling and definition of datasets:

Although a tomography experiment can generate a few gigabytes of raw tomograms, annotating phases on tomography images to "teach" CNN can be tedious and extremely time consuming for some datasets. In the case of the NMC dataset in Fig 1a, an average of one hour should be considered to obtain a good quality ground truth. On the flip side, CNN is well known, data hungry, and typically fueled by thousands, if not millions of images. Limited by the amount of annotated data and given the need to diversify the data for the robustness of the invisible data prediction, two strategies are applied: (a) the small patches are cropped randomly and synchronously in the input image and the labeled image (Figure 2e). (b) the variation in contrast, noises, and distortions are added at random to the cropped raw tomogram, namely hereafter augmentation (Figure 2f).

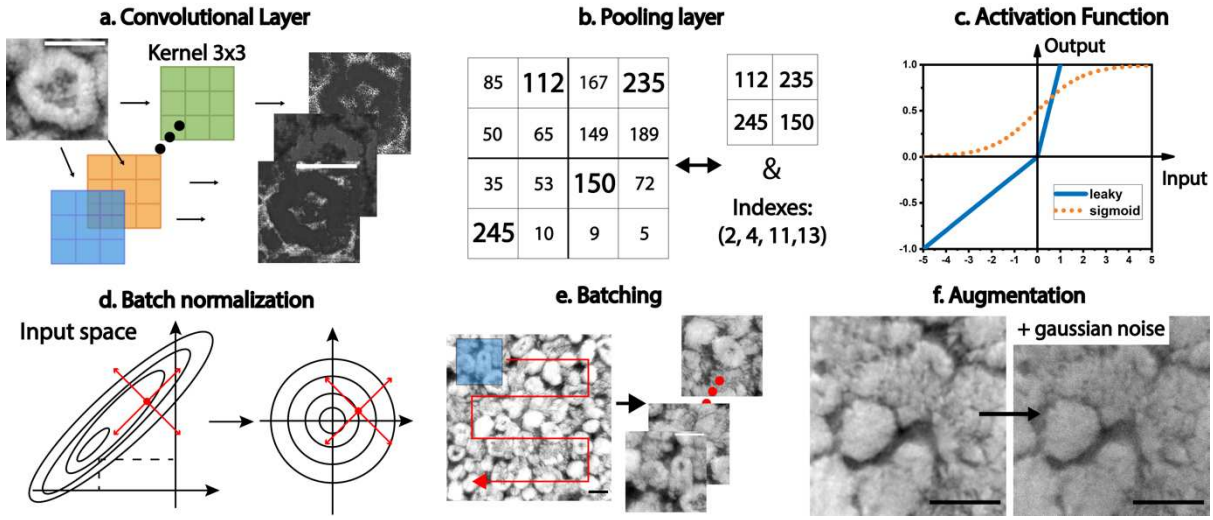

Figure 2. ***Illustration of different components of a neural network with the studied architecture.*** *(a-c) illustrate basic operations such as convolutions, pooling, and activation function in a CNN. (d) the batch normalization layer that adjusts variance between the inputs for faster convergence. (e) the random batching, which generates a substantial quantity of data from a limited number of labeled images. (f) illustration of the artificial noise augmentation*

technique applied on the input of the network to increase the data size and improve the insensibility to the noisy data while predicting. The scale bars represent 5 µm

Throughout this work, a single slice of the raw tomographic image is used for the CNN training dataset. Two more slices, perpendicular to the same direction in the studied volume and distant from each other (to avoid similarity), should be chosen and segmented as the validation and test datasets. The training dataset is only used to update the weight, while the validation data is used to assess the predicting accuracy of CNN to invisible images. The training/validation should be repeated if the structure and hyperparameters are adjusted. And the test dataset serves to confirm the performance of the final optimized CNN.

For transfer learning, a new volume of NMC cathode was used, and in the current study, the already trained NMC dataset was not diluted in the second one. All the data used in this contribution is published in TomoBank data repository [200].

5.4.b. Material preparation

The two studied 3D volumes depicted in Figures 1a and 6a are Li-ion battery cathode material $LiNi_{0.5}Mn_{0.2}Co_{0.3}O$ supplied by Renault. A Zeiss Laser Dissector is used to cut the material into a particular pattern with the central 50µm of diameter cylinder (Fig S1, the pattern under the optical microscopy). We use a strongly sharpened pencil lead slightly dipped in the epoxy and approach the pattern with a micromanipulator with an angle of 90^{o}. Let the epoxy polymerize for 15 min. We pulled back the pencil lead in the opposite direction, and the cylinder was detached from the bulky electrode. The Li-Oxygen battery material is prepared differently. Two binder-free (NanoTech Lab) electrodes from the same patch were made of MWCNTs (purchased from NanoTech Lab) with the filtration method. One of them was cycled in a Swagelok for a complete round-trip between 2-4.3V at a constant current density of $20mA/g_{carbon}$. It is then prepared in a dry room as the cycling products are unstable in the presence of water. The pristine and recharged electrodes are both chopped with a blade, and then a small piece was picked with the same method of epoxy under a microscope. The cycled Li-O_2 cathode is sealed immediately inside a Kapton capillary with Torr Seal after the sampling. As the Kapton is transparent to 8keV X-ray, the TXM can be directly performed on the capillary, where the samples are protected from the air during the transport and acquisition.

5.4.c. Nano-CT experiment and tomographic reconstruction

The pencil lead with the material was placed on the rotation stage of APS ID-32-C beamline[201]. A zone plate condenser at 8keV energy with a working distance of 3.4m is used. 1201 frames of projection with equal angle delta within 180^{o} degree are collected on the fly. The projections are reconstructed by FBP-CUDA in Astra-TomoPy[202] Python library. To obtain a better contrast, the authors noticed that analytical reconstruction such as FBP is preferred to the alternative algorithm like SIRT, with which it is unable to differentiate the CBD from the background porosity as their grayscales are too closed. A 3D median filter of kernel three and a 2D unsharp mask of radius six and weight 0.6 have been applied before all the segmentations in this work.

5.4.d. Synthetic training data algorithm

The algorithm perturbates the training dataset by pushing or pulling random units on the interfaces of a segmentation. The operation of this algorithm is to locate all the voxels firstly on three types of interfaces in our multiphase segmentation problem. A 3D kernel will randomly pick a percentage of these interface voxels to apply a dilatation on either side. It will be corrosion for one phase and dilatation for the other phase of the interface. We found that this algorithm synthesizes more realistic segmentation in 3D than in 2D. This is because there might be interfaces in a neighbor plan (e.g., Fig 5a) that will not be considered in 2D. Yet in 3D (e.g., Fig 5b), the consideration of the adjacent plans makes the synthetic results more realistic. At least ten adjacent slices of raw tomogram were well-segmented and used as the input of this algorithm. The two parameters to tune in this algorithm are the surface voxel picking ratio of the interface and the number of iterations. We found that 10 percent interface for each iteration and five iterations generate the best perturbated data with homogeneous and plausible changes.

5.4.e. Hardware and Software

The CNN training is run on a PC with Ubuntu OS equipped with Intel Xeon CPU and Quadro P5000 GPUs. The SegmentPy utilized in this work is an in-house open-source software. Its neural network part is based on TensorFlow and mpi4py. And it is open source and can be downloaded on github.SegmentPy.io.

5.5. CNN Architecture

LRCS-Net (Fig 2) used throughout this work has been optimized to segment efficiently nano-CT images of the battery electrode and is derived from Seg-Net[187] and Xlearn[203] artificial neural networks (explanation of neural network refers to Methods 1 and the structural optimization is shown in Annexes Note 2). On the encoder side, the LRCS-Net contains in total five layers of convolution with three indexing max-pooling and ends with a sigmoid function instead of a leaky function applied in the rest of the network. On the decoder side, eight layers of convolution with three up-sampling receiving indexes at the first convolution layer of each block. The model has one-tenth of trainable parameters than the frequently used network U-net[189] in semantic segmentation in other fields. The throughput of CT images per second can reach twice as much as in the U-net and the prediction speed for a volume of billion voxels is a quarter faster.

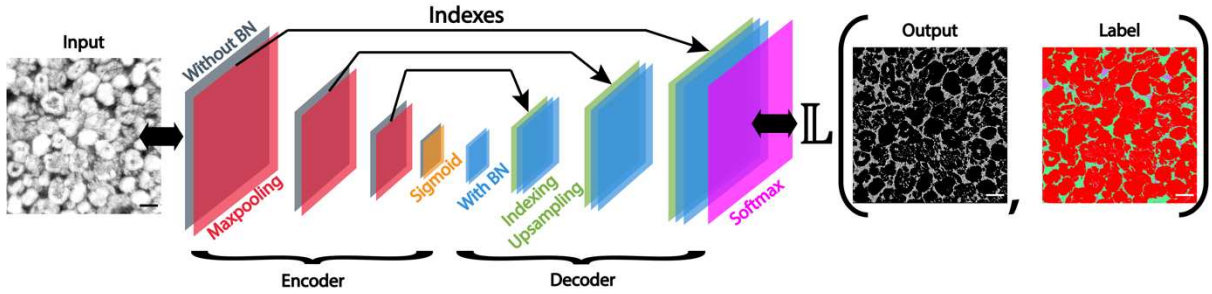

Figure 3. ***A schematic representation of LRCS-Net*** *with the input image and the composition loss function. The image scalebars are of 5 µm.*

5.6. Unavoidable hyperparameters tuning

To explore the best performance of the CNN, the hyperparameters (HPs) should be optimized for each dataset. In contrast to the trainable weights, the HPs are tunable by experimenters. They control the size of the network and determines the convergence of the training process. Comparing with the enormous datasets in the domain of object detection, real-world tomography datasets of battery materials contain fewer classes.

The CNN is prone to overfitting certain class than other if the HPs are badly initiated. As such, the network can be easily trapped by a poor local minimum that predicts only the majority class. We call it a major class pitfall as the accuracy stagnates at the value of volume fraction of the major class. In the case of NMC, this is reflected by a low variation plateau of accuracy around 80%, which corresponds to the volume fraction of NMC. This is due to the unbalanced quantity of different phases in the training data. At the beginning of training, inferring the majority phase costs

less and minimizes the loss faster. For a deeper understanding of the HPs' influence on the CNN's performance and showing the reasonable spectrum for each HP, an investigation is conducted below using the platform SegmentPy (see Fig S3).

Figure 4a-d plot the average of validation accuracy in solid lines and the standard deviation in the colored area during the training. The learning rate is a parameter that controls the momentum of the trainable variables during the backpropagation. A higher learning rate leads to an instability of the local minimum, while a lower one traps the network in a poor local minimum. This HP is delicate to tune. For example, a constant learning rate drives to poor minima and accuracy. In contrast, a periodically decreasing one with a decay ratio of 0.3 has an optimal convergence (Fig 4a, decay applied at the end of each epoch. An epoch defines the entire training dataset). Nevertheless, reducing the ratio to 0.1 starts to reduce variation and limit performance. The batch size is another HP handling the parallelization while updating the weights of the training process. We see in Fig 4b that by controlling the total amount of training images, a small batch size with less parallelization can lead to better convergence. Two other important HPs are the base number of convolution channels and kernel size defining the size of the CNN. Fig 4c and d show that increasing the CNN size does not necessarily drive to better performance and can result in overfitting.

One should note that the HPs could have interactions[204,205] among them. To illustrate this, Fig 4e plots the accuracies sorted in descending order with different combinations of HPs. We see that the value of the initial learning rate should be carefully chosen for obtaining better accuracies. Here, small batches (in purple) are prioritized, which is in accordance with Fig 4b. Other HPs, on the other hand, do not have a clear trend on the optimization. In contrast to the trainable parameters in the CNN that receive feedbacks from the loss by gradients (Method 1), seeking the best combination of HPs is indeed a black box guessing problem that can only be found by trials (*ad hoc* approach). Random search[206] and Bayesian search[207,205] based on the gaussian process are automatic tools that could help to refine the HPs.

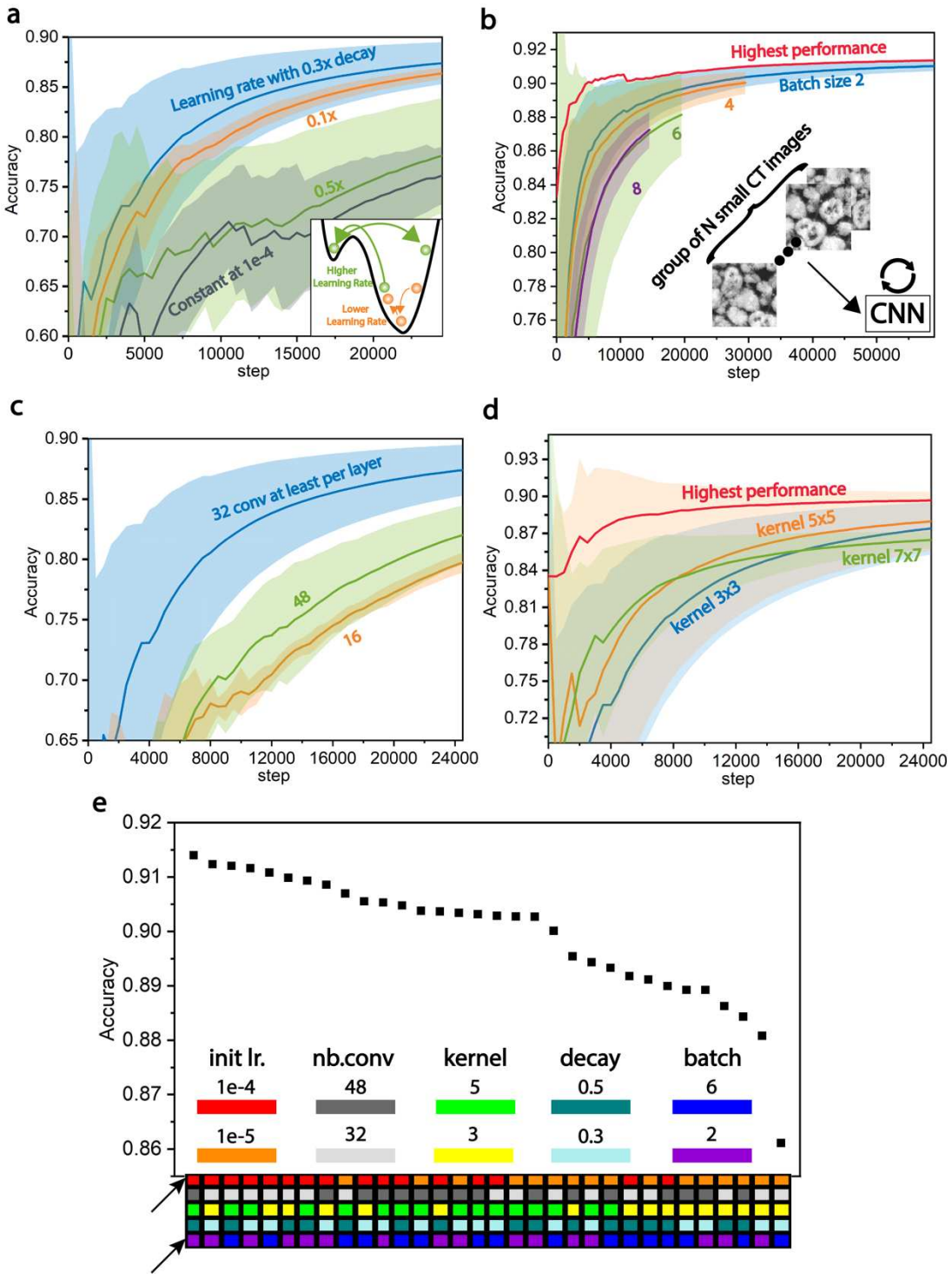

Figure 4. *The statistical score comparison important hyper-parameters (HPs). performed on the validation dataset (the unseen data during training). The line and censured area represent respectively the mean and standard deviation of validation scores of three trainings. (a) The constant learning rate turns out to overfit, which is often ascribed as inflexibility or bad generalization of the CNN onto the unseen data. An optimal decay ratio of learning rate is found to be 0.3 for this set of hyperparameters. (b) controlling the total quantities of training data, small batches are preferred for better convergence. (c) a middle value of 32 for the number of convolutional kernels leads to the best accuracy. (d) 5x5 kernels leads to optimum performance. (e) sorted validation scores in descending order of a broader hyperparameter search. The X axis is replaced by a grid of colors representing used hyperparameters for achieving the corresponding score. The initial learning rate shows particular importance for obtaining higher accuracies. The*

performance depicted in blue throughout through this figure are obtained with the Dice loss function, leaky activations, and BN implementation in the decoder and other training details are in Table ST1-2.

5.7. Decrypting and understanding CNN architecture with visualizations

Compared to connections that allow the merge of features from different pooling level[189,208–211] as in the U-Net, the index connection in LRCS-Net is less common and studied. In order to have better insights into the function of layers and the connections in LRCS-Net in a concrete application, we have developed visualization tools to monitor the activations at different layers and the evolution of gradients in the training process (implemented in SegmentPy). The two halves of LRCS-Net have their specific functions: (i) the encoder plays a role in extracting the features from the input image and passing their position and (ii) the decoder reconstructs the final segmentation by finding the corresponding phases at the positions received from the encoder.

In the encoder, the position information of the max-pooling is passed through the index-bridges and the intensities through the inner layers. This type of bridge induces a different learning behavior from a feature bridged U-Net (see Fig S4). During training, the LRCS-Net is more active at the level of the first layers of the decoder then the activities gradually decrease toward the output, whereas with the image connection such in U-net, the outermost layers have higher gradients during training.

The LRCS-Net decoder takes on the dimensionally reduced features from the input encoder. With successive layers of indexing up-sampling and convolution, it maps the input from the lower dimensions to the upper dimension toward the output of the network. We observe that this up-sampling operation first generates a highly pixelated mapping by scattering the values of the previous layer over the voxels assigned to the encoder and leaving the rest of the voxels at zero. Subsequent layers of convolution spread these unequal voxels over their adjacent voxels (Fig S5).

With successful training from the previous section, the before last layer of LRCS-Net decoder should have learned to recompose distinctive semantic features. Figures 5b-e list several channels of this layer taken from the trained LRCS-Net. It can be seen that this layer is mostly made up of intuitive features. For example, Fig 5b shows that this channel has been successfully reconstructed from the output of the previous layer of the NMC phase, while Fig 5c shows another channel sensitive to the borders of the NMC. Fig 5d and 5e, on the other hand, learned how to

classify the porosity and the binder domain, respectively. Small pores in the CBD domain around the NMC particles are identified: small bright dots in Fig 5d and dark spots in Fig 5e. This low porosity could not be segmented with the thresholding approach. With these intuitive features, the last layer can easily combine them into the final segmentation (Fig 5f).

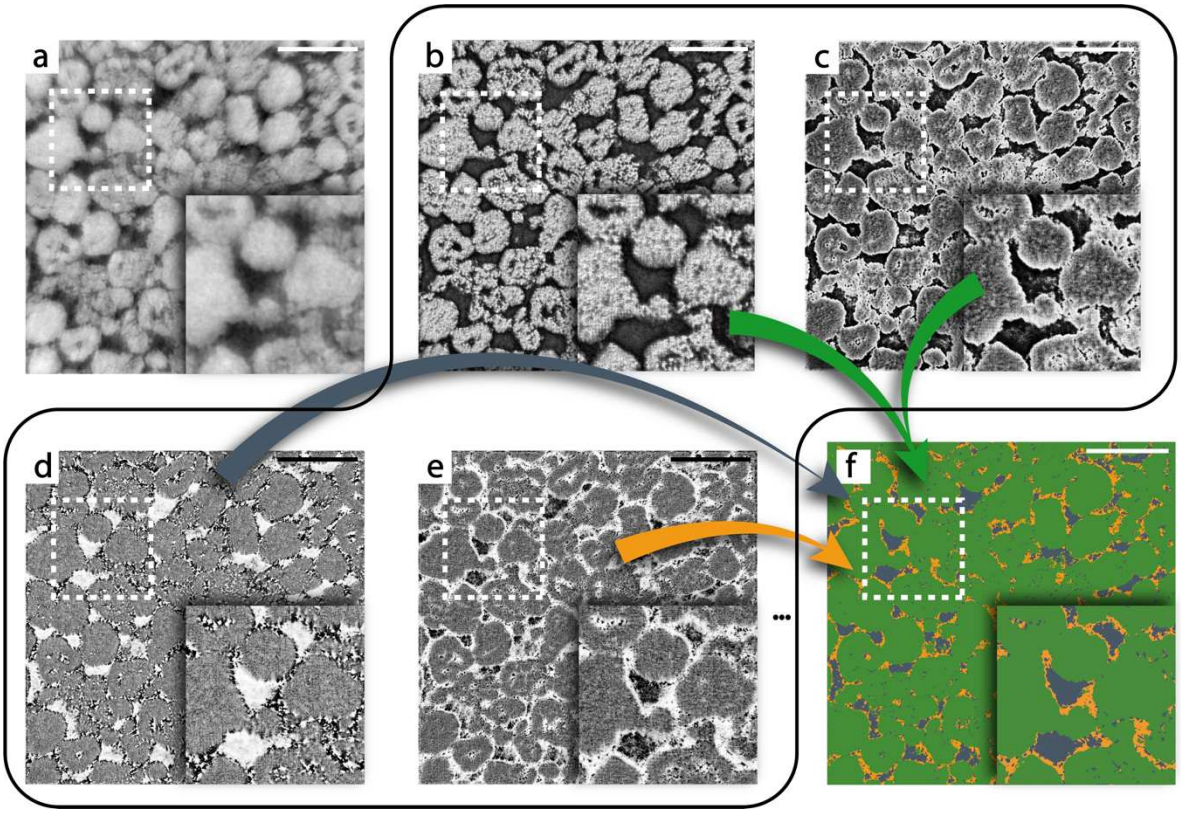

Figure 5. ***Examples of the output in the before last convolutional layer.*** *(a) Raw input tomogram of the convolutional neural network. (b-e) 4 activations out of 32 channels of the second last layer are shown, where (b) is a channel that learned the representation of the NMC particle, (c) a channel that composes the border of the NMC, (d) pores sensitive channel, and e) another channel with luminous voxels corresponding to the CBD. (f) the output segmentation of the neural network by combining and weighing all these activations and the rest of this convolutive layer. Green, yellow, and grey color represent, respectively, NMC, CBD, and pore. All scale bars are 10µm.*

5.8. Reveal the influence of biases diluted in ground truth (GT)

Segmenting large battery material volumes always involves automatic (e.g., Otsu, watershed) or semi-automatic (e.g., the current supervised learning) methods. In most of the papers, the result of segmentation is used directly for quantitative measurements, although it is justified qualitatively or sometimes the justification is even missing. Unless images of higher resolution of the exact same labeled zone by coupling with the FIB-SEM[214] is available, deploying the CNN for segmenting the XCT images must deal with the uncertainty. Apart from visually judging and inspecting the metrics such as the accuracy or the IoU, there is no other efficient way

of qualifying the segmentation. In applicative cases as shown with our previous examples, the inconsistency among the training, validation, and testing dataset due to the uncertainty causes impasse such that although the prediction is visually satisfying, the accuracy is stuck at about 90%.

In this section, we will use training CNN as paradigm to discuss the uncertainty and the origin of this roof of performance and try to quantify its impacts on the post material properties determination while dealing with real-world data. For this, we will discuss alongside with the results of two experiments: a survey of the degree of discrepancies between the experimenters and training several neural networks on slightly different labels to evaluate the resulting material properties.

First and foremost, applying a supervised-learning method will dilute human bias in the training process. Using CNN in semantic segmentation problem is to train a neural network to approach an ideal function, that transforms the input tomographic volume to a ground truth segmented volume: $\boldsymbol{GT_{ideal}} = \boldsymbol{\mathcal{F}_{ideal}}(\boldsymbol{V_{raw}}) \sim \boldsymbol{CNN_{ideal|W}}(\boldsymbol{V_{raw}})$. Here, the CNN can also be generalized to other parametrized automatic methods such as K-means. One should bury in mind that one chooses only a subset of the volume to generate labels and the labels will always accompanied with the human bias $\mathbf{GT}_{\boldsymbol{ideal}} + \boldsymbol{\varepsilon_{cog|exp,raw}} = \mathbf{GT}_{\boldsymbol{manual}}$, where the superscript denotes the subset and $\boldsymbol{\varepsilon_{cog|exp,raw}}$ the cognitive bias. In our experiences, the later mainly depends on experimenter and the raw volume including the machine and the reconstruction. And the validation (Fig 4) / test (e.g., Fig 7d) datasets is to examinate the $\boldsymbol{CNN_{train|W_{train}}}(\boldsymbol{V_{raw}^{test}})$ with $\boldsymbol{GT_{manual}^{valid/test}}$, where the subsets of valid, test, and train do not intersect one another. We see that the $\boldsymbol{\varepsilon_{cog|exp,raw}}$ intervenes three times in the process, once in training the CNN with $\boldsymbol{GT_{manual}^{train}}$ and the others in the $\boldsymbol{GT_{manual}^{valid/test}}$. The origin of the performance roof is because such bias changes in the subsets. Notably, other methods cannot rule out of such bias as the experimenter need to at some point verify the output of the method and making further improvements.

Thereby, the first experiment aims at determining and showing the degree of $\boldsymbol{\varepsilon_{cog|exp,raw}}$. We collected 20 labels from 33 experimenters to compare with a commonly accepted GT (detailed in Annexes Note 3) based on the NMC_1 dataset. The results show that the group of non-experts can substantially deviate from the common GT. And there is ~10% of difference for the experts. We see that by comparing their results to the commonly accepted GT, the main differences lie mostly on the interface between phases (for example given in Fig S6). Moreover, the magnitude of such difference in the expert group (table ST3) is in accordance with the last few percent of

previous accuracies (Fig 4). As explained above, this is because the $\boldsymbol{\varepsilon_{cog}}$ is not fixed and is unavoidably diluted in the whole process. In other words, the ceiling of performance can be interpreted as an indicator of the experimenter's self-consistency of labeling data and the degree of uncertainty in the segmentation. To reduce the segmentation ambiguity, there are newly alternative techniques such as chemical DRX-CT[215] and ptychography-XCT[170]. However, the resolution or the acquisition time of these techniques are waiting to be improved.

The second experiment is to give an estimation of the influence of the cognitive bias on the segmentation with a larger statistic. With the previous experiment, we understood that the segmentation ambiguity locates mainly on the interface. And Fig S6 shows raw tomograms and a line profile perpendicular to an NMC-CBD interface. One can see that the sharp border in Fig S7 corresponds to a slope of 10 voxels in width. In absence of larger samples of expert GTs for NMC_1 dataset, we established an algorithm to simulate perturbated GTs not exceeding the interval of 10 voxels on the interfaces to train different CNNs (detailed in Methods). The algorithm consists of locating all the interfaces and choosing a part of them to push/pull by random units. New predictions from these LRCS-Nets are evaluated by volume fractions, surface area, and IoU. Due to the computational cost, we first validated this algorithm first in 2D with a thousand repetitions. The 2D histogram of interface voxels in a thousand simulated GTs roughly underlies the Gaussian shape with a full width at half maximum of 10 voxels. It is shown in Figure 6a as a green mask on the raw tomogram. The mask has a darker green color when the number is high and transparent when it is zero. Figure 6b depicts the 3D histogram of purple interfaces for a hundred simulated perturbated 3D GTs.

15 CNNs are then trained with labeled images generated from the same training dataset and evaluated by the common ground truth in the test dataset. HPs use the best combination of hyperparameters obtained with the previous NMC datasets. Figure 6c represents the IoU distributions of the 3D predictions of these networks and the variance of the overall accuracy. The NMC phase has the most stable IoU dispersion of 92.7$\pm$0.2%, which contrasts with the CBD 37.6 $\pm$1.4% and the pores 65.9$\pm$1.3%. Fig 6d shows the ratio of the surface area and volume fraction for the three phases. We see that the higher surface area to volume ratio results in smaller IoUs, confirming our previous finding of the uncertain area. CBD is the most difficult to segment among these three phases in this dataset and tends to have inconsistencies between experimenters. Potential ways to improve IoUs of thin objects could be to use higher resolution and smaller FoV with interlaced scans or other advanced XCT techniques[170,216] or reconstruction algorithms[217].

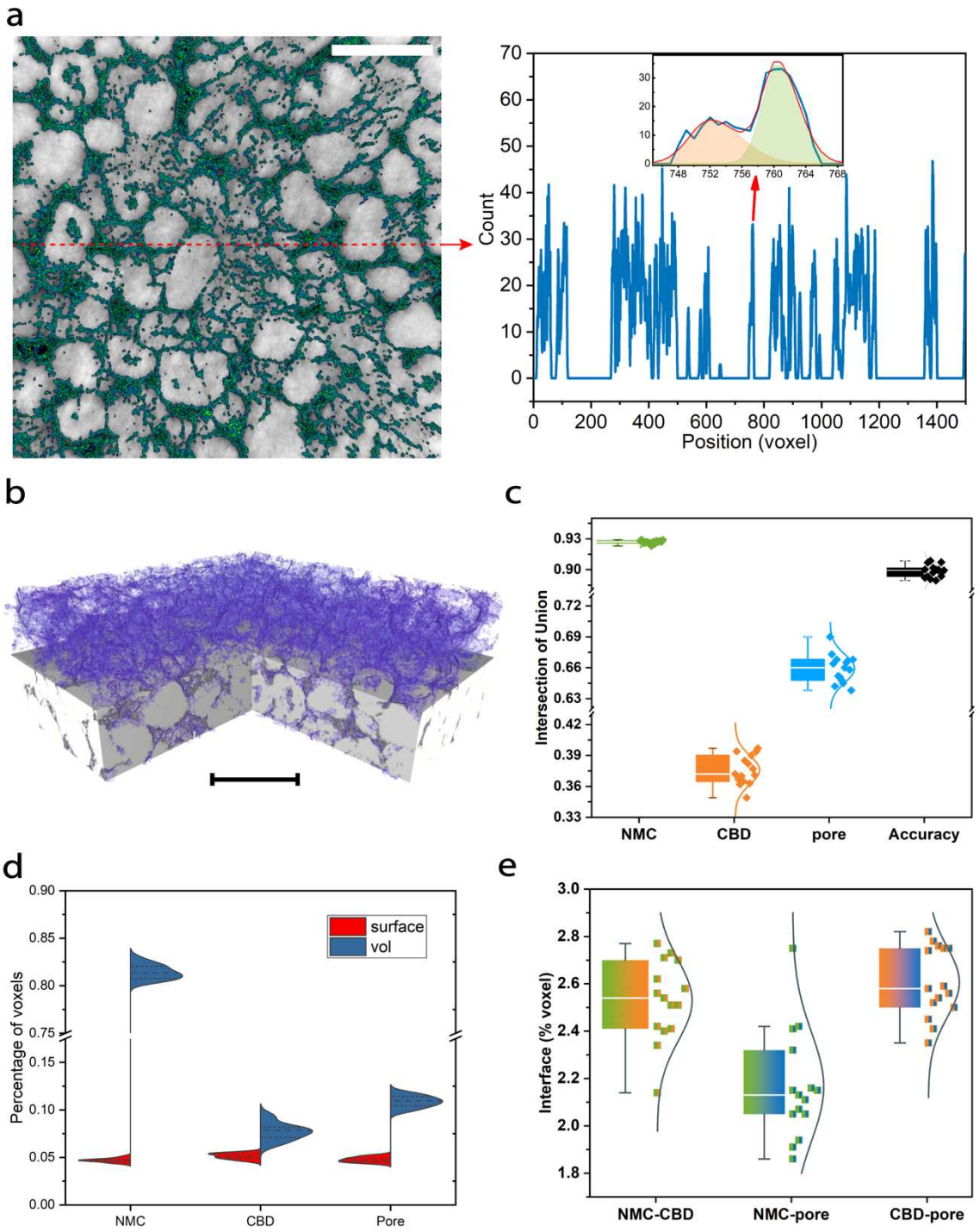

Figure 6. ***Evaluation of the uncertainty impact.*** *(a) A raw tomogram masked by the 2D histogram of interphases of a thousand simulated labeled images in the training dataset. The middle line profile of the histogram is plotted in blue and zoom onto two frontiers with a width at middle-height of about ten voxels. (b) The histogram of interfaces extended to 3D for 100 synthetic 3D volumes (c) the evaluation of IoU and accuracy of 15 CNNs trained with simulated training data d) distribution of the surfaces and volume fractions of the predicted 3D volume from the said CNNs. (e) the dispersion plot of 3 types of interfaces segmented by these 15 CNNs. The scale bar represents 10 µm.*

The 15 CNNs trained from the perturbated data are used to predict 15 volumes. The volume fractions and interfaces for each of these volumes are plotted in Fig 6d&e. The 3D interfaces vary in intervals of 2.5±0.3%, 2.1±0.3%, 2.6±0.2% respectively for NMC-CBD, NMC-pore, and CBD-pore (Figure 6e). We see that the accuracy deviations (Fig 6c) evaluated on the test data results in less than 1% of the variance for the 3D predictions (Fig 6e). Note that the interface is deliberately expressed as a percentage of voxels instead of nm^{-1} to avoid ambiguity as there are various extrapolations of tomographic voxels to a surface, such as taking the diagonal triangle or an arbitrary constant value which will result in different values. Threshold, as described in Fig 1c on NMC_1, resulted in 0.47% surface area voxels, which is 4-5 times less surface area than by the CNN segmentation.

5.9. Generalization of CNN by transfer learning

In the previous sections, we have demonstrated how to optimize HPs and gained a fundamental understanding of LRCS-Net. Here, the LRCS-Net will be tested on different tomographic datasets of battery materials. A similar dataset from NMC with the same composition but higher loading was used for training a second network using transfer learning. Then two other datasets of LOB with different morphologies will also be shown.

For the second dataset of NMC (denoted NMC_2 hereafter), instead of initializing the kernel randomly at the start of the training, we recover all the well-trained kernels of the best-trained model (denoted LRCS-Net_1) with the NMC_1 dataset (Figure 6a). This is called transfer learning. The Kernels of the LRCS-Net were saved in four different advancements during the previous training. Different starting learning-rates were applied (in Fig 6a, a descending order of starting learning-rate from blue: 1e-4, orange: 1e-4 x $0.3^{(N-1)}$, to green: 1e-4 x 0.3^N. N is epoch number, at the end of which saved the state of LRCS-Net_1^N 1). A control experiment is carried out with a random initial state of the network and with NMC_2 dataset.

	LRCS-Net_1	Transfer Learning	Control
Trained with dataset	NMC_1	NMC_2	NMC_2
Initial state of CNN	Random	LRCS-Net_1^N	Random

Table 2. *Summary of the training data for the transfer learning*

Unlike training from scratch, resumed trainings begin directly above 80% accuracies since the kernels have already been trained. These starting points of transfer learning, from the different depth of resuming point of LRCS-Net_1^N, increase and then stabilize around 83%. A final gain of more than 2% on average was obtained, which is in line with the conclusions of Yosinski *et al*.[212]

that the transfer learning of all kernels drives to better generalization of the network. The green curves show that lower starting learning rates give higher accuracies. However, this performance gain stabilizes while taking up other points from LRCS-Net$_1^N$ (>30k steps), indicating that the benefits of generalization from a trained model can be limited. Nevertheless, this finding is still beneficial in accelerating the segmentation of tomographic data. We have successfully demonstrated that LRCS-Net can achieve reasonably high accuracy by receiving only a single segmentation example image and gain accuracy by transferring already trained kernels.

The overall accuracy does not reflect the balance between classes in multi-phase segmentation. The network has no guarantee of converging towards a minimum of good quality. For instance, it could tilt in a particular class but still achieve decent accuracy (e.g., having all possible NMC particles correctly segmented, but mostly wrong for the others). The intersection of Union (IoU), on the other hand, is a more common metric in semantic segmentation that allows us to check whether the network is trained in an imbalanced manner. It is calculated by dividing the common area of the predicted segmentation and the ground truth by their union.

5.10. Validation of CNN approach on LOB datasets

The IoUs of a third dataset of pristine binder-free carbon nanotube cathode material for Li-O_2 battery developed in chapter 2 (Fig 7b) and another dataset of the same cathode material in the recharged state (Fig 7c) are shown. These materials made of low atomic number elements have a weak X-ray attenuation coefficient. Therefore, these two additional datasets are obtained using a different imaging technique, *i.e.,* chapter 2. The morphology of these materials and the complications of segmentation differed from the previous Li-ion cathode.

In Figure 7b, the pristine cathode contains tightly entangled carbon nanotubes and residual iron particles and other inclusions from the fabrication of nanotube. We have segmented three phases: nanotubes, in which grey-level is closed to the background; impurities, which present a strong contrast to X-ray and inversed by the phase contrast technique resulting in the darkest color; and the void, brighter than the other classes in the background. The halo artifact surrounding the iron particles is arbitrarily included in the background. In the 3D volume of Figure 7c, the recharged electrode is segmented differently: undissolved Li_2O_2 (blue), dissolved domain (dark grey), and background (transparent). The difficulties in segmenting these datasets are as follows. The carbon nanotube in the pristine dataset is extremely thin and almost anchored in the

background. The Li_2O_2 and the void in the recharged dataset have the same grey level but have a different texture.

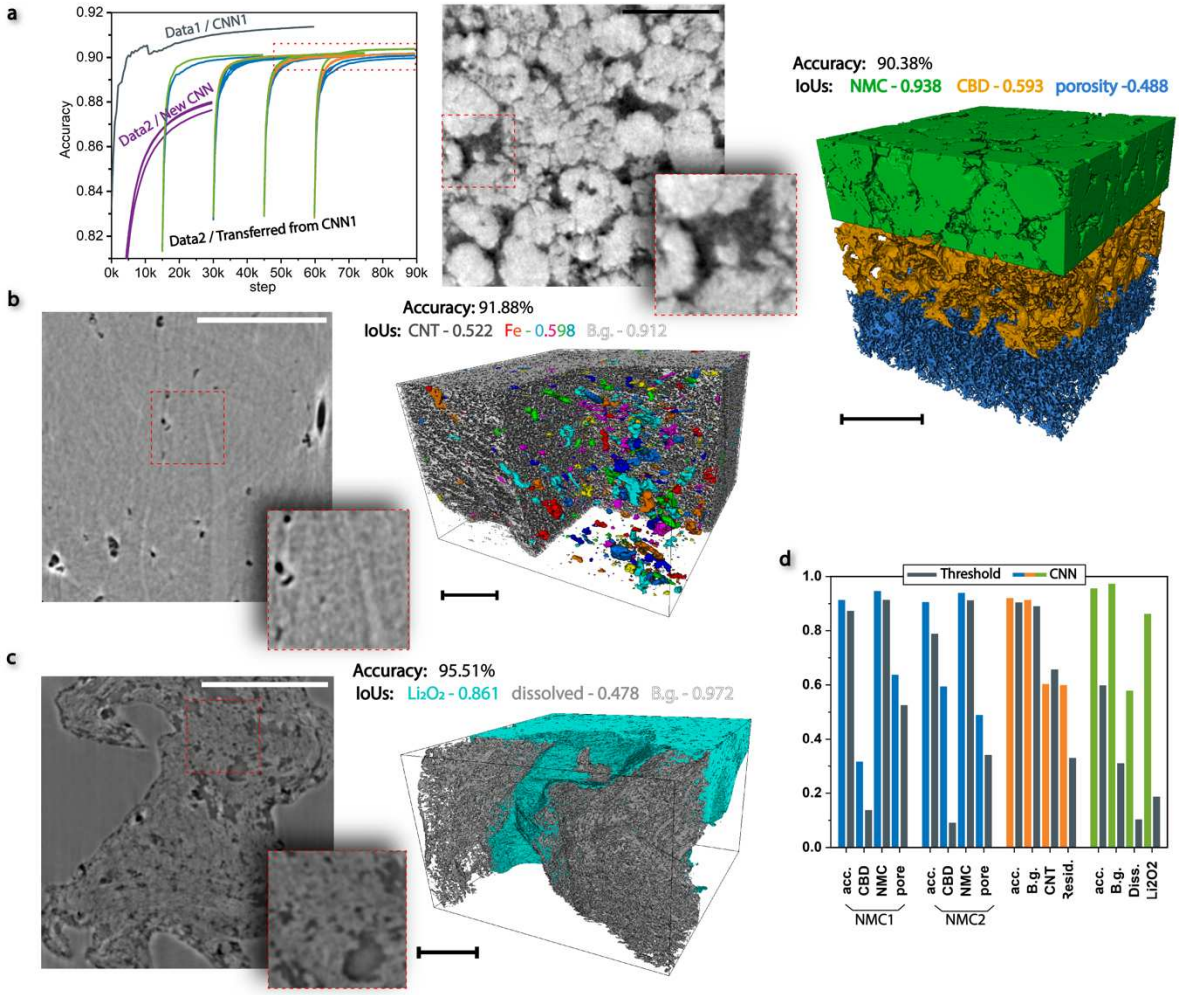

Figure 7. ***Performances for other battery datasets.*** *(a) Accuracy comparison between training from scratch and the ones that starts by kernel transfer from a well-trained LRCS-Net. Data1 and 2 are similar NMC materials from two electrodes of different loading (mg/cm^2). The purple curves of trainings from scratch with NMC_2 have lower accuracies than the transfer learnings (blue/orange/green ones of descendant initial learning-rates) from the NMC1 trained model (grey curve). A selected slice of the raw tomogram and an inset zoom is shown. On the top right, the 3D segmentation volume of NMC_2 for three phases is depicted (b) A cross-section of raw volume and the 3D rendering of the segmentation of this carbon nanotube binder-free pristine material for Li-O_2 battery. The gray color represents the carbon. The colored inclusions in the electrode separated by the 3D watershed algorithm after the segmentation. (c) The same material was treated by acid to remove the iron particles then went through a full discharge-charge round-trip. On the left-hand side, a cross-section of this material. And on the right-hand side, the cyan color domain corresponds to the non-dissolved Li_2O_2, and the gray colors are the dissolved ones. (d) Comparison between the threshold and LRCS-Net on their accuracies and Intersection over Union (IoU) for two datasets of NMC, the binder-free cathode of Li-O_2 battery, and another recharged state cathode of Li-O_2 battery. The scale bars in a-c are 10 µm.*

Fig S8 shows the synergies between the hyperparameters in LRCS-Net with descending order of scores. Similar to the NMC_1 dataset, the trend of obtaining better results with small

batches and 1e-4 as initial learning rate is again obtained. Compared to the threshold, LRCS-Net improved the IoUs of these datasets. For the pristine dataset, some background noise is included by the threshold method. The IoUs for iron particles and background are improved by LRCS-Net, while the improvement in CNT segmentation is modest (<0.02). For the recharged dataset, the threshold failed with the threshold method due to the similar gray level of Li_2O_2 and the background. In contrast, the LRCS-Net can distinguish these phases and has higher IoUs.

5.11. How to assess the segmentation?

It is often an obscure notion the segmentation quality in the literature or in the segmentation softwares. Thoughout this chapter, we have been discussing the biases diluted in the datasets and the uncertainty in the prediction. We have also shown that the ceiling of the validation/testing score of the CNN is closed to the difference in the segmentation of same images from two experimenters.

In our experiences, this finding is reproducible. In the segmentation routine, we believe that it is useful to evaluate the segmentation with different people by generating the same segmentation and compare their difference as we reported in section 5.8. A minimum statistic can give an idea of the uncertainty present in the annotations.

5.12. Conclusions and Perspectives

Nano-XCT data of battery materials is challenging to segment. The overlapping grey-levels and tomographic artifacts are factors that hamper accurate segmentation with traditional methods. We addressed this problem with a lightweight convolutional neural network (LRCS-Net) and presented the workflow of training a CNN from scratch within the framework of the open source SegmentPy software. We demonstrated that portable and computationally inexpensive models (LRCS-Net) can also easily achieve decent accuracy and make fast prediction with small training dataset.

This work has been focusing on deploying CNNs for applicative segmentation of multiphase battery materials. To have a comprehensive insight instead of tuning the CNN as a black-box, we have covered the basics of CNN including visualizing outputs of neuron layers in LRCS-Net for the understanding of the functioning. At the current state, the hyperparameters tuning is still an unavoidable task in the segmentation routines. Hence, we gave practical

examples of hyperparameters and showed their influences on the convergence. Among the studied hyperparameters, we found that the learning rate and batch size are the most sensitive and therefore need to be carefully adjusted. These findings has been verified on two XCT datasets of Li-ion battery cathode and reproducible in two other Li-O_2 battery datasets using phase contrast technique. Furthermore, we have shown the incremental effect of applying transfer learning for the training in a similar dataset.

With a survey approach and a data simulation approach, we have answered several fundamental questions. We have first identified the nature and the region of uncertainty for a NMC dataset by interrogating a group of scientists to segment the same image. We highlighted that even experts cannot be unanimously consent on voxels near the interface. We have further quantifying the impact of such uncertainty by comparing the outputs of CNNs trained with synthetic data. We have given the variances of the surface area and the volume fraction of the NMC dataset.

In summary, the current work has not only demonstrated the capability of the CNN but also addressed to a challenging topic of uncertainty in the segmentation for battery CT material, which has been considered as an unquantifiable and often neglected in the field. Finally, we would like to add that, in practice, fine adjustments can be made afterward and several area of different sizes can be used for composing each dataset.

In perspectives, a profound comparison of LRCS-net with the family of U-Net and its derived forms will be carried out[208,209,218]. Other pseudo-3D CNN model uses adjacent slices as 3D input, but 2D convolution kernels as reported in[219,220] or 3D CNN model, which uses volume as inputs and 3D convolutions by Labonte *et al.*[194] deserve to be investigated. There are also emerging automatic techniques[221,222] searching optimal CNN architecture that could be potentially deployed in our current cases. Future direction might be to train a versatile network with a larger dataset for a specific collection of material. To this end, the reported transfer learning will be a reliable supporting technique. However, emerging weak supervised few-shot segmentation methods[223,224] with a different training fashion is a potential direction in segmenting the materials of similar characteristics with few labeling interventions. Last but not least, more realistic tomographic artifacts such as motion artifacts or ring artifacts can be artificially added to the augmentation to reinforce the network capacity.

Important takeaways :

The segmentation of tomographic images of the battery electrode is a crucial processing step, which will have an additional impact on the results of material characterization and electrochemical simulation. However, manually labeling X-ray CT images (XCT) is time-consuming, and these XCT images are generally difficult to segment with histographic methods. We propose a deep learning approach with an asymmetrical depth encode-decoder convolutional neural network (CNN) for real-world battery material datasets. This network achieves high accuracy while requiring small amounts of labeled data and predicts a volume of billions voxel within few minutes. While applying supervised machine learning for segmenting real-world data, the ground truth is often absent. The results of segmentation are usually qualitatively justified by visual judgement. We try to unravel this fuzzy definition of segmentation quality by identifying the uncertainty due to the human bias diluted in the training data. And further training CNNs with synthetic data to show quantitative impact of such uncertainty on the determination of material's properties. Nano-XCT datasets of various battery materials have been successfully segmented by training this neural network from scratch. We will also show that applying the transfer learning, which consists of reusing a well-trained network, can improve the accuracy of a similar dataset.

- Segmentation Routine: hyperparameters tuning
- Eviting the visual judgement: A self-evaluating method
- Visualization can help understanding the functioning of a CNN
- Transfer learning can help improving the accuracy
- An open-source graphical interface for all above: SegmentPy
- Big network does not necessarily do better than the small ones

5.13. Annexes

5.13.a. Data availability

The battery tomography datasets used in this contribution is available for free download at https://tomobank.readthedocs.io

5.13.b. Code availability

The SegmentPy python software is available for free download at https://segmentpy.readthedocs.io

Figure S1. *Picture taken in the optical microscope where shows the laser cut pattern. A tip with epoxy installed on a micro-manipulator approaches this pattern to withdraw the NMC sample*

5.13.c. Annexes Note 1:

The convolutional layer contains kernels that map the N inputs, which is zero-padded by floor division of A and B by two units, from the previous layer with the operation (1).

$$Conv(x_{n,i,j})_p = \sum_{n=0}^{N} \sum_{a=0}^{A} \sum_{b=0}^{B} x_{n,i-a-1,j-b-1} \times w_{p,n,a,b} \quad (1)$$

With A, B are the width and height of the kernel. $i \in I$, $j \in J$ are position of the n-th input $x_{i,j}$ from the previous layer. In our case, A equals to B and takes values of odd numbers that are

superior to 3 (e.g., 3, 5, 7…, where three is the most common value). The common practice is to use a small kernel size and large number of kernels without overcharging the memory. N is the number of channels/neurons from in the previous convolutions/FCL layer. $And\ p \in P$ number of convolutive kernel in the current layer.

The fully connected layer (FCL) is a matrixes multiplication of an input $\bar{x} \in \mathbb{R}^{I,J}$ by another matrix of $\overline{w} \in \mathbb{R}^{K,P}$

$$FCL(x_{i,j})_p = \sum_{k=0}^{K} flatten(x_{i,j})_k \times w_{k,p} \tag{2}$$

Where $p \in P$ represents p-th neuron in the current layer. K = I x J is the dimension of the flattened input. Flatten function reshapes the input $\bar{x} \in \mathbb{R}^{I,J}$ to $\bar{x} \in \mathbb{R}^{K}$

Throughout this work, we apply either a bias or a batch normalization between the output of convolution/FCL (Fig 2a). The bias expresses $bias(x_{i,j}) = x_{i,j} + b_{i,j}$, whereas the Batch Normalization[225] is an operation with two trainable parameters γ and β that will be updated in the training phase. The gradient descents for γ and β can refer to Ioffe *et al.*[225] $\tilde{\mu}$ and $\tilde{\sigma}$ are in-batch statistics (rolling average and standard deviation) during training and become overall population statistics during prediction.

$$BN(x_{i,j}) = \gamma \frac{x_{i,j} - \tilde{\mu}}{\sqrt{\tilde{\sigma} + \epsilon}} + \beta \tag{3}$$

ϵ prevents the division by zero and is left at 1e-3 by default throughout this work.

In this work, the function of activation applied on the output of the bias or convolution (Fig 6c) takes form by choice of either sigmoid or leaky:

$$\begin{cases} sigmoid(x_{i,j}) = \dfrac{1}{1 + e^{-x_{i,j}}} \\ leaky(x_{i,j}) = \begin{cases} \alpha x_{i,j}, if\ x < 0 \\ x_{i,j}, otherwise \end{cases} \end{cases} \tag{4}$$

The leaky activation maps the input $x_{n,i,j}$ as itself in the positive region and with a coefficient α in negative region. If $\alpha = 0$, the leaky is equivalent to REctified Linear Unit (Relu) activation[226]. We take α = 0.2 by default in our network.

The max-pooling with index comes after the activation at each end of the convolution block in the encoder. The output of this operation (5) $\overline{MP} \in \mathbb{R}^{I/str,J/str}$ takes takes the maximum value

in a square of str by str pixels, where str stands for size of stride. The positions of the maximum in $\bar{x} \in \mathbb{R}^{I,J}$ are recorded as $\overline{index} \in \mathbb{R}^{\frac{I}{str},\frac{J}{str}}$.

$$\begin{cases} MP\left(\begin{pmatrix} x_{n,l,m} & \cdots & x_{n,l,m+str} \\ \vdots & \ddots & \vdots \\ x_{n,l+str,m} & \cdots & x_{n,l+str,m+str} \end{pmatrix}\right) = max\left(\begin{pmatrix} x_{n,l,m} & \cdots & x_{n,l,m+str} \\ \vdots & \ddots & \vdots \\ x_{n,l+str,m} & \cdots & x_{n,l+str,m+str} \end{pmatrix}\right) \\ index_{n,I/l,J/m} = argmax(\begin{pmatrix} x_{n,l,m} & \cdots & x_{n,l,m+str} \\ \vdots & \ddots & \vdots \\ x_{n,l+str,m} & \cdots & x_{n,l+str,m+str} \end{pmatrix}) \end{cases} \quad (5)$$

With $l = h \times str, h$ integer in $[0, \frac{I}{str} - 1]$ and $m = w \times str, w$ integer in $[0, \frac{J}{str} - 1]$.

The upsampling is a unit reconstructing the output from the input $x_{i,j}$ and the index conserved by the encoder. The value of input $x_{i,j}$ is dispatched to the index position.

$$Up\left(x_{i,j}, \overline{index}\right)_n = \begin{cases} x_{i,j} \; if \; i,j \; is \; in \; \overline{index} \\ else \; 0 \end{cases} \quad (6)$$

The Softmax layer converts the output of the neural network into a stack of tri-dimensional outputs in space $R^{W,H,cls}$ with elements ⊂(0,1). W and H are the width and height that correspond to the dimensions of raw tomogram and segmentation.

$$Softmax\left(x_{i,j}\right) = \frac{e^{x_{i,j}}}{\sum_i^{cls} e^{x_{i,j}}} \quad (7)$$

The Dice loss function expresses as follow:

$$\mathcal{L}\left(y_{i,j}\right) = Dice\left(y_{i,j}\right) = 1 - \frac{2\sum_{i=0}\sum_{j=0} y_{i,j} \times label_{i,j}}{\sum_{i=0}\sum_{j=0} y_{i,j} + label_{i,j}} \quad (8)$$

Where the *label* corresponds to the handcrafted GT and the y to the output of the neural network.

While computing the backpropagation, the gradients of each trainable weight in the network is calculated with respect to the loss by applying the chain rule. An optimizer will apply a change onto the weight depending on the computed gradient. The ADAM optimizer has been used throughout this work. Readers can refer to Kingma *et al.*[227]. The learning rate was studied and tuned in Fig 2b. The other two parameters beta were left by default as such in Tensorflow.

The initial LRCS as represented by Fig S1a, has four blocks of convolution that include two layers of convolution on both encoder and decoder. Three layers of FCLs have identically P number of neurons in the hidden layers, where P equals to number of $(\frac{windowSize}{32})^2$. After the transformation of the first FCL, the input has been mapped into $\mathbb{R}^{\frac{windowSize}{8} \times \frac{windowSize}{8}} \longrightarrow$

$\mathbb{R}^{\frac{windowSize^2}{8^2}\times\frac{windowSize^2}{32^2}}$. And on the output of FCLs a reduction of dimensions. This brutal change of dimensionality is rather obscure for the gradients. The Softmax eq. (7) is used on the output of the network.

5.13.d. Annexes Note 2:

The original CNN architecture (Fig S2a) includes symmetric numbers of convolution layers in the encoder and decoder and three central fully connected layers (FCL). The latest has been removed for three main reasons. First, the images passed through an FCL layer undergo a change of dimension that loses their positional information. The output of the FCLs is usually found to be non-semantic or totally noisy in the current application. Second, we found that the FCLs are notably difficult to train (Fig S2b). Compared with the VGG-like[228] CNN, in which the FCLs are just prior to the output, our FCLs are at the center of the CNN and isolated from the loss by layers in the decoder. Last, from the performance point of view, the use of FCLs hinders the prediction speed as it fixes input dimensions and prohibits to use larger images in prediction. In other words, using the FCL implies the need to stitch small prediction patches for a complete segmentation.

The resulting network binds the four convolution layers before and after the FCLs. However, this primary LRCS-Net without FCLs results in a declining tail of accuracy curve on the unseen data in Fig S2c (green and purple curve), which indicates the overfitting of the CNN on the training dataset. This issue can be redressed by switching off the BN in the encoder and using a sigmoid activation function at the last layer of the encoder. Lastly, in contrast to a deeper encoder structure, in which each block of convolutions has two successive convolutive layers (following by a max-pooling), a reduced structure with one layer per block of convolution in the encoder was retained for the steeper convergence.

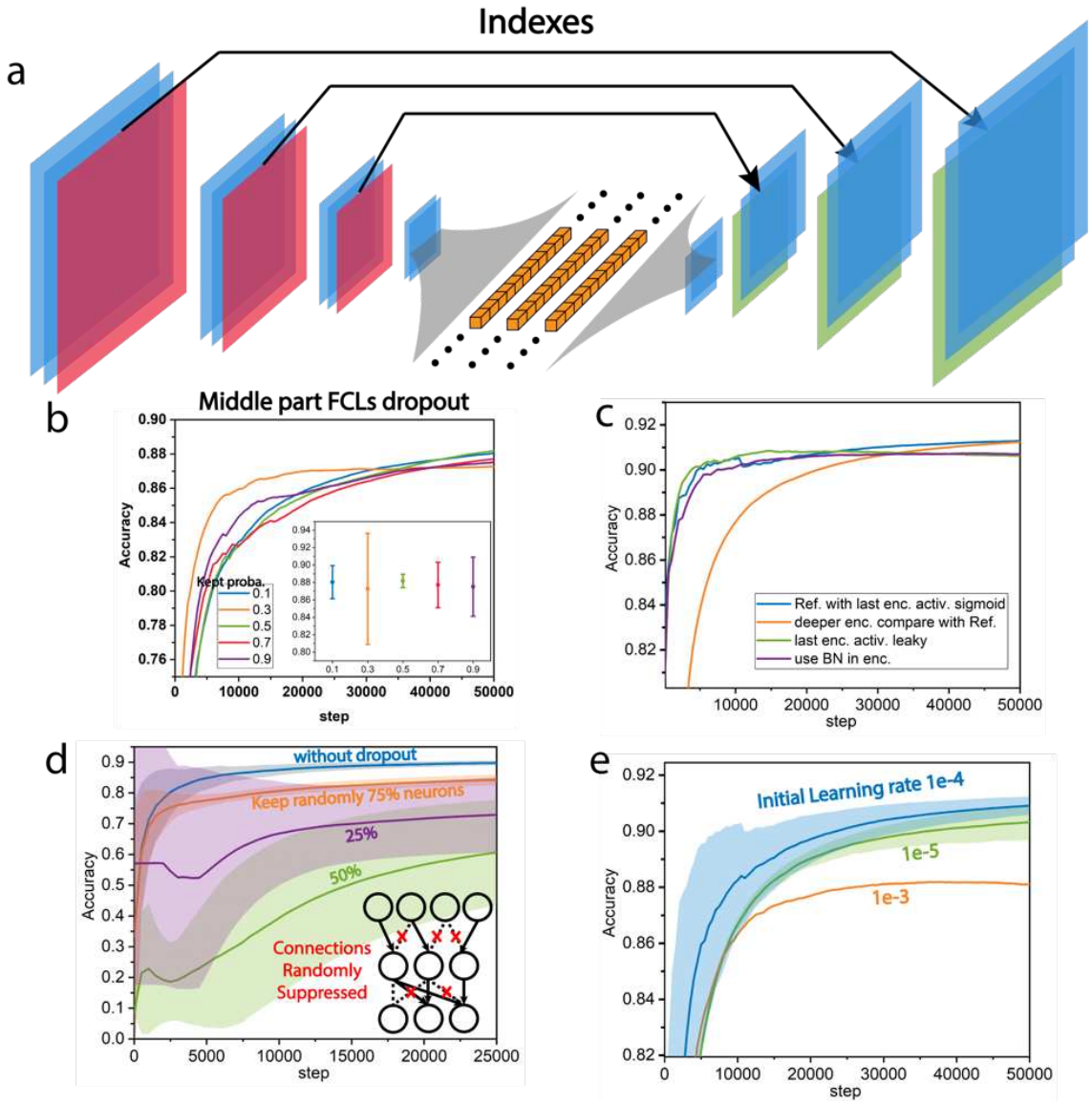

Figure S2. *(a) the initial structure of the LRCS-Net which is derived from the SegNet and Xlearn Network with three layers of fully connected neurons. (b) the average of learning curves (validation dataset) for different FCL connection keeping probability. The inset graph plots the average and standard deviation of the best accuracies for three repetitions of each keeping probability. No significant gain obtained by tuning the dropout during the training. (c) deeper encoder architecture has a slower convergence while achieving the same accuracy (orange curve vs blue reference curve); replacing the last leaky activation of the encoder by sigmoid increases the performance (green curve vs blue ref. curve); switching off the Batch Normalization can avoid de overfitting at the end of the training (purple curve vs blue ref. curve) (d) no gain was obtained with the dropout technique applying on the convolutional layers. Above 25% of drop probability, this technique has detrimental effect on the performance. (e) a comparison of initial learning rate*

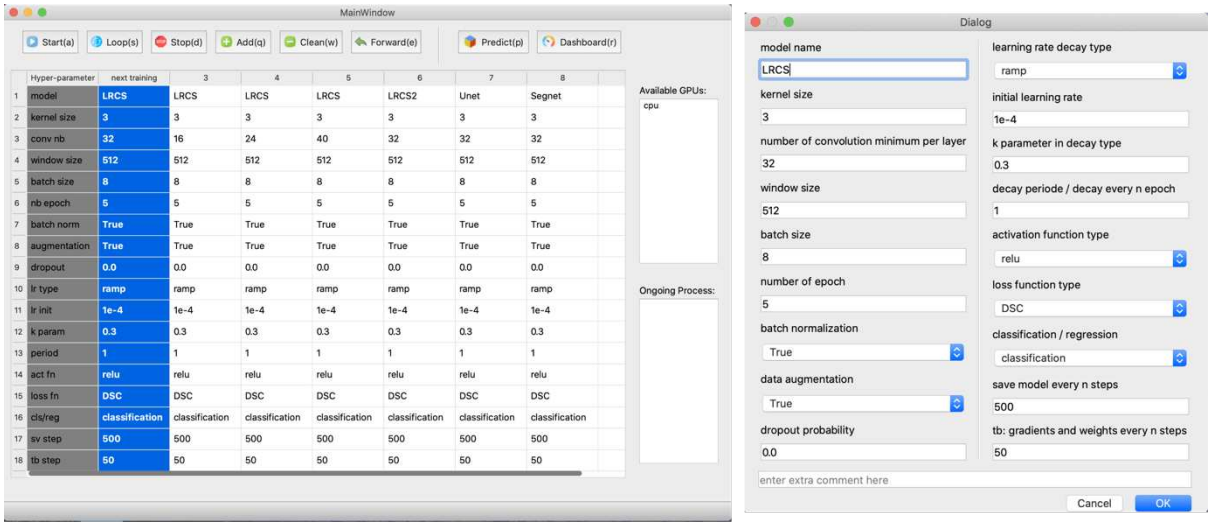

Figure S3. *(left) the SegmentPy main window user interface which manages the training schedule. On the left part, a panel of hyperparameters for future training is shown. On the right-hand side, a list of available GPUs and ongoing process are shown. User can handle the training process (start, stop, or loop, etc) with buttons. Prediction and parameters monitoring can be launched with the buttons on the top-right corner. (right) an overview of the hyper-parameters that can be tuned in the parameters dialog. Or one can directly change them in the table of the main window. All data and extracted layer activations by this code are safeguarded on disk and can be visualized by other software such as Fiji.*

	LRCS-Net
Conv1 without BN	32
Conv2 without BN	64
Conv3 without BN	128
Conv4b with sigmoid	128
Conv5 with BN	128
Conv5b with BN	128
Conv6 with BN	128
Conv6b with BN	64
Conv7 with BN	64
Conv7b with BN	32
Conv8 with BN	32
Conv8b with BN	1

Table ST1. *recapitulation of number of convolutions per layer of LRCS-Net chosen*

Name	Values
Window size	512 (Original ~1.5kx1.5k pixels)
Kernel size	3x3
Batch size	2
Activation function	leaky
Loss function	Dice

Initial LR	1e-4
LR decay ratio	0.3
LR decay period	Every 1 epoch
Noises in augmentation	gaussian, flipping, salt&pepper noise, grayscale variance
Gap of sampling	5
Splitting ratio of training/validating	9:1

Table ST2. *the best hyperparameter combination and training details on the second part of the table.*

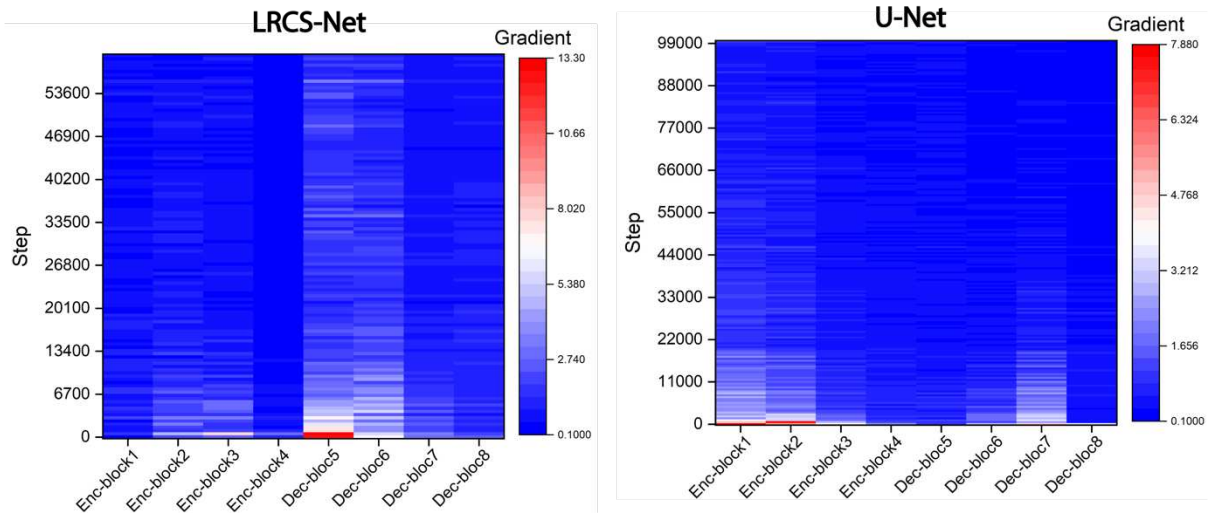

Figure S4. *Heatmap of gradients within the training step of each block of convolutions for LRCS-Net and U-Net. It explains the reason why throughout this study, the dropout technique, introduced by Hinton et al.[229] for mitigating the overfitting, does not show much incremental effect neither on the FCLs nor on convolution layers (Fig S2b & d). It is due to the dependency of the first convolutional layers of LRCS-Net decoder. The suppression of activation connections by the dropout engenders severe losses of information that disturbs the learning.*

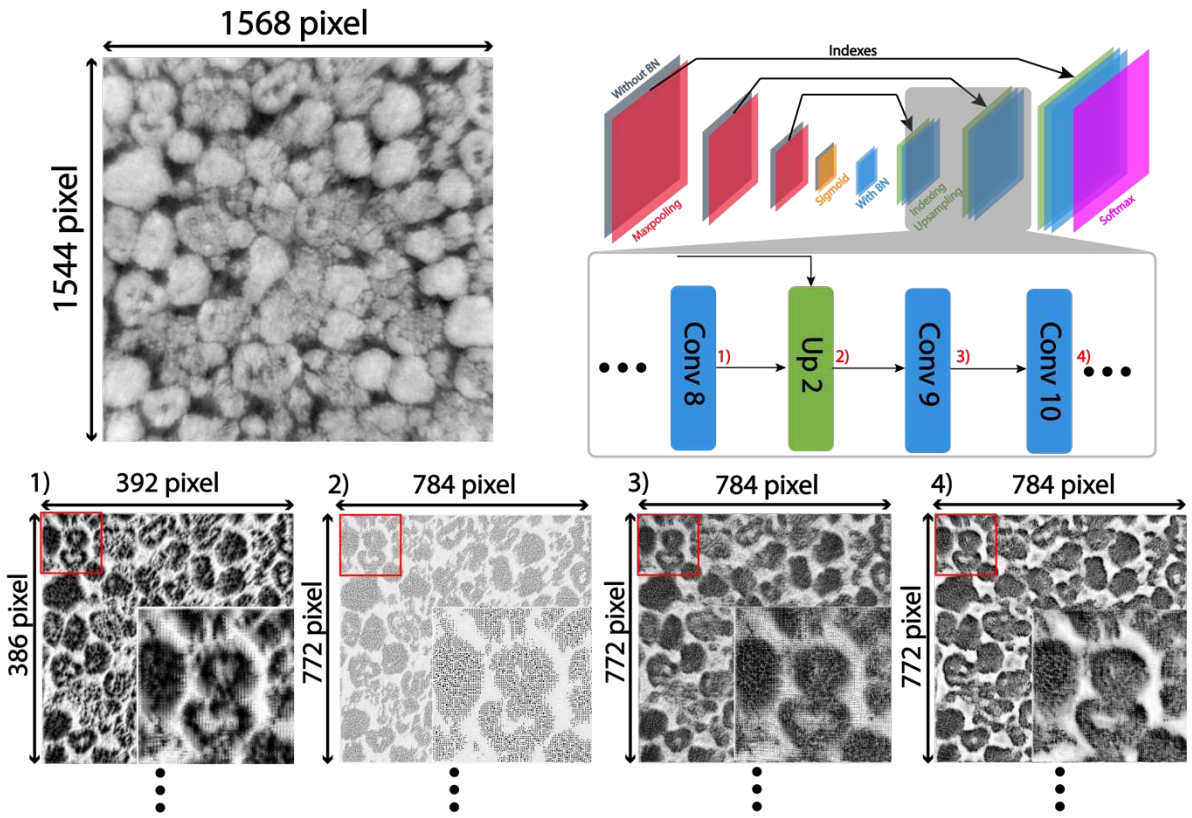

Figure S5. *(Top-left) the input tomogram of the CNN, and on the right-hand side the schematic architecture of optimized LRCS-Net (identical as Figure 2d) and its zoom of the targeted layers. (Bottom) from left to right 3 arbitrarily selected activations with similar learned features to illustrate how the decoder decrypts from lower to higher dimensional mappings. Starting with an activation of 392x386, the up sampling with index doubles the dimension and reconstruct a pixelized mappings in the middle. The successive convolution layer seems to have a smearing effect of smoothing the uneven pixel to the bottom right smoother mapping.*

SegmentPy provides a playground for users without programming pre-request training a neural network. There is a panel for hyper-parameters tuning. A single model to single gpu training strategy is now supported. Users can accelerate tuning with different models trained on parallel gpus. Other tools such as activations and gradient viewer or other practical tools are provided to facilitate the segmentation task.

5.13.e. Annexes Note 3:

In the survey, experimenters are divided into three groups, namely A, B, and C, according to their scientific background (see Table ST3). These groups are made up respectively of people working on the same material (A), people with a background in the battery field (B) and scientists with a general background in material science (C). The experimenters were asked to perform the same segmentation task with the NMC_1 dataset. During the experiment, the Weka plug-in of Fiji was used to annotate the nano-XCT images, and FIB-SEM images of the same material were

provided as a reference. The results are compared to a GT generated and confirmed in a consensually manner by experts of this NMC material. It shows that there may be more than 0.05 of the difference in the average of IoUs between group A (expert) and group B, C (non-expert groups). The average of IoUs in group C deviates considerably from that of the expert group.

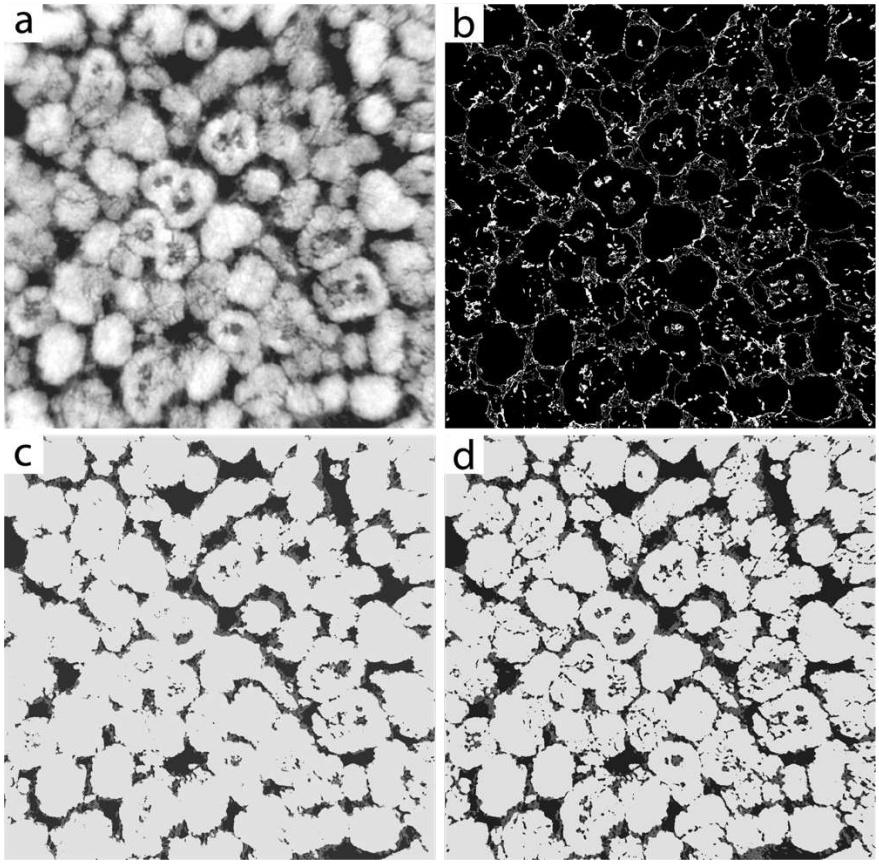

Figure S6. *Comparison of the ground truth from different experimenter. (a) the original ground truth (b) the mapping of the differences between labels generated from (c) one of the experts and (d) the commonly accepted ground truth*

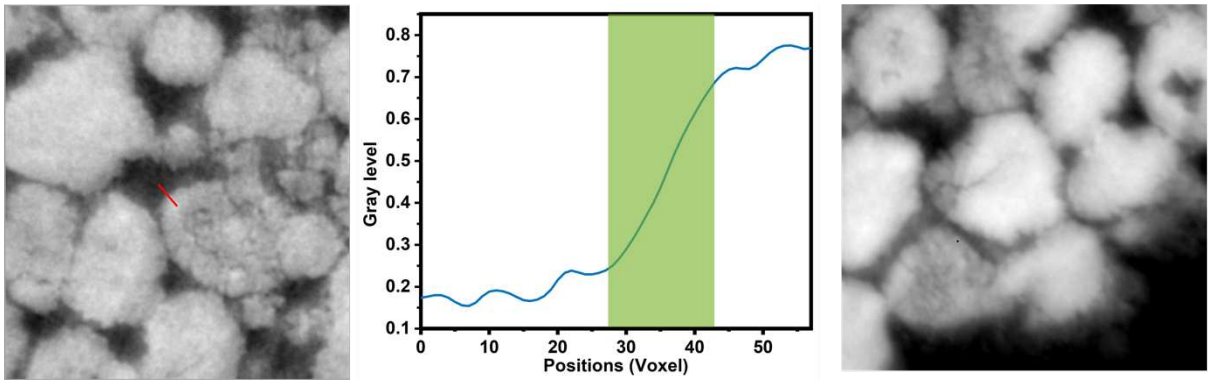

Figure S7. *(left) a close zoom of a raw tomogram and the line profile of the red line is plotted in graph in the (middle), where the clear frontier of NMC particle in the tomogram exceeds actually 10 pixels (~270nm) which is colored in green. (right) another zooms of tomogram at the sample border, where a band of porous CBD is clearly distinguishable from the void that justifies the manually labeled CBD inside the sample is not the noise.*

	GroupA (2 experts)			GroupB (5 well trained experimentators)			GroupC (26 persons in 13 duo)		
Average accuracy	90.41%			85%			76%		
IoU	NMC	CBD	pore	NMC	CBD	pore	NMC	CBD	pore
	0.948	0.385	0.611						
Average accuracy	93.6%								
IoU	CNT	Resid.	B.g.						
	0.658	0.670	0.928						
Average accuracy	94.5%								
IoU	Li_2O_2	Diss.	B.g.						
	0.788	0.641	0.943						

Table ST3. *Testing score of LRCS model trained with Ground Truths labeled by different experimenters on NMC_1, pristine, recharged dataset. These experimenters are separated in three groups namely A, B, and C which are people that have longtime experience of such material, people that in the same battery material field and, people from a vaster background of microscope, respectively. All experimenters within the same group were briefly taught and asked to label the same tomogram on the Software Fiji, with juxtaposed FIB-SEM sample images of the same material. We do see that there is an influence of people of different background.*

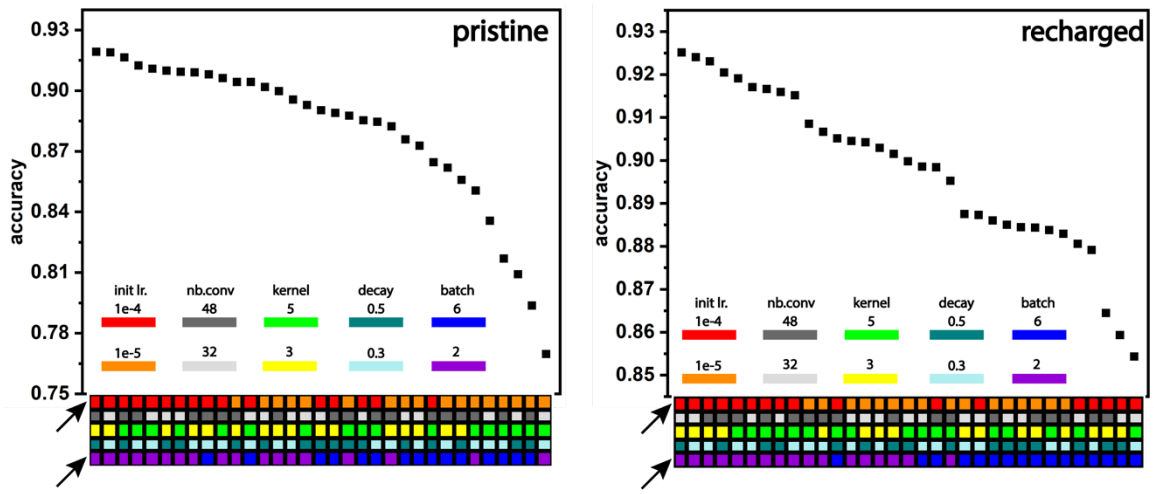

Figure S8. *Scatter plot of LRCS-Net hyperparameters grid search with sorted validation score for Li-O_2 batteries dataset, where the axis x is replaced with a grid and indicates the combination of different hyperparameters of the given scores. Preferences of the initial learning-rate (init. lr. at 1e-4) and the batch size (batch of 2) can be seen.*

Chapter 6

Conclusions and Perspectives

6.1. Summary of the achievements & outlooks

Since the invention of Li-air battery in 1996 by Abraham *et al.*, the Li-O_2 battery has been considered as a promising 'beyond Li-ion' battery technology. And in 2013, BMW and Toyota have announced a foreseeable commercialization of LOB. However, nothing follows up to date. The current chapter attempts to summarize the current work and give some perspectives with the findings of the chapters.

In the academic public research, many works have been devoted during the last decade in stabilizing the cathode cycling including adding mediator[29] and catalyst[59,230–233], techniques of protecting the anode[31,52]. Characterizations such as electrochemical[80], spectroscopies and microscopies[88,97] have been utilized to understand the reaction and failure mechanisms in the LOB. Although the mainstream of the academy is still using the pure oxygen atmosphere, pioneers have been attempted the feasibility of this battery in the presence of moistures and azote. Interesting results such as cycling LOB in 2000 ppm of water[75,114] have been recently reported, which shows the potential of this technology.

The current manuscript has centered on the development of the robust technique of X-ray nano-Computed Tomography to 3D visualize the LOB cathode. From *ex situ* to *in situ*, from reconstruction to segmentation in the workflow, from highly tortuous material to a self-standing binder-free airy one, and from one-usage to recyclable LOB cathode, new ingredients have been added into the nano-XCT 3D imagery technique for studying LOB as well as for the LOB cathode material.

The following table lists the main achievements, takeaways, and outlooks of this thesis.

Achievements	Takeaways	Outlooks
Zernike Phase Contrast	• Overcome the transparency issue of imaging the carbon and Li_2O_2 • Potential structural modification	• Other phase contrast techniques • Increase the resolution instead of FoV (Zernike Actifacts)
Recyclability of LOB cathode	• Low tortuosity binder free cathode • Inexpensive recycling method	• Applicable to other metal-air batteries
In situ LOB	• Visualizing the first germination • No evidence expansion of material by marker checking • The growing mechanism is more likely to 'pop-corn' then a	• Improvement of the Tu-cell to have more growth • Change electrolyte to minimize the bubbling

	homogeneous growth at same progression	
Deep learning on segmentation	• SegmentPy • Transfer learning • Critical opinion on the convergence • Clarifying the fuzzy definition of segmentation quality and proposing self-evaluation routine	• Plug-in descriptors to help convergence • Generalization to larger range of materials

Table 1. *A recapitulative table of achievements, takeaways, and outlook of this project*

6.2. How far from a practical LOB? A glance on the remaining challenges in LOB

To better wrap up and further make use of the findings in this thesis, we would like to answer a frequently asked question: how far is it from a practical LOB? To fully understand the distance from a typical academic work of LOB to a real application, a set of data are listed in Table 2. It compares the two standard Li-ion battery based on LFP and NMC cathodes (data from CATL company website of 2020) and the LOBs in current state. Although the LOB in this work or in a recent Samsung paper of cm-square-folded-cell by Lee *et al.*[234] have achieved high specific energy than the commercialized Li-ion batteries, the current density and the lifespan of LOB are completely left behind.

	Li-ion (LFP)	Li-ion(NMC)	Li-O_2 (this work)	(Samsung) Lee *et al.*[234]
Cell Energy Density (Wh/kg)	136	215	**~300***	**300**
Highest Cell Current Density (mA/g)	10	**117**	0.4*	<1
Lifespan (Cycles)	**3500**	3000	~20-30	<10
** cell level values are scaled from the Swagelok data including other components mass in chapter 2*				

Table 2. *Comparison table of cell-level (inactive mass included) characteristic current commercialized Li-ion and the LOB in this work*

This section will be devoted to briefly discuss in a different angle few remaining issues in LOB and give some potential routes forward of LOB in a modeling perspective that some material reviews do not provide:

- Low O_2 diffusivity and solubility [Low current density]
- Inhomogeneous current and Li_2O_2 distribution [Upscaling effect]
- Low reversibility of Li_2O_2 [Low lifespan]

First, the low current density (mA/g_{cell}, mA/cm^2) is strongly limited by the diffusion and solubility of oxygen for an EV propulsion application. In most of papers or in our chapter 3, increasing the current density leads to an exponential drop of capacity.

To illustrate the limitation and to estimate oxygen properties needed for matching an EV application, we use a published LOB model (to exclude the lateral gas diffusion and convection phenomena of oxygen, the model is simplified into 1D and applying a constant pressure of oxygen above the electrolyte, meaning only the vertical intersection of the 2D model in Fig 1a. Later, we will apply other phenomena like in the paper of Samsung). The low solubility leads to a fast local depletion of oxygen, which is shown by Fig 1 in the separator side of cathode. We can see that the diffusivity and solubility of O_2 plays important role in the depth of lithium peroxide deposition. A high diffusivity compensates the oxygen depletion and leverage the usage ratio of the electrode. This also justifies why we develop a low tortuosity cathode in chapter 3. It is worth noting that increasing the thickness of the electrode without optimizing the oxygen diffusion and solubility does not necessarily optimize the areal energy.

To approach the current density of an EV Li-ion battery, this 1D model suggest a 5-times increase of diffusion and solubility in the electrolyte to meet the need of current density. These are from $7x10^{-11}$ m^2/s to $3.5x10^{-10}$ m^2/s and from 3.72 mM to 18.6 mM, for the diffusion coefficient and solubility of oxygen, respectively.

To note that a 500 km range 100 kWh Tesla battery pack weights 625 kg. For providing the same amount of energy, a LOB should absorbe 23.879 kg of O_2. It is equivalent to 18.37 m^3 of 1 atm pure oxygen (or the quantity of oxygen inhaled by a person during a month). This also shows the importance of a high air-electrolyte interface to insure a high simultaneous oxygen exchange and high current density. This point is not often covered in the LOB papers.

In the reality, it is difficult to be find an electrolyte of 5-times diffusivity and solubility. Using thinner electrode to voluntarily limit the in-depth O_2 depletion and engineering higher air-liquid interface could be a second option.

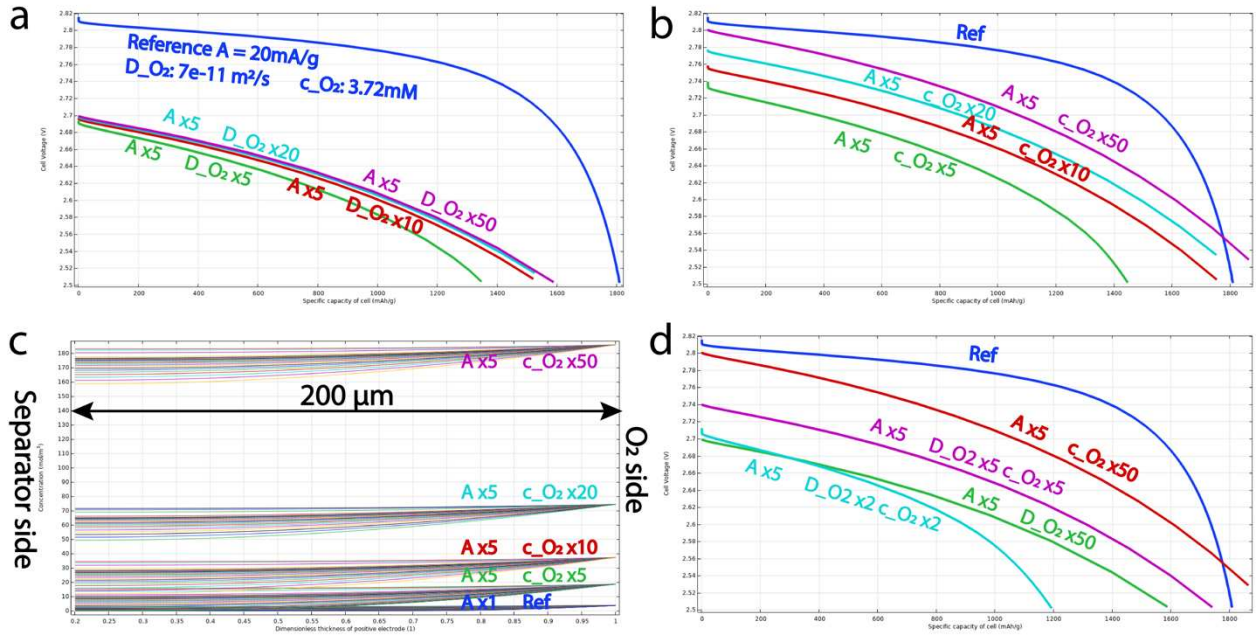

Figure 1. ***Simulated electrochemical responses while varying oxygen coefficient of diffusion and concentration to enable a 5 times current density without loss of capacity.*** *a&b) shows increasing either coefficient of diffusion or solubility of oxygen has limited incremental effect on the capacity a) a comparison of electrochemical curves by increasing the oxygen diffusion coefficient. b) increasing the oxygen solubility. c) O_2 concentration profile of the electrode for different initial concentration in b). d) tuning* ***both the oxygen diffusivity and solubility*** *has synergisitic effect and approach easier the 5-times current density without losing specific energy.*

Second, after having an insight of the relation current density and transport properties of oxygen the upscaling of LOB is most likely to increase in area than in thickness. But it will not be as simple as increasing high air-liquid interface and using thinner electrode to make a larger cell. Other factors such as electrical and ionic conductivity can also engender inhomogeneous deposition of Li_2O_2.

To explain this, we still use the model of *Lee et al.* and their strategy of upscaling the LOB. This model[234] (Fig 2a) applies 1) Henry's law at the liquid air interface, 2) Newman's model for the diffusion and migration of ions in the porous cathode and separator, 3) a parallel Fick's law for the soluble oxygen in the electrolyte, 4) Ohm's law in the current collector and the lithium (Detailed equations can refer to the supporting information of this paper).

They stack a gas diffusion layer (GDL) on the top of the electrolytes (Fig 2a). As such, this cell can be potentially rolled or stacked into a standard format of 18650 cylindrical cell or pouch cell. The GDL made of large carbon fiber is for the air transport convection, but not filled with the electrolyte, there is no Li_2O_2 deposition on GDL. However, the GDL is mandatory, due to the low diffusivity of dissolved O_2 mentioned above in Fig 1c in the 1D model or in the chapter 4 while

developing the *in situ* LOB cell. The pathway of O_2 passes from GDL (gas) → gas-liquid interface → electrolyte (dissolved) must be short.

Lee *et al.* in their paper associated experimental data and model outcomes and pointed out that the formation of Li_2O_2 becomes inhomogeneous while increasing the electrode surface area. We injected the properties of our p-CNT determined in the chapter 2 into their upscaling model (0.83 porosity, 1.15 tortuosity, 150 µm as thickness, and other parameters remained the same as provided in the Annexes in this paper).

By doing so, same inhomogeneity of peroxide deposition was observed (Fig 2b). The current flux is concentrated on the oxygen input side of the cell at the beginning of the discharge and the Li_2O_2 is mainly formed in a 1cm wide area of the top-left corner next to the oxygen inlet (Fig 2b). This upscaling effect is often overlooked in the centimeter-square disc Swagelok electrode in chapter 2 because it is less pronounced.

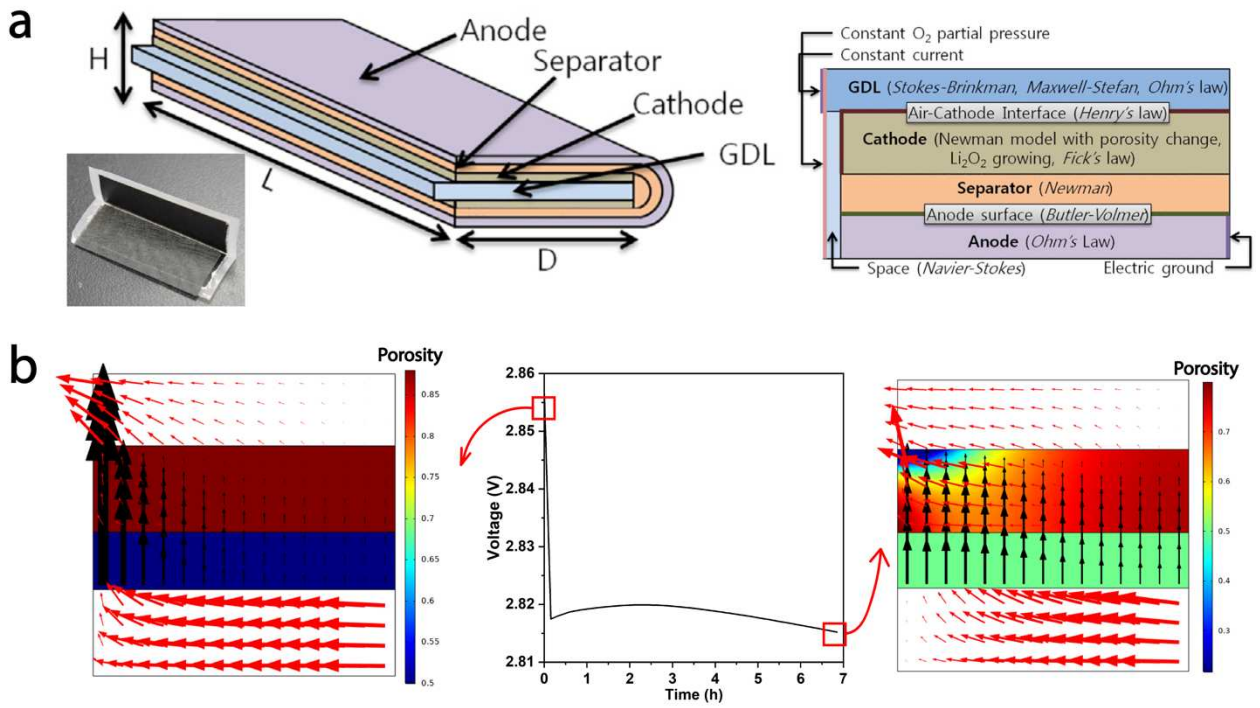

Figure 2. ***Simulation results of upscaling LOB.*** *(a) a Samsung designed LOB folded upscaling cell by Lee et al.[234]. The digital picture of the cell and the explicative schema of the cell are retrieved from this paper and shown on the left, and the associated electrochemical model scheme on the right. The gas diffusion layer (GDL) is a current collector and for the gas intake. No electrolyte is filled, only the cathode and separator are wet by the electrolyte. The governing equations: Stokes-Brinkman; Maxwell-Stefan for describing the gas flow; the Newman's model, and the Fick's law for Li_2O_2 depositing, dissolved oxygen transport in porous media, ion flows, and other physical laws applied on the interface are all indicated in this right-hand side scheme (b) an example of current flux and porosity evolution within the battery using this model. The applied current is same as their paper 0.24 mA/cm^2.*

Third, for the issue of LOB lifespan, although we did not spend heavy pen and ink in this manuscript to discuss the charging process of LOB, many hints herein are showing the charging is another difficult obstacle to overcome (e.g., chapter 2 recharge volumes, chapter 3 accumulating products, and chapter 5 non-dissolved peroxide after charging). Meanwhile, it is worth noting that the chapter 2 is a work around of giving a second life to the LOB but not a solution for expanding the LOB's cycling lifespan. We believe that the cyclability of LOB could be investigated by optimizing the electrolyte and lithium foil.

In the literature, many have reported using heavy metal or metal oxide as OER catalyst[59–61]. These methods showed promising results but reduce the specific energy and the increase the price of the cathode, thus in my opinion unrealistic. Furthermore, the global production such as ruthenium[235,236] is less than 2 trucks per year. To avoid the geo-scarcity problem of the raw material as the cobalt to Li-ion battery, using charge mediator such as LiI[115] could be a more pragmatic solution in my point of view, if the redox shuttle can be controlled.

We have also a small discussion in chapter 2's Annexes of using constant current then holding a low constant voltage (CCCV) can significantly suppressed the Li_2O_2 without degrading electrolyte. This might be a useful solution not degrading the electrolyte to charge the LOB instead of galvanostatic charging (CC) in most papers.

The evaporation of electrolyte, which raises problem to the LOB lifespan, is often overlooked in academic paper. To the best of my knowledge, no such a paper reported relation between the lifespan and volatility of the electrolyte. The ionic liquid with low vapor pressure, low inflammability, large electrochemical stability window seems to be promising, with which many groups[237,238] have demonstrated great rechargeability and high tolerance towards moistures.

Finally, using lithium as anode in LOB still seems to be critical in the current state for several reasons based on our observations in this work:

- the quality of protective layer is difficult to control (see Fig 3a caption)
- the forming lithium protective layer is fragile, for example the Fig 3b shows that by scratching the protective layer of a lithium issued from an experiment of chapter 3 to expose the underneath lithium. The bare lithium reacts immediately and chemically with the solvent. Future investigations should be done for stabilizing the lithium foil or finding stable materials of anode for LOB.

In conclusion, the current small discussion shows that LOB might not be ready for the power application at the current state due to the transport limitation explained above. However, it is possible for other capacity applications if the stability of cycling and upscaling problems can be solved.

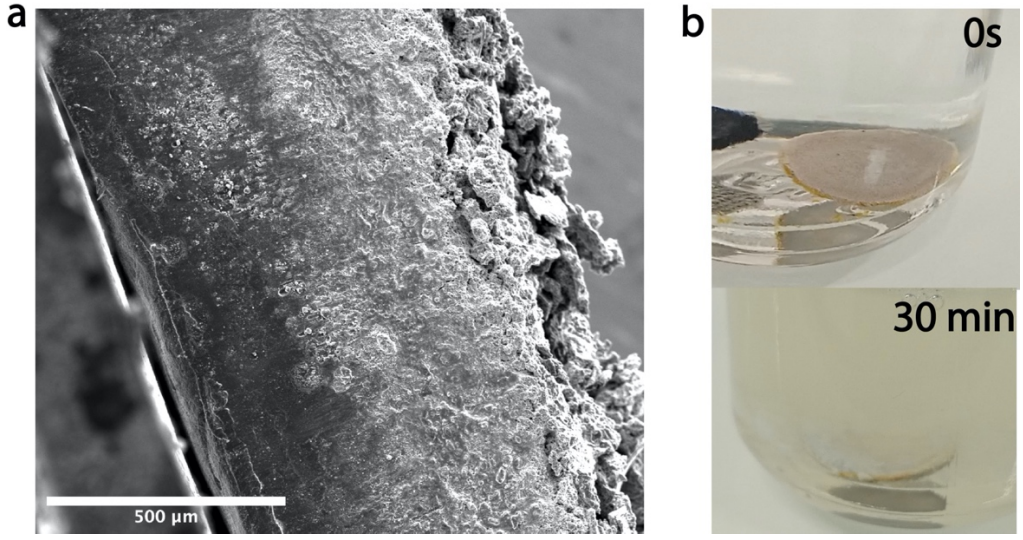

Figure 3. ***Instability of lithium and an outlook of the binder-free filtration technique in chapter 2.*** *a) SEM image of the cycled lithium in chapter 2. Note that the pristine lithium foil is <250 µm. The bright contrast part is a >250 µm protective film formed electrochemically using the electrolyte of chapter 3. This layer is thicker than reported in [125]. b) Scratching this layer to expose the lithium and soak it in the solvent Dimethylacetamide. The bare surface of lithium will bubble immediately indicating a reaction is going on, and the solvent became turbid after 30 minutes.*

6.3. Future investigations

To wrap up all above, the current manuscript has detailed the development of *ex situ* and *in situ* nano-XCT technique for LOB in the 2nd and 4th chapters. And further developed a homogeneous binder-free recyclable cathode material in the 3rd chapter. Assisting technique of deep learning has been implemented to facilitate the segmentation routine in the before last chapter. In the end, we have analyzed the opened possibilities during this project. With the data reported in the previous chapters, we gave the directions of further investigations towards a practical LOB application.

In this exploratory project, we have opened a lot of possibilities both in 3D characterization and in the materials for LOB. We would like to stress out that the in-line Zernike Phase Contrast is only one of the cutting-edge 3D imaging techniques. Other techniques such as holo-tomography and ptychography are emerging, showing promising preliminary results in our recent experiments. Concerning the development of LOB system, only cathode has been studied in this thesis. But we

had observed different electrochemical behaviors with other electrolytes, that worth to dig deeper. Lastly but not least, conventional CNN such as LRCS-net and U-net tend to be sensitive of high frequency features. We recently saw tools like difference of gaussian, that can be plugged into the neural network to force it learning the shape of objects. We see much more advanced engineering work could have been done for each of these topics in the following works.

References

(1) Battery Pack Prices Cited Below $100/kWh for the First Time in 2020, While Market Average Sits at $137/kWh https://about.bnef.com/blog/battery-pack-prices-cited-below-100-kwh-for-the-first-time-in-2020-while-market-average-sits-at-137-kwh/.

(2) Tollefson, J. How Trump Damage the Science. *Nature* **2020**, *586*.

(3) U.S. Global Change Research Program; Wuebbles, D. J.; Fahey, D. W.; Hibbard, K. A.; Dokken, D. J.; Stewart, B. C.; Maycock, T. K. *Climate Science Special Report: Fourth National Climate Assessment, Volume I*; U.S. Global Change Research Program, 2017. https://doi.org/10.7930/J0J964J6.

(4) Parmesan, C. Ecological and Evolutionary Responses to Recent Climate Change. *Annu. Rev. Ecol. Evol. Syst.* **2006**, *37* (1), 637–669. https://doi.org/10.1146/annurev.ecolsys.37.091305.110100.

(5) Walther, G.-R.; Post, E.; Convey, P.; Menzel, A.; Parmesan, C.; Beebee, T. J. C.; Fromentin, J.-M.; Hoegh-Guldberg, O.; Bairlein, F. Ecological Responses to Recent Climate Change. *Nature* **2002**, *416* (6879), 389–395. https://doi.org/10.1038/416389a.

(6) Lüthi, D.; Le Floch, M.; Bereiter, B.; Blunier, T.; Barnola, J.-M.; Siegenthaler, U.; Raynaud, D.; Jouzel, J.; Fischer, H.; Kawamura, K.; Stocker, T. F. High-Resolution Carbon Dioxide Concentration Record 650,000–800,000 Years before Present. *Nature* **2008**, *453* (7193), 379–382. https://doi.org/10.1038/nature06949.

(7) Lenssen, N. J. L.; Schmidt, G. A.; Hansen, J. E.; Menne, M. J.; Persin, A.; Ruedy, R.; Zyss, D. Improvements in the GISTEMP Uncertainty Model. *J. Geophys. Res. Atmos.* **2019**, *124* (12), 6307–6326. https://doi.org/10.1029/2018JD029522.

(8) Aschwanden, A.; Fahnestock, M. A.; Truffer, M.; Brinkerhoff, D. J.; Hock, R.; Khroulev, C.; Mottram, R.; Khan, S. A. Contribution of the Greenland Ice Sheet to Sea Level over the next Millennium. *Sci. Adv.* **2019**, *5* (6), eaav9396. https://doi.org/10.1126/sciadv.aav9396.

(9) Fawcett, A. A.; Iyer, G. C.; Clarke, L. E.; Edmonds, J. A.; Hultman, N. E.; McJeon, H. C.; Rogelj, J.; Schuler, R.; Alsalam, J.; Asrar, G. R.; Creason, J.; Jeong, M.; McFarland, J.; Mundra, A.; Shi, W. Can Paris Pledges Avert Severe Climate Change? *Science* **2015**, *350* (6265), 1168–1169. https://doi.org/10.1126/science.aad5761.

(10) Aye, G. C.; Edoja, P. E.; Charfeddine, L. Effect of Economic Growth on CO_2 Emission in Developing Countries: Evidence from a Dynamic Panel Threshold Model. *Cogent Economics & Finance* **2017**, *5* (1), 1379239. https://doi.org/10.1080/23322039.2017.1379239.

(11) Kasperowicz, R. Economic Growth and CO2 Emissions: The ECM Analysis. *Journal of International Studies* **2015**, *8*, 8.

(12) Saidi, K.; Hammami, S. The Impact of CO2 Emissions and Economic Growth on Energy Consumption in 58 Countries. *Energy Reports* **2015**, *1*, 62–70. https://doi.org/10.1016/j.egyr.2015.01.003.

(13) Stern, D. I. The Rise and Fall of the Environmental Kuznets Curve. *World Development* **2004**, *32* (8), 1419–1439. https://doi.org/10.1016/j.worlddev.2004.03.004.

(14) EM-DAT https://www.emdat.be.

(15) List of Countries by Projected GDP Growth https://statisticstimes.com/economy/countries-by-projected-gdp-growth.php.

(16) Cut Global Emissions by 7.6 Percent Every Year for Next Decade to Meet 1.5°C Paris Target - UN Report https://unfccc.int/news/cut-global-emissions-by-76-percent-every-year-for-next-decade-to-meet-15degc-paris-target-un-report.

(17) Lu, X.; McElroy, M. B.; Kiviluoma, J. Global Potential for Wind-Generated Electricity. 6.

(18) Deng, Y. Y.; Haigh, M.; Pouwels, W.; Ramaekers, L.; Brandsma, R.; Schimschar, S.; Grözinger, J.; de Jager, D. Quantifying a Realistic, Worldwide Wind and Solar Electricity Supply. *Global Environmental Change* **2015**, *31*, 239–252. https://doi.org/10.1016/j.gloenvcha.2015.01.005.

(19) Dufo-López, R.; Bernal-Agustín, J. L.; Domínguez-Navarro, J. A. Generation Management Using Batteries in Wind Farms: Economical and Technical Analysis for Spain. *Energy Policy* **2009**, *37* (1), 126–139. https://doi.org/10.1016/j.enpol.2008.08.012.

(20) World battery production https://www.nextbigfuture.com/2020/02/world-battery-production.html.

(21) Pillot, C. The Rechargeable Battery Market and Main Trends 2011-2020. **2018**, 34.

(22) Olivetti, E. A.; Ceder, G.; Gaustad, G. G.; Fu, X. Lithium-Ion Battery Supply Chain Considerations: Analysis of Potential Bottlenecks in Critical Metals. *Joule* **2017**, *1* (2), 229–243. https://doi.org/10.1016/j.joule.2017.08.019.

(23) Fu, X.; Beatty, D. N.; Gaustad, G. G.; Ceder, G.; Roth, R.; Kirchain, R. E.; Bustamante, M.; Babbitt, C.; Olivetti, E. A. Perspectives on Cobalt Supply through 2030 in the Face of Changing Demand. *Environ. Sci. Technol.* **2020**, *54* (5), 2985–2993. https://doi.org/10.1021/acs.est.9b04975.

(24) Gallagher, K. G.; Goebel, S.; Greszler, T.; Mathias, M.; Oelerich, W.; Eroglu, D.; Srinivasan, V. Quantifying the Promise of Lithium–Air Batteries for Electric Vehicles. *Energy Environ. Sci.* **2014**, *7* (5), 1555. https://doi.org/10.1039/c3ee43870h.

(25) Su, Z.; De Andrade, V.; Cretu, S.; Yin, Y.; Wojcik, M. J.; Franco, A. A.; Demortière, A. X-Ray Nanocomputed Tomography in Zernike Phase Contrast for Studying 3D Morphology of Li–O2 Battery Electrode. *ACS Applied Energy Materials* **2020**, *3* (5), 4093–4102. https://doi.org/10.1021/acsaem.9b02236.

(26) Abraham, K. M. A Polymer Electrolyte-Based Rechargeable Lithium/Oxygen Battery. *Journal of The Electrochemical Society* **1996**, *143* (1), 1. https://doi.org/10.1149/1.1836378.

(27) Sato, T.; Hamada, Y.; Sumikawa, M.; Araki, S.; Yamamoto, H. Solubility of Oxygen in Organic Solvents and Calculation of the Hansen Solubility Parameters of Oxygen. *Ind. Eng. Chem. Res.* **2014**, *53* (49), 19331–19337. https://doi.org/10.1021/ie502386t.

(28) Schürmann, A.; Haas, R.; Murat, M.; Kuritz, N.; Balaish, M.; Ein-Eli, Y.; Janek, J.; Natan, A.; Schröder, D. Diffusivity and Solubility of Oxygen in Solvents for Metal/Oxygen Batteries: A Combined Theoretical and Experimental Study. *Journal of The Electrochemical Society* **2018**, *165* (13), A3095–A3099. https://doi.org/10.1149/2.0601813jes.

(29) Bergner, B. J.; Schürmann, A.; Peppler, K.; Garsuch, A.; Janek, J. TEMPO: A Mobile Catalyst for Rechargeable Li-O_2 Batteries. *J. Am. Chem. Soc.* **2014**, *136* (42), 15054–15064. https://doi.org/10.1021/ja508400m.

(30) Leverick, G.; Tułodziecki, M.; Tatara, R.; Bardé, F.; Shao-Horn, Y. Solvent-Dependent Oxidizing Power of LiI Redox Couples for Li-O2 Batteries. *Joule* **2019**, *3* (4), 1106–1126. https://doi.org/10.1016/j.joule.2018.12.014.

(31) Yoo, E.; Zhou, H. LiF Protective Layer on a Li Anode: Toward Improving the Performance of Li–O_2 Batteries with a Redox Mediator. *ACS Applied Materials & Interfaces* **2020**, *12* (16), 18490–18495. https://doi.org/10.1021/acsami.0c00431.

(32) Xue, K.-H.; Nguyen, T.-K.; Franco, A. A. Impact of the Cathode Microstructure on the Discharge Performance of Lithium Air Batteries: A Multiscale Model. *Journal of The Electrochemical Society* **2014**, *161* (8), E3028–E3035. https://doi.org/10.1149/2.002408jes.

(33) Torayev, A.; Rucci, A.; Magusin, P. C. M. M.; Demortière, A.; De Andrade, V.; Grey, C. P.; Merlet, C.; Franco, A. A. Stochasticity of Pores Interconnectivity in Li–O_2 Batteries and Its Impact on the Variations in Electrochemical Performance. *The Journal of Physical Chemistry Letters* **2018**, *9* (4), 791–797. https://doi.org/10.1021/acs.jpclett.7b03315.

(34) Torayev, A.; Magusin, P. C. M. M.; Grey, C. P.; Merlet, C.; Franco, A. A. Importance of Incorporating Explicit 3D-Resolved Electrode Mesostructures in Li–O_2 Battery Models. *ACS Applied Energy Materials* **2018**, *1* (11), 6433–6441. https://doi.org/10.1021/acsaem.8b01392.

(35) Xiao, J.; Mei, D.; Li, X.; Xu, W.; Wang, D.; Graff, G. L.; Bennett, W. D.; Nie, Z.; Saraf, L. V.; Aksay, I. A.; Liu, J.; Zhang, J.-G. Hierarchically Porous Graphene as a Lithium–Air Battery Electrode. *Nano Letters* **2011**, *11* (11), 5071–5078. https://doi.org/10.1021/nl203332e.

(36) Gaya, C.; Yin, Y.; Torayev, A.; Mammeri, Y.; Franco, A. A. Investigation of Bi-Porous Electrodes for Lithium Oxygen Batteries. *Electrochimica Acta* **2018**, *279*, 118–127. https://doi.org/10.1016/j.electacta.2018.05.056.

(37) Torayev, A.; Magusin, P. C. M. M.; Grey, C. P.; Merlet, C.; Franco, A. A. Text Mining Assisted Review of the Literature on Li-O_2 Batteries. *J. Phys. Mater.* **2019**, *2* (4), 044004. https://doi.org/10.1088/2515-7639/ab3611.

(38) Ding, F.; Xu, W.; Graff, G. L.; Zhang, J.; Sushko, M. L.; Chen, X.; Shao, Y.; Engelhard, M. H.; Nie, Z.; Xiao, J.; Liu, X.; Sushko, P. V.; Liu, J.; Zhang, J.-G. Dendrite-Free Lithium Deposition via Self-Healing Electrostatic Shield Mechanism. *J. Am. Chem. Soc.* **2013**, *135* (11), 4450–4456. https://doi.org/10.1021/ja312241y.

(39) Cheng, X.-B.; Zhang, R.; Zhao, C.-Z.; Zhang, Q. Toward Safe Lithium Metal Anode in Rechargeable Batteries: A Review. *Chem. Rev.* **2017**, *117* (15), 10403–10473. https://doi.org/10.1021/acs.chemrev.7b00115.

(40) Kushima, A.; So, K. P.; Su, C.; Bai, P.; Kuriyama, N.; Maebashi, T.; Fujiwara, Y.; Bazant, M. Z.; Li, J. Liquid Cell Transmission Electron Microscopy Observation of Lithium Metal Growth and Dissolution: Root Growth, Dead Lithium and Lithium Flotsams. *Nano Energy* **2017**, *32*, 271–279. https://doi.org/10.1016/j.nanoen.2016.12.001.

(41) Fang, C.; Li, J.; Zhang, M.; Zhang, Y.; Yang, F.; Lee, J. Z.; Lee, M.-H.; Alvarado, J.; Schroeder, M. A.; Yang, Y.; Lu, B.; Williams, N.; Ceja, M.; Yang, L.; Cai, M.; Gu, J.; Xu, K.; Wang, X.; Meng, Y. S. Quantifying Inactive Lithium in Lithium Metal Batteries. *Nature* **2019**, *572* (7770), 511–515. https://doi.org/10.1038/s41586-019-1481-z.

(42) Walker, W.; Giordani, V.; Uddin, J.; Bryantsev, V. S.; Chase, G. V.; Addison, D. A Rechargeable Li–O_2 Battery Using a Lithium Nitrate/ *N* , *N* -Dimethylacetamide Electrolyte. *Journal of the American Chemical Society* **2013**, *135* (6), 2076–2079. https://doi.org/10.1021/ja311518s.

(43) Cota, L. G.; de la Mora, P. On the Structure of Lithium Peroxide, Li_2O_2. *Acta Crystallogr B Struct Sci* **2005**, *61* (2), 133–136. https://doi.org/10.1107/S0108768105003629.

(44) Chan, M. K. Y.; Shirley, E. L.; Karan, N. K.; Balasubramanian, M.; Ren, Y.; Greeley, J. P.; Fister, T. T. Structure of Lithium Peroxide. *J. Phys. Chem. Lett.* **2011**, *2* (19), 2483–2486. https://doi.org/10.1021/jz201072b.

(45) Wang, F.; Li, X.; Hao, X.; Tan, J. Review and Recent Advances in Mass Transfer in Positive Electrodes of Aprotic Li–O_2 Batteries. *ACS Appl. Energy Mater.* **2020**, *3* (3), 2258–2270. https://doi.org/10.1021/acsaem.9b02237.

(46) Yao, X.; Dong, Q.; Cheng, Q.; Wang, D. Why Do Lithium-Oxygen Batteries Fail: Parasitic Chemical Reactions and Their Synergistic Effect. *Angew. Chem. Int. Ed.* **2016**, *55* (38), 11344–11353. https://doi.org/10.1002/anie.201601783.

(47) Shui, J.-L.; Okasinski, J. S.; Kenesei, P.; Dobbs, H. A.; Zhao, D.; Almer, J. D.; Liu, D.-J. Reversibility of Anodic Lithium in Rechargeable Lithium–Oxygen Batteries. *Nat Commun* **2013**, *4* (1), 2255. https://doi.org/10.1038/ncomms3255.

(48) Sun, F.; Gao, R.; Zhou, D.; Osenberg, M.; Dong, K.; Kardjilov, N.; Hilger, A.; Markötter, H.; Bieker, P. M.; Liu, X.; Manke, I. Revealing Hidden Facts of Li Anode in Cycled Lithium–Oxygen Batteries through X-Ray and Neutron Tomography. *ACS Energy Letters* **2019**, *4* (1), 306–316. https://doi.org/10.1021/acsenergylett.8b02242.

(49) Wang, Y.; Zhou, H. A Lithium-Air Battery with a Potential to Continuously Reduce O2 from Air for Delivering Energy. *Journal of Power Sources* **2010**, *195* (1), 358–361. https://doi.org/10.1016/j.jpowsour.2009.06.109.
(50) Balaish, M.; Leskes, M.; Ein-Eli, Y. Investigation of Rechargeable Poly(Ethylene Oxide)-Based Solid Lithium–Oxygen Batteries. *ACS Applied Energy Materials* **2018**, *1* (7), 3048–3056. https://doi.org/10.1021/acsaem.8b00702.
(51) Huang, Z.; Ren, J.; Zhang, W.; Xie, M.; Li, Y.; Sun, D.; Shen, Y.; Huang, Y. Protecting the Li-Metal Anode in a Li-O_2 Battery by Using Boric Acid as an SEI-Forming Additive. *Advanced Materials* **2018**, *30* (39), 1803270. https://doi.org/10.1002/adma.201803270.
(52) Zhang, X.; Zhang, Q.; Wang, X.-G.; Wang, C.; Chen, Y.-N.; Xie, Z.; Zhou, Z. An Extremely Simple Method for Protecting Lithium Anodes in Li-O_2 Batteries. *Angew. Chem. Int. Ed.* **2018**, *57* (39), 12814–12818. https://doi.org/10.1002/anie.201807985.
(53) Zhang, T.; Liao, K.; He, P.; Zhou, H. A Self-Defense Redox Mediator for Efficient Lithium–O_2 Batteries. *Energy Environ. Sci.* **2016**, *9* (3), 1024–1030. https://doi.org/10.1039/C5EE02803E.
(54) Wu, S.; Yi, J.; Zhu, K.; Bai, S.; Liu, Y.; Qiao, Y.; Ishida, M.; Zhou, H. A Super-Hydrophobic Quasi-Solid Electrolyte for Li-O_2 Battery with Improved Safety and Cycle Life in Humid Atmosphere. *Advanced Energy Materials* **2017**, *7* (4), 1601759. https://doi.org/10.1002/aenm.201601759.
(55) Lim, H.-D.; Song, H.; Kim, J.; Gwon, H.; Bae, Y.; Park, K.-Y.; Hong, J.; Kim, H.; Kim, T.; Kim, Y. H.; Lepró, X.; Ovalle-Robles, R.; Baughman, R. H.; Kang, K. Superior Rechargeability and Efficiency of Lithium-Oxygen Batteries: Hierarchical Air Electrode Architecture Combined with a Soluble Catalyst. *Angewandte Chemie* **2014**, *126* (15), 4007–4012. https://doi.org/10.1002/ange.201400711.
(56) Kwak, W.-J.; Kim, H.; Jung, H.-G.; Aurbach, D.; Sun, Y.-K. Review—A Comparative Evaluation of Redox Mediators for Li-O_2 Batteries: A Critical Review. *J. Electrochem. Soc.* **2018**, *165* (10), A2274–A2293. https://doi.org/10.1149/2.0901810jes.
(57) Balaish, M.; Ein-Eli, Y. Meso-Pores Carbon Nano-Tubes (CNTs) Tissues-Perfluorocarbons (PFCs) Hybrid Air-Electrodes for Li-O2 Battery. *Journal of Power Sources* **2018**, *379*, 219–227. https://doi.org/10.1016/j.jpowsour.2018.01.049.
(58) Balaish, M.; Ein-Eli, Y. Enhancing Oxygen Adsorption Capabilities in Li–O_2 Battery Cathodes through Solid Perfluorocarbons. *Journal of Materials Chemistry A* **2017**, *5* (27), 14152–14164. https://doi.org/10.1039/C7TA03376A.
(59) Huang, J.; Jin, Z.; Xu, Z.-L.; Qin, L.; Huang, H.; Sadighi, Z.; Yao, S.; Cui, J.; Huang, B.; Kim, J.-K. Porous RuO2 Nanosheet/CNT Electrodes for DMSO-Based Li-O2 and Li Ion O2 Batteries. *Energy Storage Materials* **2017**, *8*, 110–118. https://doi.org/10.1016/j.ensm.2017.05.004.
(60) Lee, Y. J.; Park, S. H.; Kim, S. H.; Ko, Y.; Kang, K.; Lee, Y. J. High-Rate and High-Areal-Capacity Air Cathodes with Enhanced Cycle Life Based on RuO_2 /MnO_2 Bifunctional Electrocatalysts Supported on CNT for Pragmatic Li–O_2 Batteries. *ACS Catalysis* **2018**, *8* (4), 2923–2934. https://doi.org/10.1021/acscatal.8b00248.
(61) Xu, P.; Chen, C.; Zhu, J.; Xie, J.; Zhao, P.; Wang, M. RuO2-Particle-Decorated Graphene-Nanoribbon Cathodes for Long-Cycle Li–O2 Batteries. *Journal of Electroanalytical Chemistry* **2019**, *842*, 98–106. https://doi.org/10.1016/j.jelechem.2019.04.055.
(62) Shui, J.; Lin, Y.; Connell, J. W.; Xu, J.; Fan, X.; Dai, L. Nitrogen-Doped Holey Graphene for High-Performance Rechargeable Li–O_2 Batteries. *ACS Energy Letters* **2016**, *1* (1), 260–265. https://doi.org/10.1021/acsenergylett.6b00128.
(63) Xue, H.; Mu, X.; Tang, J.; Fan, X.; Gong, H.; Wang, T.; He, J.; Yamauchi, Y. A Nickel Cobaltate Nanoparticle-Decorated Hierarchical Porous N-Doped Carbon Nanofiber Film as a Binder-Free Self-Supported Cathode for Nonaqueous Li–O_2 Batteries. *Journal of Materials Chemistry A* **2016**, *4* (23), 9106–9112. https://doi.org/10.1039/C6TA01712F.
(64) Liu, J.; Li, D.; Zhang, S.; Wang, Y.; Sun, G.; Wang, Z.; Xie, H.; Sun, L. Hierarchical N-Doped Carbon Nanocages/Carbon Textiles as a Flexible O2 Electrode for Li–O2 Batteries. *Journal of Energy Chemistry* **2020**, *46*, 94–98. https://doi.org/10.1016/j.jechem.2019.10.024.
(65) Ottakam Thotiyl, M. M.; Freunberger, S. A.; Peng, Z.; Bruce, P. G. The Carbon Electrode in Nonaqueous Li–O_2 Cells. *Journal of the American Chemical Society* **2013**, *135* (1), 494–500. https://doi.org/10.1021/ja310258x.
(66) Papp, J. K.; Forster, J. D.; Burke, C. M.; Kim, H. W.; Luntz, A. C.; Shelby, R. M.; Urban, J. J.; McCloskey, B. D. Poly(Vinylidene Fluoride) (PVDF) Binder Degradation in Li–O_2 Batteries: A Consideration for the Characterization of Lithium Superoxide. *The Journal of Physical Chemistry Letters* **2017**, *8* (6), 1169–1174. https://doi.org/10.1021/acs.jpclett.7b00040.
(67) Adams, B. D.; Black, R.; Williams, Z.; Fernandes, R.; Cuisinier, M.; Berg, E. J.; Novak, P.; Murphy, G. K.; Nazar, L. F. Towards a Stable Organic Electrolyte for the Lithium Oxygen Battery. *Adv. Energy Mater.* **2015**, *5* (1), 1400867. https://doi.org/10.1002/aenm.201400867.
(68) Zhang, T. A Lithium-Ion Oxygen Battery with a Si Anode Lithiated in Situ by a Li3N-Containing Cathode. **2018**, 4.
(69) Li, D.; Lang, X.; Guo, Y.; Wang, Y.; Wang, Y.; Shi, H.; Wu, S.; Wang, W.; Yang, Q.-H. A Photo-Assisted Electrocatalyst Coupled with Superoxide Suppression for High Performance Li-O2 Batteries. *Nano Energy* **2021**, *85*, 105966. https://doi.org/10.1016/j.nanoen.2021.105966.
(70) Zhu, Z.; Shi, X.; Fan, G.; Li, F.; Chen, J. Photo-energy Conversion and Storage in an Aprotic Li-O_2 Battery. *Angew. Chem.* **2019**, *131* (52), 19197–19202. https://doi.org/10.1002/ange.201911228.

(71) Yang, X.; Feng, X.; Jin, X.; Shao, M.; Yan, B.; Yan, J.; Zhang, Y.; Zhang, X. An Illumination-Assisted Flexible Self-Powered Energy System Based on a Li–O $_2$ Battery. *Angew. Chem. Int. Ed.* **2019**, *58* (46), 16411–16415. https://doi.org/10.1002/anie.201907805.
(72) Ruggeri, I.; Arbizzani, C.; Soavi, F. Carbonaceous Catholyte for High Energy Density Semi-Solid Li/O2 Flow Battery. *Carbon* **2018**, *130*, 749–757. https://doi.org/10.1016/j.carbon.2018.01.056.
(73) Balaish, M.; Ein-Eli, Y. Meso-Pores Carbon Nano-Tubes (CNTs) Tissues-Perfluorocarbons (PFCs) Hybrid Air-Electrodes for Li-O2 Battery. *Journal of Power Sources* **2018**, *379*, 219–227. https://doi.org/10.1016/j.jpowsour.2018.01.049.
(74) Yin, W.; Grimaud, A.; Azcarate, I.; Yang, C.; Tarascon, J.-M. Electrochemical Reduction of CO $_2$ Mediated by Quinone Derivatives: Implication for Li–CO $_2$ Battery. *J. Phys. Chem. C* **2018**, *122* (12), 6546–6554. https://doi.org/10.1021/acs.jpcc.8b00109.
(75) Temprano, I.; Liu, T.; Petrucco, E.; Ellison, J. H. J.; Kim, G.; Jónsson, E.; Grey, C. P. Toward Reversible and Moisture-Tolerant Aprotic Lithium-Air Batteries. *Joule* **2020**, *4* (11), 2501–2520. https://doi.org/10.1016/j.joule.2020.09.021.
(76) Zhang, Z.; Wu, S.; Yang, C.; Zheng, L.; Xu, D.; Zha, R.; Tang, L.; Cao, K.; Wang, X.; Zhou, Z. Li-N $_2$ Batteries: A Reversible Energy Storage System? *Angew. Chem. Int. Ed.* **2019**, *58* (49), 17782–17787. https://doi.org/10.1002/anie.201911338.
(77) Knipping, E.; Aucher, C.; Guirado, G.; Fauth, F.; Aubouy, L. In Operando X-Ray Diffraction of Lithium–Oxygen Batteries Using an Ionic Liquid as an Electrolyte Co-Solvent. *New Journal of Chemistry* **2017**, *41* (15), 7267–7272. https://doi.org/10.1039/C7NJ01027C.
(78) Gittleson, F. S.; Yao, K. P. C.; Kwabi, D. G.; Sayed, S. Y.; Ryu, W.-H.; Shao-Horn, Y.; Taylor, A. D. Raman Spectroscopy in Lithium-Oxygen Battery Systems. *ChemElectroChem* **2015**, *2* (10), 1446–1457. https://doi.org/10.1002/celc.201500218.
(79) McCloskey, B. D.; Valery, A.; Luntz, A. C.; Gowda, S. R.; Wallraff, G. M.; Garcia, J. M.; Mori, T.; Krupp, L. E. Combining Accurate O $_2$ and Li $_2$ O $_2$ Assays to Separate Discharge and Charge Stability Limitations in Nonaqueous Li–O $_2$ Batteries. *J. Phys. Chem. Lett.* **2013**, *4* (17), 2989–2993. https://doi.org/10.1021/jz401659f.
(80) Bardenhagen, I.; Yezerska, O.; Augustin, M.; Fenske, D.; Wittstock, A.; Bäumer, M. In Situ Investigation of Pore Clogging during Discharge of a Li/O 2 Battery by Electrochemical Impedance Spectroscopy. *Journal of Power Sources* **2015**, *278*, 255–264. https://doi.org/10.1016/j.jpowsour.2014.12.076.
(81) Torayev, A.; Engelke, S.; Su, Z.; Marbella, L. E.; Andrade, V. D.; Demortière, A. Probing and Interpreting the Porosity and Tortuosity Evolution of Li-O2 Cathodes on Discharge through a Combined Experimental and Theoretical Approach. *J. Phys. Chem. C* **2021**, 13.
(82) Pelt, D. M.; Gürsoy, D.; Palenstijn, W. J.; Sijbers, J.; De Carlo, F.; Batenburg, K. J. Integration of TomoPy and the ASTRA Toolbox for Advanced Processing and Reconstruction of Tomographic Synchrotron Data. *Journal of Synchrotron Radiation* **2016**, *23* (3), 842–849. https://doi.org/10.1107/S1600577516005658.
(83) Du, M.; Jacobsen, C. Relative Merits and Limiting Factors for X-Ray and Electron Microscopy of Thick, Hydrated Organic Materials. *Ultramicroscopy* **2018**, *184*, 293–309. https://doi.org/10.1016/j.ultramic.2017.10.003.
(84) Gürsoy, D.; De Carlo, F.; Xiao, X.; Jacobsen, C. TomoPy: A Framework for the Analysis of Synchrotron Tomographic Data. *Journal of Synchrotron Radiation* **2014**, *21* (5), 1188–1193. https://doi.org/10.1107/S1600577514013939.
(85) Liu, S.; Wang, Z.; Yu, C.; Zhao, Z.; Fan, X.; Ling, Z.; Qiu, J. Free-Standing, Hierarchically Porous Carbon Nanotube Film as a Binder-Free Electrode for High-Energy Li–O2 Batteries. *Journal of Materials Chemistry A* **2013**, *1* (39), 12033. https://doi.org/10.1039/c3ta13069j.
(86) Lim, H. D.; Song, H.; Kim, J.; Gwon, H.; Bae, Y.; Park, K. Y.; Hong, J.; Kim, H.; Kim, T.; Kim, Y. H.; Leprõ, X.; Ovalle-Robles, R.; Baughman, R. H.; Kang, K. Superior Rechargeability and Efficiency of Lithium-Oxygen Batteries: Hierarchical Air Electrode Architecture Combined with a Soluble Catalyst. *Angewandte Chemie - International Edition* **2014**, *53* (15), 3926–3931. https://doi.org/10.1002/anie.201400711.
(87) Gaya, C.; Yin, Y.; Torayev, A.; Mammeri, Y.; Franco, A. A. Investigation of Bi-Porous Electrodes for Lithium Oxygen Batteries. *Electrochimica Acta* **2018**, *279*, 118–127. https://doi.org/10.1016/j.electacta.2018.05.056.
(88) Adams, B. D.; Radtke, C.; Black, R.; Trudeau, M. L.; Zaghib, K.; Nazar, L. F. Current Density Dependence of Peroxide Formation in the Li–O2 Battery and Its Effect on Charge. *Energy & Environmental Science* **2013**, *6* (6), 1772. https://doi.org/10.1039/c3ee40697k.
(89) Bardenhagen, I.; Yezerska, O.; Augustin, M.; Fenske, D.; Wittstock, A.; Bäumer, M. In Situ Investigation of Pore Clogging during Discharge of a Li/O 2 Battery by Electrochemical Impedance Spectroscopy. *Journal of Power Sources* **2015**, *278*, 255–264. https://doi.org/10.1016/j.jpowsour.2014.12.076.
(90) Takechi, K.; Singh, N.; Arthur, T. S.; Mizuno, F. Decoupling Energy Storage from Electrochemical Reactions in Li–Air Batteries toward Achieving Continuous Discharge. *ACS Energy Letters* **2017**, *2* (3), 694–699. https://doi.org/10.1021/acsenergylett.7b00056.
(91) Wang, J.; Zhang, Y.; Guo, L.; Wang, E.; Peng, Z. Identifying Reactive Sites and Transport Limitations of Oxygen Reactions in Aprotic Lithium-O 2 Batteries at the Stage of Sudden Death. **2016**, 5201–5205. https://doi.org/10.1002/anie.201600793.
(92) Olivares-Marín, M.; Sorrentino, A.; Lee, R.-C.; Pereiro, E.; Wu, N.-L.; Tonti, D. Spatial Distributions of Discharged Products of Lithium–Oxygen Batteries Revealed by Synchrotron X-Ray Transmission Microscopy. *Nano Letters* **2015**, *15* (10), 6932–6938. https://doi.org/10.1021/acs.nanolett.5b02862.

(93) Dong, H.; Blunt, M. J. Pore-Network Extraction from Micro-Computerized-Tomography Images. *Physical Review E* **2009**, *80* (3). https://doi.org/10.1103/PhysRevE.80.036307.
(94) Torayev, A.; Magusin, P. C. M. M.; Grey, C. P.; Merlet, C.; Franco, A. A. Importance of Incorporating Explicit 3D-Resolved Electrode Mesostructures in Li–O $_2$ Battery Models. *ACS Applied Energy Materials* **2018**, *1* (11), 6433–6441. https://doi.org/10.1021/acsaem.8b01392.
(95) Tan, C.; Heenan, T. M. M.; Ziesche, R. F.; Daemi, S. R.; Hack, J.; Maier, M.; Marathe, S.; Rau, C.; Brett, D. J. L.; Shearing, P. R. Four-Dimensional Studies of Morphology Evolution in Lithium–Sulfur Batteries. *ACS Applied Energy Materials* **2018**, *1* (9), 5090–5100. https://doi.org/10.1021/acsaem.8b01148.
(96) Vanpeene, V.; King, A.; Maire, E.; Roué, L. In Situ Characterization of Si-Based Anodes by Coupling Synchrotron X-Ray Tomography and Diffraction. *Nano Energy* **2019**, *56*, 799–812. https://doi.org/10.1016/j.nanoen.2018.11.079.
(97) Zhong, L.; Mitchell, R. R.; Liu, Y.; Gallant, B. M.; Thompson, C. V; Huang, J. Y.; Mao, S. X.; Shao-horn, Y. In Situ Transmission Electron Microscopy Observations of Electrochemical Oxidation of Li 2 O 2. **2013**. https://doi.org/10.1021/nl400731w.
(98) Leskes, M.; Drewett, N. E.; Hardwick, L. J.; Bruce, P. G.; Goward, G. R.; Grey, C. P. Direct Detection of Discharge Products in Lithium-Oxygen Batteries by Solid-State NMR Spectroscopy. *Angewandte Chemie International Edition* **2012**, *51* (34), 8560–8563. https://doi.org/10.1002/anie.201202183.
(99) Dai, W.; Cui, X.; Zhou, Y.; Zhao, Y.; Wang, L.; Peng, L.; Chen, W. Defect Chemistry in Discharge Products of Li-O $_2$ Batteries. *Small Methods* **2019**, *3* (3), 1800358. https://doi.org/10.1002/smtd.201800358.
(100) CRED—Human Cost of Disasters: An Overview of the Last 20 Years (2000-2019).
(101) Yu, A.; Sumangil, M. Top electric vehicle markets dominate lithium-ion battery capacity growth https://www.spglobal.com/marketintelligence/en/news-insights/blog/top-electric-vehicle-markets-dominate-lithium-ion-battery-capacity-growth.
(102) Richa, K.; Babbitt, C. W.; Gaustad, G.; Wang, X. A Future Perspective on Lithium-Ion Battery Waste Flows from Electric Vehicles. *Resources, Conservation and Recycling* **2014**, *83*, 63–76. https://doi.org/10.1016/j.resconrec.2013.11.008.
(103) Mayyas, A.; Steward, D.; Mann, M. The Case for Recycling: Overview and Challenges in the Material Supply Chain for Automotive Li-Ion Batteries. *Sustainable Materials and Technologies* **2019**, *19*, e00087. https://doi.org/10.1016/j.susmat.2018.e00087.
(104) Arshad, F.; Li, L.; Amin, K.; Fan, E.; Manurkar, N.; Ahmad, A.; Yang, J.; Wu, F.; Chen, R. A Comprehensive Review of the Advancement in Recycling the Anode and Electrolyte from Spent Lithium Ion Batteries. *ACS Sustainable Chem. Eng.* **2020**, *8* (36), 13527–13554. https://doi.org/10.1021/acssuschemeng.0c04940.
(105) Armand, M.; Tarascon, J.-M. Building Better Batteries. *Nature* **2008**, *451* (7179), 652–657. https://doi.org/10.1038/451652a.
(106) Larcher, D.; Tarascon, J.-M. Towards Greener and More Sustainable Batteries for Electrical Energy Storage. *Nature Chemistry* **2015**, *7* (1), 19–29. https://doi.org/10.1038/nchem.2085.
(107) Harlow, J. E.; Ma, X.; Li, J.; Logan, E.; Liu, Y.; Zhang, N.; Ma, L.; Glazier, S. L.; Cormier, M. M. E.; Genovese, M.; Buteau, S.; Cameron, A.; Stark, J. E.; Dahn, J. R. A Wide Range of Testing Results on an Excellent Lithium-Ion Cell Chemistry to Be Used as Benchmarks for New Battery Technologies. *J. Electrochem. Soc.* **2019**, *166* (13), A3031–A3044. https://doi.org/10.1149/2.0981913jes.
(108) Bruce, P. G.; Freunberger, S. A.; Hardwick, L. J.; Tarascon, J.-M. Li–O2 and Li–S Batteries with High Energy Storage. *Nature Materials* **2012**, *11* (1), 19–29. https://doi.org/10.1038/nmat3191.
(109) Lu, J.; Li, L.; Park, J.-B.; Sun, Y.-K.; Wu, F.; Amine, K. Aprotic and Aqueous Li–O $_2$ Batteries. *Chemical Reviews* **2014**, *114* (11), 5611–5640. https://doi.org/10.1021/cr400573b.
(110) Su, Z.; De Andrade, V.; Cretu, S.; Yin, Y.; Wojcik, M. J.; Franco, A. A.; Demortière, A. X-Ray Nanocomputed Tomography in Zernike Phase Contrast for Studying 3D Morphology of Li–O $_2$ Battery Electrode. *ACS Applied Energy Materials* **2020**, *3* (5), 4093–4102. https://doi.org/10.1021/acsaem.9b02236.
(111) Zhang, H.; Eshetu, G. G.; Judez, X.; Li, C.; Rodriguez-Martínez, L. M.; Armand, M. Electrolyte Additives for Lithium Metal Anodes and Rechargeable Lithium Metal Batteries: Progress and Perspectives. *Angewandte Chemie International Edition* **2018**, *57* (46), 15002–15027. https://doi.org/10.1002/anie.201712702.
(112) Lu, J.; Jung Lee, Y.; Luo, X.; Chun Lau, K.; Asadi, M.; Wang, H.-H.; Brombosz, S.; Wen, J.; Zhai, D.; Chen, Z.; Miller, D. J.; Sub Jeong, Y.; Park, J.-B.; Zak Fang, Z.; Kumar, B.; Salehi-Khojin, A.; Sun, Y.-K.; Curtiss, L. A.; Amine, K. A Lithium–Oxygen Battery Based on Lithium Superoxide. *Nature* **2016**, *529* (7586), 377–382. https://doi.org/10.1038/nature16484.
(113) Halder, A.; Wang, H.-H.; Lau, K. C.; Assary, R. S.; Lu, J.; Vajda, S.; Amine, K.; Curtiss, L. A. Identification and Implications of Lithium Superoxide in Li–O $_2$ Batteries. *ACS Energy Letters* **2018**, *3* (5), 1105–1109. https://doi.org/10.1021/acsenergylett.8b00385.
(114) Liu, T.; Kim, G.; Jónsson, E.; Castillo-Martinez, E.; Temprano, I.; Shao, Y.; Carretero-González, J.; Kerber, R. N.; Grey, C. P. Understanding LiOH Formation in a Li-O $_2$ Battery with LiI and H $_2$ O Additives. *ACS Catal.* **2019**, *9* (1), 66–77. https://doi.org/10.1021/acscatal.8b02783.
(115) Liu, T.; Leskes, M.; Yu, W.; Moore, A. J.; Zhou, L.; Bayley, P. M.; Kim, G.; Grey, C. P. Cycling Li-O2 Batteries via LiOH Formation and Decomposition. *Science* **2015**, *350* (6260), 530–533. https://doi.org/10.1126/science.aac7730.

(116) Wandt, J.; Jakes, P.; Granwehr, J.; Gasteiger, H. A.; Eichel, R.-A. Singlet Oxygen Formation during the Charging Process of an Aprotic Lithium-Oxygen Battery. *Angew. Chem.* **2016**, *128* (24), 7006–7009. https://doi.org/10.1002/ange.201602142.

(117) Mahne, N.; Schafzahl, B.; Leypold, C.; Leypold, M.; Grumm, S.; Leitgeb, A.; Strohmeier, G. A.; Wilkening, M.; Fontaine, O.; Kramer, D.; Slugovc, C.; Borisov, S. M.; Freunberger, S. A. Singlet Oxygen Generation as a Major Cause for Parasitic Reactions during Cycling of Aprotic Lithium–Oxygen Batteries. *Nat Energy* **2017**, *2* (5), 17036. https://doi.org/10.1038/nenergy.2017.36.

(118) Luntz, A. C.; McCloskey, B. D. Li–Air Batteries: Importance of Singlet Oxygen. *Nat Energy* **2017**, *2* (5), 17056. https://doi.org/10.1038/nenergy.2017.56.

(119) Black, R.; Oh, S. H.; Lee, J.-H.; Yim, T.; Adams, B.; Nazar, L. F. Screening for Superoxide Reactivity in Li-O_2 Batteries: Effect on Li_2O_2/LiOH Crystallization. *J. Am. Chem. Soc.* **2012**, *134* (6), 2902–2905. https://doi.org/10.1021/ja2111543.

(120) Wu, H.; Sun, W.; Wang, Y.; Wang, F.; Liu, J.; Yue, X.; Wang, Z.; Qiao, J.; Rooney, D. W.; Sun, K. Facile Synthesis of Hierarchical Porous Three-Dimensional Free-Standing $MnCo_2O_4$ Cathodes for Long-Life Li—O_2 Batteries. *ACS Applied Materials & Interfaces* **2017**, *9* (14), 12355–12365. https://doi.org/10.1021/acsami.6b16090.

(121) Chen, Y.; Li, F.; Tang, D.-M.; Jian, Z.; Liu, C.; Golberg, D.; Yamada, A.; Zhou, H. Multi-Walled Carbon Nanotube Papers as Binder-Free Cathodes for Large Capacity and Reversible Non-Aqueous Li–O2 Batteries. *Journal of Materials Chemistry A* **2013**, *1* (42), 13076. https://doi.org/10.1039/c3ta11792h.

(122) Kim, D. Y.; Kim, M.; Kim, D. W.; Suk, J.; Park, O. O.; Kang, Y. Flexible Binder-Free Graphene Paper Cathodes for High-Performance Li-O2 Batteries. *Carbon* **2015**, *93*, 625–635. https://doi.org/10.1016/j.carbon.2015.05.097.

(123) Li, F.; Chen, Y.; Tang, D.-M.; Jian, Z.; Liu, C.; Golberg, D.; Yamada, A.; Zhou, H. Performance-Improved Li–O_2 Battery with Ru Nanoparticles Supported on Binder-Free Multi-Walled Carbon Nanotube Paper as Cathode. *Energy Environ. Sci.* **2014**, *7* (5), 1648–1652. https://doi.org/10.1039/C3EE44043E.

(124) Li, K.; Dong, H.; Wang, Y.; Yin, Y.; Yang, S. Preparation of Low-Load Au-Pd Alloy Decorated Carbon Fibers Binder-Free Cathode for Li-O2 Battery. *Journal of Colloid and Interface Science* **2020**, *579*, 448–454. https://doi.org/10.1016/j.jcis.2020.06.084.

(125) Yu, Y.; Huang, G.; Du, J.-Y.; Wang, J.-Z.; Wang, Y.; Wu, Z.-J.; Zhang, X.-B. A Renaissance of *N* , *N* -Dimethylacetamide-Based Electrolytes to Promote the Cycling Stability of Li–O_2 Batteries. *Energy Environ. Sci.* **2020**, *13* (9), 3075–3081. https://doi.org/10.1039/D0EE01897J.

(126) Lepoivre, F.; Grimaud, A.; Larcher, D.; Tarascon, J.-M. Long-Time and Reliable Gas Monitoring in Li-O_2 Batteries via a Swagelok Derived Electrochemical Cell. *Journal of The Electrochemical Society* **2016**, *163* (6), A923–A929. https://doi.org/10.1149/2.0421606jes.

(127) Shin, H.-J.; Kwak, W.-J.; Aurbach, D.; Sun, Y.-K. Large-Scale Li□O_2 Pouch Type Cells for Practical Evaluation and Applications. *Adv. Funct. Mater.* **2017**, *27* (11), 1605500. https://doi.org/10.1002/adfm.201605500.

(128) Ben Osman, M.; Yin, W.; Petenzi, T.; Jousselme, B.; Cornut, R.; Raymundo-Pinero, E.; Grimaud, A.; Robert, C. L. Electrospun Carbon Fibers as Air Cathodes for Aprotic Li–O2 Battery: Towards Cathode Design for Enhanced Capacity. *Electrochimica Acta* **2020**, *354*, 136643. https://doi.org/10.1016/j.electacta.2020.136643.

(129) Lee, E.; Salgado, R. A.; Lee, B.; Sumant, A. V.; Rajh, T.; Johnson, C.; Balandin, A. A.; Shevchenko, E. V. Design of Lithium Cobalt Oxide Electrodes with High Thermal Conductivity and Electrochemical Performance Using Carbon Nanotubes and Diamond Particles. *Carbon* **2018**, *129*, 702–710. https://doi.org/10.1016/j.carbon.2017.12.061.

(130) Jaiser, S.; Müller, M.; Baunach, M.; Bauer, W.; Scharfer, P.; Schabel, W. Investigation of Film Solidification and Binder Migration during Drying of Li-Ion Battery Anodes. *Journal of Power Sources* **2016**, *318*, 210–219. https://doi.org/10.1016/j.jpowsour.2016.04.018.

(131) Liu, Y.; Zhang, R.; Wang, J.; Wang, Y. Current and Future Lithium-Ion Battery Manufacturing. *iScience* **2021**, *24* (4), 102332. https://doi.org/10.1016/j.isci.2021.102332.

(132) Shui, J.-L.; Wang, H.-H.; Liu, D.-J. Degradation and Revival of Li–O2 Battery Cathode. *Electrochemistry Communications* **2013**, *34*, 45–47. https://doi.org/10.1016/j.elecom.2013.05.020.

(133) Chen, X.; Chen, Y.; Zhou, T.; Liu, D.; Hu, H.; Fan, S. Hydrometallurgical Recovery of Metal Values from Sulfuric Acid Leaching Liquor of Spent Lithium-Ion Batteries. *Waste Management* **2015**, *38*, 349–356. https://doi.org/10.1016/j.wasman.2014.12.023.

(134) Yao, Y.; Zhu, M.; Zhao, Z.; Tong, B.; Fan, Y.; Hua, Z. Hydrometallurgical Processes for Recycling Spent Lithium-Ion Batteries: A Critical Review. *ACS Sustainable Chem. Eng.* **2018**, *6* (11), 13611–13627. https://doi.org/10.1021/acssuschemeng.8b03545.

(135) Yermukhambetova, A.; Tan, C.; Daemi, S. R.; Bakenov, Z.; Darr, J. A.; Brett, D. J. L.; Shearing, P. R. Exploring 3D Microstructural Evolution in Li-Sulfur Battery Electrodes Using in-Situ X-Ray Tomography. *Scientific Reports* **2016**, *6* (1). https://doi.org/10.1038/srep35291.

(136) Tan, C.; Heenan, T. M. M.; Ziesche, R. F.; Daemi, S. R.; Hack, J.; Maier, M.; Marathe, S.; Rau, C.; Brett, D. J. L.; Shearing, P. R. Four-Dimensional Studies of Morphology Evolution in Lithium–Sulfur Batteries. *ACS Applied Energy Materials* **2018**, *1* (9), 5090–5100. https://doi.org/10.1021/acsaem.8b01148.

(137) Zielke, L.; Barchasz, C.; Waluś, S.; Alloin, F.; Leprêtre, J.-C.; Spettl, A.; Schmidt, V.; Hilger, A.; Manke, I.; Banhart, J.; Zengerle, R.; Thiele, S. Degradation of Li/S Battery Electrodes On 3D Current Collectors Studied Using X-Ray Phase Contrast Tomography. *Scientific Reports* **2015**, *5* (1). https://doi.org/10.1038/srep10921.

(138) Tonin, G.; Vaughan, G.; Bouchet, R.; Alloin, F.; Di Michiel, M.; Boutafa, L.; Colin, J.-F.; Barchasz, C. Multiscale Characterization of a Lithium/Sulfur Battery by Coupling Operando X-Ray Tomography and Spatially-Resolved Diffraction. *Scientific Reports* **2017**, *7* (1). https://doi.org/10.1038/s41598-017-03004-4.

(139) Pietsch, P.; Hess, M.; Ludwig, W.; Eller, J.; Wood, V. Combining Operando Synchrotron X-Ray Tomographic Microscopy and Scanning X-Ray Diffraction to Study Lithium Ion Batteries. *Scientific Reports* **2016**, *6* (1). https://doi.org/10.1038/srep27994.

(140) Vanpeene, V.; Etiemble, A.; Bonnin, A.; Maire, E.; Roué, L. In-Situ X-Ray Tomographic Study of the Morphological Changes of a Si/C Paper Anode for Li-Ion Batteries. *Journal of Power Sources* **2017**, *350*, 18–27. https://doi.org/10.1016/j.jpowsour.2017.03.044.

(141) Vanpeene, V.; Villanova, J.; King, A.; Lestriez, B.; Maire, E.; Roué, L. Dynamics of the Morphological Degradation of Si-Based Anodes for Li-Ion Batteries Characterized by In Situ Synchrotron X-Ray Tomography. *Advanced Energy Materials* **2019**, *9* (18), 1803947. https://doi.org/10.1002/aenm.201803947.

(142) Vanpeene, V.; Villanova, J.; Suuronen, J.-P.; King, A.; Bonnin, A.; Adrien, J.; Maire, E.; Roué, L. Monitoring the Morphological Changes of Si-Based Electrodes by X-Ray Computed Tomography: A 4D-Multiscale Approach. *Nano Energy* **2020**, *74*, 104848. https://doi.org/10.1016/j.nanoen.2020.104848.

(143) Lewis, J.; Cortes, F. J. Q.; Liu, Y.; Miers, J. C.; Verma, A.; Vishnugopi, B. S.; Tippens, J.; prakash, dhruv; Marchese, T. S.; Han, S. Y.; Lee, C.; Lee, H.-W.; Shevchenko, P.; Carlo, F. D.; Saldana, C.; Mukherjee, P. P.; McDowell, M. T. *Linking Void and Interphase Evolution to Electrochemistry in Solid-State Batteries Using Operando X-Ray Tomography*; preprint; 2020. https://doi.org/10.26434/chemrxiv.12468170.v1.

(144) Wang, J.; Eng, C.; Chen-Wiegart, Y. K.; Wang, J. Probing Three-Dimensional Sodiation–Desodiation Equilibrium in Sodium-Ion Batteries by in Situ Hard X-Ray Nanotomography. *Nature Communications* **2015**, *6* (1). https://doi.org/10.1038/ncomms8496.

(145) Wang, J.; Chen-Wiegart, Y. K.; Wang, J. In Situ Three-Dimensional Synchrotron X-Ray Nanotomography of the (De)Lithiation Processes in Tin Anodes. *Angew. Chem. Int. Ed.* **2014**, 5.

(146) Li, T.; Zhou, X.; Cui, Y.; Meyerson, M. L.; Mullins, C. B.; Andrade, V. D.; Carlo, D.; Liu, Y.; Zhu, L. In Situ Characterization of Dynamic Morphological and Phase Changes of Selenium-doped Germanium Using a Single Particle Cell and Synchrotron Transmission X-ray Microscopy. 25.

(147) Rahman, Md. A.; Wang, X.; Wen, C. High Energy Density Metal-Air Batteries: A Review. *Journal of The Electrochemical Society* **2013**, *160* (10), A1759–A1771. https://doi.org/10.1149/2.062310jes.

(148) Wang, H.-F.; Xu, Q. Materials Design for Rechargeable Metal-Air Batteries. *Matter* **2019**, *1* (3), 565–595. https://doi.org/10.1016/j.matt.2019.05.008.

(149) Schröder, D.; Bender, C. L.; Osenberg, M.; Hilger, A.; Manke, I.; Janek, J. Visualizing Current-Dependent Morphology and Distribution of Discharge Products in Sodium-Oxygen Battery Cathodes. *Scientific Reports* **2016**, *6* (1). https://doi.org/10.1038/srep24288.

(150) Schröder, D.; Arlt, T.; Krewer, U.; Manke, I. Analyzing Transport Paths in the Air Electrode of a Zinc Air Battery Using X-Ray Tomography. *Electrochemistry Communications* **2014**, *40*, 88–91. https://doi.org/10.1016/j.elecom.2014.01.001.

(151) Arlt, T.; Schröder, D.; Krewer, U.; Manke, I. *In Operando* Monitoring of the State of Charge and Species Distribution in Zinc Air Batteries Using X-Ray Tomography and Model-Based Simulations. *Phys. Chem. Chem. Phys.* **2014**, *16* (40), 22273–22280. https://doi.org/10.1039/C4CP02878C.

(152) Franke-Lang, R.; Arlt, T.; Manke, I.; Kowal, J. X-Ray Tomography as a Powerful Method for Zinc-Air Battery Research. *Journal of Power Sources* **2017**, *370*, 45–51. https://doi.org/10.1016/j.jpowsour.2017.10.010.

(153) Sun, F.; Gao, R.; Zhou, D.; Osenberg, M.; Dong, K.; Kardjilov, N.; Hilger, A.; Markötter, H.; Bieker, P. M.; Liu, X.; Manke, I. Revealing Hidden Facts of Li Anode in Cycled Lithium–Oxygen Batteries through X-Ray and Neutron Tomography. *ACS Energy Letters* **2019**, *4* (1), 306–316. https://doi.org/10.1021/acsenergylett.8b02242.

(154) Goris, B.; Van den Broek, W.; Batenburg, K. J.; Heidari Mezerji, H.; Bals, S. Electron Tomography Based on a Total Variation Minimization Reconstruction Technique. *Ultramicroscopy* **2012**, *113*, 120–130. https://doi.org/10.1016/j.ultramic.2011.11.004.

(155) Ding, G.; Liu, Y.; Zhang, R.; Xin, H. L. A Joint Deep Learning Model to Recover Information and Reduce Artifacts in Missing-Wedge Sinograms for Electron Tomography and Beyond. *Scientific Reports* **2019**, *9* (1). https://doi.org/10.1038/s41598-019-49267-x.

(156) Huang, Y.; Wang, S.; Guan, Y.; Maier, A. Limited Angle Tomography for Transmission X-Ray Microscopy Using Deep Learning. *arXiv:2001.02469 [cs, eess, stat]* **2020**.

(157) Huang, Y.; Würfl, T.; Breininger, K.; Liu, L.; Lauritsch, G.; Maier, A. Some Investigations on Robustness of Deep Learning in Limited Angle Tomography. In *Medical Image Computing and Computer Assisted Intervention – MICCAI 2018*; Frangi, A. F., Schnabel, J. A., Davatzikos, C., Alberola-López, C., Fichtinger, G., Eds.; Lecture Notes in Computer Science; Springer International Publishing: Cham, 2018; Vol. 11070, pp 145–153. https://doi.org/10.1007/978-3-030-00928-1_17.

(158) Zhang, H.; Li, L.; Qiao, K.; Wang, L.; Yan, B.; Li, L.; Hu, G. Image Prediction for Limited-Angle Tomography via Deep Learning with Convolutional Neural Network. 21.

(159) Huang, Y.; Huang, X.; Taubmann, O.; Xia, Y.; Haase, V.; Hornegger, J.; Lauritsch, G.; Maier, A. Restoration of Missing Data in Limited Angle Tomography Based on Helgason–Ludwig Consistency Conditions. *Biomedical Physics & Engineering Express* **2017**, *3* (3), 035015. https://doi.org/10.1088/2057-1976/aa71bf.
(160) Bak, S.-M. In Situ/Operando Synchrotron-Based X-Ray Techniques for Lithium-Ion Battery Research. **2018**, 18.
(161) Xia, M.; Liu, T.; Peng, N.; Zheng, R.; Cheng, X.; Zhu, H.; Yu, H.; Shui, M.; Shu, J. Lab-Scale In Situ X-Ray Diffraction Technique for Different Battery Systems: Designs, Applications, and Perspectives. *Small Methods* **2019**, *3* (7), 1900119. https://doi.org/10.1002/smtd.201900119.
(162) Schoonjans, T.; Brunetti, A.; Golosio, B.; Sanchez del Rio, M.; Solé, V. A.; Ferrero, C.; Vincze, L. The Xraylib Library for X-Ray–Matter Interactions. Recent Developments. *Spectrochimica Acta Part B: Atomic Spectroscopy* **2011**, *66* (11–12), 776–784. https://doi.org/10.1016/j.sab.2011.09.011.
(163) Henke, B. L.; Gulikson, E. M.; Davis, J. C. X-Ray Interactions: Photoabsorption, Scattering, Transmission, and Reflection at E=50-30000 EV, Z=1-92. Atomic Data and Nuclear Data Tables July 1993.
(164) Henke, B. L. Https://Henke.Lbl.Gov/Optical_constants/Filter2.Html.
(165) Bailey, J. J.; Heenan, T. M. M.; Finegan, D. P.; Lu, X.; Daemi, S. R.; Iacoviello, F.; Backeberg, N. R.; Taiwo, O. O.; Brett, D. J. L.; Atkinson, A.; Shearing, P. R. Laser-Preparation of Geometrically Optimised Samples for X-Ray Nano-CT: LASER-PREPARATION OF GEOMETRICALLY OPTIMISED SAMPLES FOR X-RAY NANO-CT. *Journal of Microscopy* **2017**, *267* (3), 384–396. https://doi.org/10.1111/jmi.12577.
(166) Gürsoy, D.; De Carlo, F.; Xiao, X.; Jacobsen, C. TomoPy: A Framework for the Analysis of Synchrotron Tomographic Data. *Journal of Synchrotron Radiation* **2014**, *21* (5), 1188–1193. https://doi.org/10.1107/S1600577514013939.
(167) Ebner, M.; Chung, D.-W.; García, R. E.; Wood, V. Tortuosity Anisotropy in Lithium-Ion Battery Electrodes. *Advanced Energy Materials* **2014**, *4* (5), 1301278. https://doi.org/10.1002/aenm.201301278.
(168) Finegan, D. P.; Scheel, M.; Robinson, J. B.; Tjaden, B.; Hunt, I.; Mason, T. J.; Millichamp, J.; Di Michiel, M.; Offer, G. J.; Hinds, G.; Brett, D. J. L.; Shearing, P. R. In-Operando High-Speed Tomography of Lithium-Ion Batteries during Thermal Runaway. *Nature Communications* **2015**, *6* (1). https://doi.org/10.1038/ncomms7924.
(169) Pietsch, P.; Wood, V. X-Ray Tomography for Lithium Ion Battery Research: A Practical Guide. *Annual Review of Materials Research* **2017**, *47* (1), 451–479. https://doi.org/10.1146/annurev-matsci-070616-123957.
(170) Müller, S.; Lippuner, M.; Verezhak, M.; De Andrade, V.; De Carlo, F.; Wood, V. Multimodal Nanoscale Tomographic Imaging for Battery Electrodes. *Advanced Energy Materials* **2020**, *10* (28), 1904119. https://doi.org/10.1002/aenm.201904119.
(171) Pietsch, P.; Westhoff, D.; Feinauer, J.; Eller, J.; Marone, F.; Stampanoni, M.; Schmidt, V.; Wood, V. Quantifying Microstructural Dynamics and Electrochemical Activity of Graphite and Silicon-Graphite Lithium Ion Battery Anodes. *Nature Communications* **2016**, *7* (1). https://doi.org/10.1038/ncomms12909.
(172) Yu, Y.-S.; Farmand, M.; Kim, C.; Liu, Y.; Grey, C. P.; Strobridge, F. C.; Tyliszczak, T.; Celestre, R.; Denes, P.; Joseph, J.; Krishnan, H.; Maia, F. R. N. C.; Kilcoyne, A. L. D.; Marchesini, S.; Leite, T. P. C.; Warwick, T.; Padmore, H.; Cabana, J.; Shapiro, D. A. Three-Dimensional Localization of Nanoscale Battery Reactions Using Soft X-Ray Tomography. *Nature Communications* **2018**, *9* (1). https://doi.org/10.1038/s41467-018-03401-x.
(173) Eastwood, D. S.; Yufit, V.; Gelb, J.; Gu, A.; Bradley, R. S.; Harris, S. J.; Brett, D. J. L.; Brandon, N. P.; Lee, P. D.; Withers, P. J.; Shearing, P. R. Lithiation-Induced Dilation Mapping in a Lithium-Ion Battery Electrode by 3D X-Ray Microscopy and Digital Volume Correlation. *Advanced Energy Materials* **2014**, *4* (4), 1300506. https://doi.org/10.1002/aenm.201300506.
(174) Vanpeene, V.; King, A.; Maire, E.; Roué, L. In Situ Characterization of Si-Based Anodes by Coupling Synchrotron X-Ray Tomography and Diffraction. *Nano Energy* **2019**, *56*, 799–812. https://doi.org/10.1016/j.nanoen.2018.11.079.
(175) Nguyen, T.-T.; Demortière, A.; Fleutot, B.; Delobel, B.; Delacourt, C.; Cooper, S. J. The Electrode Tortuosity Factor: Why the Conventional Tortuosity Factor Is Not Well Suited for Quantifying Transport in Porous Li-Ion Battery Electrodes and What to Use Instead. *npj Computational Materials* **2020**, *6* (1). https://doi.org/10.1038/s41524-020-00386-4.
(176) Müller, S.; Eller, J.; Ebner, M.; Burns, C.; Dahn, J.; Wood, V. Quantifying Inhomogeneity of Lithium Ion Battery Electrodes and Its Influence on Electrochemical Performance. *Journal of The Electrochemical Society* **2018**, *165* (2), A339–A344. https://doi.org/10.1149/2.0311802jes.
(177) Chouchane, M.; Rucci, A.; Lombardo, T.; Ngandjong, A. C.; Franco, A. A. Lithium Ion Battery Electrodes Predicted from Manufacturing Simulations: Assessing the Impact of the Carbon-Binder Spatial Location on the Electrochemical Performance. *Journal of Power Sources* **2019**, *444*, 227285. https://doi.org/10.1016/j.jpowsour.2019.227285.
(178) Shodiev, A.; Primo, E. N.; Chouchane, M.; Lombardo, T.; Ngandjong, A. C.; Rucci, A.; Franco, A. A. 4D-Resolved Physical Model for Electrochemical Impedance Spectroscopy of Li(Ni1-x-YMnxCoy)O2-Based Cathodes in Symmetric Cells: Consequences in Tortuosity Calculations. *Journal of Power Sources* **2020**, *454*, 227871. https://doi.org/10.1016/j.jpowsour.2020.227871.
(179) Lu, X.; Bertei, A.; Finegan, D. P.; Tan, C.; Daemi, S. R.; Weaving, J. S.; O'Regan, K. B.; Heenan, T. M. M.; Hinds, G.; Kendrick, E.; Brett, D. J. L.; Shearing, P. R. 3D Microstructure Design of Lithium-Ion Battery Electrodes Assisted by X-Ray Nano-Computed Tomography and Modelling. *Nature Communications* **2020**, *11* (1). https://doi.org/10.1038/s41467-020-15811-x.

(180) Pietsch, P.; Ebner, M.; Marone, F.; Stampanoni, M.; Wood, V. Determining the Uncertainty in Microstructural Parameters Extracted from Tomographic Data. *Sustainable Energy & Fuels* **2018**, *2* (3), 598–605. https://doi.org/10.1039/C7SE00498B.
(181) Arganda-Carreras, I.; Kaynig, V.; Rueden, C.; Eliceiri, K. W.; Schindelin, J.; Cardona, A.; Sebastian Seung, H. Trainable Weka Segmentation: A Machine Learning Tool for Microscopy Pixel Classification. *Bioinformatics* **2017**, *33* (15), 2424–2426. https://doi.org/10.1093/bioinformatics/btx180.
(182) Berg, S.; Kutra, D.; Kroeger, T.; Straehle, C. N.; Kausler, B. X.; Haubold, C.; Schiegg, M.; Ales, J.; Beier, T.; Rudy, M.; Eren, K.; Cervantes, J. I.; Xu, B.; Beuttenmueller, F.; Wolny, A.; Zhang, C.; Koethe, U.; Hamprecht, F. A.; Kreshuk, A. Ilastik: Interactive Machine Learning for (Bio)Image Analysis. *Nature Methods* **2019**, *16* (12), 1226–1232. https://doi.org/10.1038/s41592-019-0582-9.
(183) Demir, I.; Koperski, K.; Lindenbaum, D.; Pang, G.; Huang, J.; Basu, S.; Hughes, F.; Tuia, D.; Raskar, R. DeepGlobe 2018: A Challenge to Parse the Earth through Satellite Images. *2018 IEEE/CVF Conference on Computer Vision and Pattern Recognition Workshops (CVPRW)* **2018**, 172–17209. https://doi.org/10.1109/CVPRW.2018.00031.
(184) Tuccillo, D.; Huertas-Company, M.; Decencière, E.; Velasco-Forero, S.; Sánchez, H. D.; Dimauro, P. Deep Learning for Galaxy Surface Brightness Profile Fitting. *Monthly Notices of the Royal Astronomical Society* **2018**, *475* (1), 894–909. https://doi.org/10.1093/mnras/stx3186.
(185) Taigman, Y.; Yang, M.; Ranzato, M.; Wolf, L. DeepFace: Closing the Gap to Human-Level Performance in Face Verification. In *2014 IEEE Conference on Computer Vision and Pattern Recognition*; IEEE: Columbus, OH, USA, 2014; pp 1701–1708. https://doi.org/10.1109/CVPR.2014.220.
(186) Bochkovskiy, A.; Wang, C.-Y.; Liao, H.-Y. M. YOLOv4: Optimal Speed and Accuracy of Object Detection. *arXiv:2004.10934 [cs, eess]* **2020**.
(187) Badrinarayanan, V.; Kendall, A.; Cipolla, R. SegNet: A Deep Convolutional Encoder-Decoder Architecture for Image Segmentation. *IEEE Transactions on Pattern Analysis and Machine Intelligence* **2017**, *39* (12), 2481–2495. https://doi.org/10.1109/TPAMI.2016.2644615.
(188) Geurts, P.; Irrthum, A.; Wehenkel, L. Supervised Learning with Decision Tree-Based Methods in Computational and Systems Biology. *Molecular BioSystems* **2009**, *5* (12), 1593. https://doi.org/10.1039/b907946g.
(189) Ronneberger, O.; Fischer, P.; Brox, T. U-Net: Convolutional Networks for Biomedical Image Segmentation. *arXiv:1505.04597 [cs]* **2015**.
(190) Shashank Kaira, C.; Yang, X.; De Andrade, V.; De Carlo, F.; Scullin, W.; Gursoy, D.; Chawla, N. Automated Correlative Segmentation of Large Transmission X-Ray Microscopy (TXM) Tomograms Using Deep Learning. *Materials Characterization* **2018**, *142*, 203–210. https://doi.org/10.1016/j.matchar.2018.05.053.
(191) Tekawade, A.; Sforzo, B. A.; Matusik, K. E.; Kastengren, A. L.; Powell, C. F. High-Fidelity Geometry Generation from CT Data Using Convolutional Neural Networks. In *Developments in X-Ray Tomography XII*; Müller, B., Wang, G., Eds.; SPIE: San Diego, United States, 2019; p 67. https://doi.org/10.1117/12.2540442.
(192) Simpson, A. L.; Antonelli, M.; Bakas, S.; Bilello, M.; Farahani, K.; van Ginneken, B.; Kopp-Schneider, A.; Landman, B. A.; Litjens, G.; Menze, B.; Ronneberger, O.; Summers, R. M.; Bilic, P.; Christ, P. F.; Do, R. K. G.; Gollub, M.; Golia-Pernicka, J.; Heckers, S. H.; Jarnagin, W. R.; McHugo, M. K.; Napel, S.; Vorontsov, E.; Maier-Hein, L.; Cardoso, M. J. A Large Annotated Medical Image Dataset for the Development and Evaluation of Segmentation Algorithms. *arXiv:1902.09063 [cs, eess]* **2019**.
(193) Jiang, Z.; Li, J.; Yang, Y.; Mu, L.; Wei, C.; Yu, X.; Pianetta, P.; Zhao, K.; Cloetens, P.; Lin, F.; Liu, Y. Machine-Learning-Revealed Statistics of the Particle-Carbon/Binder Detachment in Lithium-Ion Battery Cathodes. *Nature Communications* **2020**, *11* (1). https://doi.org/10.1038/s41467-020-16233-5.
(194) LaBonte, T.; Martinez, C.; Roberts, S. A. We Know Where We Don't Know: 3D Bayesian CNNs for Uncertainty Quantification of Binary Segmentations for Material Simulations. *arXiv:1910.10793 [cs, eess]* **2019**.
(195) Ioffe, S.; Szegedy, C. Batch Normalization: Accelerating Deep Network Training by Reducing Internal Covariate Shift. In *Proceedings of the 32nd International Conference on Machine Learning*; Bach, F., Blei, D., Eds.; Proceedings of Machine Learning Research; PMLR: Lille, France, 2015; Vol. 37, pp 448–456.
(196) Wu, Y.; He, K. Group Normalization. *International Journal of Computer Vision* **2020**, *128* (3), 742–755. https://doi.org/10.1007/s11263-019-01198-w.
(197) Glorot, X.; Bengio, Y. Understanding the Difficulty of Training Deep Feedforward Neural Networks. 8.
(198) Kingma, D. P.; Ba, J. Adam: A Method for Stochastic Optimization. In *3rd International Conference on Learning Representations, ICLR 2015, San Diego, CA, USA, May 7-9, 2015, Conference Track Proceedings*; Bengio, Y., LeCun, Y., Eds.; 2015.
(199) Ruder, S. An Overview of Gradient Descent Optimization Algorithms. *arXiv:1609.04747 [cs]* **2017**.
(200) De Carlo, F.; Gürsoy, D.; Ching, D. J.; Batenburg, K. J.; Ludwig, W.; Mancini, L.; Marone, F.; Mokso, R.; Pelt, D. M.; Sijbers, J.; Rivers, M. TomoBank: A Tomographic Data Repository for Computational x-Ray Science. *Measurement Science and Technology* **2018**, *29* (3), 034004. https://doi.org/10.1088/1361-6501/aa9c19.
(201) De Andrade, V.; Deriy, A.; Wojcik, M. J.; Gürsoy, D.; Shu, D.; Fezzaa, K.; De Carlo, F. Nanoscale 3D Imaging at the Advanced Photon Source. *SPIE Newsroom* **2016**. https://doi.org/10.1117/2.1201604.006461.
(202) Pelt, D. M.; Gürsoy, D.; Palenstijn, W. J.; Sijbers, J.; De Carlo, F.; Batenburg, K. J. Integration of TomoPy and the ASTRA Toolbox for Advanced Processing and Reconstruction of Tomographic Synchrotron Data. *Journal of Synchrotron Radiation* **2016**, *23* (3), 842–849. https://doi.org/10.1107/S1600577516005658.

(203) Yang, X.; De Andrade, V.; Scullin, W.; Dyer, E. L.; Kasthuri, N.; De Carlo, F.; Gürsoy, D. Low-Dose x-Ray Tomography through a Deep Convolutional Neural Network. *Scientific Reports* **2018**, *8* (1). https://doi.org/10.1038/s41598-018-19426-7.

(204) Schuman, C. D.; Plank, J. S.; Bruer, G.; Anantharaj, J. Non-Traditional Input Encoding Schemes for Spiking Neuromorphic Systems. In *2019 International Joint Conference on Neural Networks (IJCNN)*; IEEE: Budapest, Hungary, 2019; pp 1–10. https://doi.org/10.1109/IJCNN.2019.8852139.

(205) Parsa, M.; Mitchell, J. P.; Schuman, C. D.; Patton, R. M.; Potok, T. E.; Roy, K. Bayesian Multi-Objective Hyperparameter Optimization for Accurate, Fast, and Efficient Neural Network Accelerator Design. *Front. Neurosci.* **2020**, *14*, 667. https://doi.org/10.3389/fnins.2020.00667.

(206) Bergstra, J.; Bengio, Y. Random Search for Hyper-Parameter Optimization. 25.

(207) Shahriari, B.; Swersky, K.; Wang, Z.; Adams, R. P.; de Freitas, N. Taking the Human Out of the Loop: A Review of Bayesian Optimization. *Proc. IEEE* **2016**, *104* (1), 148–175. https://doi.org/10.1109/JPROC.2015.2494218.

(208) Zhou, Z.; Rahman Siddiquee, M. M.; Tajbakhsh, N.; Liang, J. UNet++: A Nested U-Net Architecture for Medical Image Segmentation. In *Deep Learning in Medical Image Analysis and Multimodal Learning for Clinical Decision Support*; Stoyanov, D., Taylor, Z., Carneiro, G., Syeda-Mahmood, T., Martel, A., Maier-Hein, L., Tavares, J. M. R. S., Bradley, A., Papa, J. P., Belagiannis, V., Nascimento, J. C., Lu, Z., Conjeti, S., Moradi, M., Greenspan, H., Madabhushi, A., Eds.; Springer International Publishing: Cham, 2018; pp 3–11.

(209) Z. Zhou; M. M. R. Siddiquee; N. Tajbakhsh; J. Liang. UNet++: Redesigning Skip Connections to Exploit Multiscale Features in Image Segmentation. *IEEE Transactions on Medical Imaging* **2020**, *39* (6), 1856–1867. https://doi.org/10.1109/TMI.2019.2959609.

(210) Drozdzal, M.; Vorontsov, E.; Chartrand, G.; Kadoury, S.; Pal, C. The Importance of Skip Connections in Biomedical Image Segmentation. In *Deep Learning and Data Labeling for Medical Applications*; Carneiro, G., Mateus, D., Peter, L., Bradley, A., Tavares, J. M. R. S., Belagiannis, V., Papa, J. P., Nascimento, J. C., Loog, M., Lu, Z., Cardoso, J. S., Cornebise, J., Eds.; Lecture Notes in Computer Science; Springer International Publishing: Cham, 2016; Vol. 10008, pp 179–187. https://doi.org/10.1007/978-3-319-46976-8_19.

(211) Fourure, D.; Emonet, R.; Fromont, E.; Muselet, D.; Tremeau, A.; Wolf, C. Residual Conv-Deconv Grid Network for Semantic Segmentation. In *BMVC 2017*; Londre, United Kingdom, 2017.

(212) Yosinski, J.; Clune, J.; Bengio, Y.; Lipson, H. How Transferable Are Features in Deep Neural Networks? In *Advances in Neural Information Processing Systems*; Ghahramani, Z., Welling, M., Cortes, C., Lawrence, N., Weinberger, K. Q., Eds.; Curran Associates, Inc., 2014; Vol. 27.

(213) Ebner, M.; Geldmacher, F.; Marone, F.; Stampanoni, M.; Wood, V. X-Ray Tomography of Porous, Transition Metal Oxide Based Lithium Ion Battery Electrodes. *Advanced Energy Materials* **2013**, *3* (7), 845–850. https://doi.org/10.1002/aenm.201200932.

(214) Moroni, R.; Börner, M.; Zielke, L.; Schroeder, M.; Nowak, S.; Winter, M.; Manke, I.; Zengerle, R.; Thiele, S. Multi-Scale Correlative Tomography of a Li-Ion Battery Composite Cathode. *Sci Rep* **2016**, *6* (1), 30109. https://doi.org/10.1038/srep30109.

(215) Finegan, D. P.; Vamvakeros, A.; Tan, C.; Heenan, T. M. M.; Daemi, S. R.; Seitzman, N.; Di Michiel, M.; Jacques, S.; Beale, A. M.; Brett, D. J. L.; Shearing, P. R.; Smith, K. Spatial Quantification of Dynamic Inter and Intra Particle Crystallographic Heterogeneities within Lithium Ion Electrodes. *Nat Commun* **2020**, *11* (1), 631. https://doi.org/10.1038/s41467-020-14467-x.

(216) Nguyen, T.; Villanova, J.; Su, Z.; Tucoulou, R.; Fleutot, B.; Delobel, B.; Delacourt, C.; Demortière, A. 3D Quantification of Microstructural Properties of $LiNi_{0.5}Mn_{0.3}Co_{0.2}O_2$ High-Energy Density Electrodes by X-Ray Holographic Nano-Tomography. *Adv. Energy Mater.* **2021**, 2003529. https://doi.org/10.1002/aenm.202003529.

(217) Nikitin, V.; Andrade, V. D.; Slyamov, A.; Gould, B. J.; Zhang, Y.; Sampathkumar, V.; Kasthuri, N.; Gürsoy, D.; Carlo, F. D. Distributed Optimization for Nonrigid Nano-Tomography. *IEEE Transactions on Computational Imaging* **2021**, *7*, 272–287. https://doi.org/10.1109/TCI.2021.3060915.

(218) Pelt, D. M.; Sethian, J. A. A Mixed-Scale Dense Convolutional Neural Network for Image Analysis. *Proc Natl Acad Sci USA* **2018**, *115* (2), 254–259. https://doi.org/10.1073/pnas.1715832114.

(219) Ziabari, A.; Ye, D. H.; Srivastava, S.; Sauer, K. D.; Thibault, J.; Bouman, C. A. 2.5D Deep Learning For CT Image Reconstruction Using A Multi-GPU Implementation. In *2018 52nd Asilomar Conference on Signals, Systems, and Computers*; 2018; pp 2044–2049. https://doi.org/10.1109/ACSSC.2018.8645364.

(220) Strohmann, T.; Bugelnig, K.; Breitbarth, E.; Wilde, F.; Steffens, T.; Germann, H.; Requena, G. Semantic Segmentation of Synchrotron Tomography of Multiphase Al-Si Alloys Using a Convolutional Neural Network with a Pixel-Wise Weighted Loss Function. *Scientific Reports* **2019**, *9* (1). https://doi.org/10.1038/s41598-019-56008-7.

(221) Shaw, A.; Hunter, D.; Landola, F.; Sidhu, S. SqueezeNAS: Fast Neural Architecture Search for Faster Semantic Segmentation. In *2019 IEEE/CVF International Conference on Computer Vision Workshop (ICCVW)*; IEEE: Seoul, Korea (South), 2019; pp 2014–2024. https://doi.org/10.1109/ICCVW.2019.00251.

(222) Yan, X.; Jiang, W.; Shi, Y.; Zhuo, C. MS-NAS: Multi-Scale Neural Architecture Search for Medical Image Segmentation. In *Medical Image Computing and Computer Assisted Intervention – MICCAI 2020*; Martel, A. L., Abolmaesumi, P., Stoyanov, D., Mateus, D., Zuluaga, M. A., Zhou, S. K., Racoceanu, D., Joskowicz, L., Eds.; Springer International Publishing: Cham, 2020; pp 388–397.

(223) Amirreza Shaban, I. E., Shray Bansal, Zhen Liu; Boots, B. One-Shot Learning for Semantic Segmentation. In *Proceedings of the British Machine Vision Conference (BMVC)*; Tae-Kyun Kim, G. B., Stefanos Zafeiriou, Mikolajczyk, K., Eds.; BMVA Press, 2017; p 167.1-167.13. https://doi.org/10.5244/C.31.167.
(224) Wang, K.; Liew, J. H.; Zou, Y.; Zhou, D.; Feng, J. PANet: Few-Shot Image Semantic Segmentation With Prototype Alignment. In *2019 IEEE/CVF International Conference on Computer Vision (ICCV)*; IEEE: Seoul, Korea (South), 2019; pp 9196–9205. https://doi.org/10.1109/ICCV.2019.00929.
(225) Ioffe, S.; Szegedy, C. Batch Normalization: Accelerating Deep Network Training by Reducing Internal Covariate Shift. *arXiv:1502.03167 [cs]* **2015**.
(226) Glorot, X.; Bordes, A.; Bengio, Y. Deep Sparse Rectifier Neural Networks. 9.
(227) Kingma, D. P.; Ba, J. Adam: A Method for Stochastic Optimization. *arXiv:1412.6980 [cs]* **2017**.
(228) Simonyan, K.; Zisserman, A. Very Deep Convolutional Networks for Large-Scale Image Recognition. In *3rd International Conference on Learning Representations, ICLR 2015, San Diego, CA, USA, May 7-9, 2015, Conference Track Proceedings*; Bengio, Y., LeCun, Y., Eds.; 2015.
(229) Srivastava, N.; Hinton, G.; Krizhevsky, A.; Sutskever, I.; Salakhutdinov, R. Dropout: A Simple Way to Prevent Neural Networks from Overfitting. 30.
(230) Cho, S. A.; Jang, Y. J.; Lim, H.-D.; Lee, J.-E.; Jang, Y. H.; Nguyen, T.-T. H.; Mota, F. M.; Fenning, D. P.; Kang, K.; Shao-Horn, Y.; Kim, D. H. Hierarchical Porous Carbonized Co_3O_4 Inverse Opals via Combined Block Copolymer and Colloid Templating as Bifunctional Electrocatalysts in Li-O_2 Battery. *Advanced Energy Materials* **2017**, *7* (21), 1700391. https://doi.org/10.1002/aenm.201700391.
(231) Qin, L.; Lv, W.; Wei, W.; Kang, F.; Zhai, D.; Yang, Q.-H. Oxygen-Enriched Carbon Nanotubes as a Bifunctional Catalyst Promote the Oxygen Reduction/Evolution Reactions in Li-O2 Batteries. *Carbon* **2019**, *141*, 561–567. https://doi.org/10.1016/j.carbon.2018.10.025.
(232) Schroeder, M. A.; Pearse, A. J.; Kozen, A. C.; Chen, X.; Gregorczyk, K.; Han, X.; Cao, A.; Hu, L.; Lee, S. B.; Rubloff, G. W.; Noked, M. Investigation of the Cathode–Catalyst–Electrolyte Interface in Aprotic Li–O_2 Batteries. *Chemistry of Materials* **2015**, *27* (15), 5305–5313. https://doi.org/10.1021/acs.chemmater.5b01605.
(233) Salehi, M.; Shariatinia, Z. An Optimization of MnO 2 Amount in CNT-MnO 2 Nanocomposite as a High Rate Cathode Catalyst for the Rechargeable Li-O 2 Batteries. *Electrochimica Acta* **2016**, *188*, 428–440. https://doi.org/10.1016/j.electacta.2015.12.016.
(234) Lee, H. C.; Park, J. O.; Kim, M.; Kwon, H. J.; Kim, J.-H.; Choi, K. H.; Kim, K.; Im, D. High-Energy-Density Li-O2 Battery at Cell Scale with Folded Cell Structure. *Joule* **2019**, *3* (2), 542–556. https://doi.org/10.1016/j.joule.2018.11.016.
(235) Jiang, J.; He, P.; Tong, S.; Zheng, M.; Lin, Z.; Zhang, X.; Shi, Y.; Zhou, H. Ruthenium Functionalized Graphene Aerogels with Hierarchical and Three-Dimensional Porosity as a Free-Standing Cathode for Rechargeable Lithium-Oxygen Batteries. *NPG Asia Materials* **2016**, *8* (1), e239–e239. https://doi.org/10.1038/am.2015.141.
(236) Liu, T.; Liu, Z.; Kim, G.; Frith, J. T.; Garcia-Araez, N.; Grey, C. P. Understanding LiOH Chemistry in a Ruthenium-Catalyzed Li-O_2 Battery. *Angew. Chem. Int. Ed.* **2017**, *56* (50), 16057–16062. https://doi.org/10.1002/anie.201709886.
(237) Kuboki, T.; Okuyama, T.; Ohsaki, T.; Takami, N. Lithium-Air Batteries Using Hydrophobic Room Temperature Ionic Liquid Electrolyte. *Journal of Power Sources* **2005**, *146* (1–2), 766–769. https://doi.org/10.1016/j.jpowsour.2005.03.082.
(238) Neale, A. R.; Li, P.; Jacquemin, J.; Goodrich, P.; Ball, S. C.; Compton, R. G.; Hardacre, C. Effect of Cation Structure on the Oxygen Solubility and Diffusivity in a Range of Bis{(Trifluoromethyl)Sulfonyl}imide Anion Based Ionic Liquids for Lithium–Air Battery Electrolytes. *Physical Chemistry Chemical Physics* **2016**, *18* (16), 11251–11262. https://doi.org/10.1039/C5CP07160G.

Valorizations

- Software:
  - SegmentPy: https://segmentpy.readthedocs.io (Open Source)

- Publication:
  - Facile synthesis of a self-standing and recyclable binder-free cathode for Li-O_2 battery, Z. Su, I. Temprano, N. Folastre, G. Gachot, V. De Andrade, E. Shevchenko, C. Grey, A. A. Franco, A. Demortière ACS. *Sustainable Chem. Eng.* (in submission)
  - Towards a Local In-situ X-ray nano-Computed Tomography under realistic cycling condition for Battery Research Z. Su, T. T. Nguyen, C. Le Bourlot, F. Cadiou, A. Jamali, V. De Andrade, A. A. Franco, A. Demortière, Chem. Method. (in review)
  - Artificial Neural Network Approach for Multiphase Segmentation of Battery Electrode Nano-CT Images, Z.Su, E. Decencière, T.T. Nguyen, K. El-Amiry, V. De Andrade, A. A. Franco, A. Demortière, NPJ. Nat. Comp. Mat. (in review)
  - Operando XANES-Tomography nanoCT for studying NMC cathodeelectrode, T.T. Nguyen, Z. Su, V. De Andrade, B. Delobel, C. Delacourt, A. Demortière, ACS Energy letters, 2021 (en préparation)
  - Self-supervised image quality assessment for X-ray tomographic images of Li-ion battery materials, Kai Zhang, T.T. Nguyen, Z. Su, A. Demortière (in review)
  - 3D Quantification of Microstructural Properties of LiNi0.5Mn0.3Co0.2O2 High-Energy Density Electrodes by X-Ray Holographic Nano-Tomography, T.T. Nguyen, J. Villanova, Z. Su, R. Tucoulou, B. Fleutot, B. Delobel, C. Delacourt, Charles, A. Demortière, Adv. Energy Mater. 11, 2003529. (2021)
  - Probing and Interpreting the Porosity and Tortuosity Evolution of Li-O2 Cathodes on Discharge through a Combined Experimental and Theoretical Approach, A. Torayev, S. Engelke, Z. Su, L.E. Marbella, V. De Andrade, A. Demortière, P.C.M.M Magusin, C. Merlet, A.A. Franco, C.P. Grey J. Phys. Chem. C 4955−4967 125 (2021)
  - X‐ray Nanocomputed Tomography in Zernike Phase Contrast for Studying 3D Morphology of Li−O_2 Battery Electrode, Z. Su, V. De Andrade, S. Cretu, Y. Yin, M.J. Wojcik, A.A. Franco, A. Demortière, ACS Appl. Energy Mater. 4093−4102 3 (2020)

- Presentation / Seminar:
  - 2018 Strasbourg: 3D and 4D development by Synchrotron X Ray Tomography for morphological and kinetical study of Li-O2 battery (Zernike, *in situ* nano-XCT)

    - 2018 Lyon: 3D and 4D development by Synchrotron X Ray Tomography for morphological and kinetical study of Li-O2 battery (Zernike, *in situ* nano-XCT)
    - 2019 Lille: *Développement de l'outil d'apprentissage automatique pour le traitement des données massives en tomographie aux rayonnements X du synchrotron* (Deep Learning)
    - 2020 Chicago: Charactizing the light elements in batteries using X-ray tomography (Zernike, in situ XCT, Deep Learning)
- Workshop hosted:
    - 2019 Amiens: GdR CNRS nanOperando – Machine Learning Section: Hands-on practices on Machine Learning
- Poster:
    - 2019 Paris: Development of 3D and 4D imaging by X-ray synchrotron tomography for morphological and kinetic studies of new generation Li-S and Li-air Batteries (Zernike)
    - 2021 Reims: Using Convolutional Neural Network for segmenting nano-XCT Images of battery materials (Deep Learning)